Applications of the Octet Baryon Quark-Meson Coupling Model to Hybrid Stars

Jonathan David Carroll

(Supervisors: Prof. D. B. Leinweber, Prof. A. G. Williams)

A Thesis presented for the degree of
Doctor of Philosophy

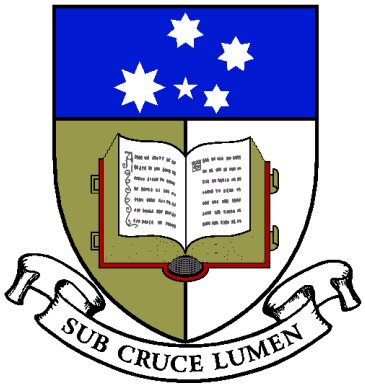

Special Research Centre
for the Subatomic Structure of Matter
School of Chemistry & Physics
University of Adelaide
South Australia

November 2009

Dedicated to my wife, Susanne;
for her love, sacrifice, and support of
a student for so many years.

Abstract

The study of matter at extreme densities has been a major focus in theoretical physics in the last half-century. The wide spectrum of information that the field produces provides an invaluable contribution to our knowledge of the world in which we live. Most fascinatingly, the insight into the world around us is provided from knowledge of the intangible, at both the smallest and largest scales in existence.

Through the study of nuclear physics we are able to investigate the fundamental construction of individual particles forming nuclei, and with further physics we can extrapolate to neutron stars. The models and concepts put forward by the study of nuclear matter help to solve the mystery of the most powerful interaction in the universe; the strong force.

In this study we have investigated a particular state-of-the-art model which is currently used to refine our knowledge of the workings of the strong interaction and the way that it is manifested in both neutron stars and heavy nuclei, although we have placed emphasis on the former for reasons of personal interest. The main body of this work has surrounded an effective field theory known as Quantum Hadrodynamics (QHD) and its variations, as well as an extension to this known as the Quark-Meson Coupling (QMC) model, and variations thereof. We further extend these frameworks to include the possibility of a phase transition from hadronic matter to deconfined quark matter to produce hybrid stars, using various models.

We have investigated these pre-existing models to deeply understand how they are justified, and given this information, we have expanded them to incorporate a modern understanding of how the strong interaction is manifest.

Statement of Originality

This work contains no material which has been accepted for the award of any other degree or diploma in any university or other tertiary institution to Jonathan David Carroll and, to the best of my knowledge and belief, contains no material previously published or written by another person, except where due reference has been made in the text.

I give consent to this copy of my thesis when deposited in the University Library, being made available for loan and photocopying, subject to the provisions of the Copyright Act 1968. The author acknowledges that copyright of published works contained within this thesis (as listed below*) resides with the copyright holder(s) of those works.

I also give permission for the digital version of my thesis to be made available on the web, via the University's digital research repository, the Library catalogue, the Australasian Digital Theses Program (ADTP) and also through web search engines, unless permission has been granted by the University to restrict access for a period of time.

*Published article: Carroll *et al.* Physical Review C 79, 045810

Jonathan David Carroll

Acknowledgements

The work contained herein would not have been possible without the guidance, support, and co-operation of my supervisors: Prof. Anthony G. Williams and Prof. Derek B. Leinweber, nor that of Prof. Anthony W. Thomas at Jefferson Lab, Virginia, USA. Their time and knowledge has been volunteered to seed my learning, and I hope that the pages that follow are a suitable representation of what has sprouted forth.

I would also like to acknowledge the help I have received from the staff of—and access I have been given to the facilities at—eResearchSA (formerly SAPAC). Many of the calculations contained within this thesis have required computing power beyond that of standard desktop machines, and I am grateful for the use of supercomputer facilities, along with general technical support.

In addition, I would also like to thank everyone else who has provided me with countless hours of conversation both on and off topic which have lead me to where I am now: Mr. Mike D'Antuoni, Dr. Padric McGee, Dr. Sarah Lawley, Dr. Ping Wang, Dr. Sam Drake, Dr. Alexander Kallionatis, Dr. Sundance Bilson-Thompson, and all of my teachers, lecturers and fellow students who have helped me along the way.

I owe a lot of thanks to the CSSM office staff, who have played the roles of 'mums at work' for so many of us: Sara Boffa, Sharon Johnson, Silvana Santucci, Rachel Boutros and Bronwyn Gibson. Also, a special thanks to both Ramona Adorjan and Grant Ward, for providing their inimitable support with computers, and for their friendship; it is rare to find people who can give both.

My sincere thanks go to Benjamin Menadue for his thorough proof-reading of this thesis, saving me from making several erroneous and poorly worded statements.

Of course, I would like to thank my family (and family-in-law) for all of their support and patience over the years, and for feigning interest while I described something that I found particularly remarkable.

Lastly, I would like to thank the cafés who have supported my 'passionate interest in coffee' over the past few years; I am now known by name at several of these, and their abilities to make a great latté have kept me going through many a tired day (and night).

Contents

List of Figures

List of Tables

Introduction

The world we live in is a strange and wonderful place. The vast majority of our interactions with objects around us can be described and predicted by relatively simple equations and relations, which have been fully understood for centuries now. The concept of this tactile world is however, a result of averaging a vast ensemble of smaller effects on an unimaginably small scale, all conspiring together to produce what we observe at the macroscopic level. In order to investigate this realm in which particles can fluctuate in and out of existence in the blink of an eye, we must turn to more sophisticated descriptions of the players on this stage.

This research has the goal of furthering our understanding of the interior of what are loosely called 'neutron stars', though as shall be shown herein, the contents are not necessarily only neutrons. With this in mind, further definitions include '*hyperon stars*', '*quark stars*', and '*hybrid stars*', to describe compact stellar objects containing hyperons[1], quarks, and a mixture of each, respectively. In order to do this, we require physics beyond that which describes the interactions of our daily lives; we require physics that describes the individual interactions between particles, and physics that describes the interactions between enormous quantities of particles.

Only by uniting the physics describing the realm of the large and that of the small can one contemplate so many orders of magnitude in scale; from individual particles with a diameter of less than 10^{-22} m, up to neutron stars with a diameter of tens of kilometers. Yet the physics at each end of this massive scale are unified in this field of nuclear matter in which interactions of the smallest theorized entities conspire in such a way that densities equivalent to the mass of humanity compressed to the size of a mere sugar cube become commonplace, energetically favourable, and stable.

The sophistication of the physics used to describe the world of the tiny and that of the enormous has seen much development over time. The current knowledge of particles has reached a point where we are able to make incredibly precise predictions about the properties of single particles and have them confirmed with equally astonishing accuracy from experiments. The physics describing neutron stars has progressed from relatively simple (yet sufficiently consistent with experiment) descriptions of neutron (and nucleon) matter to many more sophisticated descriptions involving various species of baryons, mesons, leptons and even quarks.

The outcome of work such as this is hopefully a better understanding of matter at both the microscopic and macroscopic scales, as well as the theory and formalism that unites these two extremes. The primary methods which we have used to construct models in this thesis are Quantum Hadrodynamics (QHD)—which shall be described in Sec. 3.1—and the Quark-Meson Coupling (QMC) model, which shall be described in Sec. 3.2.

In this thesis, we will outline the research undertaken in which we produce a model for neutron star structure which complies with current theories for dense matter at and above nuclear density and is consistent with current data for both finite nuclei and observed neutron stars. Although only experimental evidence can successfully validate any theory, we hope

[1] Baryons for which one or more of the three valence quarks is a strange quark. For example, the Σ^+ hyperon contains two up quarks and a strange quark. For a table of particle properties, including quark content, refer to Table B.1

to convey a framework and model that possesses a minimum content of inconsistencies or unjustified assumptions such that any predictions that are later shown to be fallacious can only be attributed to incorrect initial conditions.

As a final defense of any inconsistencies that may arise between this research and experiment, we refer the reader to one of the author's favourite quotes:

> "There is a theory which states that if ever anyone discovers exactly what the Universe is for and why it is here, it will instantly disappear and be replaced by something even more bizarre and inexplicable.
>
> There is another theory which states that this has already happened."
>
> – Douglas Adams, The Hitchhiker's Guide To The Galaxy.

Our calculations will begin at the particle interaction level, which will be described in more detail in Section 2, from which we are able to reproduce the bulk properties of matter at high densities, and which we shall discuss in Sections 3.1–3.5. The methods for producing our simulations of the interactions and bulk properties will be detailed in Section 4, along with a discussion on how this is applied to the study of compact stellar objects. The results of the simulations and calculations will be discussed in detail in Section 5, followed by discussions on the interpretation of these results in Section 6. For the convenience of the reader, and for the sake of completeness, derivations for the majority of the equations used herein are provided in Appendix A, and useful information regarding particles is provided in Appendix B. For now however, we will provide a brief introduction to this field of study.

1.1 The Four Forces

Theoretical particle physics has seen much success and found many useful applications; from calculating the individual properties of particles to precisions that rival even the best experimental setups, to determining the properties of ensembles of particles of greater and greater scale, and eventually to the properties of macroscopic objects as described by their constituents.

In order to do this, we need to understand each of the four fundamental forces in Nature. The weakest of these forces—gravity—attracts any two masses, and will become most important in the following section. Slightly stronger is electromagnetism; the force responsible for electric charge and magnetism. This force provides an attraction between opposite electric charges (and of course, repulsion between like charges), and thus helps to bind electrons to nuclei. The mathematical description of this effect is Quantum Electrodynamics (QED).

The 'weak nuclear force'—often abbreviated to 'the weak force'—is responsible for the decay of particles and thus radioactivity in general. At high enough energies, this force is unified with electromagnetism into the 'electro-weak force'. The strongest of all the forces is the 'strong nuclear force', abbreviated to 'the strong force'. This force is responsible for attraction between certain individual particles over a very short scale, and is responsible for the binding of protons within nuclei which would otherwise be thrown apart by the repulsive electromagnetic force between the positively charged protons. Each of these forces plays a part in the work contained herein, but the focus of our study will be the strong force.

A remarkably successful description of the strongest force at the microscopic level is 'Quantum Chromodynamics' (QCD) which is widely believed to be the true description of strong interactions, relying on quark and gluon degrees of freedom. The major challenge of this theory is that at low energies it is non-perturbative[2], in that the coupling constant —which one would normally perform a series-expansion in powers of—is large, and thus is not suitable for such an expansion. Regularisation techniques have been produced to create perturbative descriptions of QCD, but perturbative techniques fail to describe both dynamical chiral symmetry breaking and confinement; two properties observed in Nature.

Rather than working directly with the quarks and gluons of QCD, another option is to construct a model which reproduces the effects of QCD using an effective field theory. This is a popular method within the field of nuclear physics, and the route that has be taken for this work. More precisely, we utilise a balance between attractive and repulsive meson fields to reproduce the binding between fermions that the strong interaction is responsible for.

1.2 Neutron Stars

Although gravity may be the weakest of the four fundamental forces over comparable distance scales, it is the most prevalent over (extremely) large distances. It is this force that must be overcome for a star to remain stable against collapse. Although a description of this force that unifies it with the other three forces has not been (satisfactorily) found, General Relativity has proved its worth for making predictions that involve large masses.

At the time when neutron stars were first proposed by Baade and Zwicky [2], neutrons had only been very recently proven to exist by Chadwick [3]. Nonetheless, ever increasingly more sophisticated and applicable theories have continually been produced to model the interactions that may lead to these incredible structures; likely the most dense configuration of particles that can withstand collapse.

The current lack of experimental data for neutron stars permits a wide variety of models [4–9], each of which is able to successfully reproduce the observed properties of neutron stars, and most of which are able to reproduce current theoretical and experimental data for finite nuclei and heavy-ion collisions [10, 11]. The limits placed on models from neutron star observations [12–14] do not sufficiently constrain the models, so we have the opportunity to enhance the models based on more sophisticated physics, while still retaining the constraints above.

The story of the creation of a neutron star begins with a reasonably massive star, with a mass greater than eight solar masses ($M > 8\ M_\odot$). After millions to billions of years or so (depending on the exact properties of the star), this star will have depleted its fuel by fusion of hydrogen into ^{3}He, ^{4}He, and larger elements up to iron (the most stable element since has the highest binding energy per nucleon).

At this point, the core of the star will consist of solid iron, as the heaviest elements are gravitationally attracted to the core of the star, with successively lighter elements layered on top in accordance with the traditional onion analogy. The core is unable to become any more stable via fusion reactions and is only held up against gravitational collapse by the

[2] At high energies, QCD becomes asymptotically free [1] and can be treated perturbatively. The physics of our world however is largely concerned with low energies.

degeneracy pressure of the electrons[3]. The contents of the upper layers however continue to undergo fusion to heavier elements which also sink towards the core, adding to the mass of the lower layers and thus increasing the gravitational pressure below.

This causes the temperature and pressure of the star to increase, which encourages further reactions in the upper levels. Iron continues to pile on top of the core until it reaches the Chandrasekhar limit of $M = 1.4\ M_\odot$, at which point the electron degeneracy pressure is overcome. The next step is not fully understood[4], but the result is a Type II supernova.

At the temperatures and pressures involved here, it is energetically favourable for the neutrons to undergo β-decay into protons, electrons (or muons), and antineutrinos according to

$$n \to p^+ + e^- + \bar{\nu}_{e^-}. \tag{1.1}$$

These antineutrinos have a mean-free path of roughly 10 cm [15] at these energies, and are therefore trapped inside the star, causing a neutrino pressure bubble with kinetic energy of order 10^{51} erg $= 6.2 \times 10^{56}$ MeV [15]. With the core collapsing (and producing even more antineutrinos) even the rising pressure of the bubble cannot support the mass of the material above and the upper layers begin falling towards the core.

The sudden collapse causes a shock-wave which is believed to '*bounce*' at the core and expel the outer layers of the star in a mere fraction of a second, resulting in what we know as a supernova, and leaving behind the expelled material which, when excited by radiation from another star, can be visible from across the galaxy as a supernova remnant (SNR).

At the very centre of the SNR, the remaining core of the star (naïvely a sphere of neutrons, with some fraction of protons, neutrons and electrons) retains the angular momentum of the original star, now with a radius on the order of 10 km rather than 10^9 km and thus neutron stars are thought to spin very fast, with rotational frequencies of up to 0.716 MHz [16]. Via a mechanism involving the magnetic field of the star, these spinning neutron stars may produce a beam of radiation along their magnetic axis, and if that beam happens to point towards Earth to the extent that we can detect it, we call the star a pulsar. For the purposes of this research, we shall assume the simple case that the objects we are investigating are static and non-rotating. Further calculations can be used to extrapolate the results to rotating solutions, but we shall not focus on this aspect here.

A further option exists; if the pressure and temperature (hence energy) of the system become great enough, other particles can be formed via weak reactions; for example, hyperons. The methods employed in this thesis have the goal of constructing models of matter at super-nuclear densities, and from these, models of neutron stars. The outcome of these calculations is a set of parameters which describe a neutron star (or an ensemble of them). Of these, the mass of a neutron star is an observable quantity. Other parameters, such as radius, energy, composition and so forth are unknown, and only detectable via higher-order (or proxy) observations.

The ultimate goal would be finding a physically realistic model based on the interactions of particles, such that we are able to deduce the structure and global properties of a neutron star based only on an observed mass. This however—as we shall endeavor to show—is easier said than done.

[3] In accordance with the Pauli Exclusion Principle, no two fermions can share the same quantum state. This limits how close two fermions—in this case, electrons—can be squeezed, leading to the degeneracy pressure.

[4] At present, models of supernova production have been unable to completely predict observations.

Particle Physics & Quantum Field Theory

In our considerations of the models that follow we wish to explore ensembles of particles and their interactions. In order to describe these particles we rely on Quantum Field Theory (QFT), which mathematically describes the 'rules' these particles obey. The particular set of rules that are believed to describe particles obeying the strong force at a fundamental level is Quantum Chromodynamics (QCD), but as mentioned in the introduction, this construction is analytically insolvable, so we rely on a model which simulates the properties that QCD predicts.

In the following sections, we will outline the methods of calculating the properties of matter from a field theoretic perspective.

2.1 Lagrangian Density

The first step to calculating any quantity in a Quantum Field Theory is to construct a Lagrangian density, which summarizes the dynamics of the system, and from which the equations of motion can be calculated. In order to do this, we must define precisely what it is that we wish to calculate the properties of.

The classification schemes of particle physics provide several definitions into which particles are identified, however each of these provides an additional piece of information about those particles. We wish to describe nucleons N (consisting of protons p, and neutrons n) which are hadrons[1], and are also fermions[2].

We will extend our description to include the hyperons Y (baryons with one or more valence strange quarks) consisting of Λ, Σ^-, Σ^0, Σ^+, Ξ^-, and Ξ^0 baryons. The hyperons, together with the nucleons, form the octet of baryons (see Fig. B.1).

We can describe fermions as four-component spinors ψ of plane-wave solutions to the Dirac Equation (see later), such that

$$\psi = u(\vec{p})e^{-ip_\mu x^\mu}, \tag{2.1}$$

where $u(\vec{p})$ are four-component Dirac spinors related to plane-waves with wave-vector $\vec{p}$ that carry the spin information for a particle, and which shall be discussed further in Appendix A.3. For convenience, we can group the baryon spinors by isospin group, since this is a degree of freedom that will become important. For example, we can collectively describe nucleons as a (bi-)spinor containing protons and neutrons, as

$$\psi_N = \begin{pmatrix} \psi_p(s) \\ \psi_n(s') \end{pmatrix}. \tag{2.2}$$

Here we have used the labels for protons and neutrons rather than explicitly using a label for isospin. We will further simplify this by dropping the label for spin, and it can be assumed

[1] Bound states of quarks. In particular, bound states of three 'valence' quarks plus any number of quark-antiquark pairs (the 'sea' quarks, which are the result of particle anti-particle production via gluons) are called baryons.

[2] Particles which obey Fermi–Dirac statistics, in which the particle wavefunction is anti-symmetric under exchange of particles; the property which leads to the Pauli Exclusion Principle.

that this label is implied. We will also require the Dirac Adjoint to describe the antibaryons, and this is written as

$$\bar{\psi} = \psi^\dagger \gamma^0. \tag{2.3}$$

Similarly, we can construct spinors for all the baryons. With these spinors we can construct a Lagrangian density to describe the dynamics of these particles. Since we are describing spin-$\frac{1}{2}$ particles we expect the spinors to be solutions of the Dirac equation which in natural units (for which $\hbar = c = 1$) is written as

$$(i\gamma^\mu \partial_\mu - M)\,\psi = (i\not{\partial} - M)\,\psi = 0, \tag{2.4}$$

and similarly for the antiparticle $\bar{\psi}$. Feynman slash notation is often used to contract and simplify expressions, and is simply defined as $\not{A} = \gamma_\mu A^\mu$. Here, ∂_μ is the four-derivative, M is the mass of the particle, and γ^μ are the (contravariant) Dirac Matrices, which due to the anti-commutation relation of

$$\left\{\gamma^\alpha, \gamma^\beta\right\} = \gamma^\alpha\gamma^\beta - \gamma^\beta\gamma^\alpha = 2\eta^{\alpha\beta}\mathbb{I}, \tag{2.5}$$

(where $\eta = \mathrm{diag}(+1, -1, -1, -1)$ is the Minkoswki metric) generate a matrix representation of the Clifford Algebra $Cl(1,3)$. They can be represented in terms of the 2×2 identity matrix $\mathbb{I}$, and the Pauli Matrices $\vec{\sigma}$, as

$$\gamma^0 = \begin{pmatrix} \mathbb{I} & 0 \\ 0 & -\mathbb{I} \end{pmatrix}, \qquad \gamma^i = \begin{pmatrix} 0 & \sigma^i \\ -\sigma^i & 0 \end{pmatrix}. \tag{2.6}$$

Eq. (2.4) describes free baryons, so we can use this as the starting point for our Lagrangian density, and thus if we include each of the isospin groups, we have

$$\mathcal{L} = \sum_k \bar{\psi}_k \left(i\not{\partial} - M_k\right)\psi_k \;;\; k \in \{N, \Lambda, \Sigma, \Xi\}, \tag{2.7}$$

where the baryon spinors are separated into isospin groups, as

$$\psi_N = \begin{pmatrix} \psi_p \\ \psi_n \end{pmatrix}, \quad \psi_\Lambda = \begin{pmatrix} \psi_\Lambda \end{pmatrix}, \quad \psi_\Sigma = \begin{pmatrix} \psi_{\Sigma^+} \\ \psi_{\Sigma^0} \\ \psi_{\Sigma^-} \end{pmatrix}, \quad \psi_\Xi = \begin{pmatrix} \psi_{\Xi^0} \\ \psi_{\Xi^-} \end{pmatrix}. \tag{2.8}$$

This implies that the mass term is also a diagonal matrix. In many texts this term is simply a scalar mass term multiplied by a suitable identity matrix, but that would imply the existence of a charge symmetry; that the mass of the proton and of the neutron were degenerate, and exchange of charges would have no effect on the Lagrangian density. We shall not make this assumption, and will rather work with the physical masses as found in Ref. [17], so M_k will contain distinct values along the diagonal.

To this point, we have constructed a Lagrangian density for the dynamics of free baryons. In order to simulate QCD, we require interactions between baryons and mesons to produce the correct phenomenology. Historically, the scalar-isoscalar meson[3] σ and vector-isoscalar meson ω have been used to this end. Additionally, the vector-isovector ρ meson has been included (for asymmetric matter) to provide a coupling to the isospin channel [18].

[3] Despite it's dubious status as a distinct particle state, rather than a resonance of $\pi\pi$.

In order to describe interactions of the baryons with mesons, we can include terms in the Lagrangian density for various classes of mesons by considering the appropriate bilinears that each meson couples to. For example, if we wish to include the ω meson, we first observe that as a vector meson it will couple to a vector bilinear (to preserve Lorentz invariance) as

$$-ig_\omega\bar{\psi}\gamma_\mu\omega^\mu\psi \tag{2.9}$$

with coupling strength g_ω, which as we shall see, may be dependent on the baryon that the meson is coupled to. The particular coefficients arise from the Feynman rules for meson-baryon vertices (refer to Appendix A.1). This particular vertex is written in Feynman diagram notation as shown in Fig. 2.1(b).

This is not the only way we can couple a meson to a baryon. We should also consider the Yukawa couplings of mesons to baryons with all possible Lorentz characteristics; for example, the ω meson can couple to a baryon ψ, with several different vertices:

$$\bar{\psi}\gamma_\mu\omega^\mu\psi, \quad \bar{\psi}\sigma_{\mu\nu}q^\nu\omega^\mu\psi, \text{ and } \bar{\psi}q_\mu\omega^\mu\psi, \tag{2.10}$$

where q_μ represents the baryon four-momentum transfer $(q_f - q_i)_\mu$. The latter two of these provides a vanishing contribution when considering the mean-field approximation (which shall be defined in Section 2.2), since $\sigma_{00} = 0$ and $q_\mu = 0$, as the system is on average, static.

If we include the appropriate scalar and vector terms—including an isospin-coupling of the ρ meson—in our basic Lagrangian density we have

$$\mathcal{L} = \sum_k \bar{\psi}_k \left(\gamma_\mu \left[i\partial^\mu - g_{k\omega}\omega^\mu - g_\rho(\vec{\tau}_{(k)}\cdot\vec{\rho}^\mu)\right] - M_k + g_{k\sigma}\sigma\right)\psi_k \;;\; k \in \{N, \Lambda, \Sigma, \Xi\}. \tag{2.11}$$

The isospin matrices $\vec{\tau}_{(k)}$ are scaled Pauli matrices of appropriate order for each of the isospin groups, the third components of which are given explicitly here as

$$\tau_{(N)3} = \tau_{(\Xi)3} = \frac{1}{2}\begin{bmatrix} 1 & 0 \\ 0 & -1 \end{bmatrix}, \quad \tau_{(\Lambda)3} = 0, \quad \tau_{(\Sigma)3} = \begin{bmatrix} 1 & 0 & 0 \\ 0 & 0 & 0 \\ 0 & 0 & -1 \end{bmatrix}, \tag{2.12}$$

for which the diagonal elements of $\tau_{(k)3}$ are the isospin projections of the corresponding baryons within an isospin group defined by Eq. (2.8), i.e. $\tau_{(p)3} = I_{3p} = +\frac{1}{2}$.

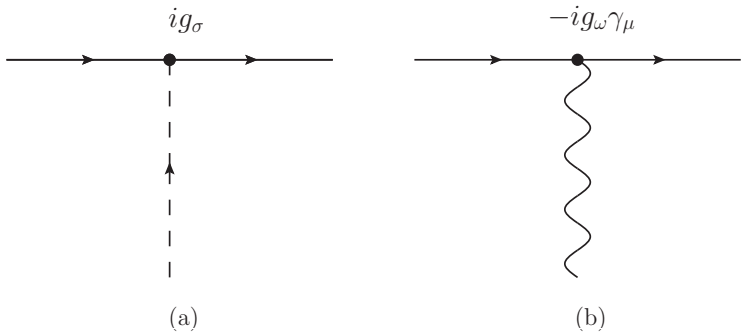

Fig. 2.1: Interaction vertex for the (a) scalar and (b) vector mesons, where the solid lines represent baryons ψ, the dashed line represents a scalar meson (e.g. σ), and the wavy line represents a vector meson (e.g. ω_μ).

At this point it is important that we remind the reader that the conventions in this field do not distinguish the use of explicit Einstein summation, and that within a single equation, indices may represent summation over several different spaces. To make this clearer, we will show an example of a term where all the indices are made explicit; the interaction term for the ρ meson in Eq. (2.11) for which we explicitly state all of the indices

$$\begin{aligned}\mathcal{L}_\rho &= \sum_k g_\rho\, \bar{\psi}_k \gamma^\mu \vec{\tau}_{(k)} \cdot \vec{\rho}_\mu \psi_k \\ &= \sum_k \sum_{i,j=1}^{f_k} \sum_{\alpha,\beta=1}^{4} \sum_{\mu=0}^{3} \sum_{a=1}^{3} g_\rho \left(\bar{\psi}_k^i\right)_\alpha \left(\gamma^\mu\right)_{\alpha\beta} \left(\tau_{(k)}^a\right)^{ij} \rho_\mu^a \left(\psi_k^j\right)_\beta ,\end{aligned} \tag{2.13}$$

where here k is summed over isospin groups N, Λ, Σ, and Ξ; i and j are summed over flavor space (within an isospin group of size f_k, e.g. $f_N = 2$, $f_\Sigma = 3$); α and β are summed over Dirac space; μ is summed over Lorentz space; and a is summed over iso-vector space. The Pauli matrices, of which $(\tau_k^a)^{ij}$ are the elements, are defined in Eq. (2.12). This level of disambiguity is overwhelmingly cluttering, so we shall return to the conventions of this field and leave the indices as implicit.

In addition to the interaction terms, we must also include the free terms and field tensors for each of the mesons, which are chosen with the intent that applying the Euler–Lagrange equations to these terms will produce the correct phenomenology, leading to

$$\begin{aligned}\mathcal{L} = &\sum_k \bar{\psi}_k \left(\gamma_\mu \left[i\partial^\mu - g_{k\omega}\omega^\mu - g_\rho(\vec{\tau}_{(k)} \cdot \vec{\rho}^\mu)\right] - M_k + g_{k\sigma}\sigma\right)\psi_k \\ &+ \frac{1}{2}(\partial_\mu\sigma\partial^\mu\sigma - m_\sigma^2\sigma^2) + \frac{1}{2}m_\omega^2\omega_\mu\omega^\mu + \frac{1}{2}m_\rho^2\rho_\mu\rho^\mu - \frac{1}{4}\Omega_{\mu\nu}\Omega^{\mu\nu} - \frac{1}{4}R_{\mu\nu}^a R_a^{\mu\nu},\end{aligned} \tag{2.14}$$

where the field tensors for the ω and ρ mesons are, respectively,

$$\Omega_{\mu\nu} = \partial_\mu\omega_\nu - \partial_\nu\omega_\mu, \quad R_{\mu\nu}^a = \partial_\mu\rho_\nu^a - \partial_\nu\rho_\mu^a - g_\rho\epsilon^{abc}\rho_\mu^b\rho_\nu^c. \tag{2.15}$$

This is the Lagrangian density that we will begin with for the models we shall explore herein. Many texts (for example, Refs. [19–22]) include higher-order terms ($\mathcal{O}(\sigma^3)$, $\mathcal{O}(\sigma^4)$, ...) and have shown that these do indeed have an effect on the state variables, but in the context of this work, we shall continue to work at this order for simplicity. It should be noted that the higher order terms for the scalar meson can be included in such a way as to trivially reproduce a framework consistent with the Quark-Meson Coupling model that shall be described later, and thus we are not entirely excluding this contribution.

2.2 Mean-Field Approximation

To calculate properties of matter, we will use an approximation to simplify the quantities we need to evaluate. This approximation, known as a Mean-Field Approximation (MFA) is made on the basis that we can separate the expression for a meson field α into two parts: a constant classical component, and a component due to quantum fluctuations;

$$\alpha = \alpha_{\text{classical}} + \alpha_{\text{quantum}}. \tag{2.16}$$

If we then take the vacuum expectation value (the average value in the vacuum) of these components, the quantum fluctuation term vanishes, and we are left with the classical component

$$\langle \alpha \rangle \equiv \langle \alpha_{\text{classical}} \rangle. \tag{2.17}$$

This component is what we shall use as the meson contribution, and we will assume that this contribution (at any given density) is constant. This can be thought of as a background 'field' on top of which we place the baryon components. For this reason, we consider the case of *infinite matter*, in which there are no boundaries to the system. The core of lead nuclei (composed of over 200 nucleons) can be thought of in this fashion, since the effects of the outermost nucleons are minimal compared to the short-range strong nuclear force.

Furthermore, given that the ground-state of matter will contain some proportion of proton and neutron densities, any flavor-changing meson interactions will provide no contribution in the MFA, since the overlap operator between the ground-state $|\Psi\rangle$ and any other state $|\xi\rangle$ is orthogonal, and thus

$$\langle\ \Psi\ |\ \xi\ \rangle = \delta_{\Psi\xi}. \tag{2.18}$$

For this reason, any meson interactions which, say, interact with a proton to form a neutron will produce a state which is not the ground state, and thus provides no contribution to the MFA. We will show in the next section that this is consistent with maintaining isospin symmetry.

2.3 Symmetries

In the calculations that will follow, there are several terms that we will exclude from our considerations *ab initio* (including for example, some that appear in Eq. (2.14)) because they merely provide a vanishing contribution, such as the quantum fluctuations mentioned above. These quantities shall be noted here, along with a brief argument supporting their absence in further calculations.

2.3.1 Rotational Symmetry and Isospin

The first example is simple enough; we assume rotational invariance of the fields to conserve Lorentz invariance. In order to maintain rotational invariance in all frames, we require that the spatial components of vector quantities vanish, leaving only temporal components. For example, in the MFA the vector-isoscalar meson four-vector ω_μ can be reduced to the temporal component ω_0, and for notational simplicity, we will often drop the subscript and use $\langle\alpha\rangle$ for the α meson mean-field contribution.

A corollary of the MFA is that the field tensor for the rho meson vanishes;

$$R^a_{\mu\nu} = \partial_\mu \rho^a_\nu - \partial_\nu \rho^a_\mu - g_\rho \epsilon^{abc} \rho^b_\mu \rho^c_\nu \underset{\text{MFA}}{\longrightarrow} R^a_{00} = 0, \tag{2.19}$$

since the derivatives of the constant terms vanish and $(\vec{\rho}_0 \times \vec{\rho}_0) = 0$. The same occurs for the omega meson field tensor

$$\Omega_{\mu\nu} = \partial_\mu \omega_\nu - \partial_\nu \omega_\mu \underset{\text{MFA}}{\longrightarrow} \Omega_{00} = 0. \tag{2.20}$$

We also require rotational invariance in isospin space along a quantization direction of $\hat{z} = \hat{3}$ (isospin invariance) as this is a symmetry of the strong interaction, thus only the neutral components of an isovector have a non-zero contribution. This can be seen if we examine the general 2×2 unitary isospin transformation, and the Taylor expansion of this term

$$\psi(x) \to \psi'(x) = e^{i\vec{\tau}\cdot\vec{\theta}/2}\psi(x) \underset{|\theta|\ll 1}{\longrightarrow} \left(1 + i\vec{\tau}\cdot\vec{\theta}/2\right)\psi(x), \tag{2.21}$$

where $\vec{\theta} = (\theta_1, \theta_2, \theta_3)$ is a triplet of real constants representing the (small) angles to be rotated through, and $\vec{\tau}$ are the usual Pauli matrices as defined in Eq. (2.12). As for the ρ mesons, we can express the triplet as linear combinations of the charged states, as

$$\vec{\rho} = (\rho_1, \rho_2, \rho_3) = \left(\frac{1}{\sqrt{2}}(\rho_+ + \rho_-),\ \frac{i}{\sqrt{2}}(\rho_- - \rho_+),\ \rho_0\right). \tag{2.22}$$

The transformation of this triplet is then

$$\vec{\rho}\,(x) \to \vec{\rho}\,'(x) = e^{i\vec{T}\cdot\vec{\theta}}\vec{\rho}\,(x). \tag{2.23}$$

where $(T^i)_{jk} = -i\epsilon_{ijk}$ is the adjoint representation of the SU(2) generators; the spin-1 Pauli matrices in the isospin basis, a.k.a. SO(3). We can perform a Taylor expansion about $\vec{\theta} = \vec{0}$, and we obtain

$$\rho_j(x) \underset{|\theta|\ll 1}{\longrightarrow} \left[\delta_{jk} + i(T^i)_{jk}\theta_i\right]\rho_k(x). \tag{2.24}$$

We can therefore write the transformation as

$$\vec{\rho}\,(x) \underset{|\theta|\ll 1}{\longrightarrow} \vec{\rho}\,(x) - \vec{\theta}\times\vec{\rho}\,(x). \tag{2.25}$$

Writing this out explicitly for the three isospin states, we obtain the individual transformation relations

$$\vec{\rho}\,(x) \to \vec{\rho}\,(x) - \vec{\theta}\times\vec{\rho}\,(x) = (\rho_1 - \theta_2\rho_3 + \theta_3\rho_2,\ \rho_2 - \theta_1\rho_3 + \theta_3\rho_1,\ \rho_3 - \theta_1\rho_2 + \theta_2\rho_1). \tag{2.26}$$

If we now consider the rotation in only the $\hat{z} = \hat{3}$ direction, we see that the only invariant component is ρ_3

$$\vec{\rho}\,(x) \underset{\substack{\theta 1=0\\ \theta_2=0}}{\longrightarrow} (\rho_1 + \theta_3\rho_2,\ \rho_2 + \theta_3\rho_1,\ \rho_3). \tag{2.27}$$

If we performed this rotation along another direction—i.e. $\hat{1}$, $\hat{2}$, or a linear combination of directions—we would find that the invariant component is still a linear combination of charged states. By enforcing isospin invariance, we can see that the only surviving ρ meson state will be the charge-neutral state $\rho_3 \equiv \rho_0$.

2.3.2 Parity Symmetry

We can further exclude entire isospin classes of mesons from contributing since the ground-state of nuclear matter (containing equal numbers of up and down spins) is a parity eigenstate, and thus the parity operator $\mathcal{P}$ acting on the ground-state produces

$$\mathcal{P}|\mathcal{O}\rangle = \pm|\mathcal{O}\rangle. \tag{2.28}$$

Noting that the parity operator is idempotent ($\mathcal{P}^2 = \mathbb{I}$), inserting the unity operator into the ground-state overlap should produce no effect;

$$\langle\mathcal{O}|\mathcal{O}\rangle = \langle\mathcal{O}|\mathbb{I}|\mathcal{O}\rangle = \langle\mathcal{O}|\mathcal{P}\mathcal{P}|\mathcal{O}\rangle = \langle\mathcal{O}|(\pm)^2|\mathcal{O}\rangle = \langle\mathcal{O}|\mathcal{O}\rangle. \tag{2.29}$$

We now turn our attention to the parity transformations for various bilinear combinations that will accompany meson interactions. For Dirac spinors $\psi(x)$ and $\bar{\psi}(x)$ the parity transformation produces

$$\begin{aligned} \mathcal{P}\psi(t,\vec{x}\,)\mathcal{P} &= \gamma^0\psi(t,-\vec{x}\,), \\ \mathcal{P}\bar{\psi}(t,\vec{x}\,)\mathcal{P} &= \bar{\psi}(t,-\vec{x}\,)\gamma^0, \end{aligned} \tag{2.30}$$

where we have removed the overall phase factor $\exp(i\phi)$ since this is unobservable and can be set to unity without loss of generalisation. We can also observe the effect of the parity transformation on the various Dirac field bilinears that may appear in the Lagrangian density. The five possible Dirac bilinears are:

$$\bar{\psi}\psi, \quad \bar{\psi}\gamma^\mu\psi, \quad i\bar{\psi}[\gamma^\mu,\gamma^\nu]\psi, \quad \bar{\psi}\gamma^\mu\gamma^5\psi, \quad i\bar{\psi}\gamma^5\psi, \tag{2.31}$$

for scalar, vector, tensor, pseudo-vector and pseudo-scalar meson interactions respectively, where γ_5 is defined as

$$\gamma_5 = i\gamma_0\gamma_1\gamma_2\gamma_3 = \begin{pmatrix} 0 & \mathbb{I} \\ \mathbb{I} & 0 \end{pmatrix}, \tag{2.32}$$

in the commonly used Dirac basis. By acting the above transformation on these bilinears we obtain a result proportional to the spatially reversed wavefunction $\psi(t,-\vec{x}\,)$,

$$\mathcal{P}\bar{\psi}\psi\mathcal{P} = +\bar{\psi}\psi(t,-\vec{x}\,), \tag{2.33}$$

$$\mathcal{P}\bar{\psi}\gamma^\mu\psi\mathcal{P} = \begin{cases} +\bar{\psi}\gamma^\mu\psi(t,-\vec{x}\,) & \text{for } \mu = 0, \\ -\bar{\psi}\gamma^\mu\psi(t,-\vec{x}\,) & \text{for } \mu = 1,2,3, \end{cases} \tag{2.34}$$

$$\mathcal{P}\bar{\psi}\gamma^\mu\gamma^5\psi\mathcal{P} = \begin{cases} -\bar{\psi}\gamma^\mu\gamma^5\psi(t,-\vec{x}\,) & \text{for } \mu = 0, \\ +\bar{\psi}\gamma^\mu\gamma^5\psi(t,-\vec{x}\,) & \text{for } \mu = 1,2,3, \end{cases} \tag{2.35}$$

$$\mathcal{P}i\bar{\psi}\gamma^5\psi\mathcal{P} = -i\bar{\psi}\gamma^5\psi(t,-\vec{x}\,). \tag{2.36}$$

By inserting the above pseudo-scalar and pseudo-vector bilinears into the ground-state overlap as above, and performing the parity operation, we obtain a result equal to its negative, and so the overall expression *must* vanish. For example

$$\langle\mathcal{O}|i\bar{\psi}\gamma^5\psi|\mathcal{O}\rangle = \langle\mathcal{O}|\mathcal{P}i\bar{\psi}\gamma^5\psi\mathcal{P}|\mathcal{O}\rangle = \langle\mathcal{O}|-i\bar{\psi}\gamma^5\psi|\mathcal{O}\rangle = 0. \tag{2.37}$$

Thus all pseudo-scalar and pseudo-vector meson contributions—such as those corresponding to π and K—provide no contribution to the ground-state in the lowest order. We will show later in Chapter 3.5 that mesons can provide higher order contributions, and the pseudo-scalar π mesons are able to provide a non-zero contribution via Fock terms, though we will not calculate these contributions here.

2.4 Fermi Momentum

Since we are dealing with fermions that obey the Pauli Exclusion Principle[4], and thus Fermi–Dirac statistics[5], there will be restrictions on the quantum numbers that these fermions may possess. When considering large numbers of a single type of fermion, they will each require a unique three-dimensional momentum $\vec{k}$ since no two fermions may share the same quantum numbers.

For an ensemble of fermions we produce a 'Fermi sea' of particles; a tower of momentum states from zero up to some value 'at the top of the Fermi sea'. This value—the Fermi momentum—will be of considerable use to us, thus it is denoted k_F.

Although the total baryon density is a useful control parameter, many of the parameters of the models we wish to calculate are dependent on the density via k_F. The relation between the Fermi momentum and the total density is found by counting the number of momentum states in a spherical volume up to momentum k_F (here, this counting is performed in momentum space). The total baryon density—a number density in units of baryons/fm^3, usually denoted as just fm^{-3}—is simply the sum of contributions from individual baryons, as

$$\rho_{\text{total}} = \sum_i \rho_i = \sum_i \frac{(2J_i+1)}{(2\pi)^3} \int \theta(k_{F_i} - |\vec{k}|)\, d^3k = \sum_i \frac{k_{F_i}^3}{3\pi^2}, \tag{2.38}$$

where here, i is the set of baryons in the model, J_i is the spin of baryon i (where for the leptons and the octet of baryons, $J_i = \frac{1}{2}$), and θ is the Heaviside step function defined as

$$\theta(x) = \begin{cases} 1, & \text{if} \quad x > 0 \\ 0, & \text{if} \quad x < 0 \end{cases}, \tag{2.39}$$

which restricts the counting of momentum states to those between 0 and k_F.

We define the species fraction for a baryon B, lepton ℓ, or quark q as the density fraction of that particle, denoted by Y_i, such that

$$Y_i = \frac{\rho_i}{\rho_{\text{total}}} \; ; \quad i \in \{B, \ell, q\}\,. \tag{2.40}$$

Using this quantity we can investigate the relative proportions of particles at a given total density.

2.5 Chemical Potential

In order to make use of statistical mechanics we must define the some important quantities. One of these will be the chemical potential μ, also known as the Fermi energy ϵ_F; the energy of a particle at the top of the Fermi sea, as described in Appendix A.5.5. This energy is the relativistic energy of such a particle, and is the energy associated with a Dirac equation for that particle. For the simple case of a non-interacting particle, this is

$$\mu_B = \epsilon_{F_B} = \sqrt{k_{F_B}^2 + M_B^2}. \tag{2.41}$$

[4] That no two fermions can share a single quantum state.

[5] The statistics of indistinguishable particles with half-integer spin. Refer to Appendix A.5.5.

In the case that the baryons are involved in interactions with mesons, we need to introduce scalar and temporal self-energy terms, which (for example) for Hartree-level QHD using a mean-field approximation are given by

$$\Sigma_B^s = -g_{B\sigma}\langle\sigma\rangle, \quad \Sigma_B^0 = g_{B\omega}\langle\omega\rangle + g_\rho I_{3B}\langle\rho\rangle, \tag{2.42}$$

where I_{3B} is the isospin projection of baryon B, defined by the diagonal elements of Eq. (2.12), and where the scalar self-energy is used to define the baryon effective mass as

$$M_B^* = M_B + \Sigma_B^s = M_B - g_{B\sigma}\langle\sigma\rangle, \tag{2.43}$$

These self-energy terms affect the energy of a Dirac equation, and thus alter the chemical potential, according to

$$\mu_B = \sqrt{k_{F_B}^2 + (M_B + \Sigma_B^s)^2} + \Sigma_B^0 \ . \tag{2.44}$$

Eq (2.43) and Eq. (2.44) define the important in-medium quantities, and the definition of each will become dependent on which model we are using.

For a relativistic system such as that which will consider here, each conserved quantity is associated with a chemical potential, and we can use the combination of these associated chemical potentials to obtain relations between chemical potentials for individual species. In our case, we will consider two conserved quantities: total baryon number and total charge, and so we have a chemical potential related to each of these. We can construct the chemical potential for each particle species by multiplying each conserved charge by its associated chemical potential to obtain a general relation. Thus

$$\mu_i = B_i\mu_n - Q_i\mu_e, \tag{2.45}$$

where; i is the particle species (which can be any of the baryons) for which we are constructing the chemical potential; B_i and Q_i are the baryon number ('baryon charge', which is unitless) and electric charge (normalized to the proton charge) respectively; and μ_n and μ_e are the chemical potentials of neutrons and electrons, respectively. Leptons have $B_\ell = 0$, and all baryons have $B_B = +1$. The relations between the chemical potentials for the octet of baryons are therefore derived to be

$$\begin{aligned} \mu_\Lambda = \mu_{\Sigma^0} = \mu_{\Xi^0} &= \mu_n, \\ \mu_{\Sigma^-} = \mu_{\Xi^-} &= \mu_n + \mu_e, \\ \mu_p = \mu_{\Sigma^+} &= \mu_n - \mu_e, \\ \mu_\mu &= \mu_e. \end{aligned} \tag{2.46}$$

A simple example of this is to construct the chemical potential for the proton (for which the associated charges are $B_p = +1$ and $Q_p = +1$);

$$\mu_p = \mu_n - \mu_e. \tag{2.47}$$

This can be rearranged to a form that resembles neutron β-decay

$$\mu_n = \mu_p + \mu_e. \tag{2.48}$$

If we were to consider further conserved charges, such as lepton number for example, we would require a further associated chemical potential. In that example, the additional

chemical potential would be for (anti)neutrinos $\mu_{\bar{\nu}}$. The antineutrino would be required to preserve the lepton number on both sides of the equation; the goal of such an addition. Since we shall consider that neutrinos are able to leave the system considered, we can ignore this contribution *ab inito*. The removal of this assumption would alter Eq. (2.48) to include the antineutrino, as would normally be expected in β-decay equations

$$\mu_n = \mu_p + \mu_e + \mu_{\bar{\nu}}. \tag{2.49}$$

2.6 Explicit Chiral Symmetry (Breaking)

One of the most interesting symmetries of QCD is chiral symmetry. If we consider the QCD Lagrangian density to be the sum of quark and gluon contributions, then in the massless quark limit ($m_q = 0$);

$$\begin{aligned} \mathcal{L}_{\text{QCD}} &= \mathcal{L}_g + \mathcal{L}_q \\ &= -\frac{1}{4} G^a_{\mu\nu} G^{\mu\nu}_a + \bar{\psi}_i i\gamma^\mu (D_\mu)_{ij} \psi_j \\ &= -\frac{1}{4} G^a_{\mu\nu} G^{\mu\nu}_a + \bar{\psi}_i i\gamma^\mu \partial_\mu \psi_i - g A^a_\mu \bar{\psi}_i \gamma^\mu T^a_{ij} \psi_j \ , \end{aligned} \tag{2.50}$$

where here, $\psi_i(x)$ is a quark field of color $i \in \{r, g, b\}$, $A^a_\mu(x)$ is a gluon field with color index $a \in \{1, \ldots, 8\}$, T^a_{ij} is a generator[6] for SU(3), g is the QCD coupling constant, and $G^a_{\mu\nu}$ represents the gauge-invariant gluonic field strength tensor, given by

$$G^a_{\mu\nu} = [\partial_\mu, A^a_\nu] - g f^{abc} A^b_\mu A^c_\nu \ , \tag{2.51}$$

written with the structure constants f^{abc}. Left- and right-handed components of Dirac fields can be separated using the projection operators

$$\psi_{\substack{L \\ R}} = \frac{1 \mp \gamma_5}{2} \psi, \tag{2.52}$$

using the definition of γ_5 of Eq. (2.32), and so the quark terms in the QCD Lagrangian density (the gluon terms are not projected) can be written in terms of these components as

$$\mathcal{L}^{(f)}_q = i\bar{\psi}^{(f)}_L D_\mu \gamma^\mu \psi^{(f)}_L + i\bar{\psi}^{(f)}_R D_\mu \gamma^\mu \psi^{(f)}_R. \tag{2.53}$$

This Lagrangian density is invariant under rotations in U(1) of the left- and right-handed fields

$$\text{U}(1)_L : \quad \psi_L \to e^{i\alpha_L} \psi_L, \quad \psi_R \to \psi_R, \tag{2.54}$$

$$\text{U}(1)_R : \quad \psi_R \to e^{i\alpha_R} \psi_R, \quad \psi_L \to \psi_L, \tag{2.55}$$

where α_L and α_R are arbitrary phases. This invariance is the chiral $\text{U}(1)_L \otimes \text{U}(1)_R$ symmetry. The Noether currents associated with this invariance are then

$$J^\mu_L = \bar{\psi}_L \gamma^\mu \psi_L, \qquad J^\mu_R = \bar{\psi}_R \gamma^\mu \psi_R, \tag{2.56}$$

[6] For example, $T^a = \lambda^a/2$ using the Hermitian Gell-Mann matrices λ_a.

and as expected, these currents are conserved, such that $\partial_\mu J_L^\mu = \partial_\mu J_R^\mu = 0$ according to the Dirac Equation. These conserved currents can be alternatively written in terms of conserved vector and axial-vector currents, as

$$J_L^\mu = \frac{V^\mu - A^\mu}{2}, \qquad J_R^\mu = \frac{V^\mu + A^\mu}{2}, \tag{2.57}$$

where here, V^μ and A^μ denote the vector and axial-vector currents respectively—the distinction of A^μ here from the gluon fields in Eq. (2.50) is neccesary—and these are defined by

$$V^\mu = \bar{\psi}\gamma^\mu\psi, \qquad A^\mu = \bar{\psi}\gamma^\mu\gamma_5\psi, \tag{2.58}$$

and which are also conserved, thus $\partial_\mu V^\mu = \partial_\mu A^\mu = 0$. The chiral symmetry of $\mathrm{U}(1)_L \otimes \mathrm{U}(1)_R$ is therefore equivalent to invariance under transformations under $\mathrm{U}(1)_V \otimes \mathrm{U}(1)_A$, where we use the transformations

$$\mathrm{U}(1)_V: \quad \psi \to e^{i\alpha_V}\psi, \qquad \bar{\psi} \to \psi^\dagger e^{-i\alpha_V}\gamma_0, \tag{2.59}$$

$$\mathrm{U}(1)_A: \quad \psi \to e^{i\alpha_A\gamma_5}\psi, \qquad \bar{\psi} \to \psi^\dagger e^{-i\alpha_A\gamma_5}\gamma_0. \tag{2.60}$$

Using the anticommutation relation

$$\{\gamma_5, \gamma_\mu\} = \gamma_5\gamma_\mu + \gamma_\mu\gamma_5 = 0 \tag{2.61}$$

we can evaluate the effect that the vector and axial-vector transformations have on the QCD Lagrangian density, and we find that both transformations are conserved. If we now consider a quark mass term $\mathcal{L}_m$ in the QCD Lagrangian density, the fermionic part becomes

$$\mathcal{L}_{\mathrm{QCD}}^{\psi} = \mathcal{L}_q + \mathcal{L}_m = \bar{\psi}_i \left(i\gamma^\mu (D_\mu)_{ij} - m\delta_{ij}\right)\psi_j. \tag{2.62}$$

For the purposes of these discussions, we can set the masses of the quarks to be equal without loss of generality. Although the massless Lagrangian density possesses both of the above symmetries, the axial vector symmetry—and hence chiral symmetry—is explicitly broken by this quark mass term;

$$\mathcal{L}_m = -\bar{\psi}m\psi \overset{\mathrm{U}(1)_A}{\longrightarrow} -\bar{\psi}me^{2i\alpha_A}\psi \neq -\bar{\psi}m\psi. \tag{2.63}$$

The vector symmetry is nonetheless preserved when including this term.

2.7 Dynamical Chiral Symmetry (Breaking)

Even with a massless Lagrangian density, it is possible that chiral symmetry becomes dynamically broken, and we refer to this as Dynamically Broken Chiral Symmetry, or DCSB.

Following the description of Ref. [23], if we consider the basic Lagrangian density of QCD to be

$$\mathcal{L}_{\mathrm{QCD}} = \bar{\psi}_i \left(i\gamma^\mu (D_\mu)_{ij} - m\delta_{ij}\right)\psi_j - \frac{1}{4}G^a_{\mu\nu}G_a^{\mu\nu}, \tag{2.64}$$

with the definitions as in the previous section, of

$$G^a_{\mu\nu} = \partial_\mu A^a_\nu - \partial_\nu A^a_\mu - g f^{abc} A^b_\mu A^c_\nu, \quad D_\mu = \partial_\nu + igA^a_\mu T^a, \tag{2.65}$$

with standard definitions of other terms, then we can write the sum of all QCD One-Particle Irreducible (1-PI) diagrams[7] with two external legs as shown in Fig. 2.2; illustrating the quark self-energy. The expression for the renormalized quark self-energy in d dimensions is

$$-i\Sigma(p) = \frac{4}{3} Z_r \, g^2 \int \frac{d^d q}{(2\pi)^d} (i\gamma_\mu)(iS(q))(iD^{\mu\nu}(p-q))(i\Gamma_\nu(q,p)), \tag{2.66}$$

where Z_r is a renormalization constant, g is the QCD coupling, and q is the loop momentum.

In the absence of matter fields or background fields (the Lorentz-covariant case), we can write this self-energy as a sum of Dirac-vector and Dirac-scalar components, as

$$\Sigma(p) = \not{p}\, \Sigma_{\rm DV}(p^2) + \Sigma_{\rm DS}(p^2). \tag{2.67}$$

where $\Sigma_{\rm DV}(p^2)$ is the Dirac-vector component, and $\Sigma_{\rm DS}(p^2)$ is the Dirac-scalar component. These must both be functions of p^2, since there are no other Dirac-fields to contract with, and $\Sigma(p)$ is a Lorentz invariant quantity in this case.

For the purposes of our discussion in this section, we will approximate the Dirac-vector component of the self-energy to be $\Sigma_{\rm DV} \sim 1$, in which case the self-energy is dependent only on the Dirac-scalar component.

Even with a massless theory ($m = 0$) it is possible that the renormalized self-energy develops a non-zero Dirac-scalar component, thus $\Sigma_{\rm DS}(p^2) \neq 0$. This leads to a non-zero value for the quark condensate $\langle \bar{\psi}_q \psi_q \rangle$, and in the limit of exact chiral symmetry, leads to the pion becoming a massless Goldstone boson. Thus chiral symmetry can be dynamically broken. With the addition of a Dirac-scalar component of the self-energy, the Lagrangian density becomes

$$\mathcal{L}_{QCD} = \bar{\psi}_i \left(i\gamma^\mu (D_\mu)_{ij} - (m + \Sigma_{\rm DS})\delta_{ij} \right) \psi_j - \frac{1}{4} G^a_{\mu\nu} G^{\mu\nu}_a, \tag{2.68}$$

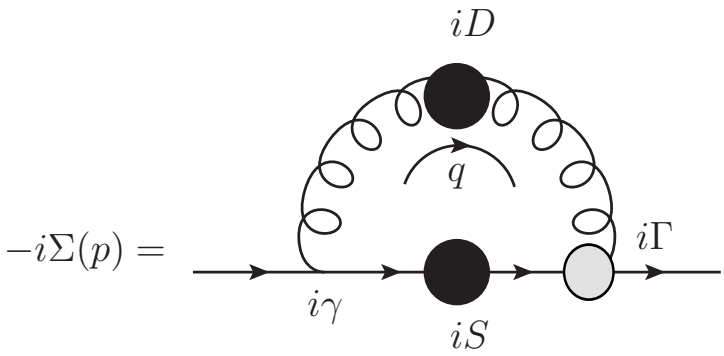

Fig. 2.2: Feynman diagram for the QCD self-energy for a quark, as given by the Dyson–Schwinger Equation (DSE). The full expression for this is given in Eq. (2.66).

[7] Diagrams that cannot be made into two separate disconnected diagrams by cutting an internal line are called One-Particle Irreducible, or 1-PI.

and we can define a dynamic quark mass via the gap equation;

$$m^* = m + \Sigma_{\rm DS}. \tag{2.69}$$

We will continue this discussion in Section 3.4, in which we will describe a particular model for $\Sigma_{\rm DS}$ in order to describe DCSB.

2.8 Equation of State

In order to investigate models of dense matter, we need to construct an Equation of State (EOS), which is simply a relation between two or more state variables—those which thermodynamically describe the current state of the system, such as temperature, pressure, volume, or internal energy—under a given set of physical conditions. With this, we will be able to investigate various aspects of a model and compare differences between models in a consistent fashion.

For our purposes, we use the total baryon density $\rho_{\rm total}$ as the control parameter of this system, and so we need to obtain the connection between, say, the energy density $\mathcal{E}$, the pressure P, and this total baryon density, i.e.

$$\mathcal{E} = \mathcal{E}(\rho_{\rm total}), \qquad P = P(\rho_{\rm total}). \tag{2.70}$$

State variables are important quantities to consider. Within any transition between states the total change in any state variable will remain constant regardless of the path taken, since the change is an exact differential, by definition. For the hadronic models described herein, the EOS are exact, in that they have an analytic form;

$$P(\rho_{\rm total}) = \rho_{\rm total}^2 \frac{\partial}{\partial \rho_{\rm total}} \left(\frac{\mathcal{E}(\rho_{\rm total})}{\rho_{\rm total}} \right). \tag{2.71}$$

As simple as this exact form may seem, the derivative complicates things, and we will find it easier to calculate the pressure independently. Nonetheless, this expression will hold true. More interestingly, this expression is equivalent to the first law of thermodynamics in the absence of heat transfer; i.e.

$$PdV = -dE, \tag{2.72}$$

(the proof of which can be found in Appendix A.5.6) which assures us that the theory is thermodynamically consistent.

A notable feature of each symmetric matter EOS we calculate is the effect of saturation; whereby the energy per baryon for the system possesses a global minimum at a particular value of the Fermi momentum. This can be considered as a binding energy of the system. In symmetric matter (in which the densities of protons and neutrons are equal), the nucleon Fermi momenta are related via $k_F = k_{F_n} = k_{F_p}$, and the energy per baryon (binding energy) E is determined via

$$E = \left[\frac{1}{\rho_{\rm total}} \left(\mathcal{E} - \sum_B \rho_B M_B \right) \right]. \tag{2.73}$$

In order to reproduce (a chosen set of) experimental results, this value should be an extremum of the curve with a value of $E_0 = -15.86$ MeV at a density of $\rho_0 = 0.16$ fm^{-3} (or the corresponding Fermi momentum k_{F_0}).

The nucleon symmetry energy $a_{\rm sym}$ is approximately a measure of the energy difference between the energy per baryon (binding energy) of a neutron-only model and a symmetric nuclear model (essentially a measure of the breaking of isospin symmetry). A more formal expression (without assuming degeneracy between nucleon masses, as derived in Appendix A.5.4) is

$$a_{\rm sym} = \frac{g_\rho^2}{3\pi^2 m_\rho^2} k_F^3 + \frac{1}{12}\frac{k_F^2}{\sqrt{k_F^2 + (M_p^*)^2}} + \frac{1}{12}\frac{k_F^2}{\sqrt{k_F^2 + (M_n^*)^2}}\,. \tag{2.74}$$

At saturation, this should take the value of $(a_{\rm sym})_0 = 32.5$ MeV (for an analysis of values, see Ref. [24]).

Another important aspect of an EOS is the compression modulus K which represents the *stiffness* of the EOS; the ability to withstand compression. This ability is intimately linked to the Pauli Exclusion Principle in that all other things being equal, a system with more available states (say, distinguishable momentum states) will have a softer EOS, and thus a smaller compression modulus. The compression modulus itself is defined as the curvature of the binding energy at saturation, the expression for which is

$$K = \left[k_F^2 \frac{d^2}{dk_F^2}\left(\frac{\mathcal{E}}{\rho_{\rm total}}\right)\right]_{k_{F_{\rm sat}}} = 9\left[\rho_{\rm total}^2 \frac{d^2}{d\rho_{\rm total}^2}\left(\frac{\mathcal{E}}{\rho_{\rm total}}\right)\right]_{\rho=\rho_0}\,. \tag{2.75}$$

The motivation for this is that by compressing the system, the energy per baryon will rise. The curvature at saturation determines how fast that rise will occur, and thus how resistant to compression the system is. Experimentally, this is linked to the properties of finite nuclei, particularly those with a large number of nucleons, and the binding of these within a nucleus.

According to Ref. [18] this should have a value in the range 200–300 MeV, and we will calculate the value of K for each of the models to follow for comparison.

2.9 Phase Transitions

In order to consider transitions between different phases of matter we must use statistical mechanics. The simplest method of constructing a phase transition—known as a 'Maxwell transition'—is an isobaric (constant pressure) transition constructed over a finite density range. A transition of this form remains useful in understanding the liquid–gas style phase transition that occurs within QHD, which is a first-order transition (similar to that of ice melting in a fluid) with the phases being separated by a non-physical negative-pressure region. The inclusion of a Maxwell transition to this simple model for QHD removes this unphysical region and replaces it with a constant pressure phase.

The method for constructing a Maxwell transition will not be covered here, though in-depth details can be found in Ref. [25]. We can however extract the transition densities from Ref. [18] to reproduce the results, which are shown later in Fig. 5.5 for the various varieties of QHD. The more sophisticated method of constructing a phase transition—the 'Gibbs transition' [26] that we have used for the results produced herein—relies on a little more statistical mechanics. A comparison between the Maxwell and Gibbs methods for models similar to those used in this work can be found in Ref. [27]. For a full in-depth discussion of this topic, see Ref. [28].

If we consider a homogeneous (suitable for these mean-field calculations) system with energy E, volume V, N_m particles of type m, and entropy S which depends on these parameters such that

$$S = S(E, V, N_1, \ldots, N_m), \tag{2.76}$$

then we can consider the variation of the entropy in the system as a function of these parameters, resulting in

$$dS = \left(\frac{\partial S}{\partial E}\right)_{V,N_1,\ldots,N_m} dE + \left(\frac{\partial S}{\partial V}\right)_{E,N_1,\ldots,N_m} dV + \sum_{i=1}^{m} \left(\frac{\partial S}{\partial N_i}\right)_{V,N_{j\neq i}} dN_i, \tag{2.77}$$

using standard statistical mechanics notation whereby a subscript X on a partial derivative $(\partial A/\partial B)_X$ denotes that X is explicitly held constant. Eq. (2.77) should be equal to the fundamental thermodynamic relation when the number of particles is fixed, namely

$$dS = \frac{đQ}{T} = \frac{dE + PdV}{T}. \tag{2.78}$$

Here, the symbol $đ$ denotes the inexact differential, since the heat Q is not a state function —does not have initial and final values—and thus the integral of this expression is only true for infinitesimal values, and not for finite values. Continuing to keep the number of each type of particle N_i constant, a comparison of coefficients between Eqs. (2.77) and (2.78) results in the following relations:

$$\left(\frac{\partial S}{\partial E}\right)_{V,N_i,\ldots,N_m} = \frac{1}{T}, \quad \left(\frac{\partial S}{\partial V}\right)_{E,N_i,\ldots,N_m} = \frac{P}{T}. \tag{2.79}$$

To provide a relation similar to Eq. (2.79) for the case where $dN_i \neq 0$, one defines μ_j—the chemical potential per molecule—as

$$\mu_i = -T\left(\frac{\partial S}{\partial N_i}\right)_{E,V,N_{j\neq i}}. \tag{2.80}$$

We can now re-write Eq. (2.77) with the definitions in Eq. (2.79) for the case where the particle number can change, as

$$dS = \frac{1}{T}dE + \frac{P}{T}dV - \sum_{i=1}^{m} \frac{\mu_i}{T} dN_i, \tag{2.81}$$

which can be equivalently written in the form of the fundamental thermodynamic relation for non-constant particle number,

$$dE = TdS - PdV + \sum_{i=1}^{m} \mu_i dN_i. \tag{2.82}$$

If we now consider a system X of two phases A and B, then we can construct relations between their parameters by considering the following relations:

$$\begin{aligned} E_X &= E_A + E_B, \\ V_X &= V_A + V_B, \\ N_X &= N_A + N_B. \end{aligned} \tag{2.83}$$

If we consider that these quantities are conserved between phases, we find the following conservation conditions

$$\begin{aligned} dE_X = 0 \quad &\Rightarrow \quad dE_A + dE_B = 0 \quad \Rightarrow \quad dE_A = -dE_B, \\ dV_X = 0 \quad &\Rightarrow \quad dV_A + dV_B = 0 \quad \Rightarrow \quad dV_A = -dV_B, \\ dN_X = 0 \quad &\Rightarrow \quad dN_A + dN_B = 0 \quad \Rightarrow \quad dN_A = -dN_B. \end{aligned} \tag{2.84}$$

The condition for phase equilibrium for the most probable situation is that the entropy must be a maximum for $S = S_X(E_X, V_X, N_X) = S(E_A, V_A, N_A; E_B, V_B, N_B)$, which leads to

$$dS_X = dS_A + dS_B = 0. \tag{2.85}$$

Thus, inserting Eq. (2.81) we find

$$dS = \left(\frac{1}{T_A}dE_A + \frac{P_A}{T_A}dV_A - \frac{\mu_A}{T_A}dN_A\right) + \left(\frac{1}{T_B}dE_B + \frac{P_B}{T_B}dV_B - \frac{\mu_B}{T_B}dN_B\right). \tag{2.86}$$

If we now apply the result of Eq. (2.84) we can simplify this relation to

$$dS = 0 = \left(\frac{1}{T_A} - \frac{1}{T_B}\right)dE_A + \left(\frac{P_A}{T_A} - \frac{P_B}{T_B}\right)dV_A - \left(\frac{\mu_A}{T_A} - \frac{\mu_B}{T_B}\right)dN_A \tag{2.87}$$

and thus for arbitrary variations of E_A, V_A and N_A, each bracketed term must vanish separately, so that

$$\frac{1}{T_A} = \frac{1}{T_B}, \quad \frac{P_A}{T_A} = \frac{P_B}{T_B}, \quad \frac{\mu_A}{T_A} = \frac{\mu_B}{T_B}. \tag{2.88}$$

Eq. (2.88) implies that at the phase transition the system will be isentropic ($dS = 0$), isothermal ($dT = 0$), isobaric ($dP = 0$), and isochemical ($d\mu = 0$), where the terms S, T, V, and μ now refer to the mean values rather than for individual particles.

We only require two systems at any one time when considering a mixture of phases, for example, a neutron ('neutron phase') can transition to a proton and an electron ('proton and electron phase') provided that the condition $\mu_n = \mu_p + \mu_e$ is met.

For a phase transition between hadronic- and quark-matter phases then, the conditions for stability are therefore that chemical, thermal, and mechanical equilibrium between the hadronic H, and quark Q phases is achieved, and thus that the independent quantities in each phase are separately equal. Thus the two independent chemical potentials (as described in Sec. 2.5) μ_n and μ_e are each separately equal to their counterparts in the other phase, i.e. $[(\mu_n)_H = (\mu_n)_Q]$, and $[(\mu_e)_H = (\mu_e)_Q]$ for chemical equilibrium; $[T_H = T_Q]$ for thermal equilibrium; and $[P_H = P_Q]$ for mechanical equilibrium.

An illustrative example of these relations is shown in Fig. 2.3 in which the values of the independent chemical potentials μ_n and μ_e, as well as the pressure P for a hadronic phase and a quark phase are plotted for increasing values of total density ρ_{total}. In this case, the quark matter data is calculated based on the hadronic matter data, using the chemical potentials in the hadronic phase as inputs for the quark phase calculations, and as such the chemical potentials are—by construction—equal between the phases. As this is an illustrative example of the relations between the phases, no constraints have been imposed to reproduce a phase transition yet.

In this figure, the low-density points correspond to small values of μ_n, and we see that for densities lower than some phase transition density $\rho_{\text{total}} < \rho_{\text{PT}}$ the hadronic pressure is

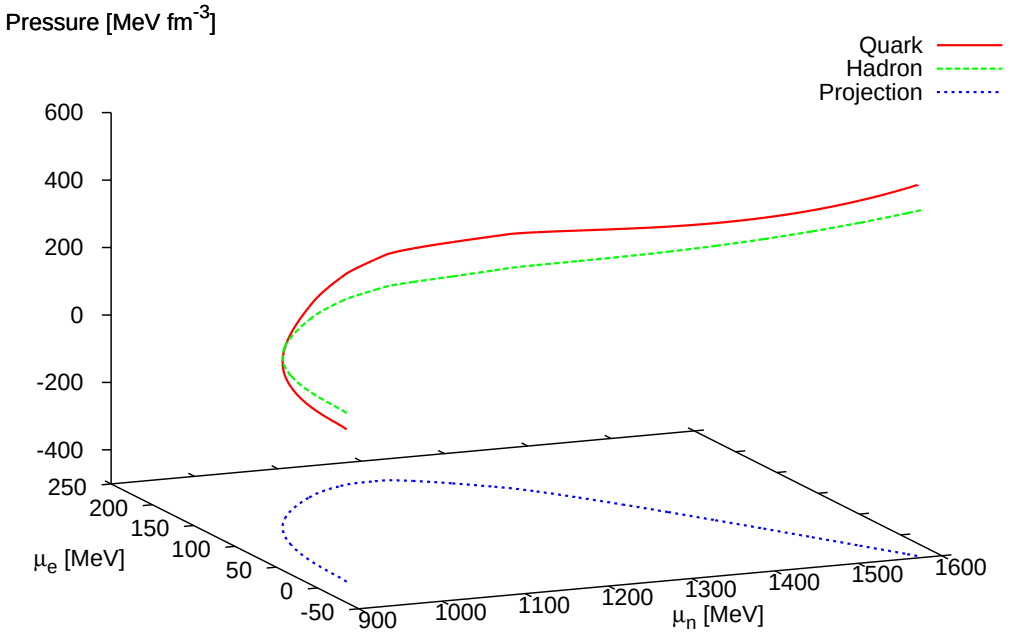

Fig. 2.3: (Color Online) Illustrative locus of values for the independent chemical potentials μ_e and μ_n, as well as the pressure P for phases of hadronic matter and deconfined quark matter. Note that pressure in each phase increases with density. and that a projection onto the $\mu_n\mu_e$ plane is a single line, as ensured by the chemical equilibrium condition.

greater than the quark pressure and thus the hadronic phase is dominant. At the transition the pressures are equal, and thus both phases can be present in a mixed phase, and beyond the transition the quark pressure is greater than the hadronic pressure indicating that the quark phase becomes dominant.

Note that for all values of the total density, the chemical potentials in each phase are equal, as shown by the projection onto the $\mu_n\mu_e$ plane.

In our calculations, we will only investigate these two phases independently up to the phase transition, at which point we will consider a mixed phase, as shall be described in the next section.

We consider both phases to be cold on the nuclear scale, and assume $T = 0$ so the temperatures are also equal, again by construction. We must therefore find the point—if it exists—at which, for a given pair of independent chemical potentials, the pressures in both the hadronic phase and the quark phase are equal.

To find the partial pressure of any baryon, quark, or lepton species i we use

$$P_i = \frac{(2J_B+1)\,\mathcal{N}_c}{3(2\pi)^3}\int \frac{\vec{k}^2\,\theta(k_{F_i}-|\vec{k}|)}{\sqrt{\vec{k}^2+(M_i^*)^2}}\,d^3k, \tag{2.89}$$

where the number of colors is $\mathcal{N}_c = 3$ for quarks, $\mathcal{N}_c = 1$ for baryons and leptons, and where θ is the Heaviside step function defined in Eq. (2.39). To find the total pressure in each phase,

we sum the pressures contributions in that phase. The pressure in the hadronic phase H is given by

$$P_H = \sum_j P_j + \sum_\ell P_\ell + \sum_m P_m, \tag{2.90}$$

in which j represents the baryons, ℓ represents the leptons, m represents the mesons appearing in the particular model being considered, if they appear, and the pressure in the quark phase Q is given by

$$P_Q = \sum_q P_q + \sum_\ell P_\ell - B, \tag{2.91}$$

where q represents the quarks, and B denotes the bag energy density, which we shall discuss further in Section 3.3.

In order to determine the EOS beyond the point at which the pressures are equal, we need to consider the properties of a mixed phase.

2.10 Mixed Phase

Once we have defined the requirements for a phase transition between two phases, we must consider the possibility of a mixed phase (MP) containing proportions of the two phases. This adds a further degree of sophistication to a model; we can not only find equations of state for hadronic matter and quark matter and simply stitch them together, but we can also allow the transition between these to occur gradually.

To calculate the mixed phase EOS, we calculate the hadronic EOS with control parameter ρ_{total}, and use the independent chemical potentials μ_n and μ_e as inputs to determine the quark matter EOS, since we can determine all other Fermi momenta given these two quantities. We increase ρ_{total} until we find a density—if it exists—at which the pressure in the quark phase is equal the pressure in the hadronic phase (if such a density cannot be found, then the transition is not possible for the given models).

Assuming that such a transition is possible, once we have the density and pressure at which the phase transition occurs, we change the control parameter to the quark fraction χ (which is an order parameter parameterizing the transition to the quark matter phase) which determines the proportions of hadronic matter and quark matter. If we consider the mixed phase to be composed of some fraction of hadronic matter and some fraction of quark matter, then the mixed phase of matter will have the following properties: the total density will be

$$\rho_{\text{MP}} = (1 - \chi)\, \rho_{\text{HP}} + \chi\, \rho_{\text{QP}}, \tag{2.92}$$

where ρ_{HP} and ρ_{QP} are the densities in the hadronic and quark phases, respectively. A factor of three in the equivalent baryon density in the quark phase,

$$\rho_{\text{QP}} = \frac{1}{3} \sum_q \rho_q = (\rho_u + \rho_d + \rho_s)/3, \tag{2.93}$$

arises because of the restriction that a baryon contains three quarks.

According to the condition of mechanical equilibrium detailed earlier, the pressure in the mixed phase will be

$$P_{\text{MP}} = P_{\text{HP}} = P_{\text{QP}}. \tag{2.94}$$

We can step through values $0<\chi<1$ and determine the properties of the mixed phase, keeping the mechanical stability conditions as they were above. In the mixed phase we need to alter our definition of charge neutrality; while previously we have used the condition that two phases were independently charge-neutral, such as $n \to p^+ + e^-$, it now becomes possible that one phase is (locally) charged, while the other phase carries the opposite charge, making the system globally charge-neutral. This is achieved by enforcing

$$0 = (1-\chi)\ \rho^c_{\mathrm{HP}} + \chi\ \rho^c_{\mathrm{QP}} + \rho^c_\ell\,, \tag{2.95}$$

where this time we are considering charge-densities, which are simply the sum of densities multiplying their respective charges

$$\rho^c_i = \sum_j Q_j \rho_j\ ; \quad i \in \{\mathrm{HP}, \mathrm{QP}, \ell\}, \tag{2.96}$$

where j are the all individual particles modelled within the grouping i. For example, the quark charge-density in a non-interacting quark phase is given by

$$\rho^c_{\mathrm{QP}} = \sum_q Q_q \rho_q = \frac{2}{3}\rho_u - \frac{1}{3}\rho_d - \frac{1}{3}\rho_s. \tag{2.97}$$

We continue to calculate the properties of the mixed phase for increasing values of χ until we reach $\chi = 1$, at which point the mixed phase is now entirely charge-neutral quark matter. This corresponds to the density at which the mixed phase ends, and a pure quark phase begins. We can therefore continue to calculate the EOS for pure charge-neutral quark matter, once again using ρ_{total} as the control parameter, but now where the total density is the equivalent density as defined in Eq. (2.93).

2.11 Stellar Matter

The equations of state described above are derived for homogeneous infinite matter. If we wish to apply this to a finite system we must investigate the manner in which large ensembles of particles are held together. The focus of this work is 'neutron stars', and we must find a way to utilise our knowledge of infinite matter to provide insight to macroscopic objects. For this reason, we turn to the theory of large masses; General Relativity.

The Tolman–Oppenheimer–Volkoff (TOV) equation [29] describes the conditions of stability against gravitational collapse for an EOS, i.e. in which the pressure gradient is sufficient to prevent gravitational collapse of the matter. The equations therefore relate the change in pressure with radius to various state variables from the EOS. To preserve continuity, the equations are solved under the condition that the pressure at the surface of the star *must* be zero.

The TOV equation is given by

$$\frac{dP}{dr} = -\frac{G\left(P/c^2 + \mathcal{E}\right)\left(M(r) + 4r^3\pi P/c^2\right)}{r(r - 2GM(r)/c^2)}, \tag{2.98}$$

or, in Planck units[8]

$$\frac{dP}{dr} = -\frac{\left(P + \mathcal{E}\right)\left(M(r) + 4\pi r^3 P\right)}{r(r - 2M(r))}, \tag{2.99}$$

[8] In which certain fundamental physical constants are normalized to unity, viz $\hbar = c = G = 1$.

where the mass within a radius R is given by integrating the energy density, as

$$M(R) = \int_0^R 4\pi r^2 \mathcal{E}(r)\, dr. \tag{2.100}$$

For a full derivation of these equations, refer to Appendix A.4.

Supplied with these equations and a derived EOS, we can calculate values for the total mass and total radius of a star[9] for a given central density. We refer to these values as the 'stellar solutions.'

This is particularly interesting, since the mass of a neutron star is observable (either via observing a pair of objects rotating about a barycenter[10], or some other indirect/proxy measurement), yet the radius is not directly observable, as stars are sufficiently distant that they all appear as 'point-sources'. With these calculations, we produce a relationship between two quantities: the stellar mass and the stellar radius, of which only the mass is currently observable, and even this is not always so. This provides useful data for further theoretical work requiring both quantities, as well as an opportunity to place theoretical bounds on future experimental observations.

In addition to this data, since we are able to solve our equations for the radial distance from the centre of the star, we can provide data that current experiments can not; we can investigate the interior of a neutron star, by calculating the proportions of various particles at successive values of internal radius and/or density. This allows us to construct a cross-section of a neutron star, investigate the possible contents, and examine the effects that various changes to the models have on both the internal and external properties.

2.12 SU(6) Spin-Flavor Baryon-Meson Couplings

We have noted earlier that the coupling of baryons to mesons is dependent on isospin group. The physics leading to this result is highly non-trivial, but is often neglected in the literature. We will therefore outline the process involved in determining the relations between baryon-meson couplings.

In order to determine the normalized relations between the point vertex couplings of various mesons to the full baryon octet g_{Bm} it is common to express the octet as a 3×3 matrix in flavor space as

$$B = \begin{pmatrix} \frac{\Sigma^0}{\sqrt{2}} + \frac{\Lambda}{\sqrt{6}} & \Sigma^+ & p \\ \Sigma^- & -\frac{\Sigma^0}{\sqrt{2}} + \frac{\Lambda}{\sqrt{6}} & n \\ -\Xi^- & \Xi^0 & -\frac{2\Lambda}{\sqrt{6}} \end{pmatrix}. \tag{2.101}$$

This has been constructed as an array where rows and columns are distinguished by rotations

[9] Stellar objects in these calculations are assumed to be static, spherically symmetric, and non-rotating, as per the derivation of this equation. For studies of the effect of rapid rotation in General Relativity see Refs. [30, 31].

[10] A common centre of mass for the system, the point about which both objects will orbit, which is the balance point of the gravitational force. In this case, the mass measurements are simplified.

in flavor space, which can be seen if we observe the quark content of these baryons;

$$B = \begin{pmatrix} uds & \mathbf{d \to u} & uus & \mathbf{s \to d} & uud \\ \mathbf{u \to d} & & & & \\ dds & & dus & & ddu \\ \mathbf{d \to s} & & & & \\ ssd & & uss & & sud \end{pmatrix}. \tag{2.102}$$

The vector meson octet ($J^P = 1^-$) can be written in a similar fashion as

$$P^{\text{vec}}_{\text{oct}} = \begin{pmatrix} \frac{\rho^0}{\sqrt{2}} + \frac{\omega_8}{\sqrt{6}} & \rho^+ & K^{*+} \\ \rho^- & -\frac{\rho^0}{\sqrt{2}} + \frac{\omega_8}{\sqrt{6}} & K^{*0} \\ K^{*-} & \overline{K^{*0}} & -2\left(\frac{\omega_8}{\sqrt{6}}\right) \end{pmatrix}, \tag{2.103}$$

which, along with the singlet state, $P^{\text{vec}}_{\text{sing}} = \frac{1}{\sqrt{3}}\text{diag}(\omega_0, \omega_0, \omega_0)$ defines the vector meson nonet

$$P^{\text{vec}} = P^{\text{vec}}_{\text{oct}} + P^{\text{vec}}_{\text{sing}}. \tag{2.104}$$

Furthermore, the scalar meson octet ($J^P = 0^+$) can be written as

$$P^{\text{sca}}_{\text{oct}} = \begin{pmatrix} \frac{a_0^0}{\sqrt{2}} + \frac{\sigma_8}{\sqrt{6}} & a_0^+ & \kappa^+ \\ a_0^- & -\frac{a_0^0}{\sqrt{2}} + \frac{\sigma_8}{\sqrt{6}} & \kappa^0 \\ \kappa^- & \overline{\kappa^0} & -2\frac{\sigma_8}{\sqrt{6}} \end{pmatrix}, \tag{2.105}$$

and along with singlet state $P^{\text{sca}}_{\text{sing}} = \frac{1}{\sqrt{3}}\text{diag}(\sigma_0, \sigma_0, \sigma_0)$, these define the scalar meson nonet. The meson octet matrices are constructed in a similar fashion to the baryon octet matrix;

$$P_{\text{oct}} = \begin{pmatrix} u\bar{u} & \bar{\mathbf{u}} \to \bar{\mathbf{d}} & u\bar{d} & \bar{\mathbf{d}} \to \bar{\mathbf{s}} & u\bar{s} \\ \mathbf{u \to d} & & & & \\ d\bar{u} & & d\bar{d} & & d\bar{s} \\ \mathbf{d \to s} & & & & \\ s\bar{u} & & s\bar{d} & & s\bar{s} \end{pmatrix}. \tag{2.106}$$

The singlet and octet representations of both ω and σ ($\omega_0, \omega_8, \sigma_0, \sigma_8$, appearing in Eqs. (2.103)–(2.105)) are not however the physical particles which we wish to include in the model; these are linear combinations of the physical particles. Due to explicit SU(3) flavor-symmetry breaking ($m_s > m_u,\ m_d$), a mixture of the unphysical ω_8 and ω_0 states produces the physical ω and ϕ mesons, while a mixture of the unphysical σ_8 and σ_0 states produces the physical σ and f_0 mesons, the properties of which we list in Appendix B.

The octet and singlet states are represented by linear combinations of quark-antiquark pairs. The state vectors for these are

$$|\omega_8\rangle = |\sigma_8\rangle = \frac{1}{\sqrt{6}}\left(|\bar{u}u\rangle + |\bar{d}d\rangle - 2|\bar{s}s\rangle\right), \quad |\omega_0\rangle = |\sigma_0\rangle = \frac{1}{\sqrt{3}}\left(|\bar{u}u\rangle + |\bar{d}d\rangle| + |\bar{s}s\rangle\right), \tag{2.107}$$

where the normalizations arise by ensuring that

$$\langle\xi|\xi\rangle = 1; \quad \xi \in \{\omega_8, \omega_0, \sigma_8, \sigma_0\}. \tag{2.108}$$

Since the quark contents of the physical states are predominantly

$$\omega = \sigma = \frac{1}{\sqrt{2}}\,(u\bar{u} + d\bar{d}), \quad \text{and} \quad \phi = f_0 = -s\bar{s}, \tag{2.109}$$

we can replace the octet and singlet combinations with the physical states via the replacements of

$$\omega_8 = \tfrac{1}{\sqrt{3}}\,\omega + \tfrac{2}{\sqrt{6}}\,\phi, \qquad \omega_0 = \sqrt{\frac{2}{3}}\,\omega - \frac{1}{\sqrt{3}}\,\phi, \tag{2.110}$$

$$\sigma_8 = \tfrac{1}{\sqrt{3}}\,\sigma + \tfrac{2}{\sqrt{6}}\,f_0, \qquad \sigma_0 = \sqrt{\frac{2}{3}}\,\sigma - \frac{1}{\sqrt{3}}\,f_0. \tag{2.111}$$

Using these definitions, we can express the octet and singlet states in terms of the physical states

$$P^{\rm vec}_{\rm oct} = \begin{pmatrix} \frac{\rho^0}{\sqrt{2}} + \frac{\omega}{\sqrt{18}} + \frac{\phi}{\sqrt{9}} & \rho^+ & K^{*+} \\ \rho^- & -\frac{\rho^0}{\sqrt{2}} + \frac{\omega}{\sqrt{18}} + \frac{\phi}{\sqrt{9}} & K^{*0} \\ K^{*-} & \overline{K^{*0}} & -2\left(\frac{\omega}{\sqrt{18}} + \frac{\phi}{\sqrt{9}}\right) \end{pmatrix}, \tag{2.112}$$

$$P^{\rm sca}_{\rm oct} = \begin{pmatrix} \frac{a_0^0}{\sqrt{2}} + \frac{\sigma}{\sqrt{18}} + \frac{f_0}{\sqrt{9}} & a_0^+ & \kappa^+ \\ a_0^- & -\frac{a_0^0}{\sqrt{2}} + \frac{\sigma}{\sqrt{18}} + \frac{f_0}{\sqrt{9}} & \kappa^0 \\ \kappa^- & \overline{\kappa^0} & -2\left(\frac{\sigma}{\sqrt{18}} + \frac{f_0}{\sqrt{9}}\right) \end{pmatrix}. \tag{2.113}$$

Each of the above mesons can interact with a pair of baryons in three possible SU(3) invariant ways, which we shall identify as F-style (anti-symmetric), D-style (symmetric) and S-style (singlet). The singlet mesons ω_0 and σ_0 are associated with an S-style coupling, while the octet particles are associated with F- and D-style couplings.

To determine these F-, D-, and S-style couplings for the vector and scalar mesons we need to calculate the SU(3) invariant Lagrangian density coefficients symbolically for each isospin group, with each SU(3) invariant combination[11] given by:

$$\begin{aligned} \left[\bar{B}BP\right]_F &= {\rm Tr}(\bar{B}PB) - {\rm Tr}(\bar{B}BP) \\ &= {\rm Tr}(\bar{B}P_{\rm oct}B) - {\rm Tr}(\bar{B}BP_{\rm oct}), \\ \left[\bar{B}BP\right]_D &= {\rm Tr}(\bar{B}PB) + {\rm Tr}(\bar{B}BP) - \frac{2}{3}{\rm Tr}(\bar{B}BP){\rm Tr}(P) \\ &= {\rm Tr}(\bar{B}P_{\rm oct}B) + {\rm Tr}(\bar{B}BP_{\rm oct}), \\ \left[\bar{B}BP\right]_S &= {\rm Tr}(\bar{B}B){\rm Tr}(P) \\ &= {\rm Tr}(\bar{B}B){\rm Tr}(P_{\rm sing}). \end{aligned} \tag{2.114}$$

where we have expanded the meson matrices P according to Eq. (2.104), and we note that the octet matrices $\bar{B}$, and B are traceless.

[11] Following the notation of Ref. [32].

Together, these terms can be combined to form an interaction Lagrangian density for all possible SU(3) invariant interactions involving each meson isospin group, with octet and singlet coupling coefficients F, D, and S (each defined separately for each isospin group) as

$$\mathcal{L}^{\text{int}} = -\sqrt{2}\left\{F\left[\bar{B}BP\right]_F + D\left[\bar{B}BP\right]_D\right\} - S\frac{1}{\sqrt{3}}\left[\bar{B}BP\right]_S, \tag{2.115}$$

where the remaining numerical factors are introduced for convenience.

If we evaluate this Lagrangian density by matrix multiplication of B, the octet and singlet matrices of P_{vec}, and $\bar{B} = B^\dagger\gamma^0$ in the combinations stated in Eq. (2.115), we can extract the coefficients of each baryon-meson vertex in terms of F, D and S factors. These are summarized in Table 2.1 for vertices involving the physical vector mesons ω and ρ^0 and ϕ, for pairs of like baryons[12]. The summary for the scalar mesons is the same under replacements of $\omega \to \sigma$, $\vec{\rho} \to \vec{a}_0$, and $\phi \to f_0$.

Table 2.1: F-, D-, and S-style couplings of like baryon-baryon pairs to vector mesons used in these models, according to vertices of type $B + P \to \bar{B}$. The summary for the scalar mesons is the same under the replacements of $\omega \to \sigma$, $\vec{\rho} \to \vec{a}_0$, and $\phi \to f_0$.

$\overline{\Sigma^-}\Sigma^-\rho^0$	$\propto$	$2F$	$\overline{\Lambda}\Lambda\omega$	$\propto$	$\frac{1}{9}\left(6D - \sqrt{6}S\right)$
$\overline{\Sigma^-}\Sigma^-\omega$	$\propto$	$\frac{1}{9}\left(-6D - \sqrt{6}S\right)$	$\overline{\Lambda}\Lambda\phi$	$\propto$	$\frac{1}{9}\left(6\sqrt{2}D + \sqrt{3}S\right)$
$\overline{\Sigma^-}\Sigma^-\phi$	$\propto$	$\frac{1}{9}\left(-6\sqrt{2}D + \sqrt{3}S\right)$	$\overline{p}p\rho^0$	$\propto$	$-D - F$
$\overline{\Sigma^0}\Sigma^0\omega$	$\propto$	$\frac{1}{9}\left(-6D - \sqrt{6}S\right)$	$\overline{p}p\omega$	$\propto$	$\frac{1}{9}\left(3D - 9F - \sqrt{6}S\right)$
$\overline{\Sigma^0}\Sigma^0\phi$	$\propto$	$\frac{1}{9}\left(-6\sqrt{2}D + \sqrt{3}S\right)$	$\overline{p}p\phi$	$\propto$	$\frac{1}{9}\left(3\sqrt{2}D - 9\sqrt{2}F + \sqrt{3}S\right)$
$\overline{\Sigma^+}\Sigma^+\rho^0$	$\propto$	$-2F$	$\overline{n}n\rho^0$	$\propto$	$D + F$
$\overline{\Sigma^+}\Sigma^+\omega$	$\propto$	$\frac{1}{9}\left(-6D - \sqrt{6}S\right)$	$\overline{n}n\omega$	$\propto$	$\frac{1}{9}\left(3D - 9F - \sqrt{6}S\right)$
$\overline{\Sigma^+}\Sigma^+\phi$	$\propto$	$\frac{1}{9}\left(-6\sqrt{2}D + \sqrt{3}S\right)$	$\overline{n}n\phi$	$\propto$	$\frac{1}{9}\left(3\sqrt{2}D - 9\sqrt{2}F + \sqrt{3}S\right)$

$\overline{\Xi^-}\Xi^-\rho^0$	$\propto$	$-D + F$
$\overline{\Xi^-}\Xi^-\omega$	$\propto$	$\frac{1}{9}\left(3D + 9F - \sqrt{6}S\right)$
$\overline{\Xi^-}\Xi^-\phi$	$\propto$	$\frac{1}{9}\left(3\sqrt{2}D + 9\sqrt{2}F + \sqrt{3}S\right)$
$\overline{\Xi^0}\Xi^0\rho^0$	$\propto$	$D - F$
$\overline{\Xi^0}\Xi^0\omega$	$\propto$	$\frac{1}{9}\left(3D + 9F - \sqrt{6}S\right)$
$\overline{\Xi^0}\Xi^0\phi$	$\propto$	$\frac{1}{9}\left(3\sqrt{2}D + 9\sqrt{2}F + \sqrt{3}S\right)$

[12] As discussed in Section 2.2, any flavor-changing meson-baryon interactions would produce a null overlap of ground-state operators, and as such we only focus on the like-baryon interactions of the form $g_{B\alpha}\bar{\psi}_B\alpha\psi_{B'}\delta_{BB'}$ for a meson α in this discussion.

The physical ϕ and f_0 states are purely strange quark components. These do not couple to nucleons significantly (since nucleons contain only up and down valence quarks) the only way to produce these mesons is via gluons. Thus we set the (normalized or not) couplings of these mesons to zero; $g_{B\phi} = g_{Bf_0} = 0$. We are then left with the physical σ and ω mesons as the effective meson degrees of freedom.

If we denote the *total* (but not normalized) coupling (now including all prefactors of Eq. (2.115)) of a (like) baryon pair $\bar{B}B$ to a meson α by $f_{B\alpha}$, and we calculate the SU(3) invariant combinations for the singlet ω_0 and mixed state ω_8, we can use the relation between these normalizations from Eq. (2.107) to relate the S-style couplings to the remaining couplings via

$$-\frac{S}{3} = f_{N\omega_0} = \sqrt{2} f_{N\omega_8} = \frac{\sqrt{2}}{\sqrt{3}}(D - 3F), \tag{2.116}$$

and so we can reduce the relation of the couplings to

$$S = \sqrt{6}(3F - D), \tag{2.117}$$

and we can therefore find the couplings of the singlet ω_0 meson in terms of just F and D factors. After removing the strange quark components and substituting the result of Eq. (2.117) we obtain a summary of couplings as shown in Table 2.2.

We note however that the couplings in Tables 2.1 and 2.2 do not display isospin symmetry manifestly, though our original Lagrangian density (refer to Section 2.1) was constructed in terms of isospin groups only with common coefficients. This can be remedied by considering a *general* Lagrangian density constructed from isospin groups, which we shall restrict to terms involving like baryons and the mesons we are interested in, to give

$$\begin{aligned} \mathcal{L}_{\text{int}}^{\text{oct}} \;=\; & -f_{N\rho}(\overline{N}\vec{\tau}^{\mathrm{T}}N)\cdot\vec{\rho} + i f_{\Sigma\rho}(\vec{\overline{\Sigma}}\times\vec{\Sigma})\cdot\vec{\rho} - f_{\Xi\rho}(\overline{\Xi}\vec{\tau}^{\mathrm{T}}\Xi)\cdot\vec{\rho} \\ & -f_{N\omega}(\overline{N}N)\omega - f_{\Lambda\omega}(\overline{\Lambda}\Lambda)\omega - f_{\Sigma\omega}(\vec{\overline{\Sigma}}\cdot\vec{\Sigma})\omega - f_{\Xi\omega}(\overline{\Xi}\Xi)\omega, \end{aligned} \tag{2.118}$$

where the N, Λ, and Ξ isospin groups are defined as before as

$$N = \begin{pmatrix} p \\ n \end{pmatrix}, \quad \Lambda = \begin{pmatrix} \Lambda \end{pmatrix}, \quad \Xi = \begin{pmatrix} \Xi^0 \\ \Xi^- \end{pmatrix}. \tag{2.119}$$

Table 2.2: Couplings of like baryon-baryon pairs to vector mesons used in these models, according to vertices of type $B + P \to \bar{B}$ using the relation of Eq. (2.117)

$\overline{\Sigma^-}\Sigma^-\rho^0$	$\propto$	$2F$	$\overline{p}p\rho^0$	$\propto$	$-D-F$	$\overline{\Xi^-}\Xi^-\rho^0$	$\propto$	$-D+F$
$\overline{\Sigma^-}\Sigma^-\omega$	$\propto$	$-\frac{2D}{3}$	$\overline{p}p\omega$	$\propto$	$\frac{D}{3}-F$	$\overline{\Xi^-}\Xi^-\omega$	$\propto$	$\frac{D}{3}+F$
$\overline{\Sigma^0}\Sigma^0\omega$	$\propto$	$-\frac{2D}{3}$	$\overline{n}n\rho^0$	$\propto$	$D+F$	$\overline{\Xi^0}\Xi^0\rho^0$	$\propto$	$D-F$
$\overline{\Sigma^+}\Sigma^+\rho^0$	$\propto$	$-2F$	$\overline{n}n\omega$	$\propto$	$\frac{D}{3}-F$	$\overline{\Xi^0}\Xi^0\omega$	$\propto$	$\frac{D}{3}+F$
$\overline{\Sigma^+}\Sigma^+\omega$	$\propto$	$-\frac{2D}{3}$	$\overline{\Lambda}\Lambda\omega$	$\propto$	$\frac{2D}{3}$			

The ρ mesons terms are defined in isospin space as linear combinations of the physical charged states (as we did in Section 2.3.1) as

$$\rho^- = \frac{1}{\sqrt{2}}(\rho_1 - i\rho_2), \quad \rho^+ = \frac{1}{\sqrt{2}}(\rho_1 + i\rho_2), \quad \rho^0 = \rho_3,$$

or, equivalently as

$$\rho_1 = \frac{1}{\sqrt{2}}(\rho^+ + \rho^-), \quad \rho_2 = \frac{i}{\sqrt{2}}(\rho^- - \rho^+), \quad \rho_3 = \rho^0, \tag{2.120}$$

with the same convention for the replacement of $\vec{\rho} \to \vec{\Sigma}$. This gives the expansion

$$\vec{\Sigma} \cdot \vec{\rho} = \Sigma^+\rho^- + \Sigma^0\rho^0 + \Sigma^-\rho^+. \tag{2.121}$$

We can expand the Lagrangian density term by term to find the individual interactions

$$\begin{aligned}
(\overline{N}\vec{\tau}^{\mathrm{T}}N)\cdot\vec{\rho} &= (\overline{p}\ \ \overline{n})\ \tau_i^{\mathrm{T}}\rho^i \begin{pmatrix} p \\ n \end{pmatrix} \\
&= (\overline{p}n + \overline{n}p)\rho_1 + i(\overline{p}n - \overline{n}p)\rho_2 + (\overline{p}p - \overline{n}n)\rho_3 \\
&= \frac{1}{\sqrt{2}}(\overline{p}n + \overline{n}p)(\rho_+ + \rho_-) - \frac{1}{\sqrt{2}}(\overline{p}n - \overline{n}p)(\rho_- - \rho_+) + (\overline{p}p - \overline{n}n)\rho_0 \\
&= \overline{p}p\rho_0 - \overline{n}n\rho_0 + \sqrt{2}\overline{p}n\rho_+ + \sqrt{2}\overline{n}p\rho_- \ ,
\end{aligned} \tag{2.122}$$

where we note that a term $\bar{B}BP$ indicates the annihilation of a baryon B with a meson P, and the creation of a baryon $\bar{B}$ according to the reaction $B + P \to \bar{B}$. Continuing to expand terms, for the Σ baryons we have

$$(\vec{\overline{\Sigma}} \times \vec{\Sigma})\cdot\vec{\rho} = -i\rho^+\left(\Sigma^-\overline{\Sigma^0} - \Sigma^0\overline{\Sigma^+}\right) - i\rho^-\left(\Sigma^0\overline{\Sigma^-} - \Sigma^+\overline{\Sigma^0}\right) - i\rho^0\left(\Sigma^+\overline{\Sigma^+} - \Sigma^-\overline{\Sigma^-}\right) \ , \tag{2.123}$$

and for the Ξ baryons,

$$\begin{aligned}
(\overline{\Xi}\vec{\tau}^{\mathrm{T}}\Xi)\cdot\vec{\rho} &= (\overline{\Xi^0}\ \ \overline{\Xi^-})\ \tau_i^{\mathrm{T}}\rho^i \begin{pmatrix} \Xi^0 \\ \Xi^- \end{pmatrix} \\
&= (\overline{\Xi^0}\Xi^- + \overline{\Xi^-}p)\rho_1 + i(\overline{\Xi^0}\Xi^- - \overline{\Xi^-}\Xi^0)\rho_2 + (\overline{\Xi^0}\Xi^0 - \overline{\Xi^-}\Xi^-)\rho_3 \\
&= \overline{\Xi^0}\Xi^0\rho_0 - \overline{\Xi^-}\Xi^-\rho_0 + \sqrt{2\overline{\Xi^0}}\Xi^-\rho_+ + \sqrt{2\overline{\Xi^-}}\Xi^0\rho_-.
\end{aligned} \tag{2.124}$$

The iso-scalar terms are more straightforward;

$$(\overline{N}N)\omega = \overline{p}p\omega + \overline{n}n\omega, \tag{2.125}$$

$$\overline{\Lambda}\Lambda\omega \quad \text{(requires no expansion)}, \tag{2.126}$$

$$(\vec{\overline{\Sigma}}\cdot\vec{\Sigma})\omega = \overline{\Sigma^+}\Sigma^+\omega + \overline{\Sigma^0}\Sigma^0\omega + \overline{\Sigma^-}\Sigma^-\omega, \tag{2.127}$$

$$(\overline{\Xi}\Xi)\omega = \overline{\Xi^0}\Xi^0\omega + \overline{\Xi^-}\Xi^-\omega. \tag{2.128}$$

Once we have calculated the full interaction Lagrangian density, and the F and D coefficients of each interaction, we have factors of the following form:

$$\mathcal{L}_{\text{int}} = \sum_B \sum_m A_{Bm} f_{Bm} X_{Bm}; \quad X_{Bm} = C_{Bm} \bar{B} B m, \tag{2.129}$$

where $A_{\Sigma\rho} = i$, and for all other interactions $A_{Bm} = -1$. The term X_{Bm} is the expanded interaction term (after expanding cross products, etc.) arising from the *general* Lagrangian density, Eq. (2.118), and contains factors of $C_{Bm} = \pm 1, \pm\sqrt{2}$. We also require a term calculated from the SU(3) invariant combinations M_{Bm}; the coefficient of the interaction $\bar{B}Bm$ in terms of F and D factors as found in Table 2.2.

To calculate the values of f_{Bm} we apply the following formula:

$$f_{Bm} = \frac{C_{Bm}}{A_{Bm}} M_{Bm}. \tag{2.130}$$

For example, consider the interaction vertex $\omega + \Sigma^0 \to \overline{\Sigma^0}$:

$$A_{\Sigma\omega} = -1, \quad C_{\Sigma\omega} = +1, \quad M_{\Sigma\omega} = -\frac{2D}{3}, \quad \Rightarrow \quad f_{\Sigma\omega} = \frac{+1}{-1}(-\frac{2D}{3}) = \frac{2D}{3}. \tag{2.131}$$

Performing these calculations for every possible interactions provides (consistently) the following couplings of the octet of baryons to the octet of mesons:

$$\begin{gathered} f_{N\rho} = D + F, \quad f_{\Lambda\rho} = 0, \quad f_{\Sigma\rho} = 2F, \quad f_{\Xi\rho} = F - D, \\ f_{N\omega} = 3F - D, \quad f_{\Lambda\omega} = -\tfrac{4}{3}D + 2F, \quad f_{\Sigma\omega} = 2F, \quad f_{\Xi\omega} = F - D. \end{gathered} \tag{2.132}$$

We can further simplify our calculations by examining all the different currents that one can form using a baryon, an antibaryon and a meson. As discussed in Ref. [33], all possible couplings of baryons to vector mesons (denoted by $\bar{B}BV$) should be considered when writing out the most general Lagrangian density. By calculating the currents (prior to making any approximations or assumptions that appear in earlier sections here) we are able to find the F-, D-, and S-style couplings of the form $\bar{B}BX$ where X is a meson with either scalar (S), vector (V), tensor (T), axial-vector (A) or pseudo-scalar (P) spin form.

Under an expanded SU(6) spin-flavor symmetry, the currents are shown in Table 2.3, where the various vector couplings are of the forms

$$V_1 = \bar{\psi}\gamma_\mu\psi, \; V_2 = \bar{\psi}\sigma_{\mu\nu}q^\nu\psi, \; V_3 = \bar{\psi}q_\mu\psi, \tag{2.133}$$

and we use the convenience definitions of

$$\sigma_{\mu\nu} = \frac{i}{2}\left[\gamma_\mu, \gamma_\nu\right], \quad H = \frac{4M^2 + q^2}{2M^2}. \tag{2.134}$$

If we now consider this as a low energy effective field theory, we can consider the case of $q^2 = 0$. We can also enforce rotational symmetry due to lack of a preferred frame (or direction) and thus remove the spatial components of both the mesons and the momenta, so that $V^\mu = (V^0, \vec{0})$ and $q^\mu = (q^0, \vec{0})$, as per Section 2.3.1. Along with $\sigma_{00} = 0$, all terms proportional to q^2 vanish, and $H = 2$. Using these assumptions, the currents are reduced to those found in Table 2.4.

Table 2.3: F-, D- and S-style Baryon currents for all types of meson vertices of the form $\bar{B}BX$ where X is a meson with either scalar (S), vector (V), tensor (T), axial(pseudo-) vector (A) or pseudo-scalar (P) spin form. Adapted from Ref. [33].

	F	D	S
S	$\frac{1}{3}H\bar{\psi}\psi$	0	$\frac{1}{3}H\bar{\psi}\psi$
V_1	$\frac{1}{3}\left(H-\frac{1}{6}\frac{q^2}{M^2}\right)\bar{\psi}\gamma_\mu\psi$	$\frac{q^2}{6M^2}\bar{\psi}\gamma_\mu\psi$	$\frac{1}{3}\left(H-\frac{1}{3}\frac{q^2}{M^2}\right)\bar{\psi}\gamma_\mu\psi$
V_2	$-\frac{1}{9M}i\bar{\psi}\sigma_{\mu\nu}\psi$	$+\frac{1}{3M}i\bar{\psi}\sigma_{\mu\nu}\psi$	$-\frac{2}{9M}i\bar{\psi}\sigma_{\mu\nu}\psi$
V_3	0	0	0
A	$\frac{2}{9}H\bar{\psi}\gamma_5\gamma_\mu\psi$	$\frac{1}{3}H\bar{\psi}\gamma_5\gamma_\mu\psi$	$\frac{1}{9}H\bar{\psi}\gamma_5\gamma_\mu\psi$
P	$\frac{2}{9}H\bar{\psi}\gamma_5\psi$	$\frac{1}{3}H\bar{\psi}\gamma_5\psi$	$\frac{1}{9}H\bar{\psi}\gamma_5\psi$

We can now observe the relations between the F- and D-style couplings (with the S-style coupling now contributing to F and D); First, as a check, we observe that the ratio D/F for the pseudo-scalars (and the axial-vectors for that matter) is indeed $\frac{3}{2}$ as commonly noted in the literature [34, 35] under SU(6) symmetry [36]. Less commonly found in the literature is that the γ_μ-type vector coupling is purely F-style, thus the vector analogy of the above relation is $D/F = 0$, implying $D = 0$.

Using the couplings of Table 2.2, we can evaluate the couplings of the vector mesons to the entire baryon octet. This provides us with a unified description of the couplings in terms of an arbitrary parameter F. These couplings are thus

$$\begin{aligned} f_{N\rho} = F, \quad f_{\Lambda\rho} = 0, \quad f_{\Sigma\rho} = 2F, \quad f_{\Xi\rho} = F, \\ f_{N\omega} = 3F, \quad f_{\Lambda\omega} = 2F, \quad f_{\Sigma\omega} = 2F, \quad f_{\Xi\omega} = F. \end{aligned} \tag{2.135}$$

We can normalize these results to the nucleon-ω coupling, since we will fit this parameter to saturation properties (refer to Section 2.8). Thus the normalized couplings are

$$g_{Bm} = g_{N\omega}\frac{f_{Bm}}{f_{N\omega}}. \tag{2.136}$$

We can then separate the meson couplings, since the the normalization above results in the following relations, using isospin I_B, and strangeness S_B of baryon B;

$$g_{B\omega} = \frac{(3-S_B)}{3}\, g_{N\omega}, \quad g_{B\rho} = \frac{2I_B}{3}\, g_{N\omega}. \tag{2.137}$$

These results are consistent with a commonly used naïve assumption that the ω meson couples to the number of light quarks, and that the ρ meson couples to isospin. To emphasize the isospin symmetry in our models, we will include the isospin as a factor in our Lagrangian densities in the form of the $\vec{\tau}$ matrices. In doing so, rather than having an independent coupling for each isospin group, we will have a global coupling for the ρ meson, g_ρ.

Table 2.4: F-, D- and S-style Baryon currents with mean-field assumptions $V^\mu = (V^0, \vec{0})$, $q^\mu = (q^0, \vec{0})$, and $q^2 = 0$.

	F	D	S
S	$\frac{2}{3}\bar{\psi}\psi$	0	$\frac{2}{3}\bar{\psi}\psi$
V_1	$\frac{2}{3}\bar{\psi}\gamma_\mu\psi$	0	$\frac{2}{3}\bar{\psi}\gamma_\mu\psi$
V_2	0	0	0
V_3	0	0	0
A	$\frac{4}{9}\bar{\psi}\gamma_5\gamma_\mu\psi$	$\frac{2}{3}\bar{\psi}\gamma_5\gamma_\mu\psi$	$\frac{2}{9}\bar{\psi}\gamma_5\gamma_\mu\psi$
P	$\frac{4}{9}\bar{\psi}\gamma_5\psi$	$\frac{2}{3}\bar{\psi}\gamma_5\psi$	$\frac{2}{9}\bar{\psi}\gamma_5\psi$

Similarly to the above relations for the vector mesons, we have the same relation for the scalar mesons; that the coupling is purely F-style ($D = 0$). Therefore the couplings for the scalar mesons are the same as for the vector mesons, under the replacements $\omega \to \sigma$, $\vec{\rho} \to \vec{a}_0$. In the calculations that follow, we shall further neglect the contributions from the scalar iso-vector $\vec{a}_0$ due to their relatively large mass (refer to Table B.1).

As an alternative to the SU(6) relations for the ρ meson coupling g_ρ, we can use an experimental constraint. As we have shown above, the ρ meson couples to isospin, and as we will show in Section 3.1 the isospin density is proportional to the asymmetry between members of an isospin group; for example the asymmetry between protons and neutrons. This asymmetry is measured by the symmetry energy $a_4 \equiv a_{\rm sym}$ (derived in Appendix A.5.4) which appears in the semi-empirical mass formula (the connection is derived in Appendix A.5.2) which in the absence of charge symmetry is defined by Eq. (2.74). The coupling of ρ to the nucleons is found such that the experimental value of the asymmetry energy of $a_{\rm sym} = 32.5$ MeV is reproduced at saturation. The coupling of ρ to the remaining baryons follows the relations above.

Models Considered

As outlined in the introduction, QCD is widely believed to be an accurate description of strong-interaction particle physics. As a non-perturbative theory, it cannot be solved analytically. In order to make any predictions for this theory we must simulate the physics of QCD, and we choose to do so using a model.

As with most fields of research, there are several choices for models to investigate. The validity of these models must always be challenged, and there is always a tendency to have a preference for a particular model. Our goal is to work with a model which does not introduce any physics that is not manifest in Nature, and does not make any assumptions that cannot be verified. To this end, we begin with a model called Quantum Hadrodynamics (QHD) which—although it is not a quark-level model—simulates the fundamental interactions of QCD with effective meson interactions.

3.1 Quantum Hadrodynamics Model (QHD)

The origins of the mean-field approximation and QHD reach back to the non-relativistic work of Johnson and Teller [37], which was reformulated by Duerr in a relativistic model [38]. Once Chin and Walecka [9, 39] successfully reproduced saturation properties (refer to section 2.8), QHD as it is known today was born. The formalism for QHD used for this work is expertly detailed by Serot and Walecka [18] and by Furnstahl and Serot [40]. QHD was the first great step towards a particle-physics understanding of nuclear matter, particularly in the form of neutron stars.

QHD is an effective[1], fully relativistic[2] field theory which makes use of a mean-field approximation (MFA, refer to Section 2.2) to describe Dirac nucleons interacting at the quantum level. The gluons of QCD are simulated by a delicate balance between attractive interactions of scalar mesons, and repulsive interactions of vector mesons which, when added together, produce an effect which approximates the strong nuclear interaction; the interaction responsible for holding protons and neutrons together inside a nucleus where the the Coulomb interaction would otherwise cause the protons to repel and prevent any nuclei from existing.

In the original formulation of QHD (later dubbed QHD-I), interactions between the degenerate[3] iso-doublet of nucleons (protons p, and neutrons n) involved the scalar-isoscalar σ and vector-isoscalar ω mesons in the zero temperature limit. This was soon expanded to QHD-II by inclusion of the uncharged vector-isovector ρ_0 meson. We extend this to include the full baryon octet by including the hyperons; Λ, Σ^+, Σ^0, Σ^-, Ξ^0, and Ξ^-. For historical purposes, and to emphasise the effects of each of these advances, when we present results we shall do so for the most sophisticated version of a particular model, but also for conditions corresponding to these variations for comparison.

We further extend this to use the SU(6) spin-flavor symmetry to relate the couplings of all the baryons to all the mesons using the F-style couplings as detailed in Section 2.12.

[1] Not involving fundamental particles as the degree of freedom, but rather composite particles which provide a useful approximation to the physics.

[2] Making use of and obeying relativity, both special and general.

[3] In which the particles share a common mass, and thus satisfy charge symmetry.

We make our model more physically realistic by using the physical masses for the baryons, since charge symmetry is violated in Nature. This provides a mass difference between the protons and neutrons, and the model becomes sufficiently precise that we may include leptons, which have a considerably smaller mass than the baryons. We may then consider the effects of β-equilibrium between species; by including leptons[4] ($\ell \in \{e^-, \mu^-\}$) we allow the possibility of considering a balance between various charged species, although we are not explicitly modelling charge-conserving interactions, as this would require the inclusion of photon terms in the Lagrangian density, photons being the mediators of the electromagnetic force. If we did not include the leptons, we would not be able to consider globally charge neutral nucleonic matter, as no negative charges would be available to balance the positive charge of the protons.

We will use the term 'configuration of a model' to indicate differences (such as types of particles included or neglected) within a particular model. The following discussion will focus on the most sophisticated configuration—the octet of baryons in β-equilibrium with leptons—and less sophisticated configurations can be obtained by restricting this description. The Lagrangian density that describes such a configuration of QHD is

$$\begin{aligned}\mathcal{L} &= \sum_k \bar{\psi}_k \left[\gamma_\mu (i\partial^\mu - g_{k\omega}\omega^\mu - g_\rho \vec{\tau}_{(k)} \cdot \vec{\rho}^\mu) - (M_k - g_{k\sigma}\sigma)\right] \psi_k \\ &+ \frac{1}{2}(\partial_\mu \sigma \partial^\mu \sigma - m_\sigma^2 \sigma^2) - \frac{1}{4} F_{\mu\nu} F^{\mu\nu} - \frac{1}{4} R^a_{\mu\nu} R^{\mu\nu}_a \\ &+ \frac{1}{2} m_\omega^2 \omega_\mu \omega^\mu + \frac{1}{2} m_\rho^2 \rho^a_\mu \rho^\mu_a + \sum_\ell \bar{\psi}_\ell \left[i\gamma_\mu \partial^\mu - m_\ell\right] \psi_\ell + \delta\mathcal{L}, \end{aligned} \tag{3.1}$$

where the indices $k \in \{N, \Lambda, \Sigma, \Xi\}$ and $\ell \in \{e^-, \mu^-\}$ represent the isospin group of the baryon states and the lepton states, respectively, $\vec{\tau}_{(k)}$ are the isospin matrices for each isospin group (refer to Eq. (2.12)), and ψ_k corresponds to the Dirac spinors for these isospin groups, i.e.

$$\psi_N = \begin{pmatrix} \psi_p \\ \psi_n \end{pmatrix}, \quad \psi_\Lambda = \begin{pmatrix} \psi_\Lambda \end{pmatrix}, \quad \psi_\Sigma = \begin{pmatrix} \psi_{\Sigma^+} \\ \psi_{\Sigma^0} \\ \psi_{\Sigma^-} \end{pmatrix}, \quad \psi_\Xi = \begin{pmatrix} \psi_{\Xi^0} \\ \psi_{\Xi^-} \end{pmatrix}. \tag{3.2}$$

The vector field strength tensors are

$$F^{\mu\nu} = \partial^\mu \omega^\nu - \partial^\nu \omega^\mu, \quad R^{\mu\nu}_a = \partial^\mu \rho^\nu_a - \partial^\nu \rho^\mu_a - g_\rho \epsilon_{abc} \rho^\mu_b \rho^\nu_c, \tag{3.3}$$

ψ_ℓ is a spinor for the leptons, and $\delta\mathcal{L}$ are renormalization terms. The values of the baryon and meson masses (in vacuum, as used in the calculations herein) are summarized later in Table 5.1. We have neglected nonlinear meson terms in this description for comparison purposes, though it has been shown that the inclusion of non-linear scalar meson terms produces a framework consistent with the QMC model without the added hyperfine interaction [41] (see Sec. 3.2).

[4] We can safely neglect the contribution of τ leptons—which have a mass in excess of 1776 MeV [17] which makes them more massive than the Ξ hyperons—since their chemical potential would be equal to that of the electrons, and thus one would require an extraordinarily large electron contribution in order to provide a non-negligible τ Fermi momentum.

Assuming that the baryon density is sufficiently large, we use a Mean-Field Approximation (MFA, as described in Section 2.2) with physical parameters (breaking charge symmetry) in which the meson fields are replaced by their classical vacuum expectation values, $\alpha \to \langle\alpha\rangle_{\text{classical}}$. With this condition, the renormalization terms $\delta\mathcal{L}$ can be neglected.

By enforcing rotational symmetry (refer to Section 2.3.1) and working in the frame where the matter as a whole is at rest, we set all of the three-vector components of the vector meson fields to zero, leaving only the temporal components. Furthermore, we remove all charged meson states as per the discussion in Section 2.3.1. Consequently, because the mean-fields are constant, all meson derivative terms vanish, and thus so do the vector field tensors. The only non-zero components of the vector meson mean fields are then the temporal components, $\langle\omega^\mu\rangle = \langle\omega\rangle\delta^{\mu 0}$ and $\langle\vec{\rho}^{\,\mu}\rangle = \langle\vec{\rho}\rangle\delta^{\mu 0}$. Similarly, only the third isospin component of the ρ meson mean-field is non-zero, corresponding to the uncharged ρ_0 meson.

The couplings of the mesons to the baryons are found via SU(6) spin-flavor symmetry [32]. This produces the following relations for the σ and ω couplings to each isospin group (and hence each baryon B in that isospin group) as per Section 2.12:

$$\frac{1}{3}\,g_{N\sigma} = \frac{1}{2}\,g_{\Lambda\sigma} = \frac{1}{2}\,g_{\Sigma\sigma} = g_{\Xi\sigma}, \quad \frac{1}{3}\,g_{N\omega} = \frac{1}{2}\,g_{\Lambda\omega} = \frac{1}{2}\,g_{\Sigma\omega} = g_{\Xi\omega}. \tag{3.4}$$

Using the formalism of Eq. (3.1) with isospin expressed explicitly in the Lagrangian density, the couplings of the ρ meson to the octet baryons are unified, and thus we can calculate the coupling of any baryon to either the σ, ω or ρ meson.

By evaluating the equations of motion from the Euler–Lagrange equations,

$$\frac{\partial\mathcal{L}}{\partial\phi_i} - \partial_\mu\frac{\partial\mathcal{L}}{\partial(\partial_\mu\phi_i)} = 0, \tag{3.5}$$

we find the mean-field equations for each of the mesons, as well as the baryons. Prior to applying the MFA for the mesons, the σ equation of motion produces a Klein–Gordon equation, while the ω and ρ equations of motion produce Maxwell equations. This is by construction, and these terms can be found in Appendix A.3. Returning to the use of the MFA, the equations of motion for the meson fields are

$$\langle\sigma\rangle = \sum_B \frac{g_{B\sigma}}{m_\sigma^2}\langle\bar{\psi}_B\psi_B\rangle, \tag{3.6}$$

$$\langle\omega\rangle = \sum_B \frac{g_{B\omega}}{m_\omega^2}\langle\bar{\psi}_B\gamma^0\psi_B\rangle = \sum_B \frac{g_{B\omega}}{m_\omega^2}\langle\psi_B^\dagger\psi_B\rangle, \tag{3.7}$$

$$\langle\rho\rangle = \sum_k \frac{g_\rho}{m_\rho^2}\langle\bar{\psi}_k\gamma^0\tau_{(k)3}\psi_k\rangle = \sum_k \frac{g_\rho}{m_\rho^2}\langle\psi_k^\dagger\tau_{(k)3}\psi_k\rangle = \sum_B \frac{g_\rho}{m_\rho^2}\langle\psi_B^\dagger I_{3B}\psi_B\rangle, \tag{3.8}$$

where the sum over B corresponds to the sum over the octet of baryons, and the sum over k corresponds to the sum over isospin groups. I_{3B} is the third component of the isospin of baryon B, as found in the diagonal elements of $\tau_{(k)3}$ in Eq. (2.12). $\langle\omega\rangle$, $\langle\rho\rangle$, and $\langle\sigma\rangle$ are proportional to the conserved baryon density, isospin density and scalar density respectively, where the scalar density is calculated self-consistently.

The Euler–Lagrange equations also provide a Dirac equation for the baryons

$$\sum_B \left[i\partial\!\!\!/ - g_{B\omega}\gamma^0\langle\omega\rangle - g_\rho\gamma^0 I_{3B}\langle\rho\rangle - M_B + g_{B\sigma}\langle\sigma\rangle\right]\psi_B = 0, \tag{3.9}$$

in which we have inserted the expressions for the self-energies in QHD. The effective mass (as defined by the scalar self-energy inserted above, as per Eq. (2.43)) is given by

$$M_B^* = M_B + \Sigma_B^s = M_B - g_{B\sigma}\langle\sigma\rangle, \tag{3.10}$$

and the evaluation of this is shown in Fig. 3.1 for the octet of baryons. We note here that this definition of the effective mass—being linear in the scalar field—has the possibility of being negative for particular values of $\langle\sigma\rangle$. We will discuss this issue (and a remedy to it) in more detail later, but for now we shall acknowledge that this definition of the effective mass includes only the first term of many as a linear approximation.

The baryon chemical potential (Fermi energy) is defined here as the energy associated with the Dirac equation Eq. (3.9), which involves the above self-energies as

$$\mu_B = \epsilon_{F_B} = \sqrt{k_{F_B}^2 + (M_B^*)^2} + g_{B\omega}\langle\omega\rangle + g_\rho I_{3B}\langle\rho\rangle. \tag{3.11}$$

The chemical potentials for the leptons are simply

$$\mu_\ell = \sqrt{k_{F_\ell}^2 + m_\ell^2}, \tag{3.12}$$

since the leptons do not interact with the mesons.

The energy density $\mathcal{E}$ and pressure P for the EOS can be obtained using the relations for the energy-momentum tensor for a perfect fluid at rest, where u^μ is the four-velocity

$$\langle T^{\mu\nu}\rangle = (\mathcal{E} + P)\, u^\mu u^\nu + P g^{\mu\nu}, \quad \Rightarrow \quad P = \frac{1}{3}\langle T^{ii}\rangle, \quad \mathcal{E} = \langle T^{00}\rangle, \tag{3.13}$$

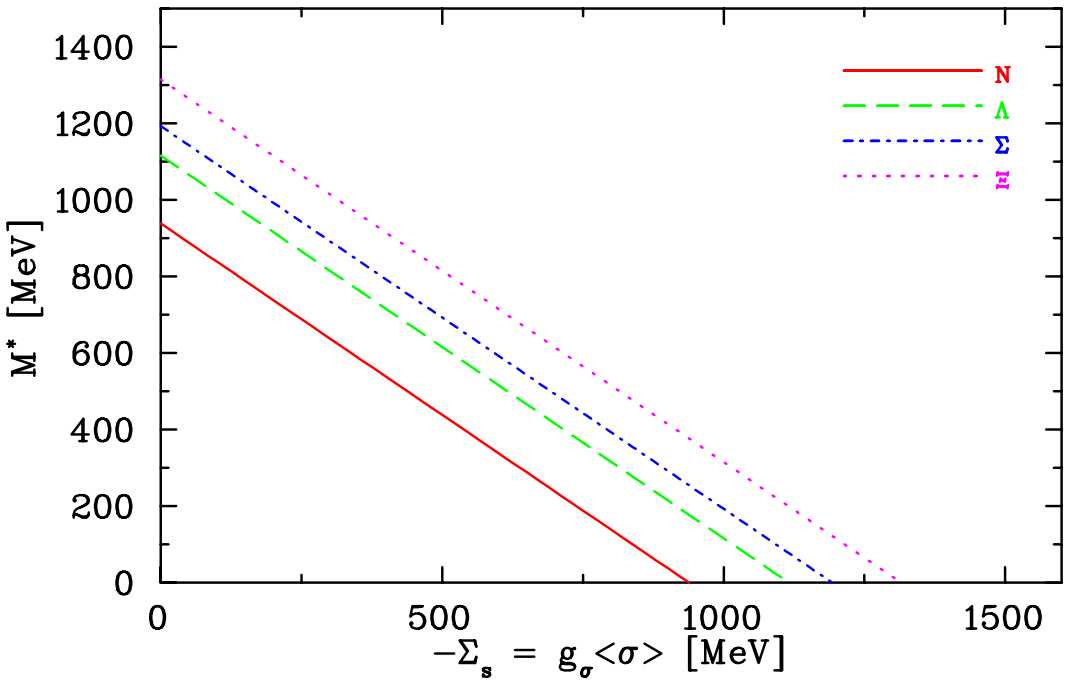

Fig. 3.1: (Color Online) Baryon effective masses M^* as defined by the scalar self-energy Σ^s for QHD. Note that it becomes possible that at some densities these effective masses may become negative. Negative effective masses in the Dirac equation imply the presence of antibaryons, which this model has neglected, so at this point the model becomes unreliable.

since $u^i = 0$ and $u_0 u^0 = -1$, where $\mathrm{g}^{\mu\nu}$ here is the inverse metric tensor having a negative temporal component, $\mathrm{g} = \mathrm{diag}(-1, +1, +1, +1)$, in contrast to the Minkowski metric of Eq. (2.5). In accordance with Noether's Theorem, the relation between the energy-momentum tensor and the Lagrangian density is

$$T^{\mu\nu} = -\mathrm{g}^{\mu\nu}\mathcal{L} + \partial^\mu\psi\frac{\partial\mathcal{L}}{\partial(\partial_\nu\psi)}. \tag{3.14}$$

We find the energy density and pressure for QHD to be the following sum of contributions from baryons B, leptons ℓ, and mesons m to be

$$\begin{aligned}
\mathcal{E} &= \sum_{j=B,\ell,m}\mathcal{E}_j \\
&= \sum_{i=B,\ell}\frac{(2J_i+1)}{(2\pi)^3}\int\theta(k_{F_i}-|\vec{k}|)\sqrt{\vec{k}^2+(M_i^*)^2}\;d^3k + \sum_{\alpha=\sigma,\omega,\rho}\frac{1}{2}m_\alpha^2\langle\alpha\rangle^2, \qquad (3.15)\\
P &= \sum_{j=B,\ell,m}P_j \\
&= \sum_{i=B,\ell}\frac{(2J_i+1)}{3(2\pi)^3}\int\frac{\vec{k}^2\;\theta(k_{F_i}-|\vec{k}|)}{\sqrt{\vec{k}^2+(M_i^*)^2}}\;d^3k + \sum_{\alpha=\omega,\rho}\frac{1}{2}m_\alpha^2\langle\alpha\rangle^2 - \frac{1}{2}m_\sigma^2\langle\sigma\rangle^2, \qquad (3.16)
\end{aligned}$$

where J_i is the spin of particle i ($J_i = \frac{1}{2}\;\forall\; i \in \{B,\ell\}$) which in this case accounts for the availability of both up and down spin-states, and θ is the Heaviside Step Function (see Eq. (2.39)). Note that the pressure arising from the vector mesons is positive, while it is negative for the scalar meson. For a full derivation of these terms, refer to Appendix A.3.

The expression for the self-consistent scalar field $\langle\sigma\rangle$ is determined by the derivative of the energy density with respect to the effective mass. In the case of QHD this expression is given by

$$\langle\sigma\rangle = \sum_B\frac{g_{B\sigma}}{m_\sigma^2}\frac{(2J_B+1)}{(2\pi)^3}\int\frac{M_B^*\;\theta(k_{F_B}-|\vec{k}|)}{\sqrt{\vec{k}^2+(M_B^*)^2}}\;d^3k, \tag{3.17}$$

which is solved self-consistently since the effective mass (appearing in the integral) is defined in terms of this quantity, as per Eq. (3.10).

The couplings $g_{N\sigma}$ and $g_{N\omega}$ are determined such that symmetric nuclear matter (in which $\rho_p = \rho_n = 0.5\rho_{\mathrm{total}}$) saturates with the appropriate minimum in the (binding) energy per baryon, as per Section 2.8. The couplings for QHD which provide a fit to saturated nuclear matter are shown in Table 5.2.

The EOS for QHD can be obtained by finding solutions to Eqs. (3.6)–(3.8) subject to charge-neutrality, conservation of a chosen total baryon number, and equivalence of chemical potentials. These conditions can be summarized as

$$\left.\begin{aligned}
0 &= \textstyle\sum_i Q_i\rho_i \\
\rho &= \textstyle\sum_i B_i\rho_i \\
\mu_i &= B_i\mu_n - Q_i\mu_e
\end{aligned}\right\} \quad i \in \{p, n, \Lambda, \Sigma^+, \Sigma^0, \Sigma^-, \Xi^0, \Xi^-, e^-, \mu^-\}. \tag{3.18}$$

Once these equations are solved, the energy density and pressure can be calculated.

It should be noted that, as with many relativistic models for baryonic matter, once we include more than one species of baryon this model eventually predicts the production of baryons with negative effective masses at sufficiently high densities ($\rho > 1$ fm^{-3}). This is a direct result of the linear nature of the effective mass as shown in Eq. (3.10). As the Fermi energy (see Eq. (3.11)) approaches zero, the cost associated with producing baryon-antibaryon pairs is reduced and at this point the model breaks down. From a more physical point of view, as the density rises one would expect that the internal structure of the baryons should play a role in the dynamics. Indeed, within the QMC model, the response of the internal structure of the baryons to the applied mean-scalar-field ensures that no baryon mass ever becomes negative.

3.2 Quark-Meson Coupling Model (QMC)

Up to this point we have only considered QHD as an effective field theory; we have considered baryons as the fundamental degrees of freedom for this scale. It may however be the case that further internal degrees of freedom are more significant at high-densities. We therefore wish to extend our model to include the effect of baryon structure in the form of quarks[5].

Deep inelastic scattering experiments have shown that nucleons do indeed have internal structure [43], and few would discount quarks as the fundamental particles involved. To include this degree of freedom, one needs to solve the boundary condition equations for the Dirac particles and include the energy contribution from a '*bag*' similar to the MIT bag model parameter, as will be shown.

The work here will focus on the latest development of the QMC model [44] which includes a quadratic term with numerical factor d in the effective mass which accounts for the scalar polarizability. Like QHD, QMC is a relativistic quantum field theory formulated in terms of the exchange of scalar and vector mesons. However, in contrast with QHD these mesons couple not to structureless baryons but to clusters of confined quarks. As the density of the medium grows and the mean-scalar and mean-vector fields grow, the structure of the clusters adjusts self-consistently in response to the mean-field coupling.

While such a model would be extremely complicated to solve in general, it has been shown by Guichon *et al.* [45] that in finite nuclei one should expect the Born–Oppenheimer approximation (in which we are able to isolate and distinguish the effects of the quarks, in the same way that one is able to separate the net effects of electrons in an atomic calculation) to be good at the 3% level. Of course, in nuclear matter it is exact at mean-field level as a result of the constant meson fields.

Within the Born–Oppenheimer approximation, the major effect of including the structure of the baryon is that the internal quark wave functions respond in a way that opposes the applied scalar field. To a very good approximation this physics is described through the 'scalar polarizability' d, which in analogy with the electric polarizability[6], describes the term in the baryon effective mass quadratic in the applied scalar field [47–51]. Recent explicit calculations of the equivalent energy functional for the QMC model have demonstrated the very natural link between the existence of the scalar polarizability and the many-body forces, or equivalently the density dependence, associated with successful, phenomenological forces

[5] Some portions of this section are adapted from Carroll *et. al.* [42].

[6] In QED, the expression for the energy shift due to the quadratic Stark effect is $\Delta E = -\frac{1}{2}\alpha|E_z|^2$, in which α is the electric polarizability and E_z is the external electric field, taken to point along the $\hat{z}$-axis [46].

of the Skyrme type [52, 53]. In nuclear matter, the scalar polarizability is the *only* effect of the internal structure in the mean-field approximation. On the other hand, in finite nuclei the variation of the vector field across the hadronic volume also leads to a spin-orbit term in the nucleon energy [45].

Once one chooses a quark model for the baryons and specifies the quark level meson couplings, there are no new parameters associated with introducing any species of baryon into the nuclear matter. Given the well known lack of experimental constraints on the forces between nucleons and hyperons (let alone hyperons and hyperons) which will be of great practical importance as the nuclear density rises above (2–3)ρ_0, this is a particularly attractive feature of the QMC approach and it is crucial for our current investigation. Indeed, we point to the very exciting recent results [54] of the QMC model—modified to include the effect of the scalar field on the hyperfine interaction—which led to Λ hypernuclei being bound in quite good agreement with experiment and Σ hypernuclei being unbound because of the modification of the hyperfine interaction, thus yielding a very natural explanation of this observed fact. We note the success that this description has generated for finite nuclei as observed in Ref. [53].

While we will use the QMC model for our considerations of baryon structure here, we note that there has been a parallel development [55] based upon the covariant, chiral symmetric NJL model [56], with quark confinement modelled using the proper time regularization proposed by the Tübingen group [57,58]. The latter model has many advantages for the computation of the medium modification of form factors and structure functions, with the results for spin structure functions [59, 60] offering a unique opportunity to test the fundamental idea of the QMC model experimentally. However, in both models it is the effect of quark confinement that leads to a positive polarizability and a natural saturation mechanism.

Comparisons between the QHD and QMC derivations *a posteriori* reveal that although the underlying physics of QHD and QMC is rather different, at the hadronic level the equations to be solved are very similar. Full discussions and derivations can be found in Refs. [41,47,61,62]. We shall rather focus on the changes to QHD which are required to produce the QMC model:

1. Because of the scalar polarizability of the hadrons, which accounts for the self-consistent response of the internal quark structure of the baryon to the applied scalar field [53], the effective masses appearing in QMC are non-linear in the mean-scalar field. We write them in the general form

$$M_B^* = M_B - w_B^\sigma \, g_{N\sigma}\langle\sigma\rangle + \frac{d}{2}\tilde{w}_B^\sigma \, (g_{N\sigma}\langle\sigma\rangle)^2 \,, \tag{3.19}$$

where the weightings w_B^σ, $\tilde{w}_B^\sigma$, and the scalar polarizability of the nucleon d, must be calculated from the underlying quark model. Note now that only the coupling to the nucleons $g_{N\sigma}$, is required to determine all the effective masses.

The most recent calculation of these effective masses, including the in-medium dependence of the spin dependent hyperfine interaction [54], yields the explicit expressions:

$$M_N(\langle\sigma\rangle) = M_N - g_{N\sigma}\langle\sigma\rangle + \left[0.0022 + 0.1055 R_N^{\rm free} - 0.0178 \left(R_N^{\rm free}\right)^2\right] (g_{N\sigma}\langle\sigma\rangle)^2 \,, \tag{3.20}$$

$$\begin{aligned} M_\Lambda(\langle\sigma\rangle) \;&=\; M_\Lambda - \left[0.6672 + 0.0462 R_N^{\rm free} - 0.0021 \left(R_N^{\rm free}\right)^2\right] g_{N\sigma}\langle\sigma\rangle \\ &\quad + \left[0.0016 + 0.0686 R_N^{\rm free} - 0.0084 \left(R_N^{\rm free}\right)^2\right] (g_{N\sigma}\langle\sigma\rangle)^2 \,, \end{aligned} \tag{3.21}$$

$$M_\Sigma(\langle\sigma\rangle) = M_\Sigma - \left[0.6706 - 0.0638 R_N^{\rm free} - 0.008\left(R_N^{\rm free}\right)^2\right] g_{N\sigma}\langle\sigma\rangle + \left[-0.0007 + 0.0786 R_N^{\rm free} - 0.0181\left(R_N^{\rm free}\right)^2\right] \left(g_{N\sigma}\langle\sigma\rangle\right)^2 , \quad (3.22)$$

$$M_\Xi(\langle\sigma\rangle) = M_\Xi - \left[0.3395 + 0.02822 R_N^{\rm free} - 0.0128\left(R_N^{\rm free}\right)^2\right] g_{N\sigma}\langle\sigma\rangle + \left[-0.0014 + 0.0416 R_N^{\rm free} - 0.0061\left(R_N^{\rm free}\right)^2\right] \left(g_{N\sigma}\langle\sigma\rangle\right)^2 . \quad (3.23)$$

We take $R_N^{\rm free} = 0.8$ fm as the preferred value of the free nucleon radius, although in practice the numerical results depend only very weakly on this parameter [53].

Given the parameters in Eqs. (3.20)–(3.23), all the effective masses for the baryon octet are entirely determined. They are plotted as functions of the Hartree scalar self-energy $\Sigma^s = -g_{N\sigma}\langle\sigma\rangle$ in Fig. 3.2 and we see clearly that they never become negative (note that the range of Σ^s covered here corresponds to densities well above (6–8)ρ_0 in QMC).

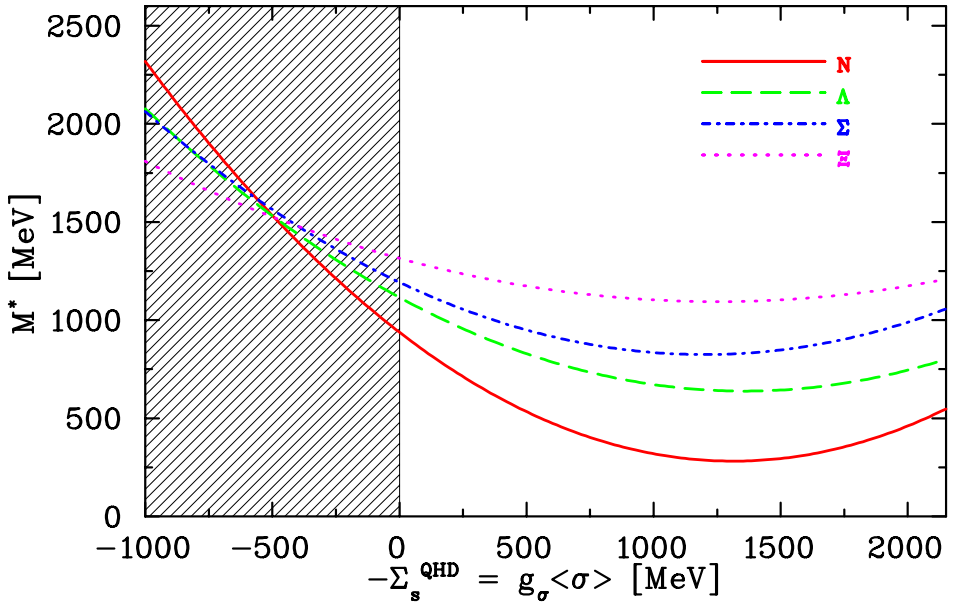

Fig. 3.2: (Color Online) Baryon effective masses for QMC as a function of the QHD (linear) scalar self-energies. The values at $\Sigma_s^{\rm QHD} = 0$ are the vacuum masses as found in Table 5.1. In order to emphasise the curve we have shown the effective masses beyond $-\Sigma_s^{\rm QHD} = 2000$ MeV, though in practice we only require values up to $-\Sigma_s^{\rm QHD} = 800$ MeV which corresponds to densities of ~ 2 fm^{-3} (6–8 ρ_0), beyond which higher order terms not shown in Eq. (3.19) become significant. The (shaded) unphysical region of $\Sigma_s^{\rm QHD} > 0$ contains a point for which all of the effective masses become unified; this is the point at which SU(3) symmetry is an accurate symmetry.

2. The mean-scalar field $\langle\sigma\rangle$ is derived self-consistently by taking the derivative of the energy density with respect to $\langle\sigma\rangle$, thus the scalar field equation

$$\langle\sigma\rangle = \sum_B \frac{g_{N\sigma}}{m_\sigma^2} C(\langle\sigma\rangle) \frac{(2J_B+1)}{(2\pi)^3} \int \frac{M_B^*\,\theta(k_{F_B} - |\vec{k}|)}{\sqrt{\vec{k}^2 + (M_B^*)^2}}\, d^3k, \tag{3.24}$$

has an extra factor when compared to Eq. (3.17), denoted by

$$C(\langle\sigma\rangle) = w_B^\sigma - \tilde{w}_B^\sigma d g_{N\sigma}\langle\sigma\rangle. \tag{3.25}$$

Note that the the scalar polarizability d term in $C(\langle\sigma\rangle)$ does not have the factor of $\frac{1}{2}$ that is found Eq. (3.19), because of the differentiation of the squared term.

Given this new term in the equation for the mean-scalar field, we can see that this allows feedback of the scalar field which is modelling the internal degrees of freedom of the baryons. This feedback prevents certain values of $\langle\sigma\rangle$ from being accessed.

3. The couplings to the nucleons are re-determined by the fit to saturation properties (as per Section 2.8) with the new effective masses for the proton and neutron. The couplings for QMC which provide a fit to saturated nuclear matter are shown in Table 5.2.

Given these changes alone, QHD is transformed into QMC. The implications of these changes however will be profound.

3.3 MIT Bag Model

We consider two models for a deconfined quark matter phase, both of which model free quarks. The first model, the MIT bag model [63], is commonly used to describe quark matter (and, by extension, hadronic matter) because of its simplicity.

In this model we construct baryons as three quarks confined within a 'bag,' a region defined by the local energy density which is greater than the energy density of the surrounding vacuum by a factor of B—which is commonly quoted to a power of one-quarter, thus $B^{1/4} \sim 180$ MeV—and which is lower in pressure by the same factor. The motivation for this is that the quarks reside in a high-energy, low pressure region which confines them.

This is the observed property of confinement—that no quarks have ever been observed, either directly or indirectly, in isolation—that perturbative approaches to QCD are unable to reproduce. This property is only of concern for hadronic matter though; at high energies, QCD predicts that the quarks become 'asymptotically free', and at this point we can consider quark matter.

The simplest Lagrangian density that can be constructed for such a scenario is

$$\mathcal{L}_{\text{MIT}} = \bar{\psi}_q \left(i\partial\!\!\!/ - m_q\right) \psi_q + B, \tag{3.26}$$

where ψ_q is a spinor for quarks with mass m_q where we typically use masses of $m_u = 3$ MeV, $m_d = 7$ MeV, and $m_s = 95$ MeV for the up, down, and strange quarks respectively, and B is the aforementioned bag energy density. In a similar fashion to the derivations for QHD and QMC, the energy density and pressure can be calculated to be

$$\mathcal{E} = B + \sum_q \frac{(2J_q+1)\mathcal{N}_c}{(2\pi)^3} \int \theta(k_{F_q} - |\vec{k}|) \sqrt{\vec{k}^2 + (m_q)^2}\, d^3k\ , \tag{3.27}$$

$$P = -B + \sum_q \frac{(2J_q+1)\mathcal{N}_c}{3(2\pi)^3} \int \frac{\vec{k}^2\ \theta(k_{F_q} - |\vec{k}|)}{\sqrt{\vec{k}^2 + (m_q)^2}}\ d^3k\ . \tag{3.28}$$

In order to utilise statistical mechanics and explore phase transitions involving this scenario, we model point objects with fixed masses which possess chemical potentials related to the independent chemical potentials of Eq. (2.45) via

$$\mu_u = \frac{1}{3}\mu_n - \frac{2}{3}\mu_e, \qquad \mu_d = \frac{1}{3}\mu_n + \frac{1}{3}\mu_e, \qquad \mu_s = \mu_d, \tag{3.29}$$

where quarks have a baryon charge of $\frac{1}{3}$ since baryons contain 3 quarks. Because the current quarks do not interact with mesons in this model, the quark chemical potential has the same form as the lepton chemical potential (no meson terms) and thus

$$\mu_q = \sqrt{k_{F_q}^2 + m_q^2}\ ; \quad q \in \{u, d, s\}. \tag{3.30}$$

The EOS can therefore be solved under the conditions of Eq. (3.18). In our calculations of this model, we use the current quark masses as found in Ref. [17], which represent the physical, bare quark masses.

3.4 Nambu–Jona-Lasinio Model (NJL)

As an alternative model for deconfined quark matter, we consider the Nambu–Jona-Lasinio (NJL) model [56], in which the quarks have dynamically generated masses, ranging from constituent quark masses at low densities to current quark masses at high densities.

Dynamical breaking of the chiral symmetry produces Nambu–Goldstone bosons—the triplet of pions in the two-flavor case—which are massless while the symmetry is preserved, but which possess a non-zero mass when the symmetry is broken. According to the Gell-Mann–Oaks–Renner relation (for example, see Ref. [64]), in the leading order of the chiral expansion,

$$m_\pi^2 = \frac{1}{f_\pi^2}\left(m_u\langle\bar{u}u\rangle + m_d\langle\bar{d}d\rangle\right), \tag{3.31}$$

or more commonly reduced to the fact that the quark mass scales as the square of the pion mass,

$$m_q \sim m_\pi^2. \tag{3.32}$$

At large densities, manifest chiral symmetry is expected to be partially restored. If it was fully restored, the quarks would be massless (in which case, $m_\pi = m_q = 0$). The symmetry is however not exact, and the quarks retain a very small mass. This small mass is the current quark mass as noted in Ref. [17], whereas the dynamically generated quark masses under broken chiral symmetry are the constituent masses that together naïvely sum to the mass of a baryon. By using the NJL model rather than a simple treatment for the quark masses we endeavor to make our phase transition models more realistic and more sophisticated by including more physics believed to represent Nature. The NJL model is a simple construction that displays the correct phenomenology, namely DCSB.

If we consider a particular choice for a massless Lagrangian density[7] with strong coupling G, in a Lorentz-covariant frame (with no matter or background fields) to be

$$\mathcal{L} = -\bar{\psi} i \not{\partial} \psi + G\left[(\bar{\psi}\psi)^2 - (\bar{\psi}\gamma_5\psi)^2\right] \tag{3.33}$$

we can see that this is invariant under the vector and axial vector symmetries of Eqs. (2.59)–(2.60). For example,

$$\begin{aligned}(\bar{\psi}\psi)^2 = \bar{\psi}\psi\bar{\psi}\psi \xrightarrow{\mathrm{U}(1)_A} \bar{\psi}e^{2i\alpha_A\gamma_5}\psi\ \bar{\psi}e^{2i\alpha_A\gamma_5}\psi &= \bar{\psi}\psi e^{2i\alpha_A\gamma_5}\ e^{-2i\alpha_A\gamma_5}\bar{\psi}\psi \\ &= (\bar{\psi}\psi)^2,\end{aligned} \tag{3.34}$$

where we recall Eq. (2.61), and that $\bar{\psi} = \psi^\dagger\gamma_0$.

The self-energy of this particular model is shown in Fig. 3.3 in which the four-fermion vertex is the 1-PI vertex (refer to Section 2.7), and the loop is the full quark propagator.

If we then approximate the four-fermion vertex to be the bare vertex with coupling G, and the loop to correspond to the bare propagator, then the loop now corresponds to the quark condensate $\langle\bar{\psi}\psi\rangle$ and the self-energy is given by the Feynman diagram as shown in Fig. 3.4. The Lagrangian density for NJL then becomes

$$\mathcal{L} = -\bar{\psi}\left(i\not{\partial} + 2G\langle\bar{\psi}\psi\rangle\right)\psi = -\bar{\psi}\left(i\not{\partial} + \Sigma_s\right)\psi. \tag{3.35}$$

where we can see from Fig. 3.4 that the self-energy is a Dirac-scalar term. We can now identify the dynamical quark mass as a scalar self-energy term in this Lagrangian density.

If we include a further constant mass term $\bar{\psi}m_0\psi$ in Eq. (3.33) that explicitly breaks the chiral symmetry, we can define the effective (dynamic) quark mass as

$$m_q^* = m_0 + \Sigma_s = m_0 - 2G\langle\bar{\psi}\psi\rangle. \tag{3.36}$$

This is called the 'gap equation' in analogy to superconductivity[8].

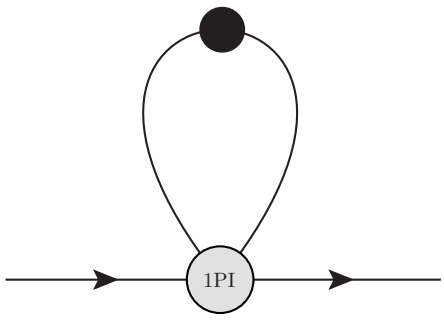

Fig. 3.3: Feynman diagram for the NJL quark self-energy, where the four-fermion vertex is 1-PI, and the loop corresponds to the full quark propagator.

[7] Following the considerations of Nambu and Jona-Lasinio [56].

[8] The BCS theory of superconductivity [65] is a primary motivation for this model, in which electrons in a metal may become a paired bosonic state—a Cooper pair—by possessing a lower energy than the Fermi energy. In that case, a temperature-dependent energy gap exists, and electron excitations must be of a minimum energy, as opposed to the continuous spectrum that the electrons would normally have.

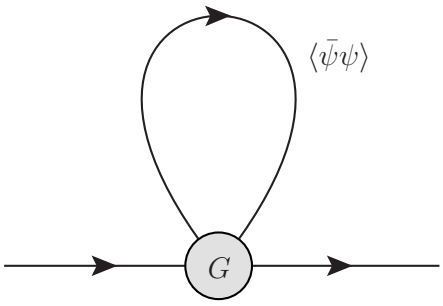

Fig. 3.4: Feynman diagram for the NJL quark self-energy, where the four-fermion vertex is the bare vertex with coupling G, and the loop corresponds to quark condensate.

To connect with Section 2.7, we can understand the NJL self-energy of Fig. 3.4 in analogy to that of Fig. 2.2 in the (albeit, unphysical) case that we shrink the gluon loop in Fig. 2.2 to a point, and in which case the Lagrangian densities are related via the (arbitrary) replacement of

$$(\bar{\psi}\Gamma\psi)^2 \to 2\bar{\psi}\Gamma\psi\ \langle\bar{\psi}\Gamma\psi\rangle, \tag{3.37}$$

where Γ is any gamma matrix appearing in the interaction Lagrangian density. The term $\langle\bar{\psi}\Gamma\psi\rangle$ denotes the ground-state (vacuum) expectation value of $\bar{\psi}\Gamma\psi$, and as noted in Section 2.3.2, the ground-state is a parity eigenstate, thus the only term in Eq. (3.33) that has a non-zero vacuum expectation value is $\langle\bar{\psi}\psi\rangle$.

The expression for the Feynman diagram in Fig. 3.4 is simply

$$\Sigma(p) = 2G\langle\bar{\psi}\psi\rangle = 2iG\,\mathrm{Tr}S_F(0) \tag{3.38}$$

where $S_F(0) = S_F(x-y)\delta(x-y)$ is the Feynman propagator for a quark (refer to Appendix A.2) which starts and ends at the same space-time point.

As with Section 2.7, we have described the above model for a Lorentz-covariant frame, in which there are no matter or background fields. In this case, the Feynman propagator in Eq. (3.38) is the free-space propagator. We make a further approximation by replacing this propagator with the in-medium propagator, one which is in the presence of matter fields, and thus we introduce a Fermi momentum. The expression for the quark condensate in this case becomes

$$\langle\bar{\psi}_q\psi_q\rangle = i\mathrm{Tr}S_F(0) = -4\,\frac{\mathcal{N}_c}{(2\pi^3)}\int\frac{m_q^*\,\theta(k_F-|\vec{k}|)\,\theta(\Lambda-k_F)}{\sqrt{\vec{k}^2+(m_q^*)^2}}\,d^3k, \tag{3.39}$$

where we have introduced a momentum cutoff of $k_F < \Lambda$ to regularize this integral, at which point we expect to recover current quark masses, and $\mathcal{N}_c$ is the number of color degrees of freedom of quarks. In order to calculate the effective quark mass at each density, we must first find the coupling G which yields the appropriate constituent quark masses in free space ($k_F = 0$). The coupling is assumed to remain constant as the density rises. Given a (free-space) constituent quark mass m_q^{free}, we can solve Eqs. (3.36) and (3.39) to find the coupling

$$G = \frac{(m_q^{\mathrm{free}}-m_0)}{4}\left[\frac{\mathcal{N}_c}{(2\pi)^3}\int\frac{m_q^{\mathrm{free}}\,\theta(|\vec{k}|-k_F)\,\theta(\Lambda-k_F)}{\sqrt{\vec{k}^2+(m_q^{\mathrm{free}})^2}}\,d^3k\right]^{-1}\Bigg|_{k_F=0}. \tag{3.40}$$

We evaluate Eq. (3.40) for $\mathcal{N}_c = 3$ to produce constituent quark masses of $m_{u,d}^{\text{free}} = 350$ MeV using current quark masses of $m_0^{u,d} = 10$ MeV for the light quarks, and a constituent quark mass of $m_s^{\text{free}} = 450$ MeV using a current quark mass of $m_0^s = 160$ MeV for the strange quark (both with a momentum cutoff of $\Lambda = 1$ GeV) as per the phenomenology of this field. At $k_F = 0$ we find the couplings to be

$$G_{u,d} = 0.148 \text{ fm}^2, \quad G_s = 0.105 \text{ fm}^2. \tag{3.41}$$

We can now use these parameters to evaluate the dynamic quark mass m_q^* for varying values of k_F by solving Eqs. (3.36) and (3.39) self-consistently. The resulting density dependence of m_q^* is illustrated in Fig. 3.5 where we observe that the quark masses—particularly the light quark masses—eventually saturate and are somewhat constant above a certain Fermi momentum (hence, density). For densities corresponding to $k_F > \Lambda$, the dynamic quark mass is constant.

We can now construct the quark matter EOS in the same way as we did for the MIT bag model, but with density-dependent masses rather than fixed masses.

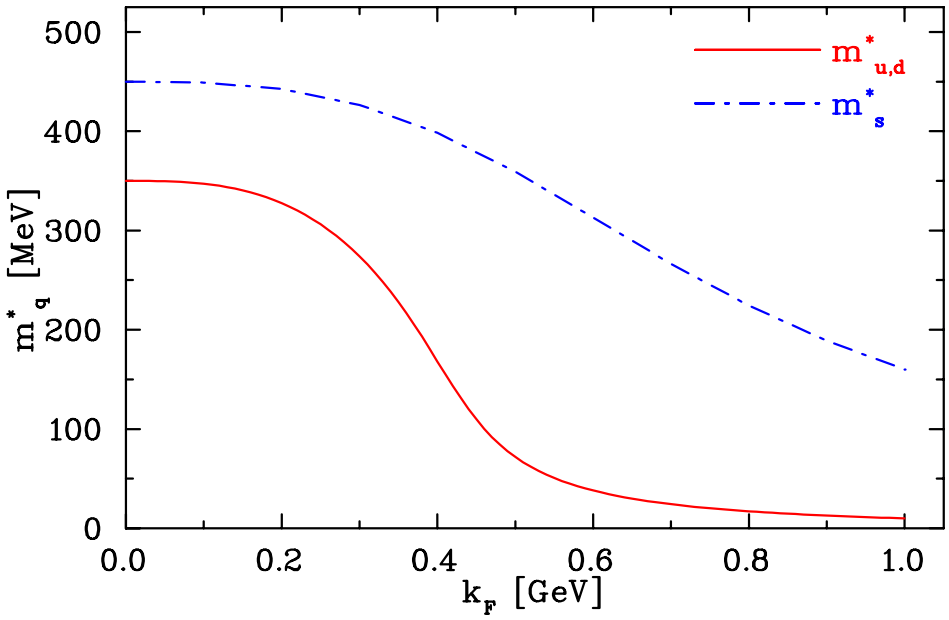

Fig. 3.5: (Color Online) Dynamic quark masses in the NJL model. The mass at $k_F = 0$ is the constituent quark mass, and the mass at the cutoff of $k_F = \Lambda = 1$ GeV is the current quark mass. This model successfully reproduces the behavior found within the Schwinger–Dyson formalism for dynamical chiral symmetry breaking.

3.5 Fock Terms

As an extension to the models described above, we now introduce terms which are of a higher order—the Fock terms—leading us to a Hartree–Fock description of matter. As we wish to work to the next leading order, we require a perturbative description of the models in which we can identify the next terms. To this end, we utilise Feynman diagrams to illustrate which terms shall be calculated, and which shall be neglected, since we can identify the order of a diagram by the number of baryon-meson vertices, each of which contributes a factor of the baryon-meson coupling.

The derivation of QHD as described in Appendix A.3 does not lend itself to such an expansion, since all the contributing terms must appear in the Lagrangian density *ab initio*, but we can re-derive QHD perturbatively which will allow the identification of the next-order terms. The diagrammatic derivation for QHD at Hartree level can be found in Appendix A.6.

The first Fock terms that we wish to calculate are the next-to-leading order contributions to the baryon self-energies $\Sigma_B(k)$, which as we shall see are momentum dependent. The full derivation of this Fock contribution can be found in Appendix A.7. In order to calculate the Hartree–Fock EOS, we consider Dyson's Equation which self-consistently relates the full momentum-dependent baryon Green's function (propagator) $G(k)$ to the bare (vacuum) baryon propagator $G^0(k)$ and the self-energy, as

$$G(k) = G^0(k) + G^0(k)\Sigma(k)G(k). \tag{3.42}$$

This can be represented with Feynman diagrams as shown in Fig. 3.6.

We can write the as-yet undefined self-energy as a sum of terms by defining components of the self-energy proportional to the identity matrix $\mathbb{I}$, or gamma matrices γ^0 and $\vec{\gamma}$ for scalar (Σ^s), temporal (Σ^0), and vector ($\Sigma^i \equiv \Sigma^v$) self-energies, such that the full self-energy (in the case where the following terms are defined in-medium) is expanded as

$$\begin{aligned} \Sigma(k) &= \Sigma^s(k) - \gamma_\mu \Sigma^\mu(k) && (3.43)\\ &= \Sigma^s(|\vec{k}|, k^0) - \gamma_0 \Sigma^0(|\vec{k}|, k^0) + \vec{\gamma}\cdot\vec{k}\,\Sigma^v(|\vec{k}|, k^0). && (3.44) \end{aligned}$$

Note the differences between Eq. (3.43) and Eq. (2.67); the components of the self-energy in the Lorentz-covariant case (free-space). In this in-medium case, we now have dependence on $\vec{k}$, which will lead to a dependence on Fermi momentum.

Dyson's Equation can be solved formally to give the baryon propagator

$$[G(k)]^{-1} = \gamma_\mu(k^\mu + \Sigma^\mu(k)) - [M + \Sigma^s(k)]. \tag{3.45}$$

For convenience, we define the following quantities;

$$\begin{aligned} M^*(k) &= M + \Sigma^s(k), && (3.46)\\ \vec{k}^* &= \vec{k} + \Sigma^v(k), && (3.47)\\ E^*(k) &= \sqrt{(\vec{k}^*)^2 + (M^*)^2}, && (3.48)\\ k^{*\mu} &= k^\mu + \Sigma^\mu(k) = [k^0 + \Sigma^0(k), \vec{k}^*]. && (3.49) \end{aligned}$$

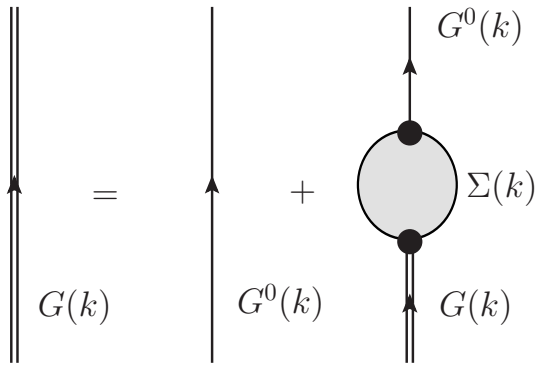

Fig. 3.6: Feynman diagram for Dyson's Equation, Eq. (3.42), providing a self-consistent description for the full baryon propagator (double line) involving the bare propagator (single line) and self-energy (filled blob).

We can express the solution to Dyson's Equation as a sum of Dirac and Fermi components, where the Dirac contribution is responsible for Pauli blocking, and the Fermi contribution accounts for antibaryons [18], which shall be neglected here[9]

$$G(k) = G_F(k) + G_D(k); \tag{3.50}$$

$$G_F(k) = [\gamma^\mu k^*_\mu + M^*(k)] \left(k^{*\mu} k^*_\mu - (M^*(k))^2 + i\epsilon\right)^{-1}, \tag{3.51}$$

$$G_D(k) = [\gamma^\mu k^*_\mu + M^*(k)] \frac{i\pi}{E^*(k)} \delta(k_0 - E(k))\theta(k_F - |\vec{k}|), \tag{3.52}$$

where the energy $E(k)$ is the self-consistent single-particle energy, calculated 'on-shell'[10]

$$E(k) = [E^*(k) - \Sigma^0(k)]_{k_0 = E(k)}. \tag{3.53}$$

In the Hartree case, the tadpole diagrams define the self-energy. If we now include the exchange contributions, the diagrams for which (for the vector meson terms) are shown in Fig. 3.7, the expressions for the total (including all Lorentz forms) σ and ω contributions to the self-energy become

$$\Sigma(k) = \sum_B \Sigma_{B\sigma}(k) + \Sigma_{B\omega}(k), \tag{3.54}$$

$$\Sigma_{B\sigma}(k) = i g_{B\sigma} \int \frac{d^4q}{(2\pi)^4} \left[e^{iq^0\eta} \sum_{B'} g_{B'\sigma} \frac{\mathrm{Tr}[G(q)]}{m^2_\sigma} + \frac{g_{B\sigma}\, G(q)}{(k-q)^2_\mu - m^2_\sigma + i\epsilon} \right], \tag{3.55}$$

$$\Sigma_{B\omega}(k) = i g_{B\omega} \int \frac{d^4q}{(2\pi)^4} \left[e^{iq^0\eta} \sum_{B'} g_{B'\omega} \frac{\mathrm{Tr}[\gamma_\mu G(q)]}{m^2_\omega} + \frac{g_{B\omega}\, \gamma_\mu \mathrm{g}^{\mu\nu} G(q) \gamma_\nu}{(k-q)^2_\lambda - m^2_\omega + i\epsilon} \right], \tag{3.56}$$

where for each case in the sum, G refers to the baryon propagator of baryon B. Here $\mathrm{g}^{\mu\nu}$ is the Minkowski metric tensor (a.k.a. $\eta^{\alpha\beta}$ in Eq. (2.5)).

[9] In their absence we will use a momentum cutoff to regularize the integrals.
[10] In which case $p_\mu p^\mu = M^2$, and thus $p^0 = E(p)$.

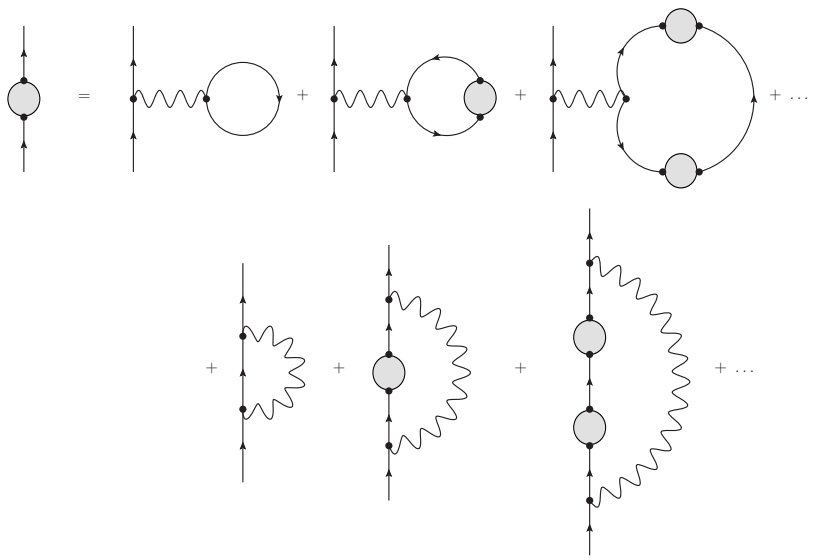

Fig. 3.7: Summation of Feynman diagrams for all possible (vector) interaction terms contributing to the self-energy. The first row of diagrams are the tadpole terms, and the second row are the exchange terms, where in both cases, each term is derived by inserting the full baryon Green's function into the previous term, which self-consistently includes the self-energy. Similar diagrams exist for the scalar meson interactions.

For simplicity, we will neglect the contribution from the ρ meson in these Fock calculations. The self-energy can now be separated into terms proportional to those in Eq. (3.43).

Since we will be using a momentum cutoff to regularize the integrals, we[11] drop the antibaryon components of the baryon propagator $G_F(k)$, leaving $G_D(k)$ as the full propagator. Some of the integrals can then be performed to produce the mean-field results plus the Fock additions

$$\begin{aligned}\Sigma_B^s(k,E(k)) &= g_{B\sigma}\sum_{B'}\frac{-(2J_{B'}+1)}{(2\pi)^3}\frac{g_{B'\sigma}}{m_\sigma^2}\int_0^{k_{F_{B'}}} d^3q\frac{M^*_{B'}(q)}{E^*_{B'}(q)} \\ &\quad +\frac{1}{4\pi^2 k}\int_0^{k_{F_B}} q\,dq\frac{M^*_B(q)}{E^*_B(q)}\left[\frac{1}{4}g^2_{B\sigma}\Theta_s(k,q)-g^2_{B\omega}\Theta_\omega(k,q)\right], \qquad (3.57)\end{aligned}$$

$$\begin{aligned}\Sigma_B^0(k,E(k)) &= g_{B\omega}\sum_{B'}\frac{-(2J_{B'}+1)}{(2\pi)^3}\frac{g_{B'\omega}}{m_\omega^2}\int_0^{k_{F_{B'}}} d^3q \\ &\quad -\frac{1}{4\pi^2 k}\int_0^{k_{F_B}} q\,dq\left[\frac{1}{4}g^2_{B\sigma}\Theta_\sigma(k,q)+\frac{1}{2}g^2_{B\omega}\Theta_\omega(k,q)\right], \qquad (3.58)\end{aligned}$$

$$\Sigma_B^v(k,E(k)) = -\frac{1}{4\pi^2 k^2}\int_0^{k_{F_B}} q\,dq\frac{q^*}{E^*_B(q)}\left[\frac{1}{2}g^2_{B\omega}\Phi_\sigma(k,q)+g^2_{B\omega}\Phi_\omega(k,q)\right], \qquad (3.59)$$

[11] Following the procedure of Ref. [18]

with the definitions (for convenience) of

$$\Theta_i(k,q) = \ln\left|\frac{A_i(k,q)+2kq}{A_i(k,q)-2kq}\right|, \tag{3.60}$$

$$\Phi_i(k,q) = \frac{1}{4kq}A_i(k,q)\Theta_i(k,q) - 1, \tag{3.61}$$

$$A_i(k,q) = \vec{k}^{\,2} + \vec{q}^{\,2} + m_i^2 - [E(q) - E(k)]^2, \tag{3.62}$$

for which $q = |\vec{q}|$, $k = |\vec{k}|$.

All of these self-energies are evaluated on-shell at the self-consistent single-particle energies defined in Eq. (3.53). To further simplify our calculations, we will use the approximation $\Sigma_B^v = 0$, since the momentum-dependence of this term is a power weaker than Σ_B^s and Σ_B^0. The only consequence of this is that in Eq. (3.47), $\vec{k}^* \to \vec{k}$.

These contributions to the self-energy will affect the effective masses of the baryons in QHD as additional terms in Eq. (3.10), and once we have made this change we can once again calculate the energy density. In this perturbative description of QHD, although the energy density is still derived using the energy-momentum tensor, the expression for this now involves the meson propagators. Using the Hartree meson propagators (since these are not affected by the Fock addition to the self-energy) we can evaluate the energy density, and we must once again re-fit the baryon-meson couplings such that the saturation properties are reproduced. The couplings which provide this are given in Table 5.2 for this case of Fock term additions to the self-energy.

The second Fock terms we can calculate are additional terms in the meson propagators—the medium polarisation—which will alter the definition of the energy density. The medium polarization is named in analogy to the vacuum polarization, the simplest example of which is in Quantum Electrodynamics (QED); in vacuum, a photon can spontaneously create a virtual[12] particle-antiparticle pair—namely an electron and a positron—which annihilate back to a photon, as shown in Fig. 3.8. While they temporarily exist, the charged pair acts as an electric dipole and can partially screen an external electromagnetic field. Similarly, the medium polarization is a contribution from the creation of a baryon loop which affects the matter field.

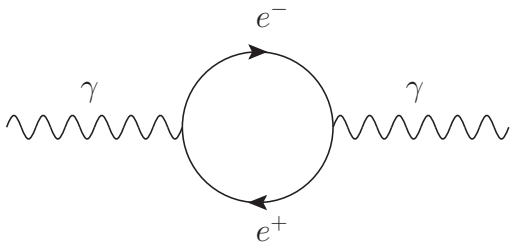

Fig. 3.8: Feynman diagram for vacuum polarization in QED. Here the photon creates two fermions which are off-shell (virtual particles) which annihilate back to a photon. The charged pair acts as an electric dipole, and thus are able to partially screen an external electromagnetic field.

[12] These particles are 'off-shell', meaning that $p_\mu p^\mu \neq m^2$.

The three terms contributing to the scalar propagator are shown in Fig. 3.9. The first of these is the bare meson propagator. The second is the Hartree contribution, essentially the square of a tadpole term. The last of these is the medium polarization, and the scalar and vector contributions to this term are given by

$$\Delta'(k) = \Delta^0\Pi_\sigma(k)\Delta^0(k) \tag{3.63}$$

$$\Pi_\sigma(k) = -i\sum_B g_{B\sigma}^2 \int \frac{d^4q}{(2\pi)^4}\,\mathrm{Tr}\left[G_D(q)G_D(k+q)\right] \tag{3.64}$$

$$D'_{\mu\nu}(k) = D^0_{\mu\lambda}\Pi^{\lambda\sigma}_\omega(k)D^0_{\sigma\nu}(k) \tag{3.65}$$

$$\Pi^{\lambda\sigma}_\omega(k) = -i\sum_B g_{B\omega}^2 \int \frac{d^4q}{(2\pi)^4}\,\mathrm{Tr}\left[\gamma^\lambda G_D(k+q)\gamma^\sigma G_D(q)\right] \tag{3.66}$$

where Π_σ and $\Pi^{\lambda\sigma}_\omega$ are the medium polarizations.

By evaluating the temporal components of the energy-momentum tensor T^{00} with the Hartree–Fock propagator as shown in Fig. 3.9 we find the full expression for the Hartree–Fock energy density

$$\begin{aligned}
\mathcal{E}_{\mathrm{HF}} = {} & \sum_B \frac{(2J_B+1)}{(2\pi)^3}\int_0^{k_F} d^3k\; E(k) + \frac{1}{2}m_\sigma^2\langle\sigma\rangle^2 - \frac{1}{2}m_\omega^2\langle\omega\rangle^2 \\
& + \frac{1}{2}\frac{(2J_B+1)}{(2\pi)^6}\int_0^{k_{F_B}}\int_0^{k_{F_B}} \frac{d^3k\,d^3q}{E^*(k)E^*(q)} \\
& \times \Big\{ g_{B\sigma}^2 D^0_\sigma(k-q)\left[\frac{1}{2} - [E(k)-E(q)]^2 D^0_\sigma(k-q)\right]\left[k^{*\mu}q^*_\mu + M^*(k)M^*(q)\right] \\
& + 2g_{B\omega}^2 D^0_\omega(k-q)\left[\frac{1}{2} - [E(k)-E(q)]^2 D^0_\omega(k-q)\right]\left[k^{*\mu}q^*_\mu - 2M^*(k)M^*(q)\right]\Big\}\,.
\end{aligned} \tag{3.67}$$

The first line of terms in Eq. (3.67) are of the same form as the Hartree contributions, but these terms are now defined using the second-order self-energies. The double integral arises from the medium polarization terms. Eq. (3.67) is fully derived in Section A.7.

For consistency, once we include Fock terms to the energy density, we must once again recalculate the couplings to fit saturation properties. The values that best reproduce the data for this Hartree–Fock description of QHD are summarized in Table 5.2.

While we have presented the results for the σ and ω mesons, it should be noted that other meson contributions are possible. We could add the contribution from the ρ meson with the appropriate coupling factors, and furthermore since the Fock terms are of a higher order than mean-field, we could now include the pion contribution, and all pseudo-scalars not otherwise excluded. For now we shall continue to neglect these terms for simplicity.

An alternative additional contribution to the energy density is the second-order exchange contribution as per Ref. [66] which shall be neglected here for simplicity.

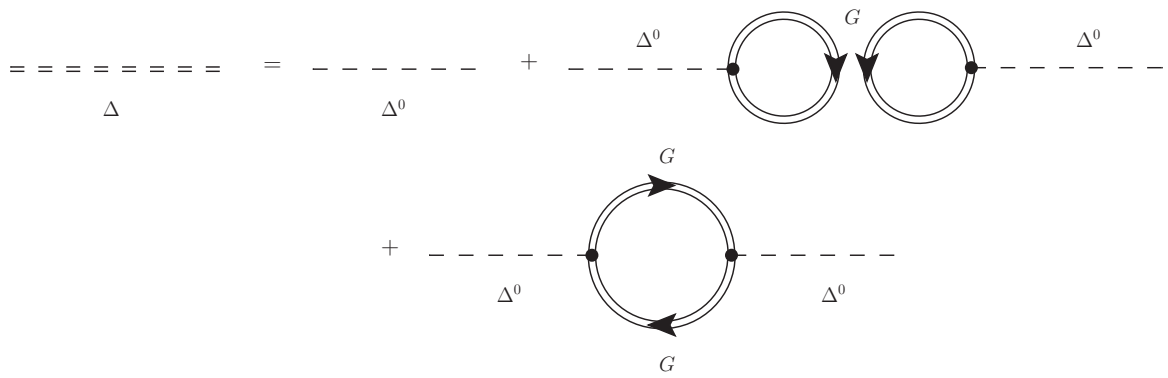

Fig. 3.9: The three leading terms contributing to the full meson propagator (double, dashed line) in this case of the scalar meson; the bare propagator Δ^0 (single, dashed line), the (squared) tadpole diagram, and the medium polarization diagram. Similar terms can be written for the vector meson also.

Methods of Calculation

As is often the case in theoretical physics, for many of the quantities mentioned in the preceding chapters we lack all the information required to evaluate them. Although we may know the vacuum mass constants and couplings, there are several quantities which are self-consistently defined—where the quantity of interest appears on both the left- and right-hand sides of an equation—for example the equation for the effective baryon mass in QHD,

$$M_B^* = M_B - g_{B\sigma}\langle\sigma\rangle = M_B - g_{B\sigma}\sum_{B'}\frac{g_{B'\sigma}}{m_\sigma^2}\int\frac{(2J_{B'}+1)}{(2\pi)^3}\frac{M_{B'}^*\,\theta(k_{F_{B'}}-|\vec{k}\,|)}{\sqrt{\vec{k}^2+M_{B'}^{*2}}}\,d^3k\ , \tag{4.1}$$

is defined self-consistently[1]. Technically, Eq. (4.1) describes N_B coupled, self-consistent equations, where N_B is the number of baryons in the model considered. Furthermore, although we use the total baryon density ρ_{total} as the control parameter, for non-trivial cases the integration limit of k_{F_B} is reliant on knowing the density of each species separately, which in turn can be reliant on M_B^* via the chemical potentials (refer to Eq. (2.44)). Equations of this form cannot be solved analytically, so we turn our attention to numerical calculations.

All of the calculations performed in this thesis have been computed in Fortran 90 using methods inspired by 'Numerical Recipes in Fortran 90' [67]. Rather than publish the particular code used to perform the exact calculations of this work, in the following sections we will briefly outline some of the challenges that have been met in performing these calculations, and the major steps required to reproduce the simulations.

4.1 Newton's Method

One of the most widely renowned methods for iteratively solving non-linear equations is the Newton–Raphson method, also known simply as 'Newton's Method'. It has the additional benefit that it is suitable for solving self-consistent equations, as above.

Newton's method is elegant in its simplicity; In order to find the value x^* which is a solution of $f(x) = 0$ where f is a general function, we begin by considering the gradient f' of a tangent to f at a point x_i that is sufficiently close to x^* (within the radius of convergence). The radius of convergence is defined in this case by the region in which the tangent to f intersects the x-axis at a point x_{i+1} such that $|x^* - x_{i+1}| < |x^* - x_i|$, as shown in Fig. 4.1.

The gradient of the tangent is given by

$$f'(x_i) = \frac{\Delta f(x)}{\Delta x} = \frac{f(x_i)}{x_i - x_{i+1}}, \tag{4.2}$$

where we have used the fact that the tangent to f intercepts the x-axis at x_{i+1}, and thus $f(x_{i+1}) = 0$. Rearranging this gives the iterative procedure for Newton's method;

$$x_{i+1} = x_i - \frac{f(x_i)}{f'(x_i)}. \tag{4.3}$$

[1] In that the effective masses of *all* the baryons are required in order to calculate the effective mass of a single baryon.

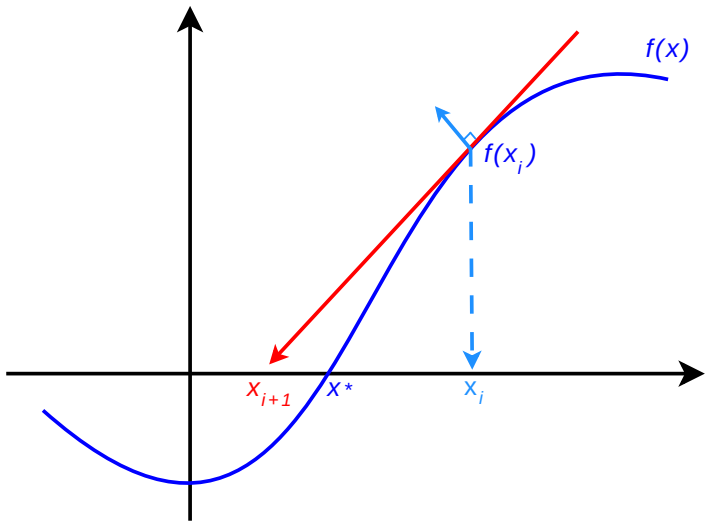

Fig. 4.1: (Color Online) Diagram for Newton's method as described in the text. Here, the starting value x_i lies within the radius of convergence which for this example is bounded somewhere between the two extrema. For example, a tangent at or beyond these points will have an x-intercept of x_{i+1} that is further from x^* than x_i is.

If the function is convergent, for some value of i it must be true that $|x_{i+1} - x_i| < \epsilon$ for some tolerance ϵ, at which point the solution x^* is considered to be found. To make use of this method, we need to define our functions, and the equations that we wish to find the solutions to.

For QHD, QMC, and in general, we use the total baryon density as the control parameter, allowing us to calculate the properties of matter at a specific density. At a given density, the total baryon density is therefore conserved (constant), and equal to the sum of individual baryon densities;

$$\rho_{\text{total}} = \sum_B \rho_B. \tag{4.4}$$

We also require that the total charge of the system, defined by

$$Q_{\text{total}} = \sum_B Q_B \rho_B \tag{4.5}$$

is constant, and vanishing. With two constraining equations we can use Newton's method to find the values of (at most) two quantities constrained by these equations. For the purpose of simplicity, we use the proton and neutron Fermi momenta k_{F_p} and k_{F_n} since these appear in the integration limits of many quantities.

In keeping with the discussion of chemical potentials in Section 2.5, we could equivalently use the neutron and electron chemical potentials; the choice is arbitrary, though using only the nucleon Fermi momenta allows us to neglect conservation of total charge, such as the case of nuclear matter where we only need a single constraining equation[2], without loss of generality.

[2]The nucleon Fermi momenta are constrained such that the densities are equal in that case.

Newton's method is a root-solving method, so our constraint equations need to be written in a form of $\vec{f}(\vec{x}) = \vec{0}$. This is achieved simply as

$$f_1(k_{F_n}) = \rho_{\text{total}} - \sum_B \rho_B \quad = \quad 0, \tag{4.6}$$

$$f_2(k_{F_p}) = Q_{\text{total}} - \sum_B Q_B \rho_B \quad = \quad 0. \tag{4.7}$$

Lastly, in order to solve the self-consistent equations for the baryon effective masses in QHD and QMC, we require an additional quantity that we can allow to vary. Considering QHD, since (at Hartree level at least) the scalar field $\langle\sigma\rangle$ is independent of baryon species (it is a sum of contributions from *all* baryons) we use this quantity in a further constraint equation

$$f_3(\langle\sigma\rangle) = \langle\sigma\rangle - \sum_B \frac{g_{B\sigma}}{m_\sigma^2} \int \frac{(2J_B+1)}{(2\pi)^3} \frac{M_B^* \, \theta(k_{F_B} - |\vec{k}|)}{\sqrt{\vec{k}^2 + M_B^{*2}}} \, d^3k = \; 0. \tag{4.8}$$

Note that since $\rho_B = k_{F_B}^3/3\pi^2$, each of the above constraint equations contains k_{F_p} and k_{F_n}, so these equations are not only non-linear, but are all also highly correlated.

Although the above derivation of Newton's method is for a function of a single variable, we can extend this concept to an arbitrary number of m functions in n variables by replacing the derivative by a Jacobian

$$J = \begin{bmatrix} \dfrac{\partial f_1}{\partial x_1} & \cdots & \dfrac{\partial f_1}{\partial x_n} \\ \vdots & \ddots & \vdots \\ \dfrac{\partial f_m}{\partial x_1} & \cdots & \dfrac{\partial f_m}{\partial x_n} \end{bmatrix}. \tag{4.9}$$

In order to include the hyperon contributions to these calculations, we do not require any further constraint equations, since all of the hyperon Fermi momenta can be derived from that of the nucleons, by rearranging Eq. (2.46). The constraint equations above, Eqs. (4.6)–(4.8) do however change as they now include terms for the hyperons in the sums.

We can use the same method to perform the quark matter calculations in this thesis, with only slight changes to the constraint equations. The conserved baryon density is now defined for quark matter as per Eq. (2.93), and the total charge remains zero, though the individual charges Q_i now reflect the quark charges; $Q_u = +2/3$, $Q_d = Q_s = -1/3$. For the calculations of the MIT Bag Model, only these two constraint equations are required, since the quark masses are constant. For the NJL Model calculations, the quark masses are calculated self-consistently in the same manner as the baryon effective masses above, so the equation for a quark condensate, Eq. (3.39) can take the place of the scalar field in Eq. (4.8).

This method is used to produce all of the calculations for this work at Hartree level, but it is not suitable for calculations involving the Fock terms; the additional factors that are included at Hartree–Fock level alter the self-consistent equations for the effective masses (via the self-energy) such that the effective masses become baryon- and momentum-dependent. Because of this, we can no longer rely on the mean-scalar field to produce a constraint equation, since we would require $2 + n_k \times n_B$ equations (n_k = number of momentum samples, n_B = number of baryons in the calculation). Clearly this is not a feasible route to take, since for a reasonable number of momentum samples, say $n_k = 100$ we would require 202 equations to just calculate properties of nucleonic matter.

The alternative is to find a new method of evaluating our self-consistent equations. The method we have used is described next.

4.2 Steffensen's Method

Until now we have described solving the self-consistent equations within Newton's method, but as stated above the Fock terms would introduce too many new equations for this to be workable. To make matters worse, the addition of the Fock terms makes the effective masses momentum dependent, and so the equations for these become integral equations

$$\begin{aligned} M_B^*(k) &= M_B - g_{B\sigma}\sum_{B'}\frac{g_{B\sigma}}{m_\sigma^2}\int_0^{q_{F_{B'}}}\frac{(2J_{B'}+1)}{(2\pi)^3}\frac{M_{B'}^*(q)}{E_{B'}^*(q)}\,d^3q \\ &\quad + \frac{1}{4\pi^2 k}\int_0^{q_{F_B}} q\,\frac{M_B^*(q)}{E_B^*(q)}\left[\frac{1}{4}g_{B\sigma}^2\Theta_\sigma(k,q) - g_{B\omega}^2\Theta_\omega(k,q)\right]dq. \end{aligned} \tag{4.10}$$

where the terms in this equation are defined in Section 3.5.

As a solution to this problem, we find a new method of solving the self-consistency. Many improvements to Newton's method are available, and we have chosen to investigate one in particular; Steffensen's Method. The advantage that this method has over Newton's method is that it doesn't require a calculation of the derivative of the function f.

As an improvement over Newton's method, we replace the derivative (the slope of the tangent to f) in the denominator of Eq. (4.3) with the slope $g(x)$ of a line joining the point $(x_i, f(x_i))$ with an auxiliary point $(x_i + \delta x_i, f(x_i + \delta x_i))$ as shown in Fig. 4.2. The choice of δx_i is somewhat arbitrary, and the choice of $\delta x_i = f(x_i)$ merely ensures that the step size is scaled appropriately according to the distance from the solution, and in fact δx_i vanishes as $f(x_i)$ approaches 0.

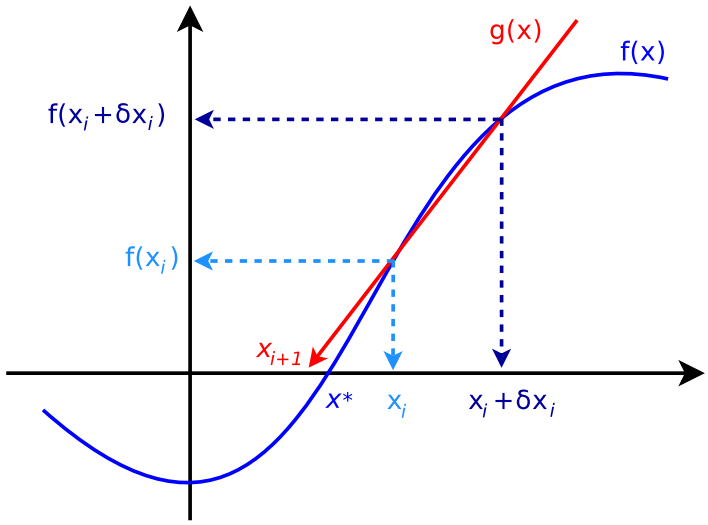

Fig. 4.2: (Color Online) Diagram for Steffensen's method as described in the text. This method has the numerical advantage that it does not require the evaluation of a derivative, though the requirement of a 'good' starting value is now somewhat more strict.

The slope of this new line is then

$$g(x) = \frac{f(x_i + f(x_i)) - f(x_i)}{f(x_i)}. \tag{4.11}$$

If we insert this into Eq. (4.3) in place of the derivative we obtain the iterative procedure for Steffensen's Method, where the x-intercept of $g(x)$ defines the next approximation to $f(x^*) = 0$;

$$x_{i+1} = x_i - \frac{f(x_i)}{g(x_i)} = x_i - \frac{f(x_i)^2}{f(x_i + f(x_i)) - f(x_i)}. \tag{4.12}$$

This method can be applied to solving integral equations such as Eq. (4.10).

An issue that the reader may notice is that the effective masses in that equation have a momentum-dependence in the form of a $1/k$ term, as well as k-dependence in the $\Theta(k, q)$ terms; this makes the definition of $M^*(0)$ very critical, since the k-dependence of the Θ term (as defined in Section 3.5) produces $\Theta_i(0, q) = \ln(1) = 0$, thus we have a $0/0$ issue. Since we require the value of $M^*(0)$ in order to calculate the integrals above, we must define this value very carefully. Since the function is fairly smooth, we use a linear interpolation of the function evaluated at the next two momentum points to define the limit of the function at $k = 0$.

This gives us all the information we need in order to solve the self-consistent equations, but we can improve the method by accelerating the convergence, as we shall show in the next section.

4.2.1 Aitken's Δ^2 Process

We can further accelerate the rate of convergence for Steffensen's Method by using Aitken's delta-squared process. If the function we are attempting to find the roots of is $f(x)$ we can iterate Steffensen's method to produce intermediate values h_0, h_1, and h_2 such that

$$\begin{aligned} h_0 &= x_i, \\ h_1 &= h_0 - \frac{f(h_0)}{g(h_0)}, \\ h_2 &= h_1 - \frac{f(h_1)}{g(h_1)}. \end{aligned} \tag{4.13}$$

With these definitions, Aitken's delta-squared process defines the next approximation to the root of the function f as

$$x_{i+1} = h_0 - \frac{(h_2 h_0 - h_1)^2}{h_2 - 2h_1 + h_0}. \tag{4.14}$$

If the process has failed to converge at this stage by satisfying the condition $|x_{i+1} - x_i| < \epsilon$ then the entire procedure is repeated for the next value of x. If convergence is achieved, it is trivial to confirm that the convergence has produced the correct value of $f(x_{i+1}) = 0$.

Once again, this description has involved only a function of a single variable. The method can be modified to handle functions of several variables, but we shall not discuss this modification here as we will only be using this method for nucleon calculations. With this method we are able to solve (at least) two self-consistent integral equations, and we shall do so for the nucleon effective masses for a suitable number of momentum points.

We nest the solving of the self-consistent effective masses within the Newton's method in the previous section which still varies the proton and neutron Fermi momenta to find the roots of the equations. The functions $\vec{f}$ that we wish to find the roots of via Steffensen's Method are simply rearrangements of Eq. (4.10) for each of the baryons such that $\vec{f}(M_p^*, M_n^*) = \vec{0}$. Once we have solved these self-consistencies, we no longer require the third constraint equation Eq. (4.8) in Newton's method.

4.2.2 Example Integral Equations

As an example, we consider the fixed-point integral equation

$$u(x) = F(u(x)) = e^x + e^{-1} \int_0^1 u(t)\, dt, \tag{4.15}$$

which has the solution

$$u^*(x) = e^x + 1. \tag{4.16}$$

Being such a simple case, we can solve Eq. (4.15) in several ways. For the sake of comparison, we will compare a naïve method; in which a previous function value is used as the next guess, the iterative procedure for which is $u_{i+1}(x) = F(u_i)$, where for this example the minimized function is the difference between the left- and right-hand sides of Eq. (4.15), viz $f(x_i) = u(x_i) - F(u(x_i))$; with the Aitken-improved Steffensen's method used for our actual calculations.

In both cases, we supply an identical initial guess of $u_0(x) = 0$, sampled over 1000 x-values, and set a tolerance for convergence (via the relative error) at each sampled value of x_j (where $j = 1, \ldots, 1000$) of

$$\epsilon_j = \frac{u_{i+1}(x_j) - u_i(x_j)}{u_{i+1}(x_j)} = 1 \times 10^{-8}. \tag{4.17}$$

In both cases the procedures converge to within the above tolerance, and the actual errors relative to $u^*(x)$ are shown in Fig. 4.3. The naïve method converges with 20 iterations, while Steffensen's method converges with just 11, a vast improvement.

The speed of convergence is one advantage of the Aitken-improved Steffensen's method, but the more important advantage comes when we try to solve a more complicated integral equation, such as Eq. (4.10) for a single baryon, which is a fixed-point integral equation.

With all constants defined the integral equation reduces to $M^* = f(M^*, k_F)$, where the value of k_F is given a fixed value before the integral equation is to be solved. For values of k_F up to some critical value of $(k_F)_{\text{critical}}$, the naïve method successfully solves the integral equation within a finite number of iterations.

In order to investigate the convergence we use a cobweb diagram, as shown in Fig. 4.4 in which we 'join-the-dots' between successive guesses and function evaluations. For clarity, the function $f(M^*, k_F)$ is shown, as is the value of M^*; the point at which these lines intersect represents the solution to the integral equation. In this way we can trace the convergence of the guesses from an initial guess of $M^* = 0$ to the value that satisfies the integral equation.

If however, we wish to solve the integral equation for a value of $k_F > (k_F)_{\text{critical}}$, the naïve method fails to converge, and rather 'flip-flops' between a pair of points. The cobweb diagram for this case is shown in Fig. 4.5, and we see that the solution is never reached.

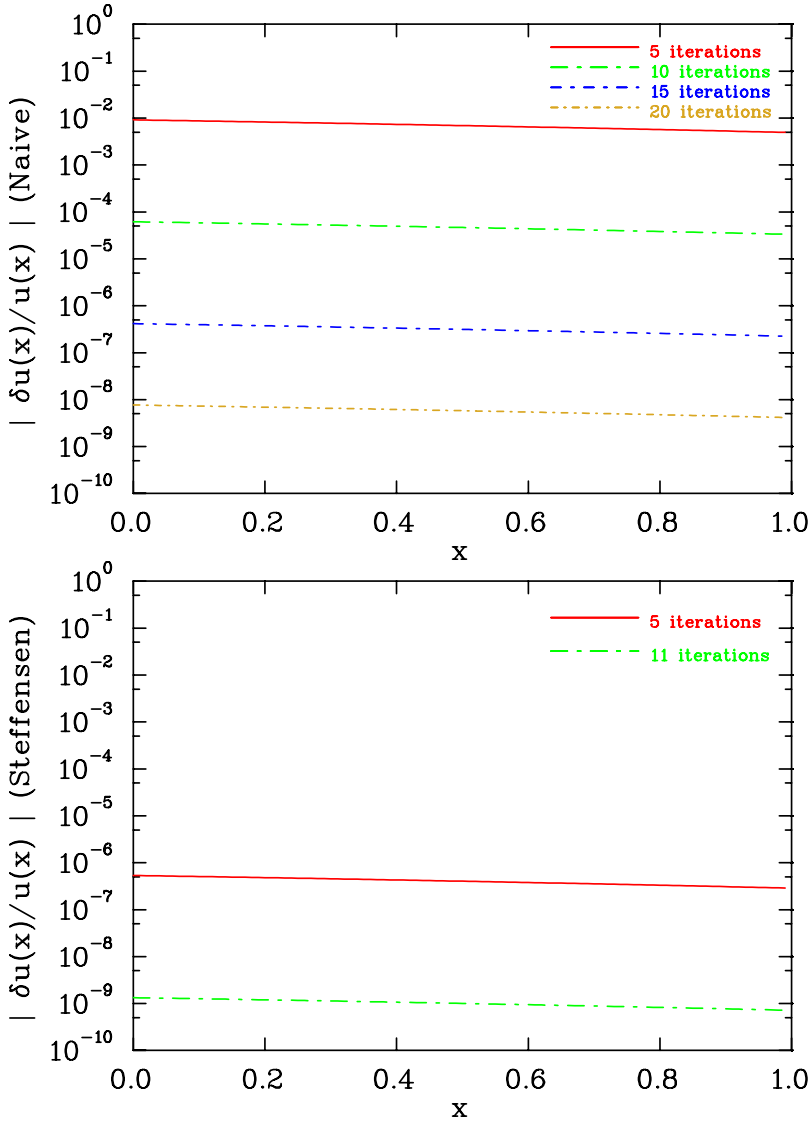

Fig. 4.3: (Color Online) Errors for convergence of a naïve method (top) and Steffensen's method (bottom) relative to the exact solution $u^*(x)$. The naïve method converges in 20 iterations, while Steffensen's method converges in 11 iterations.

The significance of the value of $(k_F)_{\text{critical}}$ is that the slope of the function at the fixed-point becomes too negative; in particular, $f'(M^*, (k_F)_{\text{critical}}) < -1$. Proving that this will cause this method to fail to converge is as easy as creating a cobweb diagram for any function with $f'(\text{fixed-point}) < -1$. Even if we select a starting point particularly close to the actual fixed-point solution and perform this iterative procedure, if $k_F > (k_F)_{\text{critical}}$ the iterations diverge to a pair of points, as shown in Fig. 4.6. Although we have only shown the case of the naïve substitution iterative procedure, we note that Newton's method suffers from the same limitation.

If however, we use Aitken-improved Steffensen's method for solving the same integral equation with the same initial value of $M^* = 0$, the procedure converges to the correct result, irrespective of the choice of k_F. Fig. 4.7 shows an example of this convergence for a value

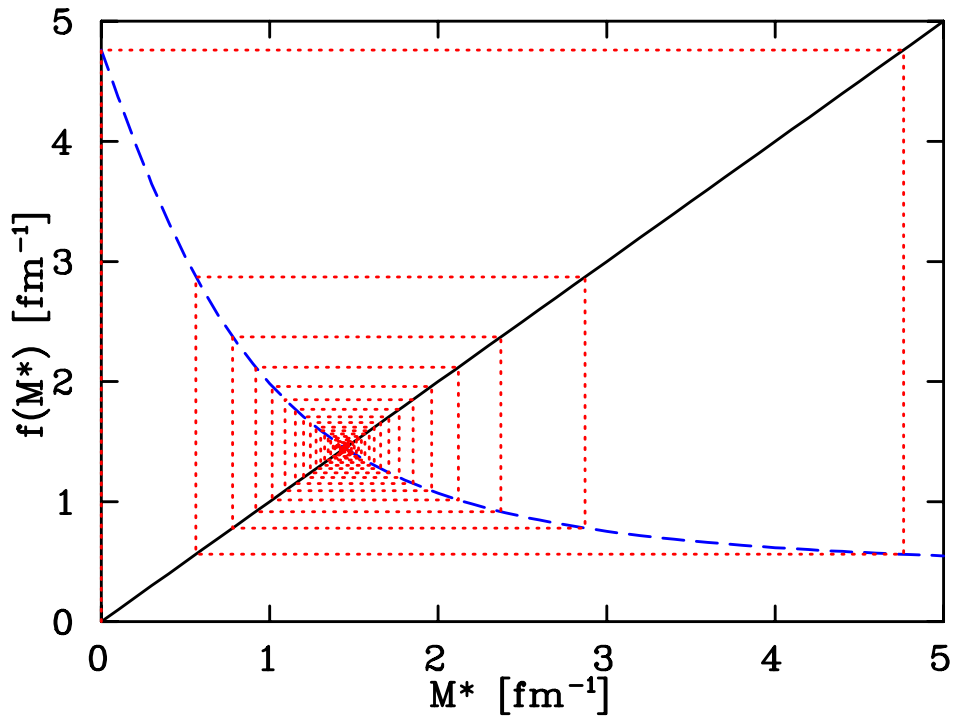

Fig. 4.4: (Color Online) Cobweb diagram for a naïve method of solving Eq. (4.10) for a single baryon, in which $k_F < (k_F)_{\text{critical}}$. The short-dashed line traces the guesses and function evaluations from the initial guess of $M^* = 0$ to the value that satisfies the integral equation.

of $k_F \gg (k_F)_{\text{critical}}$, and the solution is not only found, but is done so in a small number of iterations. We shall therefore rely on Aitken-improved Steffensen's method to solve the integral equations in the work that follows.

While we have shown an example of a single integral equation, the equations we will need to solve for our calculations will be a series of coupled integral equations, $M_B^* = f(M_p^*, M_n^*, k_{F_p}, k_{F_n})$ and this complicates matters. To be precise, we would require an equivalent of the Jacobian, Eq. (4.9) but derived in the manner of Steffensen's method. For our purposes, we are able to use the linear version to solve two coupled integral equations; one for protons and one for neutrons. This may be due to the similarities between the values of M^* for each of these. Further research will be undertaken to investigate the roles that the octet baryons take in these calculations.

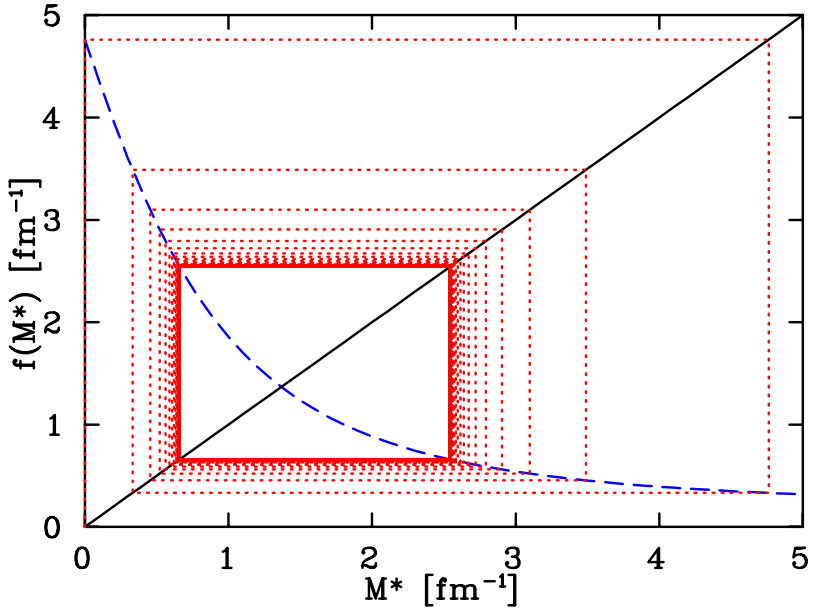

Fig. 4.5: (Color Online) Cobweb diagram for a naïve method of solving Eq. (4.10) for a single baryon, in which $k_F > (k_F)_{\text{critical}}$. In this case, the procedure does not converge to the a single solution, but alternates between a pair of points.

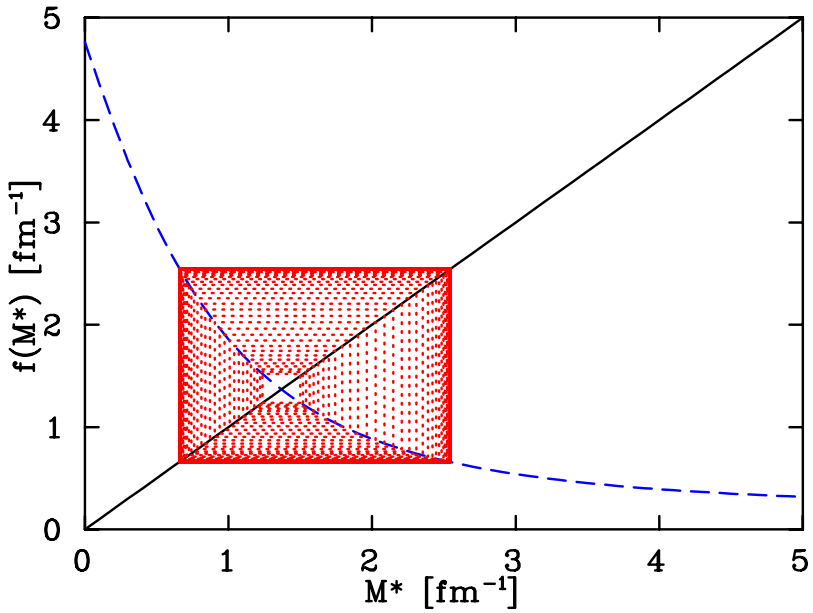

Fig. 4.6: (Color Online) Cobweb diagram for a naïve method of solving Eq. (4.10) for a single baryon, in which $k_F > (k_F)_{\text{critical}}$ and the starting point is deliberately chosen to be near the exact solution. In this case, the procedure does not converge to the a single solution, but in fact diverges, then alternate between a pair of points.

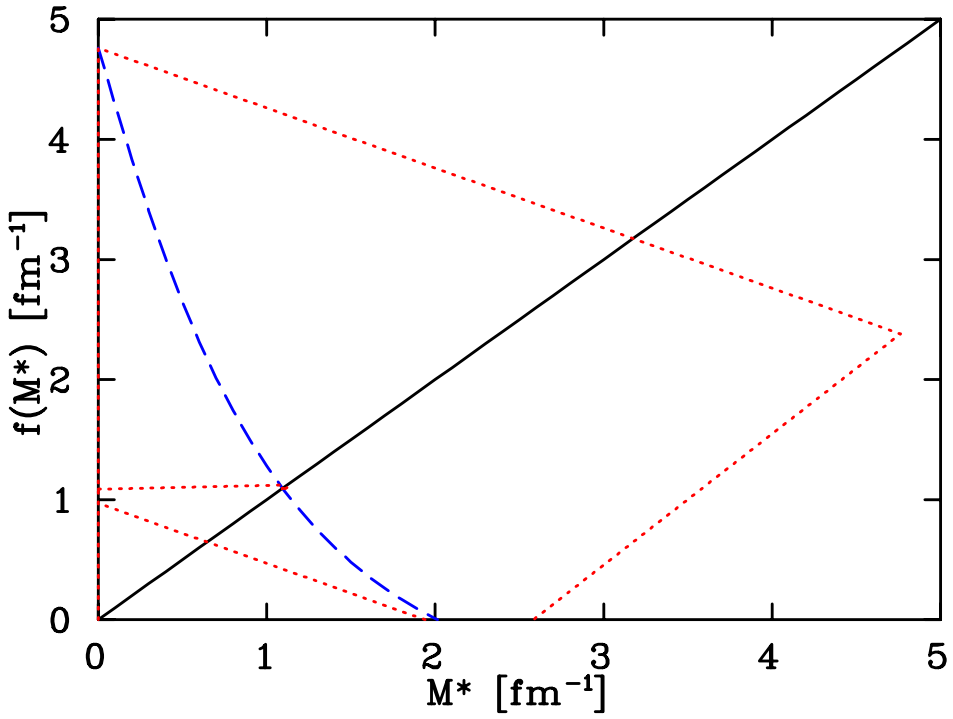

Fig. 4.7: (Color Online) Cobweb diagram for a Aitken-improved Steffensen's method of solving Eq. (4.10) for a single baryon, in which $k_F \gg (k_F)_{\text{critical}}$, with initial guess $M^* = 0$. This shows that even for cases in which the naïve method (and Newton's method for that matter) would fail, this method is sufficient to solve the integral equation.

4.3 Infinite Matter

Utilising the above techniques we are able to compute simulations of infinite matter. The entire procedure is coded in Fortran 90. The method by which we do this is as follows;

1. Define all vacuum masses, coupling constants, and internal parameters.
2. Provide suitable initial guesses for variables k_{F_p} and k_{F_n}, and if applicable, $\langle\sigma\rangle$.
3. Select a value for the control parameter ρ_{total}. We select a small non-zero value to begin with. When we are computing models involving the leptons, we also select the value of the total charge, which is always $Q_{\text{total}} = 0$.
4. Call a subroutine `SolveConstraints` which solves the constraint equations Eqs. (4.6)–(4.7) using Newton's Method. Eq. (4.8) can be excluded here even if not calculating Fock terms, but this self-consistency must then be solved independently. This subroutine takes initial guesses for k_{F_p} and k_{F_n} as well as as required tolerances as inputs, and produces the Fermi momentum values that satisfy the constraint equations above as outputs.
5. As part of the evaluation of Eqs. (4.6)–(4.7) within `SolveConstraints`, the self-consistent effective masses must be calculated by calling another subroutine `SolveEffectiveMasses`. This subroutine takes initial guesses for the effective masses and self-energies, as well as required tolerances as inputs, and produces the self-consistent effective masses that satisfy Eq. (4.8) as outputs.
6. With the Fermi momenta and effective masses determined, we finally have all the information required to evaluate quantities of interest, such as the energy density (e.g. Eq. (3.15)) and pressure (e.g. Eq. (3.16)) of the system. These values are evaluated and saved to a data-file.
7. Finally, the control parameter ρ_{total} is increased by some small step size $\delta\rho$ and the process repeated, where the initial guesses for the subroutines are now the final values from the previous iteration.

This of course assumes that the couplings constants are known quantities. In each of the models we use we require that the properties of saturated nuclear matter are reproduced, as per Eq. (2.73). In order to find the appropriate values of $g_{N\sigma}$ and $g_{N\omega}$ that reproduce the correct results we perform the above method with initial guesses for these values, and calculate the energy per baryon at saturation (as defined by the lower extrema of the data) and the Fermi momentum at which this occurs. By performing this several times for several choices of couplings, we can refine our choices for initial guesses in order to better reproduce the saturation properties. Of course, in practice we perform these steps using a Fortran 90 subroutine which minimises a function of the saturation property variables for values of the couplings, such that the couplings found using this method produce saturation properties for any EOS that match the constraints with great precision.

This process is suitable for solving all the models presented in this thesis; the model-specific details do not require changes to the method of solving the equations. This provides us with enough data to investigate fully the properties of infinite matter. To investigate compact stellar objects however, we require a further calculation.

4.4 Runge–Kutta Integration

In order to calculate the properties of compact stellar objects, we need to solve the Tolman–Oppenheimer–Volkoff Equations, as described in Section 2.11 and derived in Appendix A.4. These equations provide a connection between the infinite matter equation of state and the properties of macroscopic stellar objects which can support the enormous gravitational pressures involved without collapsing.

The relation between the state variables of the EOS; the energy density $\mathcal{E}$ and the pressure P; and the the mass-radius relationship of a compact stellar object is determined by the pressure gradient

$$\frac{dP}{dr} = -\frac{G\left(P/c^2 + \mathcal{E}\right)\left(M(r) + 4\pi r^3 P/c^2\right)}{r(r - 2GM(r)/c^2)}. \tag{4.18}$$

In order to make use of this, we will need to integrate this equation to find the pressure at some radius R'. We use fourth-order Runge–Kutta integration, which provides a useful scheme for integrating since it only requires a small number of function evaluations.

Fourth-order Runge–Kutta integration is defined by the following iterative procedure; If the differential equation $y' = G(x, y)$ is to be integrated to give

$$y(b) = y_0 + \int_0^b G(x, y)dx \tag{4.19}$$

with initial values and intervals of

$$y_0 = y(0), \quad x_0 = 0, \quad x_i = i\,\delta x, \tag{4.20}$$

where $b = n\delta x$, then we can define the Runge–Kutta steps as

$$\begin{aligned} RK1_i &= G\left(x_i, y_i\right), \\ RK2_i &= G\left(x_i + \frac{\delta x}{2},\ y_i + \frac{\delta x}{2}\,RK1_i\right), \\ RK3_i &= G\left(x_i + \frac{\delta x}{2},\ y_i + \frac{\delta x}{2}\,RK2_i\right), \\ RK4_i &= G\left(x_i + \delta x,\ y_i + \delta x\,RK3_i\right), \end{aligned} \tag{4.21}$$

where δx is a small shift in x that will determine the resolution to which we wish to know $y(x)$. The values $RK1_i$ and $RK4_i$ are the slopes of tangents to the function y at the points x_i and $x_i + \delta x$ respectively, while $RK2_i$ and $RK3_i$ are the slopes of y at the midpoint $x_i + \delta x/2$, where the y value of the former is defined by the Euler method[3] using $RK1_i$, and the latter defined by the Euler method using $RK2_i$.

The next value of the function, located at $x_{i+1} = (i + 1)\,\delta x$, is then defined using a modification of Simpson's Rule, as

$$y_{i+1} = y_i + \frac{\delta x}{6}\left(RK1_i + 2\,RK2_i + 2\,RK3_i + RK4_i\right). \tag{4.22}$$

[3]Euler's method provides a very simple approximation, utilising the first two terms of a Taylor expansion of y to solve $y'(t) = f(t, y(t))$, thus $y_{n+1} = y_n + hf(t_n, y_n)$.

By performing this procedure iteratively we can integrate a differential equation until after n steps we reach the upper integration limit of $x_n = b$.

For our purposes, we select a central density of a stellar object ρ_{central} as the control parameter. The EOS data calculated for a particular model then provides the energy density and pressure at the centre of the star.

Assuming spherical symmetry, we require that the pressure gradient dP/dr at the centre of the star ($r = 0$) be zero, thus $y'(0) = 0$. By using Runge–Kutta integration, we can evaluate the pressure at the boundary of a sphere of matter with a radius $r = R'$. By relating this pressure to the EOS we can also find the energy density at this boundary, $\mathcal{E}(R')$.

By performing this integration for larger and larger values of $r = R'$ (since Eq. (4.18) describes a negative pressure gradient, this results in smaller and smaller values of pressure P) we eventually find some value $r = R$ for which the integral of Eq. (4.18) becomes negative, i.e. $y_{i+1} < 0$; thus at a distance of approximately $r = R$ (to within the resolution of δx) the pressure is zero, and we define this point as the edge of the star, and hence the radius.

Since we have also collected data for $\mathcal{E}(r)$, we can calculate the mass residing within some radius R' as

$$M(R') = \int_0^{R'} 4\pi r^2 \mathcal{E}(r)\, dr, \tag{4.23}$$

and thus the total mass of the star is defined by $M(R)$, where R is the radius of the star. With this information we can investigate the mass-radius relation for a star with a given central density. Repeating this calculation for several values of ρ_{central} provides a locus of values as shall be shown, for example, in Section 5.1.2. We can also investigate other properties of a star as a function of internal radius by calculating them at various values of $x_i = r$ in Eq. (4.20).

4.5 Phase Transitions

In order to combine the EOS for hadronic and quark matter (since we will be using a Gibbs transition, refer to Section 2.9) we require a method of calculating the phase transitions from hadronic matter to a mixed phase, and from a mixed phase to quark matter. Following the requirements described in Section 2.10 we calculate the EOS of hadronic matter with control parameter ρ_{total}, while at each density we use μ_n and μ_e as inputs to the quark matter EOS (for a given model of quark matter). At each density we can calculate the pressure for the hadronic phase P_H and the quark phase P_Q and compare these values. At the point (if it exists) where $P_H = P_Q$ we consider the models to be in equilibrium.

We then change the control parameter in our code from ρ_{total} to χ (parameterizing the quark fraction in the mixed phase, and acting as the order parameter between the phases) at which point we have $\chi = 0$, still purely hadronic matter. We can then increase χ by $\delta\chi$ and calculate properties of the mixed phase such as the total baryon density and energy density with weightings of χ and $(1 - \chi)$ for the quark and hadronic phases respectively, with the condition that the chemical potentials are still equal for each phase, and the pressures are equal for each phase.

We continue to increase χ until we reach $\chi = 1$ at which point the EOS is described entirely by quark matter, and thus the mixed phase is in equilibrium with a pure quark phase. From this point on, we return to using ρ_{total} as the control parameter and increasing this value by $\delta\rho$ up to some arbitrary density.

Results

Within this chapter we will once again use the term 'configuration of a model' to indicate differences (such as types of particles included or neglected) within a particular model. Some of the most interesting and important numerical results are shown, though results for all calculations for all configurations will not be shown, due to the overwhelmingly large number of possibilities that exist. A summary table is provided in Section 5.5 which contains many numerical results of interest.

5.1 QHD Equation of State

Though QHD has been studied extensively, and many excellent summaries exist (e.g. Ref. [18]), we will present the results of our QHD calculations for the purpose of comparison in later sections, and to verify that our results do indeed reproduce the established results.

5.1.1 QHD Infinite Matter

To obtain numerical results, we solve the meson field equations, Eqs. (3.6)–(3.8), with the conditions of charge neutrality and fixed baryon density for various configurations of models. For configurations involving leptons, we include the condition of equivalence of chemical potentials given by Eq. (3.18). The energy per baryon given by Eq. (2.73) for various configurations of nucleonic QHD (in which QHD-I neglects contributions from ρ mesons, QHD-II includes these contributions, nuclear QHD contains equal proportions of protons and neutrons, and in each case we do not model leptons) are shown in Fig. 5.1 and we see that the saturation of nuclear matter occurs at the correct value of k_F (here we use the neutron Fermi momentum, as it is common to all three configurations; for the relation between Fermi momentum and density, refer to Section 2.4) corresponding to ρ_0 as per Eq. (2.38) by construction via the use of appropriate couplings $g_{N\sigma}$ and $g_{N\omega}$.

The compression modulus for symmetric nuclear matter, as defined by the curvature at saturation, refer to Eq. (2.75) is found to be $K = 525$ MeV, which is in agreement with Ref. [18], but as stated in that reference, not with experiment. This point will be discussed further in Sec. 5.2.1. We further note that the pressure of nuclear matter calculated via Eq. (3.16) is zero at the saturation point, as predicted by Eq. (2.71).

The case of 'symmetric' nuclear matter—in which we include protons, but not β-equilibrium with leptons—is of course purely academic, since this is infinite matter, and we are therefore considering an infinite charge. The saturation that occurs in this case and the binding (a negative energy per baryon indicates a binding energy) is considered to resemble heavy finite nuclei.

The low density EOS for nucleonic QHD is shown in Fig. 5.2 in which we see that the low density EOS is rather soft (does not approach the limit of $P = \mathcal{E}$; the stiffest possible EOS in which the speed of sound equals that of light), and nearly configuration independent in that QHD-I produces similar results to that of nuclear QHD. At higher densities, the EOS for all configurations approach the limit.

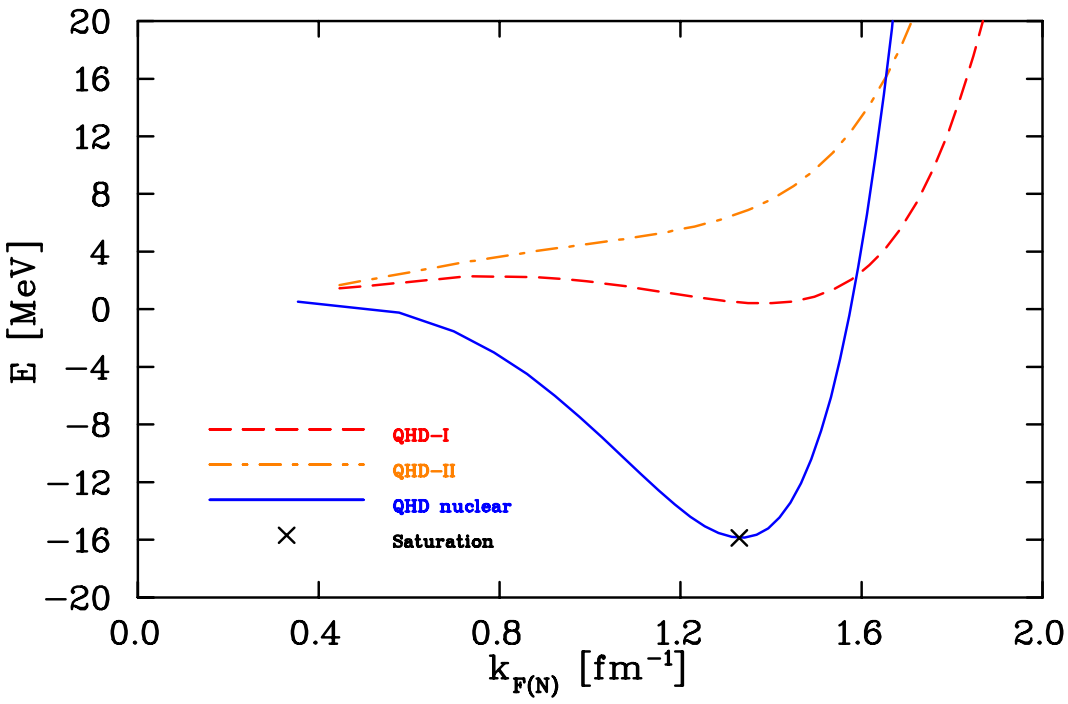

Fig. 5.1: (Color Online) Energy per baryon for nucleonic QHD-I, QHD-II, and nuclear QHD which demonstrates saturation at the correct value of E as defined in Eq. (2.73), and value of k_F (here we use the neutron Fermi momentum, as it is common to all three configurations) corresponding to ρ_0 as per Eq. (2.38). The reproduction of this value occurs by construction via the use of appropriate couplings $g_{N\sigma}$ and $g_{N\omega}$ as described in Section 4.3.

The effective masses for the various configurations of nucleonic QHD are shown in Fig. 5.3, for which we note that the neutron matter curves are identical, as the ρ meson (a vector meson) provides no contribution to the effective mass, which is a purely scalar effect. Although the form of the effective mass is linear in Fig. 3.1, in that case the effective mass is plotted against the scalar self-energy, which is shown in Fig 5.4, and we note that this quantity is non-linear, which determines the shape of the curve in Fig. 5.3. For the case of nuclear QHD we find values of the effective mass at saturation of the neutrons to be $(M_n^*/M_n)_{\rm sat} = 0.56$, corresponding to an effective mass of $M_n^* = 526$ MeV.

We can investigate the balance between the various meson fields by examining the self-energy contributions, which are defined explicitly for QHD in Eq. (2.42). These are shown in Fig. 5.4 for QHD-I and QHD-II both in β-equilibrium (the self-energies for nuclear QHD are the same as those for QHD-I, since the ρ meson does not contribute to nuclear QHD as its contribution is proportional to the asymmetry between proton and neutron densities). From this figure it is clear that there exists an important balance between the scalar and vector interactions. Note the significance of the shape of the Σ_s curve to that of the effective mass as shown in Fig. 5.3. Also note that in Hartree-level QHD, $\Sigma_v = 0$ for all baryons.

A log-log graph of the EOS for nucleonic QHD in which we show a Maxwell transition for the van der Waals style liquid-gas phase transition in QHD-I is shown in Fig. 5.5. The transition pressure is taken from Ref. [18]. In this form of a transition (in contrast to that of Section 2.9) the pressure is constant between the phases (isobaric transition) and the

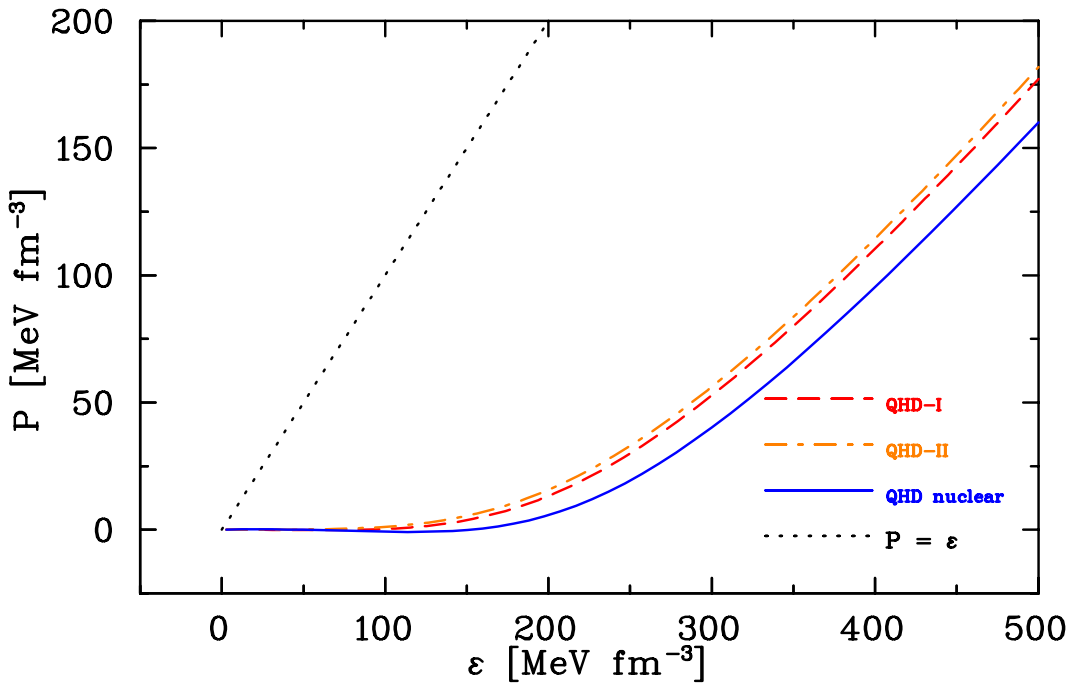

Fig. 5.2: (Color Online) Low density EOS for nucleonic QHD, as well as the causal limit of $P = \mathcal{E}$ in which the speed of sound in-medium equals the speed of light. Here we see that the low density EOS are rather similar, independent of which configuration of QHD is considered. The common feature however is that the low density EOS are rather soft, in that it does not yet approach the limit of $P = \mathcal{E}$. The EOS for all densities for these configurations are shown in Fig. 5.5.

density of the combined EOS becomes disjoint. This example refers to a liquid-gas style phase transition, where later we will discuss phase transitions between phases with different degrees of freedom. The inclusion of the ρ meson removes this transition.

For nuclear QHD, the species fractions (refer to Eq. (2.40)) are by definition equal for the protons and neutrons, i.e. $Y_p = Y_n = 0.5$. For QHD-I and QHD-II the neutrons provide the only baryonic contribution. If we include protons and leptons ($\ell = e^-, \mu^-$) we can investigate the effects of β-equilibrium matter with global charge neutrality. The species fractions Y_i are shown in Fig. 5.6 for a configuration with (and without) contributions from ρ mesons. In each case, at low densities the system is composed of nearly entirely neutron matter, but we can see that at higher densities the contributions from protons become non-negligible.

We do not show any results for the addition of hyperons to the QHD EOS. The QHD model as described in Section 3.1 is derived assuming a weak-field limit (in order to define the MFA; refer to Section 2.2) in order to define the Dirac equation for the baryons. In this limit, where the meson fields are assumed to be small in magnitude (weak), we can ignore the effects of antibaryons, since it is not possible in this limit for the creation of particle–antiparticle pairs via vacuum fluctuations[1]. The inclusion of hyperons causes the magnitudes of the fields —particular the scalar field, as can be seen by examining the form of this in Eq. (3.17)

[1]This is a well known limitation of the Dirac equation, and has been discussed in detail, for example in the case of electron scattering from a potential barrier, resulting in the 'Klein Paradox' [68].

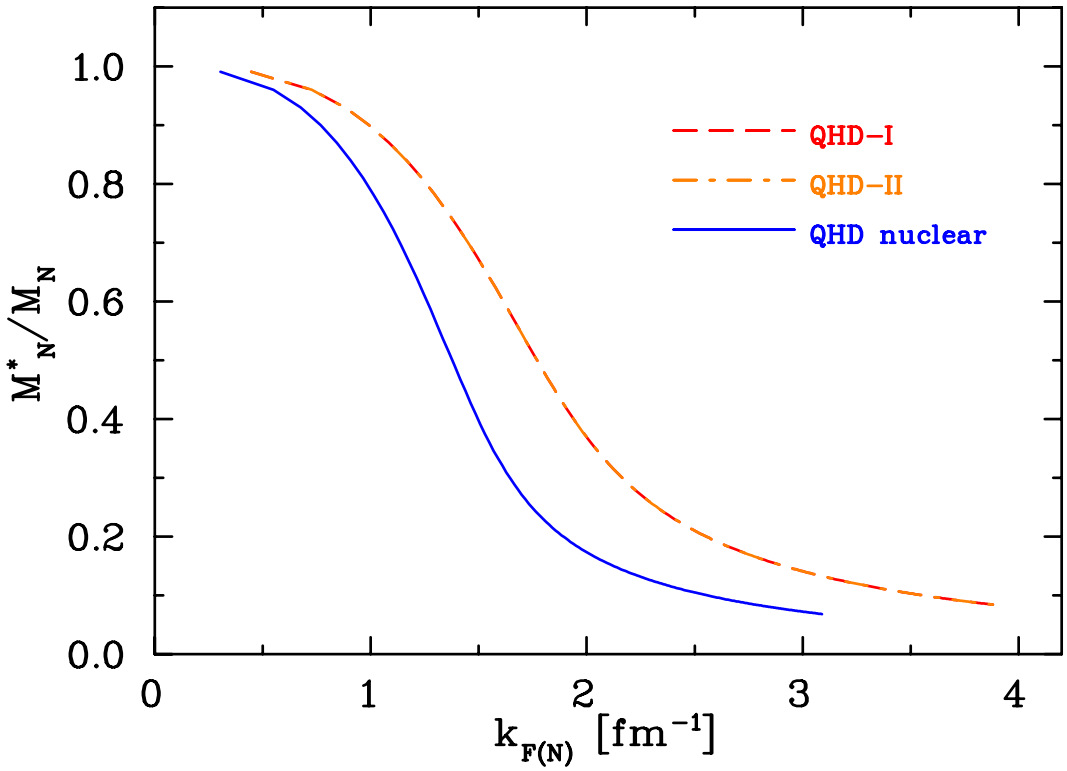

Fig. 5.3: (Color Online) Neutron effective masses for the various configurations of nucleonic QHD. Note that the curves for neutron matter (QHD-I and QHD-II) are identical; the addition of the ρ meson contribution (a vector meson) does not contribute to the effective mass, as this is a purely scalar effect. Although the form of the effective mass is linear in Fig. 3.1, in that case the effective mass is plotted against the scalar self-energy, which is shown in Fig 5.4, and we note that this quantity is non-linear, which determines the shape of the curve here.

in which we sum over *all* baryons—to become large, and thus the weak-field assumption becomes violated. We can observe that this is indeed the case by examining the effective masses. We observe that when the hyperons are included, the baryon effective masses for several of the baryons become negative, indicating that the scalar self-energy (defined by the mean-scalar field as per Eq. (3.10)) has become larger than the vacuum baryon mass. We consider this to be a breakdown of the model, and thus we do not perform calculations where this occurs. Calculations for QHD can be performed prior to this breakdown, but we elect to not present any of these results, as they represent a model which we consider to be inaccurate. We shall therefore consider it not possible to include hyperons into QHD in an interesting manner for our purposes. The issue of negative effective masses is however remedied in QMC as will be shown later.

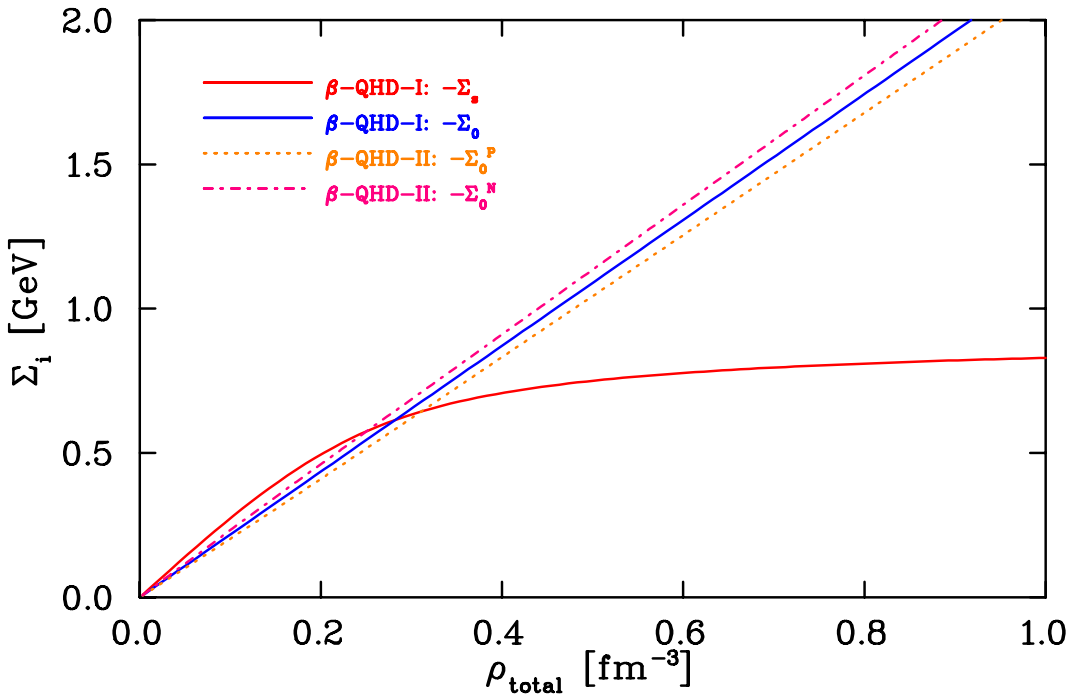

Fig. 5.4: (Color Online) Self-energies for β-equilibrium QHD-I and QHD-II. Nuclear QHD has the same self-energies as QHD-I since the ρ meson does not contribute; it is proportional to the asymmetry between proton and neutron densities. Here the density is shown up to 1.0 fm^{-3} after which the curves become linear. Note the significance of the shape of the Σ_s curve to that of the effective mass as shown in Fig. 5.3. Also note that in Hartree-level QHD, $\Sigma_v = 0$ for all baryons.

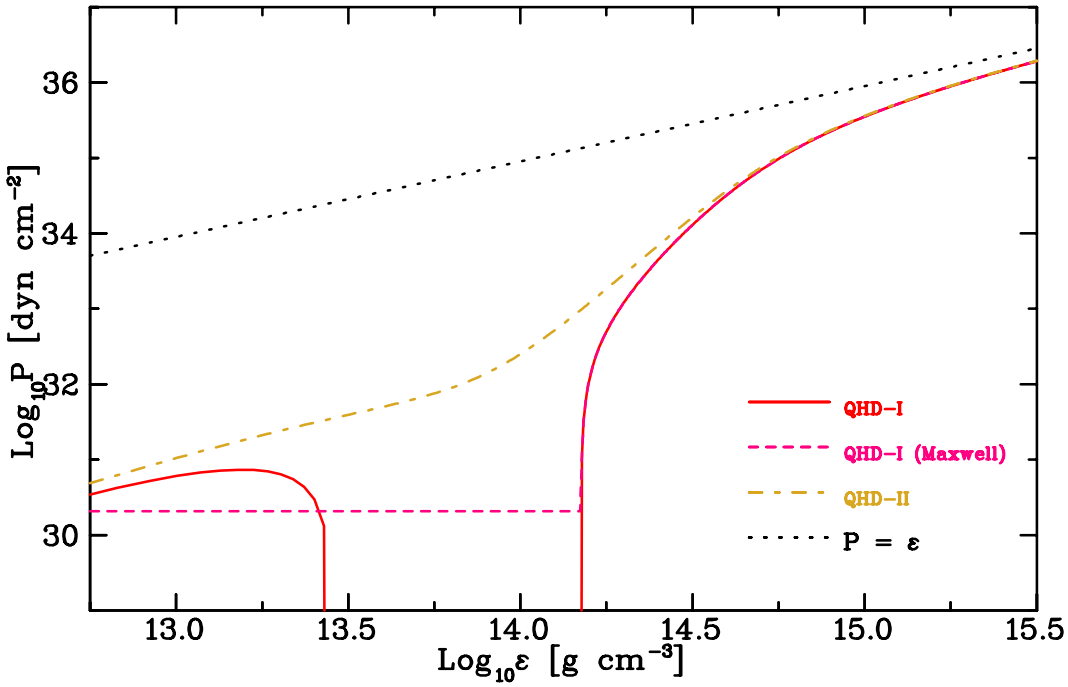

Fig. 5.5: (Color Online) Log-log EOS for nucleonic QHD-I and QHD-II. QHD-I produces features similar to that of a van der Waals EOS, which can be interpreted as a liquid-gas phase transition. The addition of the ρ meson contribution removes this transition. A Maxwell construction has been performed (using the transition pressure from Ref. [18]) to produce a constant pressure transition between the phases. Note that at high densities (large values of $\mathcal{E}$) all the configurations approach the limit of $P = \mathcal{E}$.

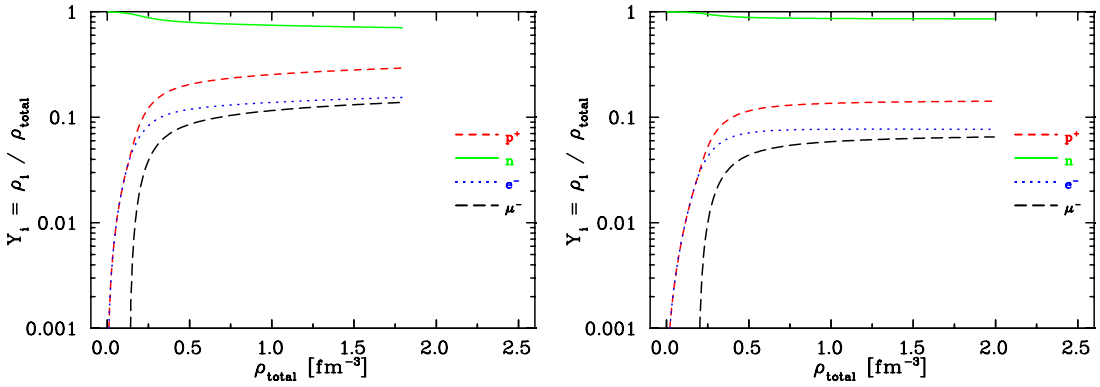

Fig. 5.6: (Color Online) Species fractions Y_i for nucleonic QHD in β-equilibrium with leptons $\ell = e^-, \mu^-$, including (left) and lacking (right) a contribution from the ρ meson. In both cases, at low densities the system is composed of nearly entirely neutron matter, but at higher densities the contribution from protons become non-negligible.

5.1.2 QHD Stars

Having found the QHD EOS by evaluating the energy density, Eq. (3.15), and pressure, Eq. (3.16), we can calculate properties of stellar objects (which we shall refer to as 'stellar solutions') based on this EOS, using the TOV equation (refer to Section 2.11). The radius of a star is defined as the radius at which the pressure is zero and is calculated using a fourth-order Runge–Kutta integration method (refer to Section 4.4).

The mass-radius relations for various configurations of nucleonic QHD are shown in Fig. 5.7 along with the 2σ results[2] of various experiments [69–71]—which detail the only measurements to date of the radii of neutron stars along with their masses, namely for the stars denoted by EXO 0748-676, 4U 1608-52, and EXO 1745-248—for comparison. The authors of Ref. [69] claim that their findings (corresponding to EXO 0748-676) rule out soft equations of state, though as noted in a response to that paper [72] and in this work, the 2σ data admits a wide variety of EOS. The results of Ref. [69] should likely be discounted, since developments in the field have shown possible large errors with that experiment [73].

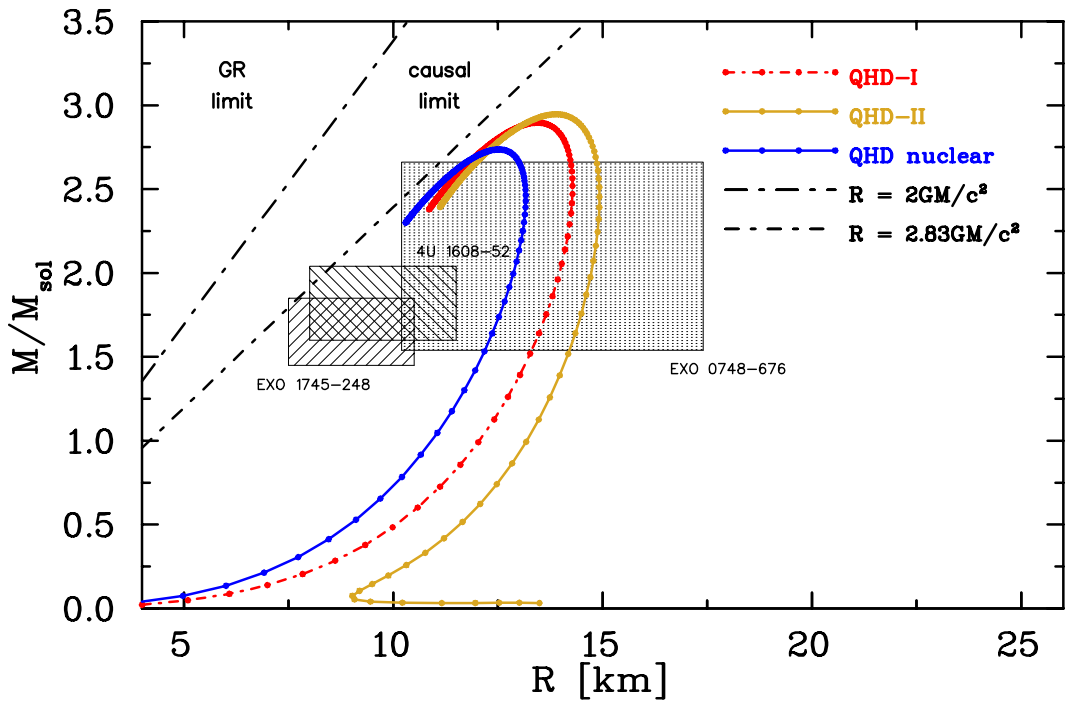

Fig. 5.7: (Color Online) Mass-radius relation for various configurations of nucleonic QHD. Also shown are the theoretical limits due to General Relativity and causality (where G is the gravitational constant, c is the speed of light), as well as the 2σ error bounds from various experiments [69–71] which illustrate how loosely the requirements of an EOS are currently defined. Note that the low-density shape of the curve changes with the addition of the ρ meson in QHD-II.

[2]The shaded areas for EXO 1745-248 and 4U 1608-52 represent a conservative reproduction of the 2σ data from the relevant reference. The shaded area for EXO 0748-676 represents the central data point plus error bars expanded to a rectangular area.

We note that the shape of the low-central-density relation changes with the addition of the ρ meson producing QHD-II, which should be expected, given the differences between the QHD-I and QHD-II EOS as shown in Fig. 5.5.

We show (as an example, for QHD-I) the relation between pressure and internal radius for a variety of stars with different central densities in Fig. 5.8. We note the trend that a star with a larger central density has a greater central pressure, and a smaller total radius. Each of the curves in that figure correspond to the high-central-density positive-gradient section of the relevant curve in Fig. 5.7.

If we now include the leptons to our calculations, we can observe the effect that these have on the mass-radius relations, as shown in Fig. 5.9 for β-equilibrium nucleonic matter. While the QHD-I and β QHD-I configurations may not be dramatically different, the similarities of the stellar solutions for these configurations demonstrates the difficulties that exist in determining the content of stars from these two parameters alone.

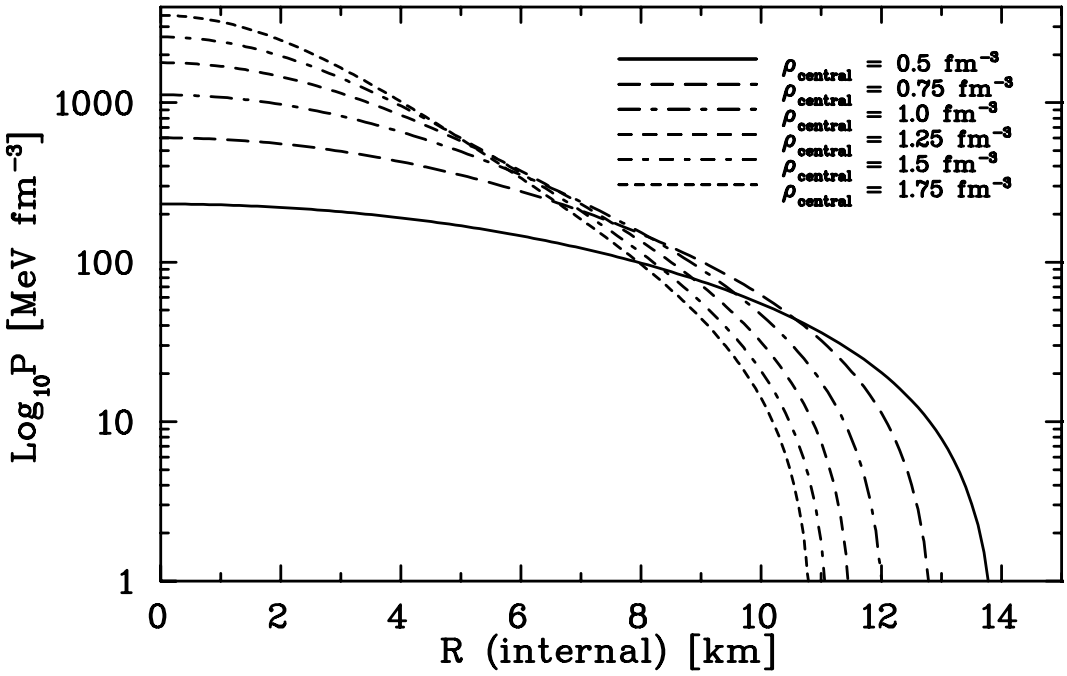

Fig. 5.8: (Log) pressure vs. internal radius for stars with various central densities for QHD-I. Note that the stars with a larger central density have a larger central pressure, and a smaller total radius. The data for $\rho_{\text{central}} = 0.5$ fm^{-3} corresponds to a star with $M = 2.84\ M_{\odot}$ and $R = 13.96$ km, while the data for $\rho_{\text{central}} = 1.75$ fm^{-3} corresponds to a star with $M = 2.39\ M_{\odot}$ and $R = 10.9$ km, both of which correspond to the high-central-density positive-gradient section of the relevant curve in Fig. 5.7.

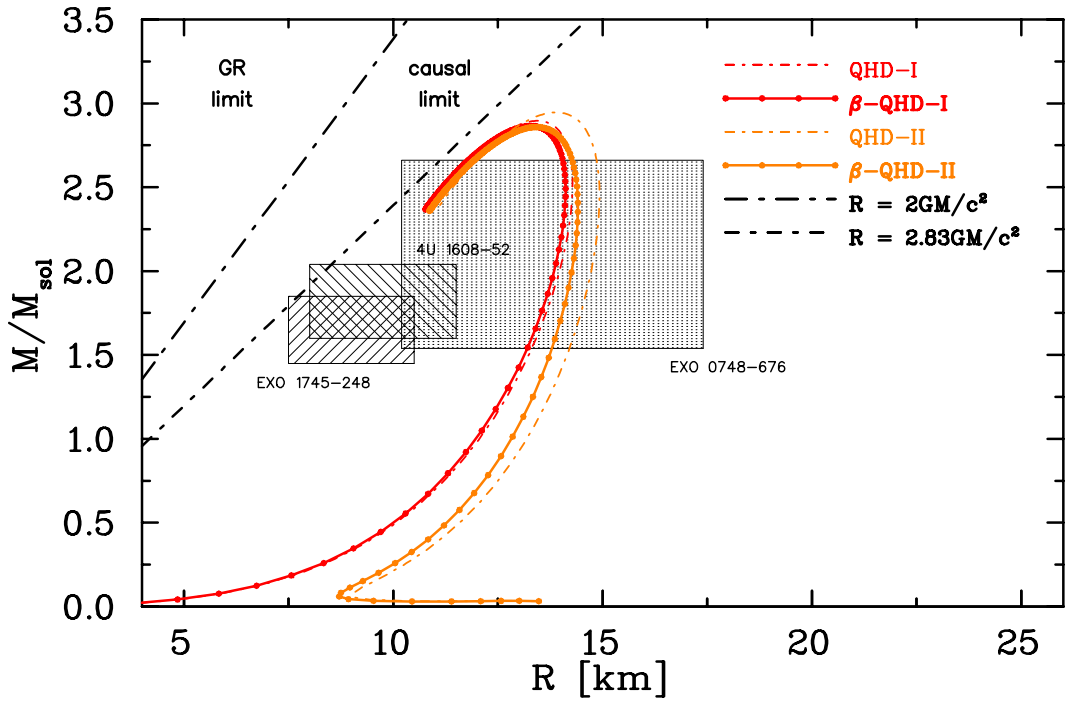

Fig. 5.9: (Color Online) Mass-radius relations for QHD-I and QHD-II in β-equilibrium, with the neutrons-only relations (as shown in Fig. 5.7) for comparison. Note that the effect of including protons and leptons does not have such a pronounced effect on QHD-I, since in that case the protons do not provide such a large contribution, as can be seen in Fig. 5.6. The similarities between the stellar solutions for each configuration emphasises the difficulty of using the mass and radius alone to constrain a model.

5.2 QMC Equation of State

By including the effect of the quark content of baryons we can investigate the impact on various quantities, using the QMC model as described in Sec. 3.2. We will see that this has profound consequences for the EOS. Many of the results presented in this section are published by the author [42] as a unique investigation of the octet QMC model.

5.2.1 QMC Infinite Matter

The energy per baryon curves for QMC are shown in Fig. 5.10 where, for the sake of comparison to Fig. 5.1 we have used the same notation for distinguishing the configurations, thus QMC-I neglects the contribution of the ρ meson, QMC-II includes it, and QMC nuclear restricts the species fractions of protons and neutrons to be equal. We neglect the contributions of leptons for these simple configurations. The couplings of the baryons to the mesons are found such that once again the appropriate saturation properties are reproduced.

An interesting feature to note for Fig. 5.10 is that the curvature for nuclear QMC at saturation is less than that of the same curve in Fig. 5.1 indicating that the compression modulus for QMC takes a smaller value. This is of particular interest, since the value of the compression modulus for QHD is known to be too large [18], which is typical of models that neglect quark level interactions. For QMC we find a significant improvement in the

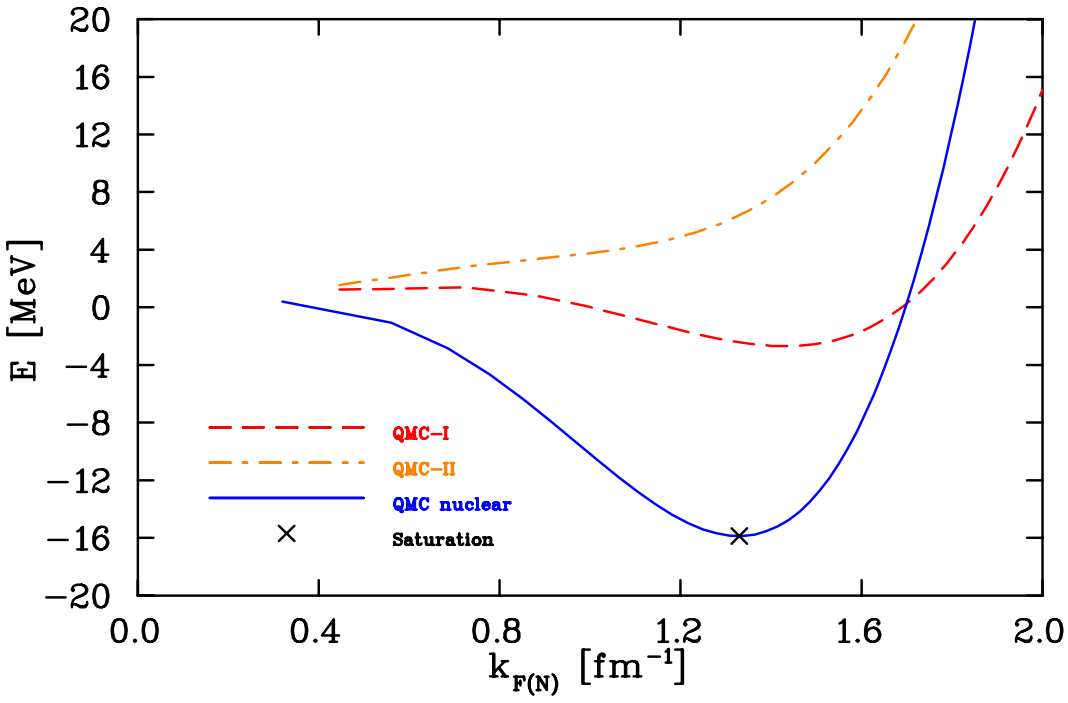

Fig. 5.10: (Color Online) Energy per baryon for nucleonic QMC-I, QMC-II, and nuclear QMC which demonstrates saturation at the correct value of E as defined in Eq. (2.73), and correct value of k_F. For comparison to Fig. 5.1 we use the same notation to differentiate between the configurations. The reproduction of the saturation value occurs by construction via the use of appropriate couplings $g_{N\sigma}$ and $g_{N\omega}$ which have been re-calculated for QMC.

compression modulus; $K = 280$ MeV which lies at the upper end of the experimental range. The nucleon effective mass at saturation for QMC is found to be $(M^*)_{\rm sat} = 735$ MeV, producing $(M^*/M)_{\rm sat} = 0.78$. The effective masses for the various configurations of nucleonic QMC are shown in Fig. 5.11 and we see that these effective masses do indeed remain positive, as opposed to the negative effective masses we encountered in QHD.

The most interesting aspects of QMC are found when we include the remainder of the octet of baryons—the hyperons—which was not possible in QHD due to the Klein Paradox. As discussed in Sec. 3.2, the baryon effective masses in QMC do not become negative at any density, and thus we do not encounter the same issues as we do when trying to calculate octet QHD. The species fractions for octet QMC are shown in Fig. 5.12, where we note that the Λ species fraction is significantly larger than that of the Σ. The investigations by Rikovska–Stone *et al.* [44] (in which alternative Fock terms were introduced to the QMC model) lead us to expect that the Σ would disappear entirely from the system if we were to include Fock terms for the hyperons.

The species fractions in Fig. 5.12 are particularly interesting when compared to the β-equilibrium nucleonic configurations (Fig. 5.13) as the leptonic contributions *decrease* at higher densities, in contrast to the plateau observed in Fig. 5.13. This is a result of the chemical potential equilibria which provide preference to hadronic charged states with large masses, rather than those with smaller masses. In this case, the system is more stable with

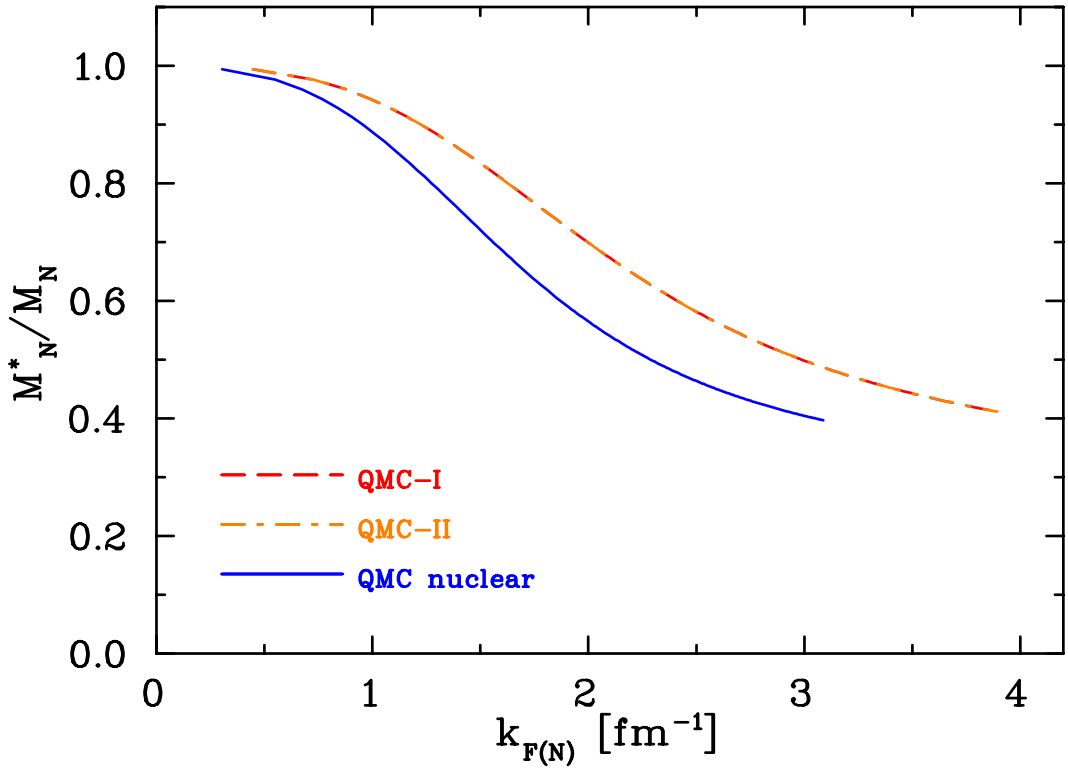

Fig. 5.11: (Color Online) Effective neutron masses for the various configurations of nucleonic QMC in which the effective masses have a quadratic form. Note the subtle differences in shape between these curves and those of Fig. 5.3, particularly the value of the effective mass at saturation.

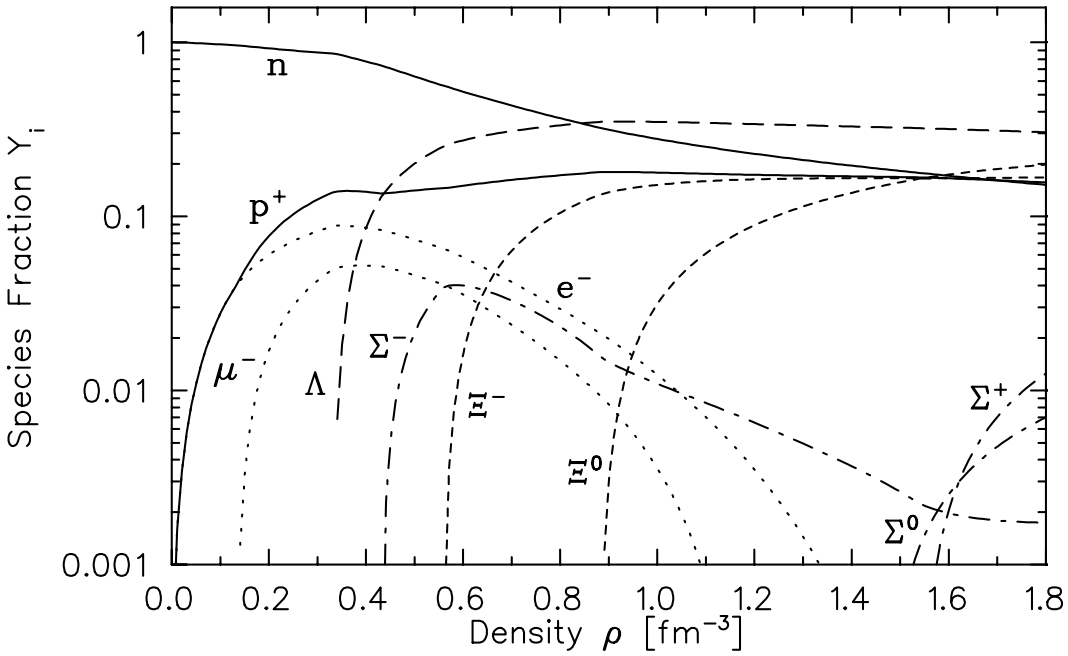

Fig. 5.12: Species fractions Y_i for octet QMC, in which the ρ meson contribution is included. The density here is the total baryon density, as per Eq. (2.38). Note that in this case, all of the octet baryons contribute at some density, and that the species fractions of Σ hyperons are suppressed—in particular that of the Σ^-—compared to the other baryons. When compared to the nucleon-only data (as in Fig. 5.13) we observe that in this case the lepton densities do not plateau, but rather decrease once the hyperons appear, as explained in the text. Note that the Λ hyperon is the first hyperon to appear, and that at high-densities the relative species fractions plateau for the nucleons, Λ, and Ξ hyperons. The relative baryon proportions at high density are ordered by isospin, in that $\rho_\Lambda > \rho_N \sim \rho_\Xi > \rho_\Sigma$. The parameters used here are shown in Table 5.2.

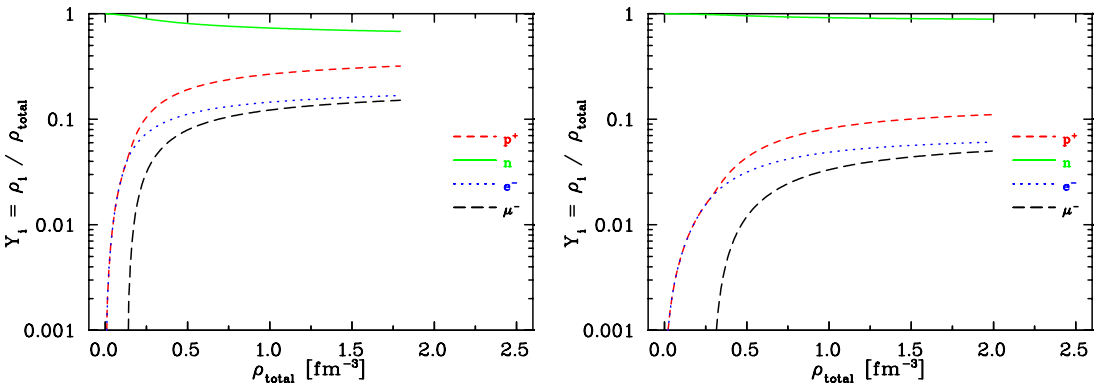

Fig. 5.13: (Color Online) Species fractions Y_i for nucleonic QMC in β-equilibrium with leptons $\ell = e^-, \mu^-$, including (left) and lacking (right) a contribution from the ρ meson. These results are very similar to those of Fig. 5.6, though the differences are most pronounced when lacking the ρ meson (right).

the negative charge (to counter that of the protons) being provided by the Ξ^- hyperon rather than the leptons.

One may reasonably ask then why the Σ^- meson does not play the role of balancing positive charge, as it is the lightest baryon with a negative electric charge. The relation between the chemical potentials in Eq. (2.46); $\mu_{\Sigma^-} = \mu_{\Xi^-}$ involves the full interacting chemical potentials of Eq. (2.44) which includes scalar meson terms that affect the mass, and vector meson terms that effect the energy. It is a balance of these effects which dictates which particle will have the greater Fermi momentum (hence, density) when considering Eq. (2.46) above. For the case shown in Fig. 5.12 the balance dictates that the Ξ hyperons will have a greater species fraction at the densities shown.

If however we exclude the contribution of the ρ meson, we can observe the effects that are attributed to this meson. The species fractions for octet QMC in which we neglect the ρ meson are shown in Fig. 5.14, and we note that the distribution is remarkably different. First, we note that the Σ^- hyperon is now the first to appear, in stark contrast to Fig 5.12 in which the Σ hyperons were largely suppressed. The effect on the chemical potentials (in particular the vector potential terms) due to neglecting the ρ meson is such that this is now possible. We also note that the high-density plateau of Fig. 5.12 is less evident, and the baryons are not sorted by isospin as distinctly. The lack of suppression for the Σ^- is made clear in this case, and indicates the strong link between this meson and baryon, which is reasonable given that the ρ meson couples to isospin, and the Σ baryons have the largest magnitude isospin ($I_\Sigma = 1$).

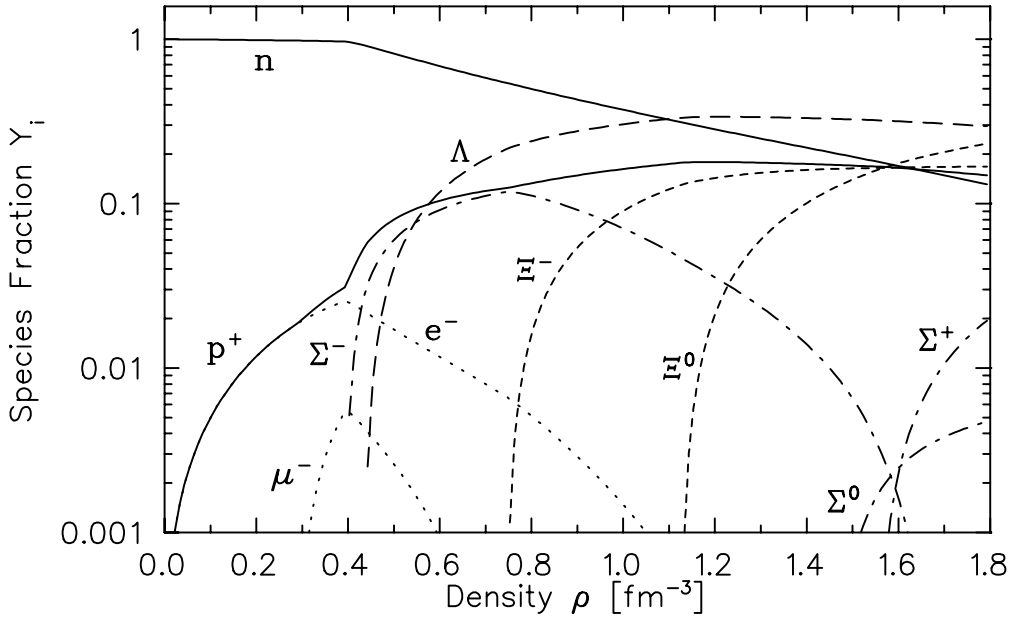

Fig. 5.14: Species fractions Y_i for octet QMC, in which the ρ meson contribution is neglected, but otherwise using the same parameters as used in Fig. 5.12. We note that at high-densities, the baryons are no longer sorted by isospin as distinctly, and that the Σ^- hyperon is now the first to appear. Furthermore, the hyperon threshold now occurs at a higher density than that of Fig. 5.12 where the Λ was the first to appear. In this case, the Σ^- species fraction is not suppressed at high density, indicating that the ρ meson plays a vital role in this.

5.2.2 QMC Stars

By solving the TOV equation, we can once again investigate 'stellar solutions'. The mass-radius relations for nucleonic QMC EOS are shown in Fig. 5.15. The maximum masses for the QMC-I and nuclear QMC EOS are much smaller than their counterparts in QHD, since the QMC EOS is much softer than that of QHD as evidenced by the smaller value of the compression modulus K in QMC. The softening is due to the effective inclusion of the response to the scalar field via the scalar polarizability, as discussed in Section 3.2. Inclusion of the ρ meson appears to undo much of this softening. We do note however that the QMC-I curves still lie within the 2σ bounds.

If we now introduce hyperons to the QMC EOS, as shown in Fig. 5.16 we see a further softening of the EOS. In this case, the addition of the ρ meson does not stiffen the EOS back to the level of the nucleonic EOS, since the ρ contribution is much smaller in the hyperonic case. As shown in Fig. 5.12, the asymmetry between the components of the isodoublets and those of the isotriplet is small, and the ρ contribution is proportional to this asymmetry (refer to Eq. (3.8)). This is an important distinction between the nucleonic and hyperonic EOS.

While the mass-radius relations for these configurations may be incapable of explaining the given observed data of [69], it is clearly a great step forward in that we may now model the effects of hyperons, which was not possible in QHD.

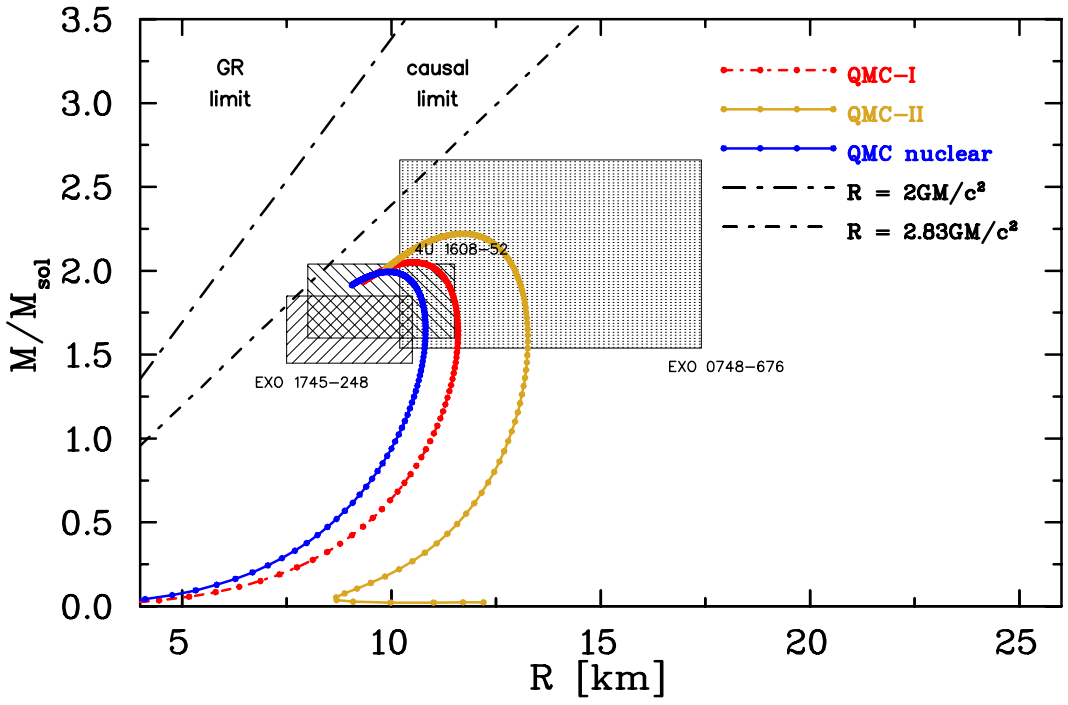

Fig. 5.15: (Color Online) Mass-radius relations for various configurations of nucleonic QMC, with additional features the same as Fig. 5.7. Note that the maximum masses of QMC-I and nuclear QMC stars are much lower than for QHD-I and nuclear QHD, indicating that the QMC EOS is much softer that that of QHD as evidenced by the smaller value of the compression modulus K in QMC.

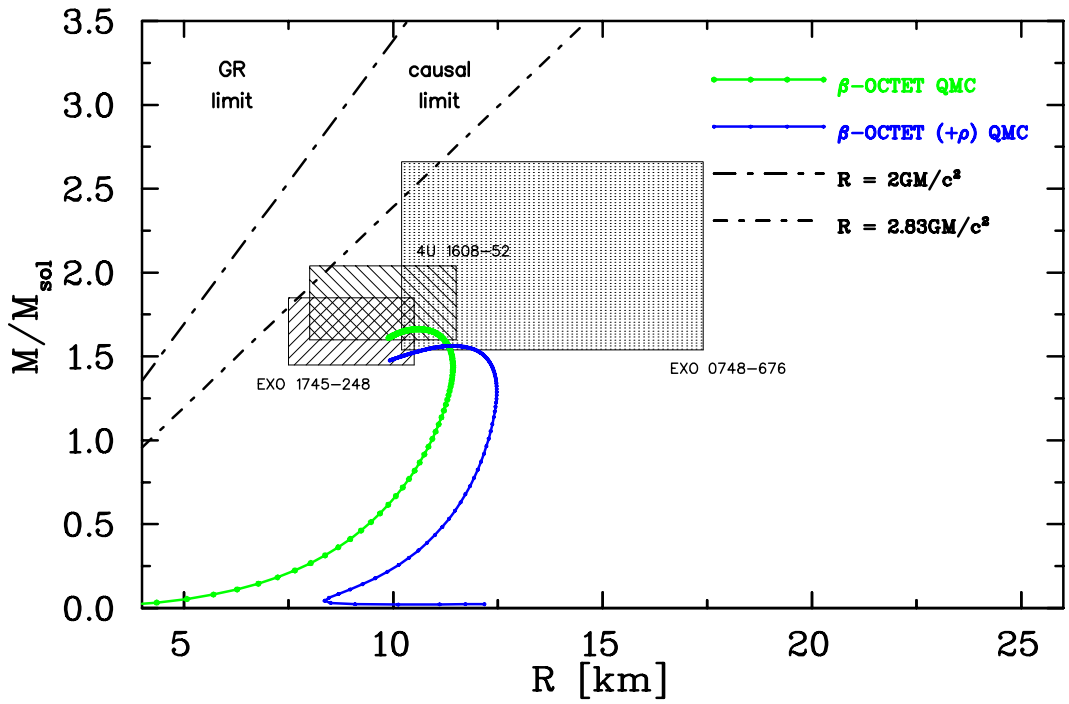

Fig. 5.16: (Color Online) Mass-radius relations for octet QMC-I (as per Fig. 5.14) and QMC-II (as per Fig. 5.12), with additional features the same as Fig. 5.7. Note that the maximum masses of octet QMC-I and octet QMC-II stars are lower than nucleonic QHD-I and nucleonic QHD-II stars, indicating that the octet QMC EOS is softer that that of the nucleonic QHD.

If we consider the case of a star with a central density of $\rho_{\rm central} = 1.2$ fm^{-3} (an arbitrary choice) as shown in Fig. 5.17 for the case of hyperonic QMC, we observe that the outermost 3 km of this 11 km star contains only nucleonic matter (in β-equilibrium). The core of this star contains roughly equal proportions of nucleons, Λ and Ξ hyperons, with a notable lack of Σ hyperons. This is the simplest case for which we produce a stellar object with hyperons, and comprises our simplest method for including a strangeness degree of freedom.

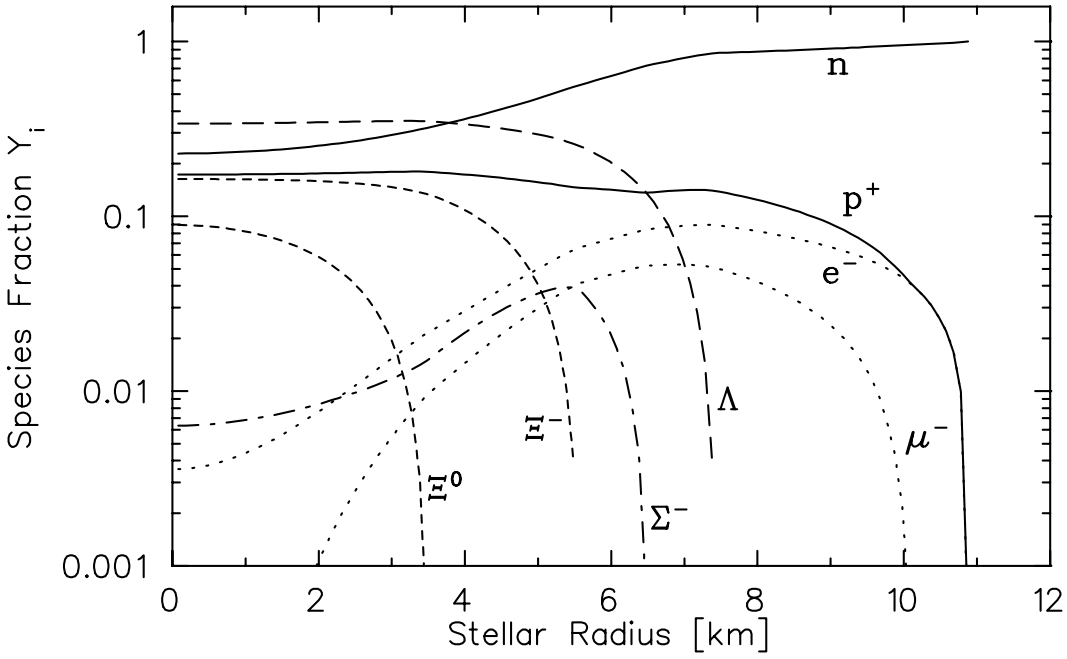

Fig. 5.17: Species fractions for octet QMC in β-equilibrium as a function of stellar radius for a stellar solution with a central density of $\rho_{\rm central} = 1.2$ fm^{-3}. The parameters used here are the same as those used to produce Fig. 5.12. We note that the outermost 3 km of this star contains only nucleons and leptons, with hyperon effects occurring much deeper.

5.3 Hybrid Equation of State

A focus of this work has been to calculate the properties of hybrid stars; involving contributions from both baryons and deconfined quarks in a statistical mechanics method. The process by which we obtain these results has been described in Section 2.9. The results presented in this section have been published by the author [42] as a novel extension of the octet QMC model.

5.3.1 Hybrid Infinite Matter

In Section 3.3 we discussed the MIT bag model for quark matter, in which we model three deconfined free quarks in a Fermi gas possessing constant masses consistent with current quark phenomenology. It is this model that we shall refer to (unless stated otherwise) for hybrid models involving quark matter. The hadronic model we will use in this section is the octet QMC model, unless otherwise specified.

The conditions for a Glendenning-style mixed phase as discussed in Section 2.10 require that for a given pair of μ_n and μ_e (common to the hadronic and quark phases) at any value of the mixing parameter χ, the quark density is greater than the hadronic density. This condition ensures that the total baryon density increases monotonically within the range $\rho_{\rm QP} > \rho_{\rm MP} > \rho_{\rm HP}$, as can be seen in Eq. (2.92). An example of this is illustrated in Fig. 5.18 for a mixed phase of octet QMC and three-flavor quark matter modelled with the MIT bag model.

Recall that the method for evaluating the properties of a mixed phase involves calculating the neutron and electron chemical potentials of the hadronic phase and using these as inputs to the quark phase calculations, providing the quark Fermi momenta via Eq. (3.30). In this case, with the dynamic quark masses of NJL and no vector potentials (self-energies) due to non-interacting quarks, the calculated quark Fermi momentum corresponds a quark density that is lower than the hadronic density, and as a result there are no configurations for a mixed phase in which the proportion of quarks increases while at the same time the total baryon density increases. It may be possible that with smaller constituent quark masses at low density, the Fermi momenta would provide sufficiently high quark densities, but we feel that it would be unphysical to use smaller constituent quark masses. This result implies that —at least for the models we have investigated—dynamical chiral symmetry breaking (in the production of constituent quark masses at low density) prevents a phase transition from a hadronic phase to a mixed phase involving quarks.

We do note, however, that if we restrict consideration to nucleons only within the QMC model (with the same parameters[3] as octet QMC), and represent quark matter with the NJL model, we do in fact find a possible mixed phase. More surprisingly, the density at which a phase transition to the mixed phase occurs for this combination is significantly larger than the case where hyperons are present (in which case we model a transition to MIT bag model quark matter). An example of this is shown in Fig. 5.19, the parameters for which can be found in Table 5.3. This produces a mixed phase at about $4\rho_0$ ($\rho = 0.64$ fm^{-3}) and a pure quark matter phase above about $10\rho_0$ ($\rho = 1.67$ fm^{-3}). In this case the u quark first appears

[3]The couplings of mesons to baryons are defined by the energy per baryon, which saturates at a lower density than the hyperon threshold. We can therefore safely assume that the inclusion or removal of hyperons plays no part in defining the couplings of mesons to the nucleons.

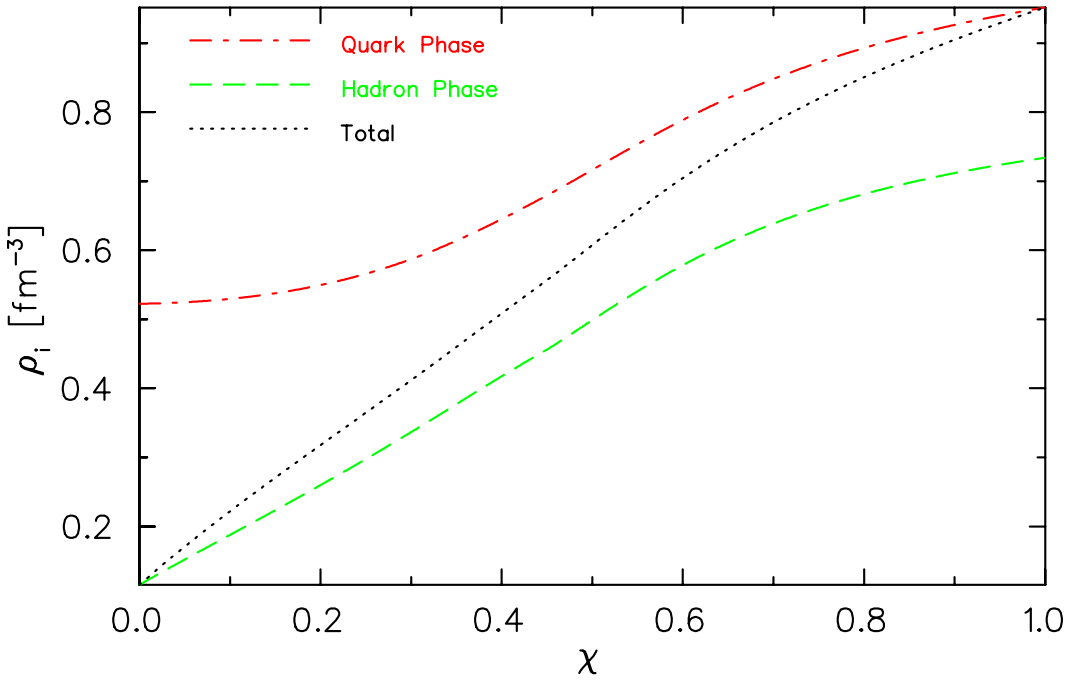

Fig. 5.18: (Color online) Densities in the mixed phase for octet QMC mixed with three-flavor quark matter modelled with the MIT bag model. Note that at all values of χ (the mixing parameter according to Eq. (2.92) which also defines the total density), the equivalent baryon density of quarks is greater than the hadronic baryon density, allowing the total baryon density to increase monotonically with increasing χ. Clearly, at $\chi = 0$ the density corresponds entirely to the hadronic phase, and at $\chi = 1$ the density corresponds entirely to the quark phase. Between these points, the density is that of the mixed phase.

at a higher density than the d or s quarks due to its positive charge which can only be balanced by the other two quarks since the leptons provide a decreasing contribution as per Eq. (2.47), since the proton and neutron densities become more and more similar. Although this example does show a phase transition, the omission of hyperons is certainly unrealistic. This does however illustrate the importance and significance of including hyperons, in that their inclusion alters the chemical potentials which satisfy the equilibrium conditions in such a way that the mixed phase is no longer produced.

Using the MIT bag model, we can calculate the hybrid EOS, which is shown in Fig. 5.20. We can see that at low densities (low energies) all of the configurations of EOS are fairly soft. At the lowest densities, each of the configurations of EOS are approximately equal; at this point they all represent nucleons in β-equilibrium.

For each of the configurations in which we find a phase transition from baryonic matter to quark matter, the EOS consists of negatively charged quark matter, positively charged hadronic matter, and a small proportion of leptons, to produce globally charge-neutral matter. The proportions of hadronic, leptonic and quark matter throughout the mixed phase (for example, during a transition from octet QMC matter to three-flavor quark matter modelled with the MIT bag model) are displayed in Fig. 5.21 in which we note that the quarks are able to satisfy charge neutrality without lepton contributions, in contrast to the cases of nucleonic β-equilibrium in which the lepton contributions remain stable at increasing densities. A

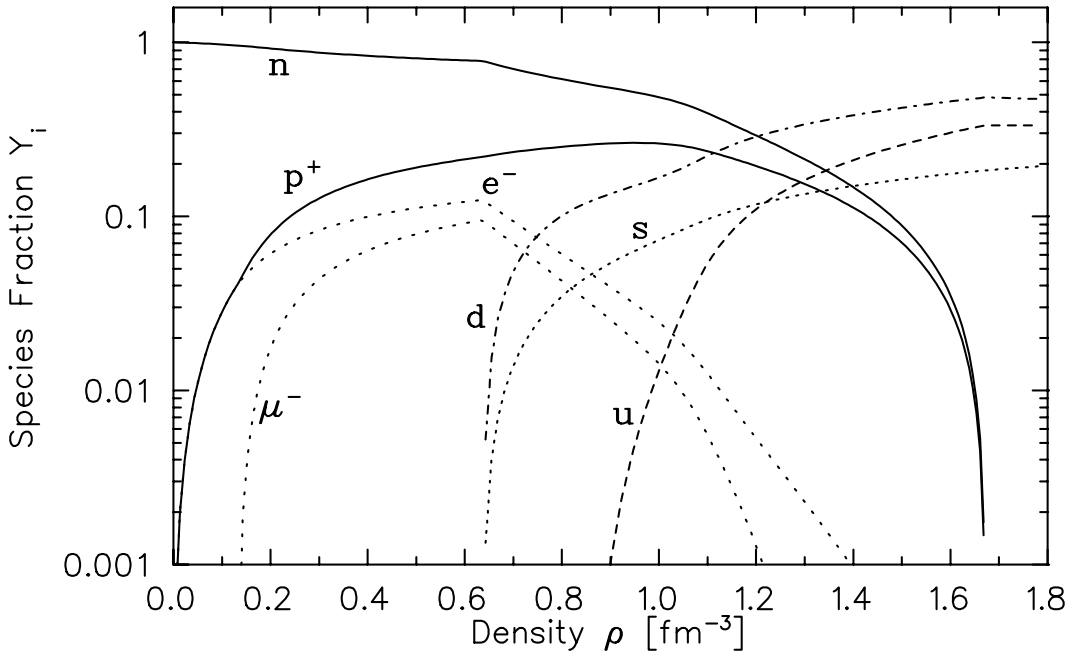

Fig. 5.19: Species fractions for a phase transition from nucleonic QMC matter to three-flavor quark matter modelled with NJL. Note that in this unphysical (we see no physical reason for which hyperons should be neglected) case, a phase transition is possible, and occurs at a value of $\rho = 0.64$ fm^{-3}. In this case the u quark first appears at a higher density than the d or s quarks due to its positive charge which can only be balanced by the other two quarks since the leptons provide a decreasing contribution as per Eq. (2.47).

summary of the results of interest is given in Table 5.3.

Results of calculations for larger quark masses are not shown, as they require a much lower bag energy density to satisfy the pressure equilibrium conditions. For constituent quark masses, we find that no phase transition is possible for any value of the bag energy density, as the quark pressure does not rise sufficiently fast to overcome the hadronic pressure. This is merely because the masses of the quarks do not allow a sufficiently large Fermi momentum at a given chemical potential, according to Eq. (3.30).

When we calculate the EOS including a mixed phase and subsequent pure quark phase, we find that small changes in the parameters can sometimes lead to very significant changes. In particular, the bag energy density B, and the quark masses in the MIT bag model have the ability to both move the phase transition points, and to vary the constituents of the mixed phase. We have investigated the range of parameters which yield a transition to a mixed phase and these are summarized in Table 5.3. For illustrative purposes we show an example of species fractions for a reasonable set of parameters ($B^{1/4} = 180$ MeV and $m_{\mathrm{u,d,s}} = 3, 7, 95$ MeV) in Fig. 5.22. Note that in this case the Λ hyperon enters the mixed phase briefly (and at a low species fraction). Note that the transition density of $\rho_{\mathrm{MP}} \sim 0.22$ fm^{-3} produced by the combination of the octet QMC and MIT bag models in that case seems unlikely to be physical as it implies the presence of deconfined quarks at densities less than $2\rho_0$, which would contradict the results of searches for such entities. A similar transition from nucleonic QMC matter to three-flavor quark matter modelled with the MIT bag model (Fig. 5.19) produces

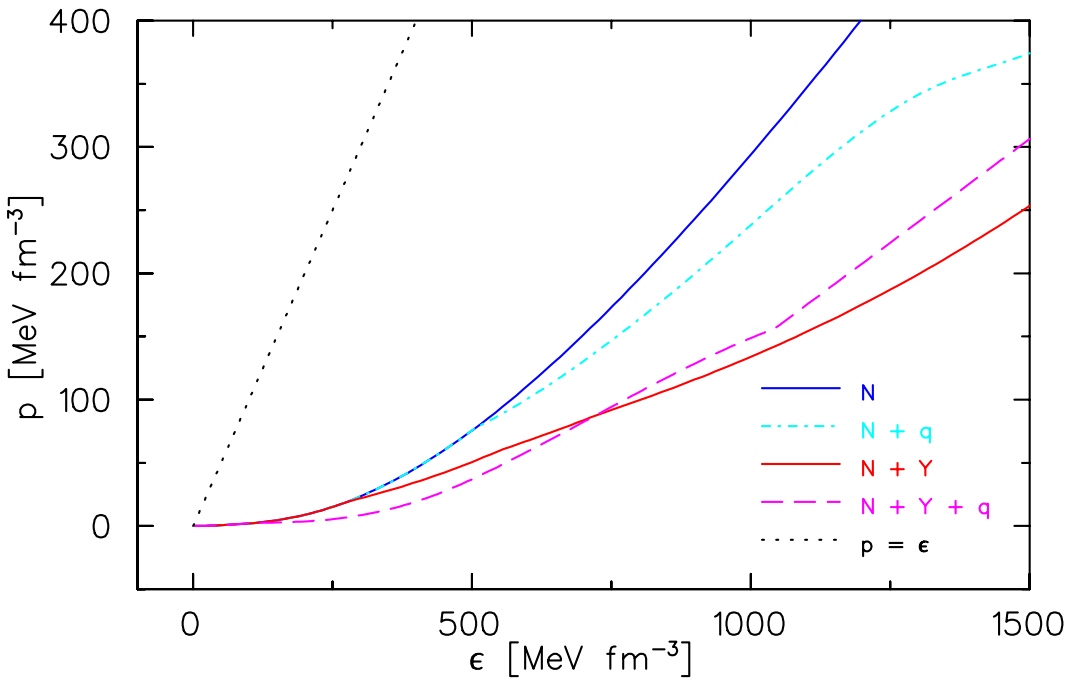

Fig. 5.20: (Color online) Equation of State for; nucleonic 'N' matter modelled with QMC; nucleonic matter where a phase transition to NJL modelled quark matter is permitted; baryonic 'N+Y' matter modelled with octet QMC; and baryonic matter where a phase transition to MIT bag modelled quark matter is permitted. The line $P = \mathcal{E}$ represents the causal limit, $v_{\rm sound} = c$. The bends in these curves indicate a change in the composition of the EOS, such as the creation of hyperons or a transition to a mixed or quark phase. Note that at very low energies (densities) the curves are identical, where only nucleonic matter in β-equilibrium is present.

results almost identical to those of Fig. 5.22, except of course that in that case there is no contribution from the Λ hyperon. We note the significant differences in threshold densities between these two cases.

With small changes to parameters, such as those used to produce Fig. 5.23 in which the bag energy density is given a slightly higher value from that used in Fig. 5.22 ($B^{1/4}$ increased from 180 MeV to 195 MeV, but the quark masses remain the same), it becomes possible for the Ξ hyperons to also enter the mixed phase, albeit in that case with small species fractions, $Y_\Sigma, Y_\Xi \leq 0.02$. This highlights the need for strict tolerances for 'known' values of model parameters.

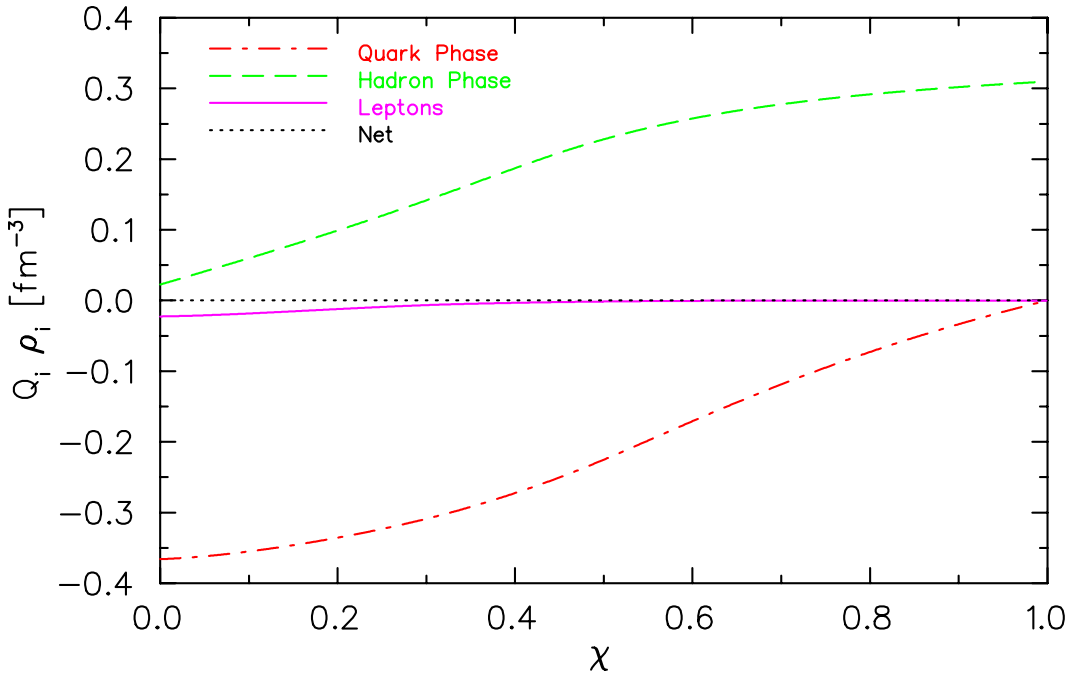

Fig. 5.21: (Color online) Charge-densities (in units of the proton charge per fm^3) in the mixed phase for a transition from octet QMC to three-flavor quark matter modelled with the MIT bag model. The net charge of the mixed phase is exactly zero, as per the constraining equation of Eq. (2.95). Note that following the mixed phase, the quarks are able to satisfy charge neutrality with no leptons, in contrast to the nucleonic cases of β-equilibrium in which the lepton contribution remains stable. χ is the mixing parameter within the mixed phase according to Eq. (2.92).

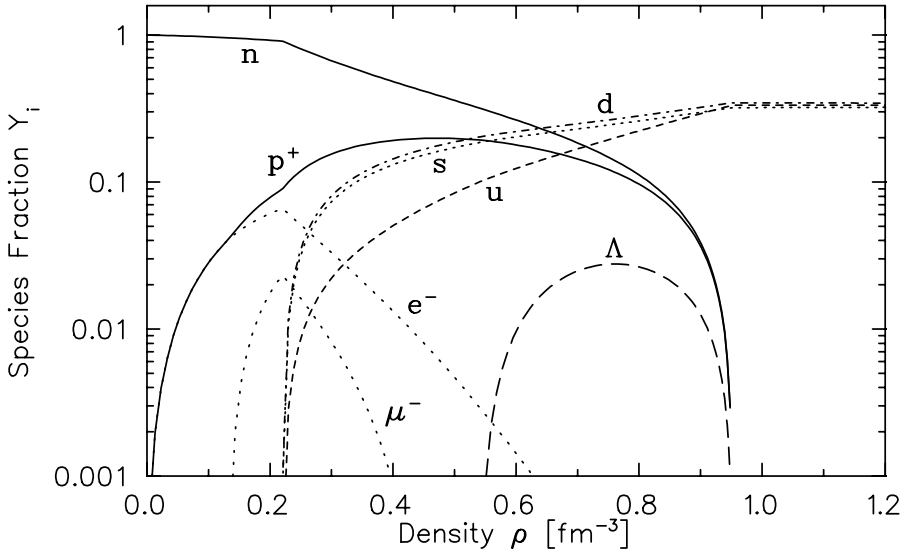

Fig. 5.22: Species fractions Y_i for octet QMC (the same as in Fig. 5.12) but where now we allow the phase transition to a mixed phase involving quark matter modelled with the MIT bag model. Note that the Λ hyperon is the only hyperon to appear in the mixed phase, and does so at a much higher density than the configuration where the transition to a mixed phase is forbidden. A similar transition from nucleonic QMC matter to three-flavor quark matter modelled with the MIT bag model (as shown in Fig. 5.19) produces results almost identical to these, except of course that in that case there is no contribution from the Λ hyperon. We note the significant differences in threshold densities when comparing these results.

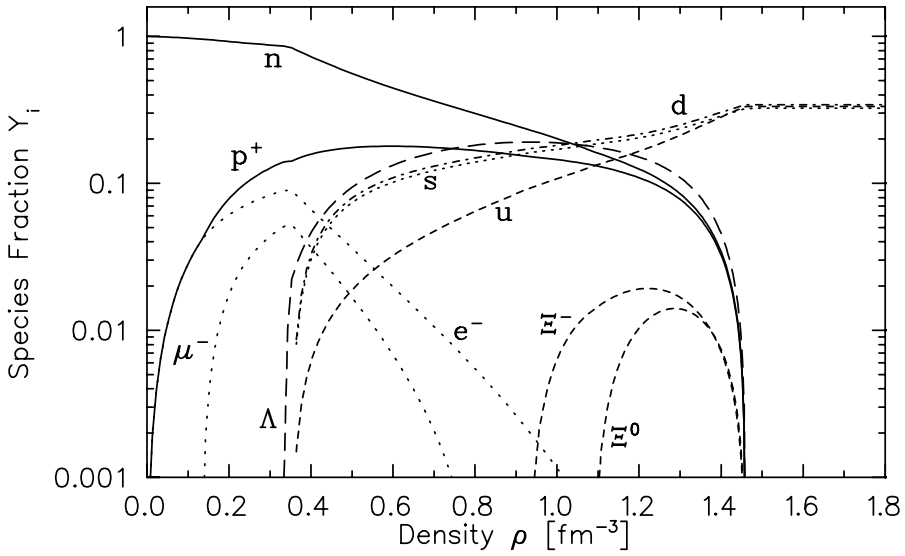

Fig. 5.23: Species fractions, Y_i, for octet QMC (the same as in Fig. 5.22 but now where the bag energy density has been increased to $B^{1/4} = 195$ MeV). Note that now the appearance of hyperons occurs at a smaller density than in the case of Fig. 5.22, the transition to a mixed phase occurs at a slightly larger density, and that now Ξ hyperons are present in the mixed phase.

5.3.2 Hybrid Stars

The stellar solutions for octet QMC hybrid stars (in which a phase transition to a mixed phase is allowed) are shown in Fig. 5.24 along with the baryon-only stellar solutions for comparison. We note that the solutions for configurations involving a phase transition are identical to those where a transition is neglected, up to some value of the central density at which point the solutions diverge. This indicates the lowest mass stars that contain quark matter.

We note that the stellar masses for configurations involving a phase transition to quark matter are lower than those in which the transition is neglected, for the same value of central density. This is due to the softening of the EOS by the introduction of quarks (see Section 2.8). Overall, the stellar masses for these configurations are similar to observed neutron star masses, though notably lower than the masses of the most massive observed neutron stars. This could be attributed to an over-softening of the EOS.

If we consider a star with a central density of $\rho_{\text{central}} = 1.2$ fm^{-3} for octet QMC with a phase transition to quark matter modelled with the MIT bag model (using the same parameters as used in Fig. 5.22) we observe the prediction of 3.5 km of quark core for a star with a radius of 10 km, with only a very small contribution from the hyperons, via Λ, as shown in Fig. 5.25.

If we increase the value of the bag energy density from $B^{1/4} = 180$ MeV as used in Fig. 5.25 to $B^{1/4} = 195$ MeV we find that the radius of a star with a central density of $\rho_{\text{central}} = 1.2$ fm^{-3} increases by around 1 km, but the baryonic contribution (in the mixed phase) is more prolific, as we now find contributions from Λ and Ξ hyperons in the core of the star, along with quark contributions. The effect of this increase in the bag energy can be seen by comparing Fig. 5.25 with Fig. 5.26, where the bag energy densities are $B^{1/4} = 180$ MeV for the former, and $B^{1/4} = 195$ MeV for the latter, and this is the only change that has been made.

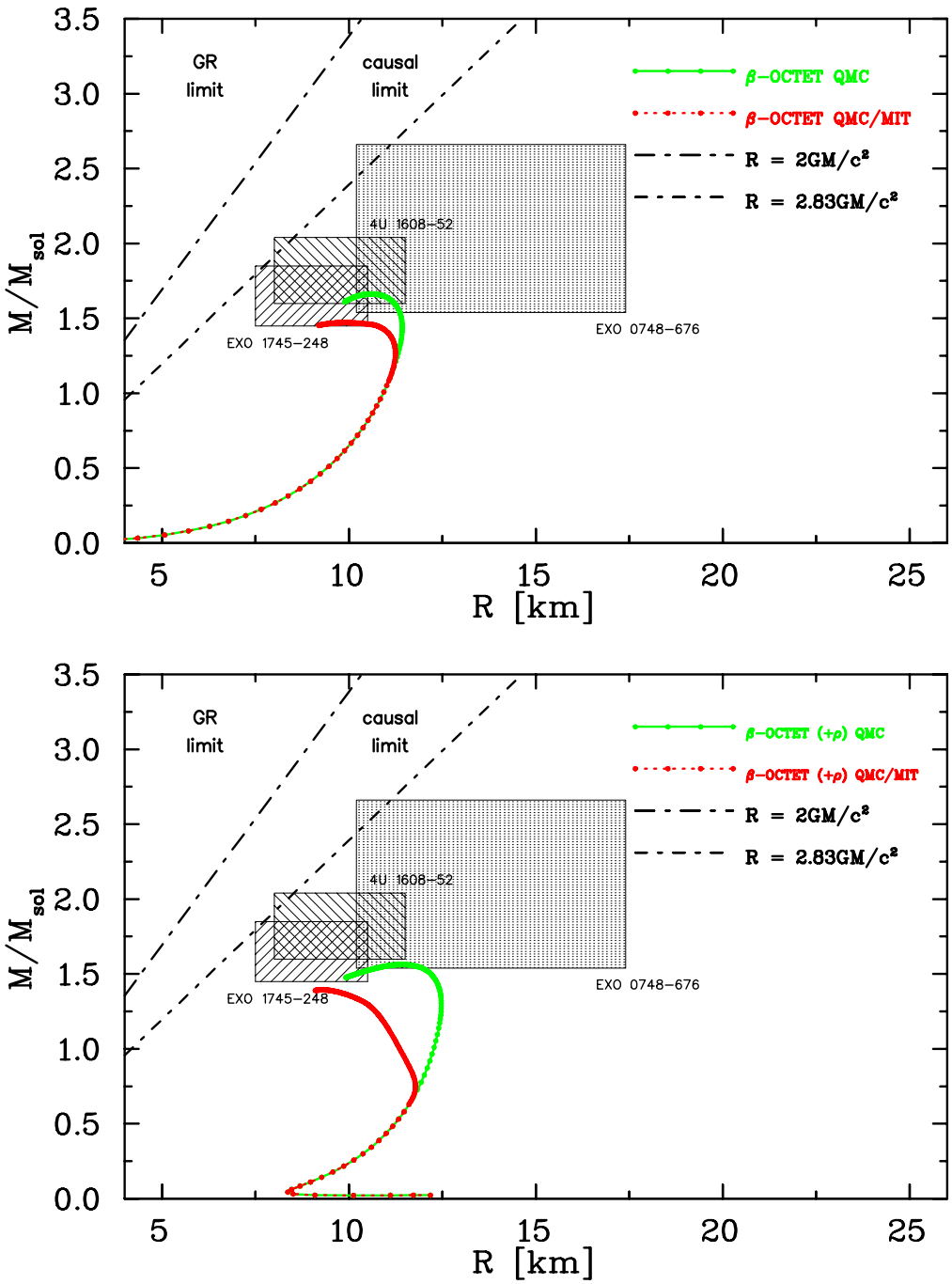

Fig. 5.24: (Color Online) Mass-radius relations for octet QMC in β-equilibrium (neglecting the ρ meson, upper; and including it, lower) for baryonic and hybrid stars. Also shown are the additional features described in Fig. 5.7. Note that the stellar solutions for configurations involving a phase transition are identical to those where the phase transition is neglected, up to some value of the central density at which the solutions diverge. This point corresponds to the lowest density stars which contain quark matter. The stars containing quark matter generally have a lower mass than those which only contain baryonic matter due to a softening of the EOS.

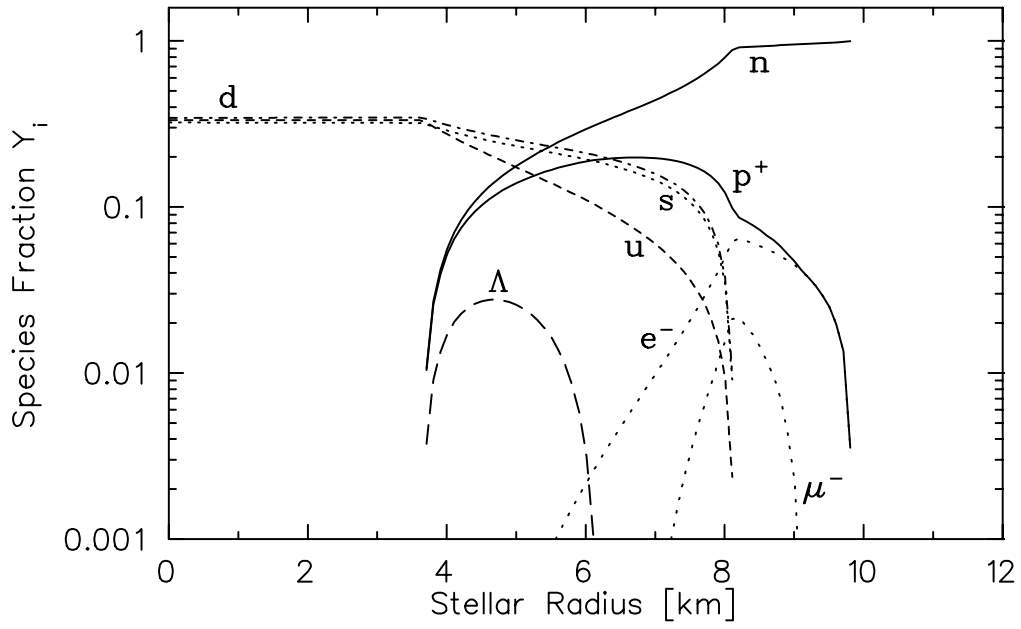

Fig. 5.25: Species fractions for octet QMC with a phase transition to three-flavor quark matter modelled with the MIT bag model, as a function of stellar radius for a stellar solution with a central density of $\rho_{\rm central} = 1.2$ fm^{-3}. The parameters used here are the same as those used to produce Fig. 5.22. Note that in this case one finds pure deconfined three-flavor quark matter at the core (all of some 3.5 km) of this star, and a small proportion of Λ in the mixed phase.

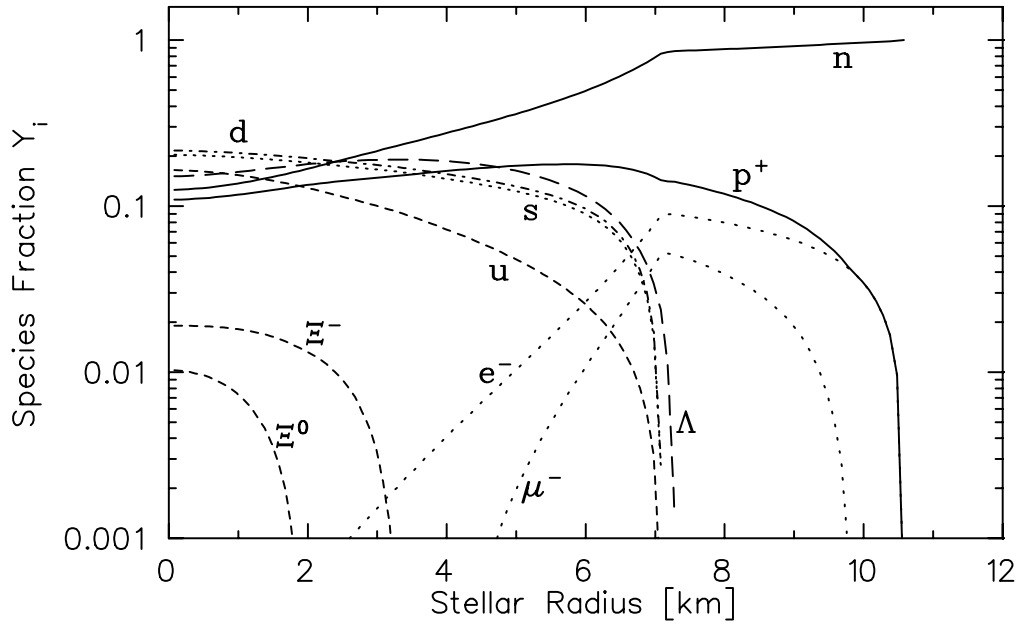

Fig. 5.26: Species fractions for the interior of a star with central density $\rho_{\rm central} = 1.2$ fm^{-3} where the bag energy density is given a slightly higher value from that used in Fig. 5.25 (increased from $B^{1/4} = 180$ MeV to 195 MeV), but the quark masses remain the same.

5.4 Hartree–Fock QHD Equation of State

As discussed in Section 3.5, we can further extend our models by including Fock terms. For comparison purposes, we show the effects of including *only* the Fock contribution to the self-energy, as well as the effects of the full Hartree–Fock calculations (including the medium polarization energy), as compared to the Hartree calculations presented earlier.

The results presented in this section extend the calculations of Ref. [18] in which the properties of Hartree–Fock nuclear matter were calculated *without* β-equilibrium. To the extent of the author's knowledge, the following calculations have not been performed or published elsewhere, and as such are further novel calculations.

For simplicity, we present the extension from Hartree to Hartree–Fock for QHD, though similar calculations can be performed for extending QMC similarly. We leave this as work for the future.

5.4.1 Hartree–Fock QHD Infinite Matter

In Fig. 5.27 we show the saturation curves for nuclear QHD, in which we observe that the saturation properties for each configuration are reproduced accurately, in order to calculate the couplings to be used for each configuration.

We also note from that figure that the curvature for each configuration is different at saturation, implying differences between the compression modulii for each configuration, with Hartree QHD having the largest value for K, and the full Hartree–Fock (Fock2) having the smallest. For comparison, the values are shown in Table 5.2. The softening of this EOS brings the compression modulus for Hartree–Fock QHD closer to the experimental range, though we note that this may further over-soften the EOS since the maximum masses in Hartree QMC appear too small already.

We can examine the effective masses for Hartree–Fock QHD for the case of only including the self-energy Fock terms, and compare these with those for Hartree QHD as shown in Fig. 5.3. The comparison is shown in Fig. 5.28 and we note that the differences are subtle at this stage. The Hartree–Fock data corresponds to two configurations; Fock1 denotes the inclusion of the self-energy Fock contribution, while Fock2 denotes the additional inclusion of the medium polarization energy Fock contribution. In each case, the effective mass is plotted for a limited range of Fermi momenta corresponding to densities up to ~ 0.5 fm^{-3}.

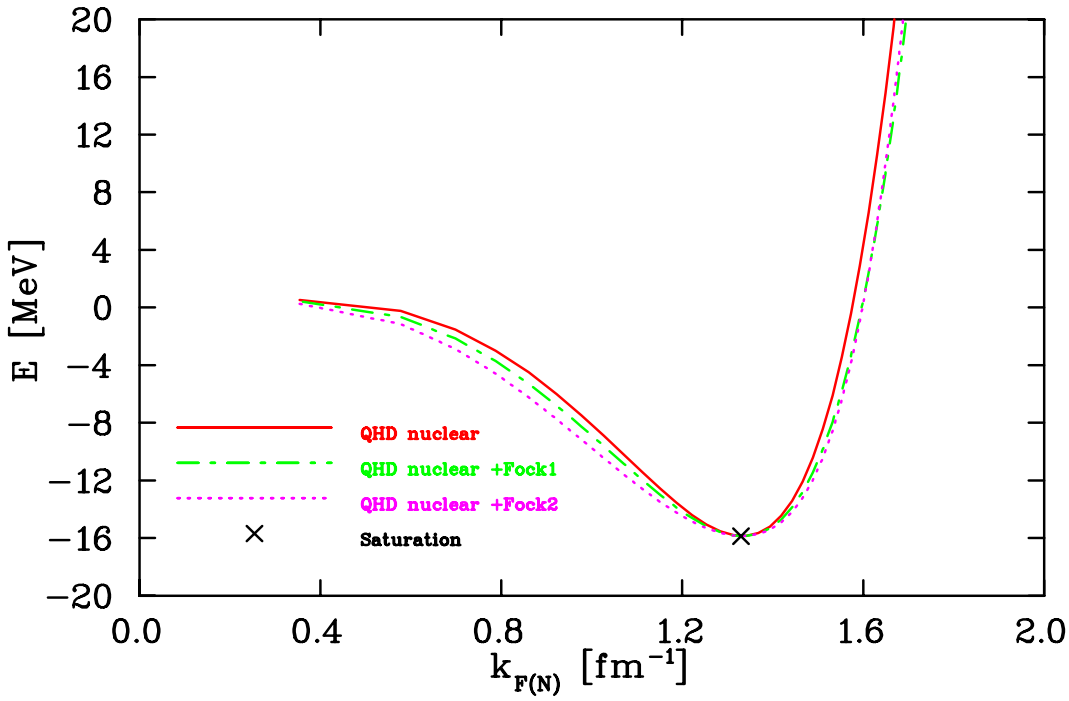

Fig. 5.27: (Color Online) EOS for nuclear QHD matter calculated for three configurations; at Hartree level, including only Fock self-energy terms, and additionally including the medium polarization energy contribution. Couplings for each configuration are found such that saturation properties are reproduced. The values of these couplings can be found in Table 5.2.

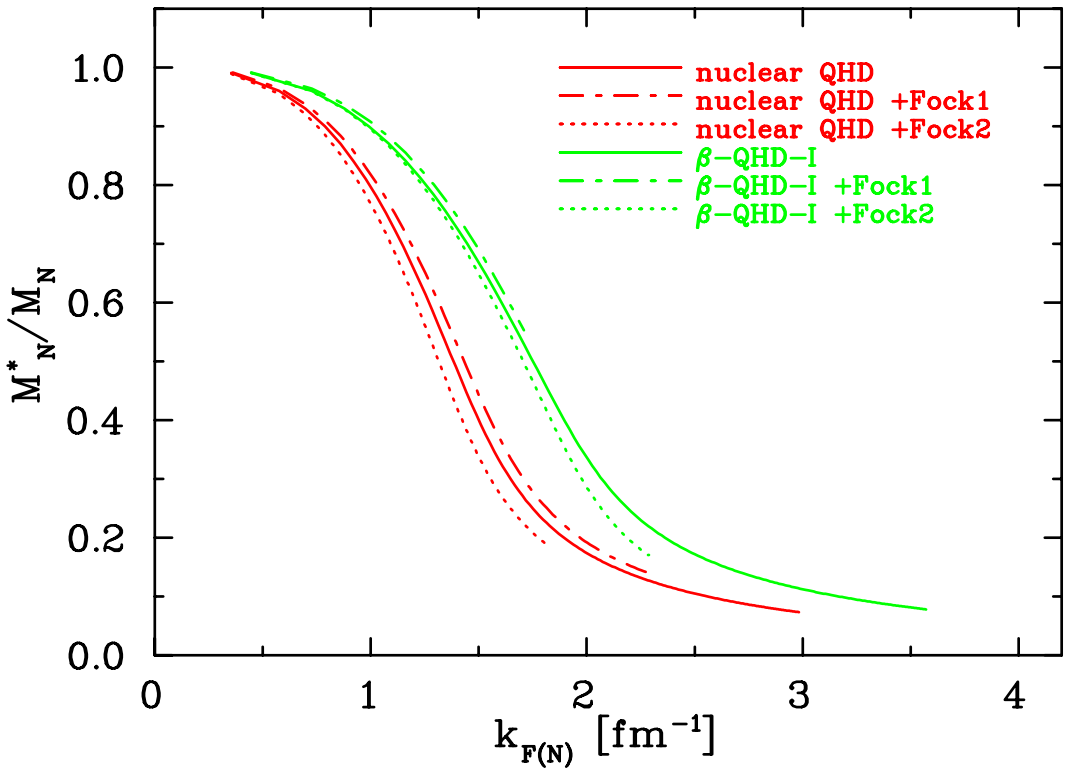

Fig. 5.28: (Color Online) Nucleon effective masses for nuclear QHD and β-equilibrium nucleon QHD-I including Fock contributions to the self-energies (Fock1) and including this term as well as the medium polarization energy contribution (Fock2). The Hartree–Fock contributions are plotted for a limited range of Fermi momenta corresponding to densities up to ~ 0.5 fm^{-3}.

5.4.2 Hartree–Fock QHD Stars

To investigate the effects that the addition of the various Fock terms have on stellar solutions for these EOS, we can solve the TOV equations in each case. Fig. 5.29 shows the mass-radius relations for nucleonic QHD-I with the additional self-energy Fock terms (Fock1) included, in which the couplings used provide a fit to the saturation properties of nuclear matter. For comparison purposes, the same stellar solutions with Fock terms neglected (as per Fig. 5.7) are shown, and we note that the maximum mass is lower when the Fock terms are included, indicating a softening of the EOS.

Since the compression modulus of the full Hartree–Fock configuration (Fock2) for QHD is smaller than than of the Fock1 configuration, we expect that maximum mass calculated with the Fock2 configuration would be lower than those in Fig. 5.29.

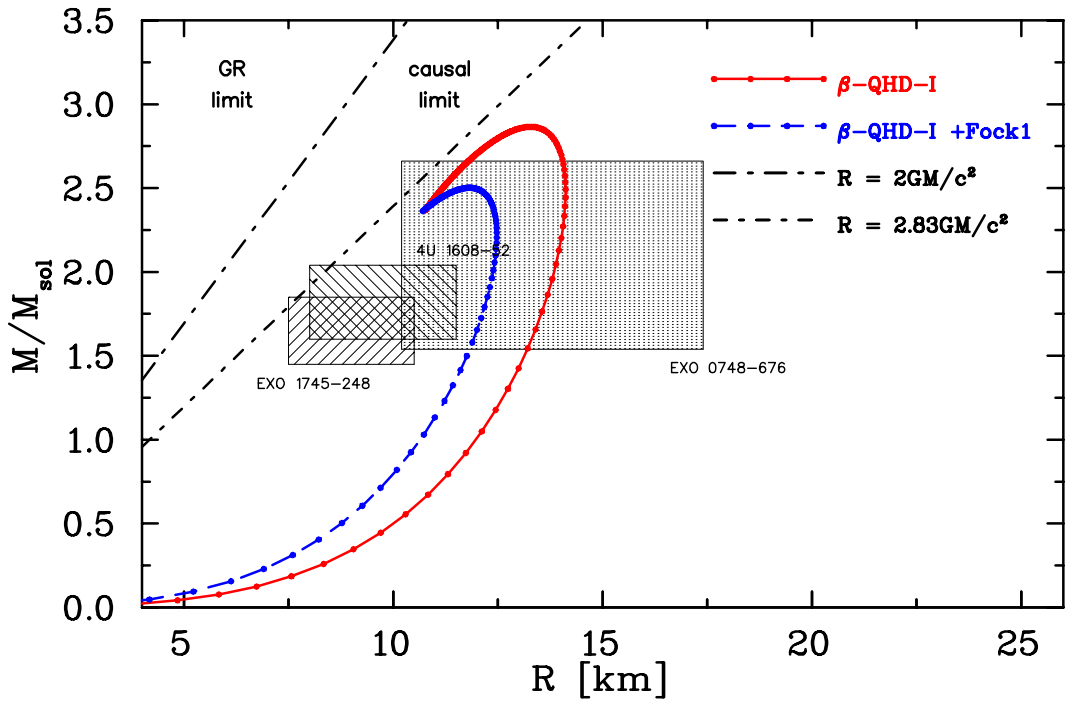

Fig. 5.29: (Color Online) Mass-radius relations for Hartree–Fock QHD-I, in which we have included the self-energy Fock terms. Also shown for comparison are the mass-radius relations of Hartree QHD-I as per Fig. 5.7. We observe that the inclusion of this Fock term softens the EOS, resulting in a reduced maximum stellar mass.

5.5 Summary Tables

The vacuum masses of the baryons, leptons, and mesons used in the calculations for this work are shown in Table 5.1, as per Ref. [17].

The couplings used in each configuration of each model are found such that the nuclear matter configuration reproduces saturation properties (as per Section 2.8). The couplings used for all of the individual configurations of QHD, QMC, and Hartree–Fock QHD are shown in Table 5.2. In the case of Hartree–Fock QHD we show the couplings that reproduce saturation properties for the case of only including the self-energy Fock contribution (denoted Hartree–Fock1), and for the case of including that contribution and additionally the medium-polarization Fock contribution (denoted Hartree–Fock2). The couplings are given to three decimal places to allow comparison between investigations, though more significant figures would be required to exactly reproduce these results.

Table 5.3 contains comparison values for each of the configurations of each model; The input parameters used to calculate each configuration, such as species modelled, and—where applicable—the quark masses and bag energy density; as well as the calculated values for phase transition densities, compression modulii, and effective mass at saturation.

Table 5.1: The vacuum (physical) baryon, lepton, and meson masses (in units of MeV) as used throughout this work [17].

M_p	M_n	M_Λ	M_{Σ^-}	M_{Σ^0}	M_{Σ^+}	M_{Ξ^-}	M_{Ξ^0}
938.27	939.57	1115.68	1197.45	1192.64	1189.37	1321.31	1314.83
	m_σ		m_ω			m_ρ	
	550.0		782.6			775.8	
		m_{e^-}			m_{μ^-}		
		0.51			105.66		

Table 5.2: Baryon-meson couplings for all configurations used in this work, found such that the saturation properties of nuclear matter (as described in Section 2.8) are reproduced. Also shown here are the resultant compression modulii for each configuration (we only need present the isospin symmetric value, as per the definition of K.

Configuration	$g_{N\sigma}$	$g_{N\omega}$	g_ρ	K (MeV)
Hartree QHD	10.644	13.179	6.976	525
Hartree QMC	8.268	8.417	4.167	281
Hartree–Fock1 QHD	10.001	11.819	–	456
Hartree–Fock2 QHD	11.289	14.170	–	366

Table 5.3: Table of species content (N = nucleons, Y = hyperons, ℓ = leptons, q = quarks); inputs ($B^{1/4}$, m_q); and results for octet QMC and quark models presented in this thesis. $\rho_{\rm Y}$, $\rho_{\rm MP}$ and $\rho_{\rm QP}$ represent the density at which hyperons first appear (Λ is the first hyperon to enter in these calculations in all but one configuration; octet QMC-I (Fig. 5.14 where the ρ meson is neglected, in which case the Σ^- is the first hyperon to enter); the density at which the mixed phase begins; and the density at which the quark phase begins, respectively. Figures for selected parameter sets are referenced in the final column. Dynamic NJL quark masses are determined by Eqs. (3.39)–(3.40).

Particles:	$B^{1/4}$ (MeV)	$\{m_u, m_d, m_s\}$ (MeV)	$\rho_{\rm Y}$ (fm^{-3})	$\rho_{\rm MP}$ (fm^{-3})	$\rho_{\rm QP}$ (fm^{-3})	Figure:
N, Y, ℓ, (σ, ω, ρ)	—	—	0.33	—	—	Fig. 5.12
N, Y, ℓ, (σ, ω)	—	—	0.39	—	—	Fig. 5.14
N, Y, ℓ, q, (σ, ω, ρ)	180	{3, 7, 95}	0.54	0.22	0.95	Fig. 5.22
N, Y, ℓ, q, (σ, ω)	180	{3, 7, 95}	0.51	0.36	0.95	—
N, Y, ℓ, q, (σ, ω, ρ)	195	{3, 7, 95}	0.33	0.35	1.46	Fig. 5.23
N, Y, ℓ, q, (σ, ω, ρ)	170	{30, 70, 150}	0.55	0.20	0.87	—
N, Y, ℓ, q, (σ, ω, ρ)	175	{100, 100, 150}	0.41	0.28	1.41	—
N, ℓ, q, (σ, ω, ρ)	180	Dynamic (NJL)	—	0.64	1.67	Fig. 5.19

Conclusions

We have derived and performed calculations for various Quantum Hadrodynamics (QHD) equation of state (EOS) configurations (preliminarily at Hartree level) as a foundation for further work, both reproducing the results of a well-known reference, viz Ref. [18] and extending the model to include β-equilibrium between baryons and leptons. In this model the baryons are treated as effective degrees of freedom and interact with a mean-field of mesons. We have shown that this model is not capable of modelling hyperons due to a breakdown in the assumptions—in particular that the meson potentials are small, an assumption made in order to require the Dirac equation to be defined for this model—and thus we have not pursued this model any further, apart from calculating the stellar solutions; the mass-radius relations.

We have investigated the latest (to date) manifestation of the quark-meson coupling (QMC) model to produce an EOS for nucleonic matter as well as investigations of the inclusion of hyperons to this model, in β-equilibrium with leptons. In this model we include the self-consistent response of the internal quark degrees of freedom to the applied scalar field, allowing the hyperons to be modelled without violating the above assumptions of the Dirac equation that prevent us from calculating hyperon effects in QHD, as evidenced by the fact that the effective baryon masses in QMC—which now include a quadratic scalar-field term —remain positive at all densities. We do note however that other models for hadronic matter exist in which hyperon degerees of freedom become accessible, and in which case a transition from hadronic matter to quark matter becomes possible, e.g. Ref [74]. We have calculated the EOS for various configurations of the models described in this thesis with various values for variable quantities, and calculated constituents of infinite matter for several of these configurations, providing information on the density fractions of various particles in equilibrium. We have investigated the effects that changing various parameters of this model have on these density fractions of particles, as well as the effects of restricting the types of particles modelled with QMC. We note that qualitatively, the relative proportions of the hyperons are in good agreement with other treatments (for example, Ref. [75]) and that we observe expected phenomenology, in particular the suppression of Σ hyperons consistent with hypernuclei studies as noted in Ref. [44]. We have calculated and investigated the stellar solutions for this EOS and compared the mass-radius relations to the current state-of-the-art experimental observations. We have noted the softening of the EOS and the corresponding decrease in the maximum stellar mass, which we attribute to the increase in the number of degrees of freedom (both due to the hyperons, and more fundamentally, to the inclusion of baryon structure) over which the Fermi momenta may be shared.

By performing the above calculations for both QHD and QMC, we have investigated the effect of introducing the quadratic term in the QMC effective masses, as compared to the linear form of the effective mass in QHD. The effect is highly non-trivial, as can be inferred by the change to the couplings that reproduce saturation properties for nucleonic matter alone. More importantly, and as noted above, the inclusion of strangeness degrees of freedom via the hyperons is a profound difference between these models.

We have produced several EOS that simulate a phase transition from octet QMC modelled hadronic matter, via a continuous Glendenning style mixed phase to a pure, deconfined quark

matter phase via a mixed phase containing some fractions of hadronic and quark matter. We believe that this should correspond to a reasonable description of the relevant degrees of freedom in each density region. We have performed investigations using the MIT bag model as a preliminary model for deconfined quark matter, as well as investigations of the Nambu–Jona-Lasinio (NJL) model for quark matter. The NJL model is more sophisticated than the MIT bag model, in that it incorporates a mechanism for simulating dynamical chiral symmetry breaking (DCSB), while the MIT bag model assumes constant current quark masses. We have shown that in the NJL scenario of DCSB the relevant chemical potential relations prevent a transition from hadronic matter modelled with either QHD or QMC to quark matter modelled with NJL in which the total baryon density increases with increasing quark content. Further investigations need to be performed in order to make any final conclusions from this, but in any case this is a particularly interesting result. Both cases of phase transitions from octet QMC matter to quark matter are novel calculations not otherwise published by any other researcher to the best of the author's knowledge.

We have thus shown that the models considered here reveal some important clues to the possible nature of dense nuclear matter. It appears that if dynamical chiral symmetry does indeed result in typical constituent quark masses in low density quark matter, then a phase transition from hadronic matter to quark matter is unlikely. This result invites further investigation, particularly in the quark matter phase with the goal of describing deconfined quarks in a manner fundamentally consistent with QCD, but also in the hadronic phase where—as we have shown—too-wide a range of model parameters are consistent with experimental observations. Once again, a future goal should involve a description of hadronic matter fundamentally consistent with QCD.

As a further extension to QHD, we have derived and calculated properties of Hartree–Fock QHD infinite matter and stellar solutions. We have investigated the effects of including only the corrections to the baryon self-energies as a method of increasing the sophistication of the model, as well as including also the corrections due to the medium polarization of baryons. Further work would include extensions of QMC to this sophistication, as well as investigations of the effects of the ρ and π mesons in Hartree–Fock QHD and QMC. The calculations performed for Hartree–Fock QHD in β-equilibrium are to the extent of the author's knowledge novel calculations not otherwise published, and will be published by the author in an upcoming article.

Of particular interest, the methods used here to solve the non-linear self-consistent integral equations required in Hartree–Fock QHD (viz, Aitken-improved Steffensen's Method) appear to be of a much greater sophistication than previous efforts, in particular that the equations are solved in full without introducing approximations such as linearization, as was the case in Ref. [76]. This is of academic interest in that we have produced a suitable, reliable method for performing these calculation in full, particularly given that—as we have shown—a simpler treatment (Newton's Method) fails for this system of equations.

The multiple-phase EOS demonstrate the complexity and intricacy of the models, as well as the dependence on small changes in parameters. The mass-radius relations predicted by the multiple-phase EOS calculations provide overlap with the current experimentally acceptable range, though the range of masses predicted is not yet able to reproduce all currently observed stellar masses. The range of predicted stellar radii are consistent with the current observational data. This is a non-trivial result, especially when one considers the scale over which we are investigating; the range of predicted radii for the most sophisticated models

in this work (for example, that used to produce Fig. 5.29) provides no predictions above twice the observed range of radii of the stars in question, yet the radius of an average main sequence star, such as our sun for example, is eight orders of magnitude larger. While this is some concession, unfortunately it is one shared by most radius predictions of stellar matter, most models for which produce stellar masses and radii that are at least order-of-magnitude consistent with observation.

The couplings of the baryons to mesons used throughout this work (as summarized in Table 5.2) have been found such that the EOS in which they are used reproduces the properties of saturated nuclear matter with the appropriate value of the energy per baryon, and occurring at the appropriate value of saturation density. These couplings are dependent on the exact specifications of the model in question, and as such are difficult to compare between treatments. In the defining study of QHD [18] the authors utilise charge symmetry for the nucleons, and thus the nucleons have a degenerate mass. This is not the case in our work, and the distinction is an important one, as neglecting charge symmetry allows us to appropriately model leptons as well as baryons. We remind the reader that these couplings are only applicable to reproducing the values of saturation properties quoted in this text, and that the use of different values will result in different coupling constants. The saturation properties used in the above reference are slightly different to those used in this work, but nonetheless, our values for the couplings of the nucleons to the mesons are suitably consistent with that reference.

According to the SU(6) quark model described in Sec. 2.12, the coupling of the nucleons to the ρ meson should relate to the coupling of the nucleons to the ω meson in a ratio of $g_\rho : g_{N\omega} = 1 : 3$. As stated in that section though, rather than using the SU(6) relations for the ρ meson we determine the ρ coupling to the nucleons via the symmetry energy a_4 as per Eq. (2.74). For both QHD and QMC, the ρ coupling g_ρ (when determined such that the particular value of $a_4 = 32.5$ MeV is reproduced) is closer to $g_{N\omega}/2$. This is intimately linked to the particular value of a_4 that is to be reproduced, as well as the values of saturation properties used to determine $g_{N\omega}$. As can be seen by comparing the values in Table 5.2, the model in question has considerable impact on the couplings that reproduce the desired properties, the cause of which is that the couplings appear in many times in many equations in highly non-linear fashions. A small change to the value of a baryon-meson coupling alters the meson potential, which in turn alters the effective masses and chemical potentials, which in turn alter the energy per baryon, and thus the saturation properties that constrain the couplings. Likewise, a change to the functional form of the effective mass (such as the difference between QHD and QMC) introduces similar alterations, and thus model-dependent couplings are essential.

A comparison between the compression modulii of various models and configurations has been made, and the range of values compared to the literature; viz the experimental range noted in Ref. [18] of $K = 200$–300 MeV. While Hartree QHD appears to produce a value corresponding to an EOS which is too stiff (K too large), QMC produces one at the upper bound of this range. This is somewhat in contradiction with experiment due to the concept that stiffness of an EOS is related to the maximum mass of a compact object modelled with that EOS; although the QHD stellar solutions include compact objects with masses in excess of much of the observed data of [69–71][1], the QMC EOS—while adequately reproducing the

[1] As examples only; none of the models here are able to reproduce the masses of the largest observed neutron stars/pulsars, though we do not necessarily conclude that this invalidates any of our calculations

value for compression modulus—results in stellar solutions with a maximum mass that are only just consistent with the range of observed data. The hybrid star stellar solutions (while these configurations do not alter the value of compression modulus) provide even smaller maximum masses, and one might conclude from this that the hybrid QMC EOS is 'too soft'. Herein lies our contradiction; how can any EOS simultaneously reproduce the data for compression modulus and yet produce stellar solutions with masses approaching 2.2 $M_{\odot}$, the masses of the largest observed pulsars? As an example of the observational data for pulsars we show the range from Ref. [77] of observed pulsar masses in Fig. 6.1. We note that in this case the largest observed mass is roughly 2.2 $M_{\odot}$, while many of these observations are consistent with our results. We do however reiterate that the predictions of our calculations correspond to static, spherically symmetric (non-rotating) compact objects, whereas observed pulsars are, by their definition rotating, and thus we caution a direct comparison between theory and experiment in this case.

We must take further caution when comparing the results of our numerical calculations with current experimental observations due to the limitations imposed by the extraordinary challenge of measuring the radius of an object over galactic distance scales. The current state-of-the-art measurement techniques used for determining the radii of these objects (such

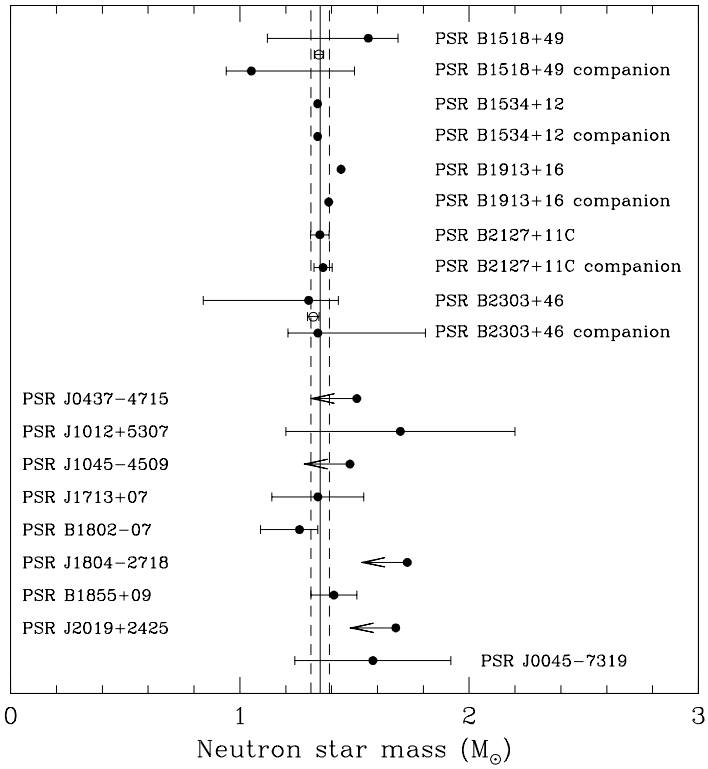

Fig. 6.1: Observed pulsar masses from Ref. [77] in which we note that the largest observed mass is 2.2 $M_{\odot}$. Many results of our calculations are consistent with much of this data, though we caution a direct comparison between the models used in this work and observed compact stellar objects, for reasons discussed in the text.

as X-ray burst timing measurements) are still undergoing development, and recent analyses of the errors introduced by the models used to determine the observational data for the most prominent bounds has shown that much remains poorly understood [78]. Until these measurements become sufficiently discriminating to the point at which we can exclude particular EOS based on their mass and radius predictions, we continue to focus our attention on improving our models of the EOS.

We note that the inclusion of the self-energy and medium polarization Fock terms to nucleonic QHD provides a softening of the EOS which appears to further lower the maximum mass of compact stellar objects modelled with such an EOS. While this may appear to be a detriment to this model, we reserve any conclusions about the validity of such contributions until we are able to perform full calculations with more complete additions; in particular the inclusions of hyperons, ρ and π mesons, and for modelling QMC. We note that the compression modulus for Hartree–Fock QHD is in better agreement with the literature value than Hartree QHD, indicating an improvement to the original model, though it is overly simplistic to use this single variable as a test of the model's validity. Further improvements to the model based on more sophisticated physics should be undertaken regardless of the experimental constraints.

We have shown that the omission of hyperons in the QMC model yields a transition to a mixed phase of either NJL or MIT bag model quark matter, as the hadronic EOS is no longer overly soft and the chemical potential relations for the two phases are such that the transition can still occur for constituent quark masses. This observation makes clear that hyperons have a significant role to play in the EOS. We do however acknowledge that their presence in neutron stars remains speculative, since no observables are explicitly dependent on the strangeness content of the system. We admit the possibility that there may be some unknown mechanism that prevents the production of hyperons in such a system, and as such we have investigated the possible effects that this may have on the EOS and stellar solutions.

The results presented in Figs. 5.24 and 5.29 indicate that the most sophisticated models presented in this work (in their current forms) are unable to reproduce sufficiently massive neutron stars to account for all observations, notably the largest observed stellar masses. This appears to be a direct result of the softness of the EOS. This issue will be explored in a future publication via the inclusion of Fock terms to QMC, which we have shown to have an effect on the softness of an EOS, in our case for QHD. We also note that other studies have shown a strong link between Fock terms and the scalar and vector potentials [66] which indicate that the effects are non-negligible.

Many open questions remain to be investigated in further work, including further investigations into the effects of Fock terms, and the density dependence of the bag energy density in the quark phase, which can be calculated explicitly within the NJL model. The quark matter models used here are still not the most sophisticated models available, and further work may involve an investigation of the effects of color-superconducting quark matter [79, 80].

Bibliography

[1] D. J. Gross and F. Wilczek, *Asymptotically Free Gauge Theories. 1*, *Phys. Rev.* **D8** (1973) 3633–3652.

[2] W. Baade and F. Zwicky, *Remarks on super-novae and cosmic rays*, *Phys. Rev.* **46** (Jul, 1934) 76–77.

[3] J. Chadwick, *Possible Existence of a Neutron*, *Nature* **129** (1932) 312.

[4] J. M. Lattimer and M. Prakash, *Neutron Star Structure and the Equation of State*, *Astrophys. J.* **550** (2001) 426 [astro-ph/0002232].

[5] H. Heiselberg and M. Hjorth-Jensen, *Phases of dense matter in neutron stars*, *Phys. Rept.* **328** (2000) 237–327 [nucl-th/9902033].

[6] F. Weber, *Strange quark matter and compact stars*, *Prog. Part. Nucl. Phys.* **54** (2005) 193–288 [astro-ph/0407155].

[7] J. Schaffner-Bielich, *Strange quark matter in stars: A general overview*, *J. Phys.* **G31** (2005) S651–S658 [astro-ph/0412215].

[8] F. Weber and M. K. Weigel, *Neutron star properties and the relativistic nuclear equation of state of many baryon matter*, *Nucl. Phys.* **A493** (1989) 549–582.

[9] S. A. Chin and J. D. Walecka, *An Equation of State for Nuclear and Higher-Density Matter Based on a Relativistic Mean-Field Theory*, *Phys. Lett.* **B52** (1974) 24.

[10] P. Danielewicz, R. Lacey and W. G. Lynch, *Determination of the equation of state of dense matter*, *Science* **298** (2002) 1592–1596 [nucl-th/0208016].

[11] A. Worley, P. G. Krastev and B.-A. Li, *Nuclear constraints on the momenta of inertia of neutron stars*, 0801.1653.

[12] P. Podsiadlowski *et. al.*, *The Double Pulsar J0737–3039: Testing the Neutron Star Equation of State*, *Mon. Not. Roy. Astron. Soc.* **361** (2005) 1243–1249 [astro-ph/0506566].

[13] H. Grigorian, D. Blaschke and T. Klahn, *Compact star constraints on the high-density EoS*, astro-ph/0611595.

[14] T. Klahn *et. al.*, *Modern compact star observations and the quark matter equation of state*, *Phys. Lett.* **B654** (2007) 170–176 [nucl-th/0609067].

[15] J. M. Lattimer and M. Prakash, *The physics of neutron stars*, astro-ph/0405262.

[16] J. W. T. Hessels, S. M. Ransom, I. H. Stairs, P. C. C. Freire, V. M. Kaspi and F. Camilo, *A Radio Pulsar Spinning at 716 Hz*, *Science* **311** (2006), no. 5769 1901–1904 [astro-ph/0601337].

[17] **Particle Data Group** Collaboration, C. Amsler *et. al.*, *Review of particle physics*, *Phys. Lett.* **B667** (2008) 1.

[18] B. D. Serot and J. D. Walecka, *The Relativistic Nuclear Many Body Problem*, *Adv. Nucl. Phys.* **16** (1986) 1–327.

[19] G. B. Alaverdyan, *Relativistic Mean-Field Theory Equation of State of Neutron Star Matter and a Maxwellian Phase Transition to Strange Quark Matter*, 0907.4150.

[20] V. Greco, M. Colonna, M. Di Toro, G. Fabbri and F. Matera, *Asymmetric nuclear matter in a Hartree–Fock approach to nonlinear QHD*, *Phys. Rev.* **C64** (2001) 045203 [nucl-th/0011033].

[21] H. Uechi, *Properties of nuclear and neutron matter and thermodynamic consistency in a nonlinear mean-field approximation*, *Nucl. Phys.* **A780** (2006) 247–273 [nucl-th/0604026].

[22] D. P. Menezes and C. Providencia, *rho -omega mixing in the nonlinear Walecka model*, *Phys. Rev.* **C66** (2002) 015206.

[23] C. D. Roberts and A. G. Williams, *Dyson-Schwinger equations and their application to hadronic physics*, *Prog. Part. Nucl. Phys.* **33** (1994) 477–575 [hep-ph/9403224].

[24] M. B. Tsang *et. al.*, *Constraints on the density dependence of the symmetry energy*, *Phys. Rev. Lett.* **102** (2009) 122701 [0811.3107].

[25] H. Muller and B. D. Serot, *Phase transitions in warm, asymmetric nuclear matter*, *Phys. Rev.* **C52** (1995) 2072–2091 [nucl-th/9505013].

[26] N. K. Glendenning, *Phase transitions and crystalline structures in neutron star cores*, *Phys. Rept.* **342** (2001) 393–447.

[27] A. Bhattacharyya, I. N. Mishustin and W. Greiner, *Deconfinement Phase Transition in Compact Stars : Maxwell vs. Gibbs Construction of the Mixed Phase*, 0905.0352.

[28] F. Reif, *Fundamentals of Statistical and Thermal Physics (Fundamentals of Physics)*. McGraw-Hill Higher Education, January, 1965.

[29] J. R. Oppenheimer and G. M. Volkoff, *On Massive neutron cores*, *Phys. Rev.* **55** (1939) 374–381.

[30] J. M. Lattimer and B. F. Schutz, *Constraining the Equation of State with Moment of Inertia Measurements*, *Astrophys. J.* **629** (2005) 979–984 [astro-ph/0411470].

[31] B. J. Owen, *Maximum elastic deformations of compact stars with exotic equations of state*, *Phys. Rev. Lett.* **95** (2005) 211101 [astro-ph/0503399].

[32] T. A. Rijken, V. G. J. Stoks and Y. Yamamoto, *Soft-core hyperon nucleon potentials*, *Phys. Rev.* **C59** (1999) 21–40 [nucl-th/9807082].

[33] B. Sakita and K. C. Wali, *Relativistic formulation of the SU(6) symmetry scheme*, *Phys. Rev.* **139** (1965) B1355–B1367.

[34] F. Gürsey, A. Pais and L. A. Radicati, *Spin and unitary spin independence of strong interactions*, *Phys. Rev. Lett.* **13** (Aug, 1964) 299–301.

[35] T. M. Aliev, A. Özpineci and M. Savc ı, *Meson-baryon couplings and the f/d ratio in light cone qcd*, *Phys. Rev. D* **64** (Jun, 2001) 034001.

[36] S. Ishida and P. Roman, *Static su*(6) *and fundamental substitution*, *Phys. Rev.* **172** (Aug, 1968) 1684–1693.

[37] M. H. Johnson and E. Teller, *Classical Field Theory of Nuclear Forces*, *Phys. Rev.* **98** (1955) 783–787.

[38] H.-P. Duerr, *Relativistic Effects in Nuclear Forces*, *Phys. Rev.* **103** (1956) 469–480.

[39] J. D. Walecka, *A theory of highly condensed matter*, *Annals Phys.* **83** (1974) 491–529.

[40] R. J. Furnstahl and B. D. Serot, *Quantum hadrodynamics: Evolution and revolution*, *Comments Nucl. Part. Phys.* **2** (2000) A23–A45 [nucl-th/0005072].

[41] H. Muller and B. K. Jennings, *Nuclear matter properties of the modified quark-meson coupling model*, *Nucl. Phys.* **A626** (1997) 966–986 [nucl-th/9706049].

[42] J. D. Carroll, D. B. Leinweber, A. G. Williams and A. W. Thomas, *Phase Transition from QMC Hyperonic Matter to Deconfined Quark Matter*, 0809.0168.

[43] E. D. Bloom *et. al.*, *High-Energy Inelastic e p Scattering at 6-Degrees and 10- Degrees*, *Phys. Rev. Lett.* **23** (1969) 930–934.

[44] J. Rikovska-Stone, P. A. M. Guichon, H. H. Matevosyan and A. W. Thomas, *Cold uniform matter and neutron stars in the quark-meson-coupling model*, *Nucl. Phys.* **A792** (2007) 341–369 [nucl-th/0611030].

[45] P. A. M. Guichon, K. Saito, E. N. Rodionov and A. W. Thomas, *The role of nucleon structure in finite nuclei*, *Nucl. Phys.* **A601** (1996) 349–379 [nucl-th/9509034].

[46] H. Friedrich, *Theoretical Atomic Physics (3^{rd} Edition)*. Birkhäuser, 2006.

[47] P. A. M. Guichon, *A Possible Quark Mechanism for the Saturation of Nuclear Matter*, *Phys. Lett.* **B200** (1988) 235.

[48] A. W. Thomas, P. A. M. Guichon, D. B. Leinweber and R. D. Young, *Towards a connection between nuclear structure and QCD*, *Prog. Theor. Phys. Suppl.* **156** (2004) 124–136 [nucl-th/0411014].

[49] M. Ericson and G. Chanfray, *Scalar field and QCD constraints in Nuclear Physics*, *AIP Conf. Proc.* **1030** (2008) 13–22 [0804.1683].

[50] E. Massot and G. Chanfray, *Relativistic Chiral Hartree–Fock description of nuclear matter with constraints from nucleon structure and confinement*, *Phys. Rev.* **C78** (2008) 015204 [0803.1719].

[51] G. Chanfray, M. Ericson and P. A. M. Guichon, *Scalar susceptibility and chiral symmetry restoration in nuclei*, *Phys. Rev.* **C68** (2003) 035209 [nucl-th/0305058].

[52] P. A. M. Guichon and A. W. Thomas, *Quark structure and nuclear effective forces*, *Phys. Rev. Lett.* **93** (2004) 132502 [nucl-th/0402064].

[53] P. A. M. Guichon, H. H. Matevosyan, N. Sandulescu and A. W. Thomas, *Physical Origin of Density Dependent Force of the Skyrme Type within the Quark Meson Coupling Model*, *Nucl. Phys.* **A772** (2006) 1–19 [nucl-th/0603044].

[54] P. A. M. Guichon, A. W. Thomas and K. Tsushima, *Binding of hypernuclei in the latest quark-meson coupling model*, *Nucl. Phys.* **A814** (2008) 66–73 [0712.1925].

[55] W. Bentz and A. W. Thomas, *The stability of nuclear matter in the Nambu-Jona-Lasinio model*, *Nucl. Phys.* **A696** (2001) 138–172 [nucl-th/0105022].

[56] Y. Nambu and G. Jona-Lasinio, *Dynamical model of elementary particles based on an analogy with superconductivity. I*, *Phys. Rev.* **122** (1961) 345–358.

[57] G. Hellstern, R. Alkofer and H. Reinhardt, *Diquark confinement in an extended NJL model*, *Nucl. Phys.* **A625** (1997) 697–712 [hep-ph/9706551].

[58] D. Ebert, T. Feldmann and H. Reinhardt, *Extended NJL model for light and heavy mesons without q anti-q thresholds*, *Phys. Lett.* **B388** (1996) 154–160 [hep-ph/9608223].

[59] I. C. Cloet, W. Bentz and A. W. Thomas, *Spin-dependent structure functions in nuclear matter and the polarized EMC effect*, *Phys. Rev. Lett.* **95** (2005) 052302 [nucl-th/0504019].

[60] I. C. Cloet, W. Bentz and A. W. Thomas, *EMC and polarized EMC effects in nuclei*, *Phys. Lett.* **B642** (2006) 210–217 [nucl-th/0605061].

[61] K. Saito, K. Tsushima and A. W. Thomas, *Variation of hadron masses in finite nuclei*, *Phys. Rev.* **C55** (1997) 2637–2648 [nucl-th/9612001].

[62] K. Saito, K. Tsushima and A. W. Thomas, *Nucleon and hadron structure changes in the nuclear medium and impact on observables*, *Prog. Part. Nucl. Phys.* **58** (2007) 1–167 [hep-ph/0506314].

[63] A. Chodos, R. L. Jaffe, K. Johnson, C. B. Thorn and V. F. Weisskopf, *A New Extended Model of Hadrons*, *Phys. Rev.* **D9** (1974) 3471–3495.

[64] S. Weinberg, *The Problem of Mass*, *Trans. New York Acad. Sci.* **38** (1977) 185–201.

[65] J. Bardeen, L. N. Cooper and J. R. Schrieffer, *Theory of superconductivity*, *Phys. Rev.* **108** (1957) 1175–1204.

[66] G. Krein, A. W. Thomas and K. Tsushima, *Fock terms in the quark meson coupling model*, *Nucl. Phys.* **A650** (1999) 313–325 [nucl-th/9810023].

[67] W. H. Press, S. A. Teukolsky, W. T. Vetterling and B. P. Flannery, *Numerical recipes in Fortran 90 (2nd ed.): the art of parallel scientific computing*. Cambridge University Press, New York, NY, USA, 1996.

[68] O. Klein, *Die Reflexion von Elektronen an einem Potentialsprung nach der relativistischen Dynamik von Dirac*, *Zeitschrift für Physik A Hadrons and Nuclei* **53** (1929) 157–165.

[69] F. Ozel, *Soft equations of state for neutron-star matter ruled out by EXO 0748-676*, *Nature* **441** (2006) 1115–1117.

[70] T. Guver, F. Ozel, A. Cabrera-Lavers and P. Wroblewski, *The Distance, Mass, and Radius of the Neutron Star in 4U 1608-52*, 0811.3979.

[71] F. Ozel, T. Guver and D. Psaltis, *The Mass and Radius of the Neutron Star in EXO 1745-248*, *Astrophys. J.* **693** (2009) 1775–1779 [0810.1521].

[72] M. Alford *et. al.*, *Quark matter in compact stars?*, *Nature* **445** (2007) E7–E8 [astro-ph/0606524].

[73] D. Galloway, F. Ozel and D. Psaltis, *Biases for neutron-star mass, radius and distance measurements from Eddington-limited X-ray bursts*, 0712.0412.

[74] G. F. Burgio, M. Baldo, P. K. Sahu and H. J. Schulze, *The hadron quark phase transition in dense matter and neutron stars*, *Phys. Rev.* **C66** (2002) 025802 [nucl-th/0206009].

[75] J. Schaffner and I. N. Mishustin, *Hyperon-rich matter in neutron stars*, *Phys. Rev. C* **53** (Mar, 1996) 1416–1429.

[76] C. J. Horowitz and B. D. Serot, *Properties of nuclear and neutron matter in a relativistic hartree–fock theory*, *Nuclear Physics A* **399** (1983), no. 2 529 – 562.

[77] S. E. Thorsett and D. Chakrabarty, *Neutron Star Mass Measurements. I. Radio Pulsars*, *Astrophys. J.* **512** (1999) 288 [astro-ph/9803260].

[78] S. Bhattacharyya, M. C. Miller and D. K. Galloway, *Systematic variation in the apparent burning area of thermonuclear bursts and its implication for neutron star radius measurement*, 0908.4245.

[79] M. G. Alford, A. Schmitt, K. Rajagopal and T. Schafer, *Color superconductivity in dense quark matter*, *Rev. Mod. Phys.* **80** (2008) 1455–1515 [0709.4635].

[80] S. Lawley, W. Bentz and A. W. Thomas, *Nucleons, nuclear matter and quark matter: A unified NJL approach*, *J. Phys.* **G32** (2006) 667–680 [nucl-th/0602014].

[81] R. P. Feynman, *Space-time approach to quantum electrodynamics*, *Phys. Rev.* **76** (1949) 769–789.

[82] E. C. G. Stuckelberg, *Relativistisch invariante Störungstheorie des Diracschen Elektrons I. Teil: Streustrahlung und Bremsstrahlung*, *Annalen der Physik* **413** (1934) 367–389.

[83] J. W. Rohlf, *Modern Physics from α to Z^0*. Wiley-VCH, 1994.

Derivations

In this section we will provide some in-depth derivations in order to provide a more complete understanding of the expressions derived and their origins. Any conventions used are noted throughout the text where appropriate, though standard particle physics conventions can generally be assumed. We present these derivations in context to the work contained herein, and acknowledge that further extensions may not be valid for the particular examples shown.

A.1 Feynman Rules/Diagrams

Although not strictly a derivation *per se*, here we present a summary for one of the most convenient and useful features of Quantum Field Theory, providing the ability to describe particle interactions in a diagram by following some simple rules; The Feynman Rules.

The diagrams were originally developed for Quantum Electrodynamics [81], and were later developed for QFT in general. These are known as Feynman Diagrams[1] and the rules as Feynman Rules. The diagrams are used throughout this work, and we will outline the rules governing them here briefly.

- To begin with, we first need to determine the particles which are to enter and leave the process we are describing. For this discussion, we shall limit ourselves to QCD. These are the 'external legs' of the diagram. The number of external legs will determine the number of required momenta. For the case of two external legs, only a single momentum is required; due to conservation of momentum, what goes in must also come out, and the external legs must correspond to 'on-shell' particles.

- For each type of particle, we can represent the propagator (see Appendix A.2) by a line. The typical line styles are shown in Fig. A.1. Each line introduces a propagator into the expression for the diagram. Internal propagators may be 'off-shell'.

- All of the lines meet at vertices, and introduce a coupling term into the expression for the diagram. For interactions of elementary particles, scalar vertices introduce a factor of ig (where g is the baryon-meson coupling) and vector particles introduce a factor of $-ig\gamma_\mu$. The four-momentum must be conserved at each vertex.

- For each internal momentum corresponding to a loop not fixed by momentum conservation, a factor of $\frac{1}{(2\pi)^4}\int d^4k$ is introduced to the expression for the diagram, and for each closed fermion loop, an additional factor of (-1) applies.

- Due to the antisymmetry under exchange of fermions, any two graphs distinguished only by the exchange of two external identical fermion lines must differ by a factor of (-1).

[1] Or Stuckelberg Diagrams, as Murray Gell-Mann allegedly preferred to call them due to a similar, earlier notation [82].

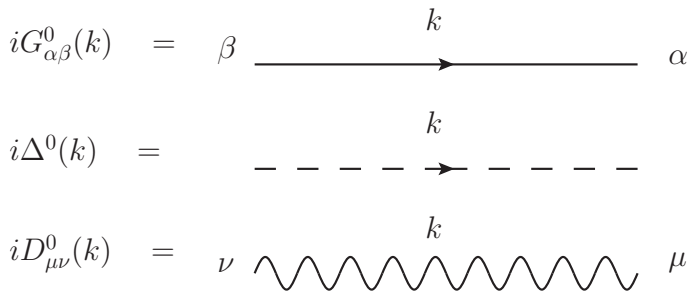

Fig. A.1: Each line represents a free propagator for either a fermion (solid line); a scalar meson (dashed line); or a vector meson (wavy line).

Given these rules, diagrams can be easily related to mathematical expressions, governed by a Lagrangian density, and the appropriate interactions can be read off. Furthermore, we can consider more complicated Feynman diagrams to address all higher-order contributions, such as an addition of gluon exchange between two external legs.

A.2 Propagators

In order to use the propagators introduced in the previous section, we need to fully understand their structure and origin. For this purpose, we provide an overview of the derivation of the scalar propagator.

First, we define the four-vector of momentum to be

$$k = k_\mu = (k_0, \vec{k}\,), \tag{A.1}$$

We can consider a free, positive-energy (frequency) scalar field ϕ^+ or negative-energy scalar field ϕ^- at a space-time point x to be expressed in terms of positive-energy creation ($a^\dagger$) and annihilation (a) operators (or equivalently, negative-energy annihilation (b) and creation ($b^\dagger$) operators) as

$$\phi(x) = \phi^+(x) + \phi^-(x) = \int \frac{d^3k}{(2\pi)^3} \frac{1}{\sqrt{2E_{\vec{k}}}} \left(a(\vec{k}\,)e^{-ik\cdot x} + b^\dagger(\vec{k}\,)e^{ik\cdot x} \right) , \tag{A.2}$$

where $E_{\vec{k}} = \sqrt{\vec{k}^2 + M^2}$, and the annihilation operators are defined by their actions on the vacuum state $|0\rangle$;

$$a(\vec{k}\,)|0\rangle = b(\vec{k}\,)|0\rangle = 0 \ \ \forall\ \vec{k}\ . \tag{A.3}$$

We can then use the commutation relation for the creation and annihilation operators

$$\left[a(\vec{k}), a^\dagger(\vec{k}\,') \right] = \delta(\vec{k} - \vec{k}\,') = \left[b(\vec{k}), b^\dagger(\vec{k}\,') \right] , \tag{A.4}$$

to define the positive- and negative-energy propagators

$$i\Delta^\pm(x - y) = \left[\phi^\pm(x), \phi^{\dagger\,\mp}(y) \right] , \tag{A.5}$$

(where the factor of i has been inserted for convenience), which satisfy

$$\Delta^-(x-y) = -\Delta^+(y-x). \tag{A.6}$$

We may then consider the positive-energy propagator for a Hermitian field (in which case $\phi^\dagger = \phi$, thus $b = a$ and $b^\dagger = a^\dagger$.)

$$\begin{aligned} i\Delta^+(x-y) &= \left[\phi^+(x), \phi^{\dagger\,-}(y)\right] \\ &= \frac{1}{2(2\pi)^3} \iint \left[a(\vec{k}), a^\dagger(\vec{k}')\right] \frac{e^{-ik\cdot x}\, e^{ik'\cdot y}}{\sqrt{E_{\vec{k}} E_{\vec{k}'}}}\, d^3k\, d^3k' \\ &= \frac{1}{2(2\pi)^3} \iint \frac{e^{-ik\cdot x}\, e^{ik'\cdot y}}{\sqrt{E_{\vec{k}} E_{\vec{k}'}}}\, \delta(\vec{k}-\vec{k}')\, d^3k\, d^3k' \\ &= \frac{1}{2(2\pi)^3} \int \frac{e^{-ik\cdot(x-y)}}{E_{\vec{k}}}\, d^3k, \end{aligned} \tag{A.7}$$

and similarly for the negative-energy propagator such that

$$i\Delta^\pm(x-y) = \pm\frac{1}{2(2\pi)^3} \int \frac{e^{\mp ik\cdot(x-y)}}{E_{\vec{k}}}\, d^3k. \tag{A.8}$$

We wish to include the energy components into this definition, but we also wish to keep the integrations over real numbers. We start by using contour integration. If we consider a function of the complex valued k_0

$$f(k_0) = \frac{e^{-ik_0(x_0-y_0)}}{k_0 + E_{\vec{k}}}, \tag{A.9}$$

then we can define this function at $E_{\vec{k}} \in \mathbb{R}$ using contour integration as shown in Fig. A.2 to be

$$f(E_{\vec{k}}) = \frac{e^{-iE_{\vec{k}}(x_0-y_0)}}{2E_{\vec{k}}} = \frac{1}{2\pi i} \oint_{C^+} \frac{f(k_0)}{k_0 - E_{\vec{k}}}\, dk_0. \tag{A.10}$$

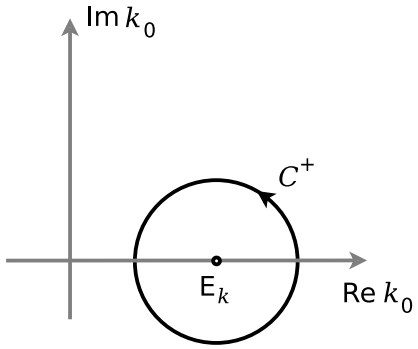

Fig. A.2: Contour integration performed counter-clockwise around contour C^+ in the complex plane of k_0 with a pole at real value $E_{\vec{k}}$.

Eq. (A.10) is obtained via Cauchy's Integral Formula which states that for every point a in the interior of a closed disk $D = \{z : |z - z_0| \leq r\}$ bounded by a curve C,

$$f(a) = \frac{1}{2\pi i} \oint_C \frac{f(z)}{z - a}\, dz, \tag{A.11}$$

provided that the curve defined by C is taken counter-clockwise.

If we consider the on-shell case in which $k_0 = E_{\vec{k}}$ and separate the temporal components, Eq. (A.7) becomes

$$\begin{aligned} i\Delta^+(x-y) &= \frac{1}{(2\pi)^3} \int e^{i\vec{k}\cdot(\vec{x}-\vec{y})}\, \frac{1}{2E_{\vec{k}}}\, e^{-iE_{\vec{k}}(x_0-y_0)} d^3k \\ &= \frac{1}{(2\pi)^3} \int e^{i\vec{k}\cdot(\vec{x}-\vec{y})} f(E_{\vec{k}})\, d^3k. \end{aligned} \tag{A.12}$$

We can then insert the contour integrated form of $f(E_{\vec{k}})$ from Eq. (A.10)

$$i\Delta^+(x-y) = \frac{1}{(2\pi)^3}\frac{1}{2\pi i} \int e^{i\vec{k}\cdot(\vec{x}-\vec{y})} \oint_{C^+} \frac{f(k_0)}{k_0 - E_{\vec{k}}}\, dk_0\, d^3k, \tag{A.13}$$

and then insert the form of $f(k_0)$ from Eq. (A.9) to give

$$\begin{aligned} i\Delta^+(x-y) &= \frac{1}{(2\pi)^3}\frac{1}{2\pi i} \int e^{i\vec{k}\cdot(\vec{x}-\vec{y})} \oint_{C^+} \frac{e^{-ik_0(x_0-y_0)}}{(k_0 + E_{\vec{k}})(k_0 - E_{\vec{k}})}\, dk_0\, d^3k \\ &= \frac{-i}{(2\pi)^4} \oint_{C^+} \frac{e^{-ik\cdot(x-y)}}{(k_0)^2 - (E_{\vec{k}})^2}\, d^4k \\ &= \frac{-i}{(2\pi)^4} \oint_{C^+} \frac{e^{-ik\cdot(x-y)}}{k^2 - M^2}\, d^4k, \end{aligned} \tag{A.14}$$

where the integration over the three-momentum is for $-\infty < k_i \in \mathbb{R} < \infty$ and the energy is over a contour integral $k_0 \in \mathbb{C}$ such that $k_0 \neq E_{\vec{k}}$. The last line arises from

$$(k_0)^2 - (E_{\vec{k}})^2 = k^2 + (\vec{k}\,)^2 - M^2 - (\vec{k}\,)^2 = k^2 - M^2. \tag{A.15}$$

A similar derivation is possible for the negative-energy propagator $i\Delta^-(x-y)$, where the only difference will be the contour over which the integration is performed, in that case C^- to avoid the point of $k_0 = -E_{\vec{k}}$, but which results in the same expression as that of Eq. (A.14). The two integrations required are illustrated in Fig. A.3.

To combine the two propagators together, we need to take care of the contour integrations around both $E_{\vec{k}}$ and $-E_{\vec{k}}$. To do this, we can shift both away from the real axis via

$$E_{\vec{k}} \to E_{\vec{k}} - i\eta, \tag{A.16}$$

which displaces these points to $-E_{\vec{k}} + i\eta$ and $E_{\vec{k}} - i\eta$ such that the denominator for the positive propagator is now

$$(k_0)^2 - (E_{\vec{k}} - i\eta)^2. \tag{A.17}$$

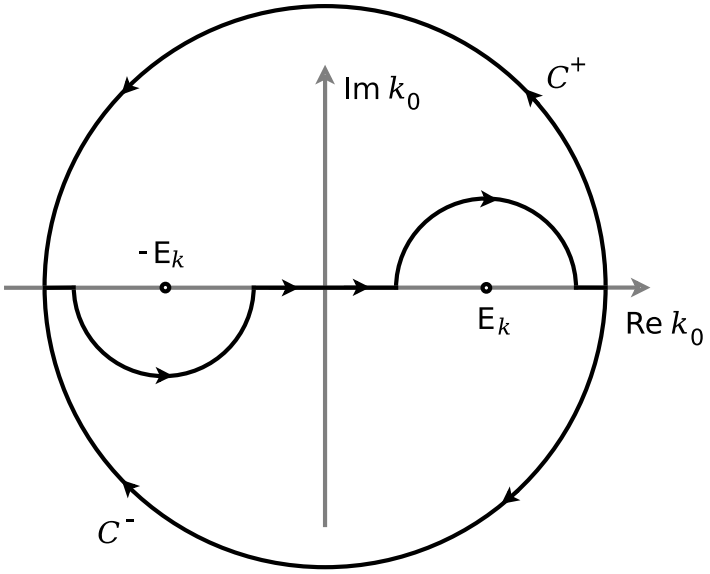

Fig. A.3: Contour integration performed around contours $C^{\mp}$ in the complex plane of k_0 with poles at real values $\pm E_{\vec{k}}$. Note that the contour containing $E_{\vec{k}}$ (the lower contour) produces a negative value since it is taken clockwise.

Depending on which of x_0 and y_0 is larger, the exponential in Eq. (A.14) will have a different sign. In order to unify these, we use the time-ordered product to define the Feynman propagator

$$\Delta_F(x-y) = \langle \Psi_0 | T[\phi(y)\phi(x)] | \Psi_0 \rangle = \begin{cases} \Delta^+(x-y), & \text{if} \quad y_0 < x_0 \\ \Delta^-(x-y), & \text{if} \quad x_0 < y_0 \end{cases} . \tag{A.18}$$

If we define the small parameter $\epsilon = 2\eta E_{\vec{k}}$, neglect terms of $\mathcal{O}(\eta^2)$, and enlarge the contour over which we integrate in the complex plane as shown in Fig. A.4 then the Feynman scalar propagator can be written as

$$\Delta_F(x-y) = \frac{1}{(2\pi)^4} \int_{-\infty}^{\infty} \frac{e^{-ik\cdot(x-y)}}{k^2 - M^2 + i\epsilon}\, d^4k, \tag{A.19}$$

which has the advantage that now our integrals are all over real numbers, and we have a single expression (since we no longer depend on the contour). The factor of ϵ is removed after the integration is performed by taking $\epsilon \to 0$.

We note that Eq. (A.19) now takes the form of a Fourier transform, and thus we can write the propagator in either position-space or momentum-space, as

$$\Delta_F(x-y) = \int \frac{d^4k}{(2\pi)^4}\, e^{-ik\cdot(x-y)} \Delta_F(k), \tag{A.20}$$

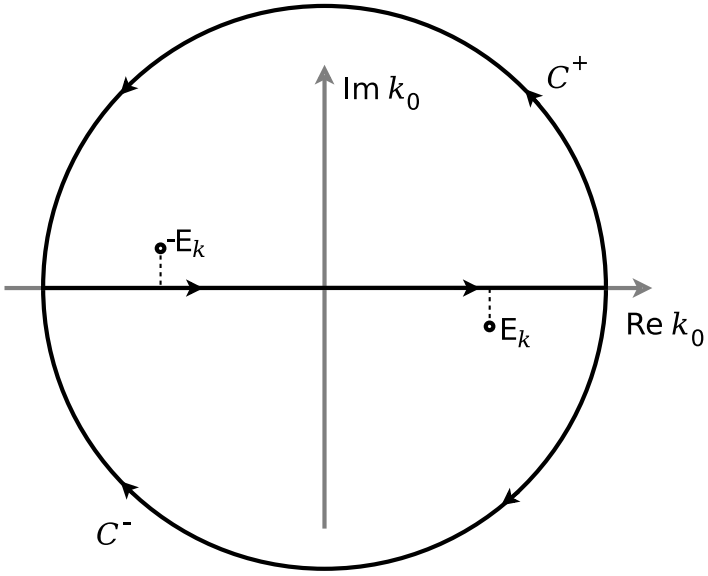

Fig. A.4: Contour integration performed around contours $C^{\mp}$ in the complex plane of k_0 with offset poles at $\pm E_{\vec{k}} \mp i\epsilon$.

where we can define the momentum-space propagator using Eq. (A.19) as

$$\Delta_F(k) = (k^2 - M^2 + i\epsilon)^{-1}. \tag{A.21}$$

This is the definition of the free scalar field ($\Delta_F(k) \equiv \Delta^0(k)$) and we can similarly define a vector meson propagator and a baryon propagator; for a vector field V the free propagator is

$$iD^0_{\mu\nu}(y-x) = \langle \Psi_0 | T[V_\mu(y) V_\nu(x)] | \Psi_0 \rangle = i \int \frac{d^4k}{(2\pi)^4}\, e^{-ik\cdot(y-x)} D^0_{\mu\nu}(k), \tag{A.22}$$

and for a baryon ψ,

$$iG^0_{\alpha\beta}(y-x) = \langle \Psi_0 | T[\psi_\alpha(y) \bar{\psi}_\beta(x)] | \Psi_0 \rangle = i \int \frac{d^4k}{(2\pi)^4}\, e^{-ik\cdot(y-x)} G^0_{\alpha\beta}(k). \tag{A.23}$$

The explicit forms of the momentum-space propagators are

$$\Delta^0(k) = (k_\lambda^2 - m_\sigma^2 + i\epsilon)^{-1}, \tag{A.24}$$

$$\begin{aligned} D^0_{\mu\nu}(k) &= \left[-g_{\mu\nu} + \frac{k_\mu k_\nu}{m_\omega^2} \right] (k_\lambda^2 - m_\omega^2 + i\epsilon)^{-1} \\ &= -g_{\mu\nu} (k_\lambda^2 - m_\omega^2 + i\epsilon)^{-1}, \end{aligned} \tag{A.25}$$

$$G^0_{\alpha\beta}(k) = (\not{k} - M)_{\alpha\beta} \left[(k_\lambda^2 - M^2 + i\epsilon)^{-1} + \frac{i\pi}{E^*(\vec{k})} \delta(k_0 - E_{\vec{k}}) \theta(k_F - |\vec{k}|) \right], \tag{A.26}$$

using the definitions given later in Eq. (A.160), and where the baryon propagator has two parts, the second of which arises as a result of the immersion in a Fermi sea.

A.3 QHD Equation of State

Here we will fully derive the EOS (refer to Section 2.8) for Quantum Hadrodynamics (of which the Quark-Meson Coupling model can be considered an *a posteriori* extension) in more detail than in the main text. Although we have performed calculations for several configurations of QHD, the derivation provided here should be a suitable framework to expand on in order to reproduce all of the results of this work.

In the derivation of QHD that follows, we consider a collection of nucleons (protons and neutrons) with strong interactions (which in QCD are a result of quark-gluon interactions) modelled by σ, ω and ρ mesons (i.e. QHD-II) in a Relativistic Effective Field Theory.

In order to describe the nucleons we combine them into a Dirac spinor as

$$\psi \equiv \psi_N = \begin{pmatrix} \psi_p \\ \psi_n \end{pmatrix}. \tag{A.27}$$

We can then write the QHD Lagrangian density with this spinor and meson terms (as described in Section 2.1) as

$$\begin{aligned} \mathcal{L} \;=\; & \bar{\psi}\left[\gamma_\mu(i\partial^\mu - g_{N\omega}\omega^\mu - g_\rho \vec{\rho}^{\,\mu}\cdot\vec{\tau}\,) - (M - g_{N\sigma}\sigma)\right]\psi \\ & + \frac{1}{2}(\partial_\mu\sigma\partial^\mu\sigma - m_\sigma^2\sigma^2) - \frac{1}{4}\Omega_{\mu\nu}\Omega^{\mu\nu} - \frac{1}{4}R^a_{\mu\nu}R^{\mu\nu}_a \\ & + \frac{1}{2}m_\omega^2\omega_\mu\omega^\mu + \frac{1}{2}m_\rho^2\rho_\mu\rho^\mu + \delta\mathcal{L} \end{aligned} \tag{A.28}$$

where the field strength tensors for the vector mesons are

$$\Omega_{\mu\nu} = \partial_\mu\omega_\nu - \partial_\nu\omega_\mu, \qquad R^a_{\mu\nu} = \partial_\mu\rho^a_\nu - \partial_\nu\rho^a_\mu + g_\rho\epsilon^{abc}\rho^b_\mu\rho^c_\nu. \tag{A.29}$$

The mass term M should be understood to be a diagonal matrix with the proton and neutron masses on the diagonal. As discussed in Section 2.12 the couplings g of the baryons to the mesons are baryon dependent, with the exception of g_ρ which appears with the isospin-group dependent $\vec{\tau}$ as defined in Eq. (2.12).

The Lagrangian density can also be written in a more familiar form if we recognize that the vector field terms take the form of the temporal component of an energy four-vector and hence have units of energy and act to reduce the energy of the nucleon, whilst the scalar term takes the form of a scalar mass, and hence acts to reduce the effective mass of the nucleon. We can observe this better if we define the covariant derivative as

$$D_\mu = \partial_\mu + ig_{N\omega}\omega_\mu + ig_\rho\rho^a_\mu\tau_a, \tag{A.30}$$

so, neglecting the scalar field for a moment, we have a term that appears similar to the Dirac equation

$$(i\not{D} - M)\,\psi = 0. \tag{A.31}$$

The Euler–Lagrange Equations describe the equations of motion for all particles Φ involved in the above Lagrangian density,

$$\frac{\partial\mathcal{L}}{\partial\Phi} - \partial_\mu\frac{\partial\mathcal{L}}{\partial(\partial_\mu\Phi)} = 0. \tag{A.32}$$

When we calculate the equations of motion for Eq. (A.28) for the mesons we arrive at a Klein–Gordon equation for the σ field and Maxwell equations for the ω and ρ fields (by construction, since the free terms in the Lagrangian density were chosen such that this phenomenology would be reproduced), thus

$$\begin{aligned} \left(\Box + m_\sigma^2\right)\sigma &= g_{N\sigma}\bar{\psi}\psi, && \text{(A.33)}\\ \partial^\mu \Omega_{\mu\nu} &= g_{N\omega}\bar{\psi}\gamma_\nu\psi - m_\omega^2\omega_\nu, && \text{(A.34)}\\ \partial^\mu R^a_{\mu\nu} &= g_\rho\bar{\psi}\gamma_\nu\tau^a\psi - m_\rho^2\rho^a_\nu. && \text{(A.35)} \end{aligned}$$

Applying Eq. (A.32) to the nucleons (and similarly for the conjugate) we obtain a Dirac equation,

$$\left[i\,\partial\!\!\!/ - g_{N\omega}\,\omega\!\!\!/ - g_\rho\,\rho\!\!\!/^a\tau_a - M + g_{N\sigma}\sigma\right]\psi = 0. \qquad \text{(A.36)}$$

We now consider a Mean-Field Approximation (MFA, see Section 2.2) in which the meson fields are described by only their constant, classical components. We separate the meson fields into classical and quantum components as

$$\begin{aligned} \sigma &= \sigma_{\text{classical}} + \sigma_{\text{quantum}},\\ \omega &= \omega_{\text{classical}} + \omega_{\text{quantum}},\\ \rho &= \rho_{\text{classical}} + \rho_{\text{quantum}}. \end{aligned} \qquad \text{(A.37)}$$

If we now consider vacuum expectation values, the quantum operator component for the mesons vanishes leaving only a constant classical component

$$\begin{aligned} \sigma &\to \langle\sigma\rangle,\\ \omega^\mu &\to \langle\omega\rangle \equiv \langle\omega_0\rangle\delta^{\mu 0},\\ \rho^\mu &\to \langle\rho\rangle \equiv \langle\rho_0\rangle\delta^{\mu 0}. \end{aligned} \qquad \text{(A.38)}$$

The $\delta^{\mu 0}$ terms for the vector mesons arise due to rotational invariance as per Section 2.3.1. Isospin invariance requires that only the third isospin component of the isovector meson ρ_0 will be non-vanishing, for which we shall drop the subscript.

Applying the MFA For the σ field we obtain

$$\begin{aligned} \left(\Box + m_\sigma^2\right)\langle\sigma\rangle &= g_{N\sigma}\langle\bar{\psi}\psi\rangle \overset{\text{MFA}}{\longrightarrow} m_\sigma^2\langle\sigma\rangle = g_{N\sigma}\langle\bar{\psi}\psi\rangle\\ \therefore\ \langle\sigma\rangle &= \frac{g_{N\sigma}}{m_\sigma^2}\langle\bar{\psi}\psi\rangle. \end{aligned} \qquad \text{(A.39)}$$

For the ω field we obtain

$$\begin{aligned} \partial_\mu\Omega^{\mu\nu} = g_{N\omega}\langle\bar{\psi}\gamma^\nu\psi\rangle - m_\omega^2\omega^\nu &\overset{\text{MFA}}{\longrightarrow} 0 = g_{N\omega}\langle\bar{\psi}\gamma^0\psi\rangle - m_\omega^2\langle\omega\rangle\\ \therefore\ \langle\omega\rangle = \frac{g_{N\omega}}{m_\omega^2}\langle\bar{\psi}\gamma^0\psi\rangle &= \frac{g_{N\omega}}{m_\omega^2}\langle\psi^\dagger\psi\rangle, \end{aligned} \qquad \text{(A.40)}$$

and similarly for the ρ field,

$$\begin{aligned} \partial_\mu R_3^{\mu\nu} = g_\rho\langle\bar{\psi}\gamma^\nu\tau_3\psi\rangle - m_\rho^2\rho^\nu &\overset{\text{MFA}}{\longrightarrow} 0 = g_\rho\langle\bar{\psi}\gamma^0\tau_3\psi\rangle - m_\rho^2\langle\rho\rangle\\ \therefore\ \langle\rho\rangle = \frac{g_\rho}{m_\rho^2}\langle\bar{\psi}\gamma^0\tau_3\psi\rangle &= \frac{g_\rho}{m_\rho^2}\langle\psi^\dagger\tau_3\psi\rangle. \end{aligned} \qquad \text{(A.41)}$$

We can define in each of these cases a density associated with the mean-fields of the mesons. These are the scalar, vector, and isovector densities,

$$\rho_\sigma \equiv \rho_S = \langle\bar{\psi}\psi\rangle, \tag{A.42}$$
$$\rho_\omega \equiv \rho_{\text{total}} = \langle\psi^\dagger\psi\rangle = \rho_p + \rho_n, \tag{A.43}$$
$$\rho_\rho \equiv \rho_I = \langle\psi^\dagger\tau_3\psi\rangle = \frac{1}{2}\left(\rho_p - \rho_n\right). \tag{A.44}$$

The vector density ρ_{total} and the isovector density ρ_I are the conserved baryon density and isovector density respectively, the expressions for which can be found using the nucleon spinor. The closed form of the scalar density $\rho_S \equiv \rho_\sigma$ will be derived in Appendix A.5.1.

Finally, calculating the equations of motion for the nucleons we obtain

$$\left[i\partial\!\!\!/ - g_{N\omega}\langle\omega\rangle\gamma_0 - g_\rho\langle\rho\rangle\gamma_0\tau_3 - M + g_{N\sigma}\langle\sigma\rangle\right]\psi = \left[i\not{D} - M^*\right]\psi = 0, \tag{A.45}$$

(and similarly for the conjugate spinor $\bar{\psi}$). We can now rewrite the QHD Lagrangian density with the surviving mean-field terms, as

$$\begin{aligned}\langle\mathcal{L}\rangle &= \bar{\psi}\left[i\gamma_\mu\partial^\mu - g_{N\omega}\langle\omega\rangle\gamma_0 - g_\rho\langle\rho\rangle\gamma_0\tau_3 - M^*\right]\psi \\ &\quad -\frac{1}{2}m_\sigma^2\langle\sigma\rangle^2 + \frac{1}{2}m_\omega^2\langle\omega\rangle^2 + \frac{1}{2}m_\rho^2\langle\rho\rangle^2 \\ &= \bar{\psi}\left[i\gamma_\mu\partial^\mu - g_{N\omega}\langle\omega\rangle\gamma_0 - g_{N\rho}\langle\rho\rangle\gamma_0\tau_3 - M^*\right]\psi \\ &\quad -\frac{g_{N\sigma}^2}{2m_\sigma^2}\rho_\sigma^2 + \frac{g_{N\omega}^2}{2m_\omega^2}\rho_\omega^2 + \frac{g_\rho^2}{2m_\rho^2}\rho_\rho^2.\end{aligned} \tag{A.46}$$

Note that the σ meson mas term has an opposite sign to the vector meson terms.

For a uniform system, the energy-momentum tensor has the form

$$\langle T_{\mu\nu}\rangle = \left(\mathcal{E} + P\right)u_\mu u_\nu + P\mathrm{g}_{\mu\nu}, \tag{A.47}$$

where the four-velocity for a fluid at rest is $u = (1, \vec{0}\,)$, and satisfies $u^\mu u_\mu = -1$. We use the standard identity for the energy-momentum tensor;

$$P = \frac{1}{3}\langle T_{ii}\rangle, \quad \mathcal{E} = \langle T_{00}\rangle, \tag{A.48}$$

and the Lagrangian form of the energy-momentum tensor

$$T_{\mu\nu} = -\mathrm{g}_{\mu\nu}\mathcal{L} + \partial_\nu q_i\frac{\partial\mathcal{L}}{\partial\partial^\mu q_i}, \tag{A.49}$$

then insert the MFA Lagrangian of Eq. (A.46) to obtain

$$\langle T_{\mu\nu}\rangle = i\langle\bar{\psi}\gamma_\mu\partial_\nu\psi\rangle - \left(-\frac{g_{N\sigma}^2}{2m_\sigma^2}\rho_\sigma^2 + \frac{g_{N\omega}^2}{2m_\omega^2}\rho_\omega^2 + \frac{g_\rho^2}{2m_\rho^2}\rho_\rho^2\right)\mathrm{g}_{\mu\nu}. \tag{A.50}$$

Note that there is only one term involving ∂^μ in the Lagrangian density, and that the equation of motion for the nucleon (the Dirac equation, Eq. (A.36)) will prevent any fermion factors

in the term proportional to $g_{\mu\nu}$. We can rearrange this using Eq. (A.36) if we expand the Einstein summation, as

$$\begin{aligned}
\left(i\gamma_\mu\partial^\mu - g_{N\omega}\langle\omega\rangle\gamma_0 - g_\rho\langle\rho\rangle\gamma_0\tau_3 - M^*\right)\psi &= 0 \\
\left(i\gamma_0\partial^0 + i\gamma_i\partial^i - g_{N\omega}\langle\omega\rangle\gamma_0 - g_\rho\langle\rho\rangle\gamma_0\tau_3 - M^*\right)\psi &= 0 \\
\left(i\gamma^0\partial^0 - i\gamma^i\partial^i - g_{N\omega}\langle\omega\rangle\gamma_0 - g_\rho\langle\rho\rangle\gamma_0\tau_3 - M^*\right)\psi &= 0 \\
\therefore \quad i\gamma^0\partial^0\psi = \left(i\gamma^i\partial^i + g_{N\omega}\langle\omega\rangle\gamma_0 + g_\rho\langle\rho\rangle\gamma_0\tau_3 + M^*\right)\psi. &\qquad \text{(A.51)}
\end{aligned}$$

We can now substitute Eq. (A.51) into the expression for the energy-momentum tensor, Eq. (A.50) to obtain an expression for the energy density

$$\begin{aligned}
\mathcal{E} = \langle T_{00}\rangle &= \bar\psi\left[i\gamma^i\partial^i + g_{N\omega}\langle\omega\rangle\gamma_0 + g_\rho\langle\rho\rangle\gamma_0\tau_3 + M^*\right]\psi \\
&\quad - \left(-\frac{g_{\sigma N}^2}{2m_\sigma^2}\rho_\sigma^2 + \frac{g_{\omega N}^2}{2m_\omega^2}\rho_\omega^2 + \frac{g_{\rho N}^2}{2m_\rho^2}\rho_\rho^2\right). \qquad \text{(A.52)}
\end{aligned}$$

We can furthermore extract a γ_0 term from $\bar\psi = \psi^\dagger\gamma_0$ to obtain

$$\begin{aligned}
\mathcal{E} &= \psi^\dagger\left[i\gamma_0\gamma^i\partial^i + g_{N\omega}\langle\omega\rangle\gamma_0^2 + g_\rho\langle\rho\rangle\gamma_0^2\tau_3 + \gamma_0 M^*\right]\psi \\
&\quad - \left(-\frac{g_{\sigma N}^2}{2m_\sigma^2}\rho_\sigma^2 + \frac{g_{\omega N}^2}{2m_\omega^2}\rho_\omega^2 + \frac{g_\rho^2}{2m_\rho^2}\rho_\rho^2\right). \qquad \text{(A.53)}
\end{aligned}$$

Using Dirac's notation, in which

$$\alpha^i = \gamma_0\gamma^i, \quad \beta = \gamma_0, \quad \gamma_0^2 = I, \quad \partial^i = (-\vec\nabla)^i, \qquad \text{(A.54)}$$

we can write Eq. (A.53) as

$$\begin{aligned}
\mathcal{E} &= \psi^\dagger\left[-i\vec\alpha\cdot\vec\nabla + g_{N\omega}\langle\omega\rangle + g_\rho\langle\rho\rangle\tau_3 + \beta M^*\right]\psi \\
&\quad - \left(-\frac{g_{N\sigma}^2}{2m_\sigma^2}\rho_\sigma^2 + \frac{g_{N\omega}^2}{2m_\omega^2}\rho_\omega^2 + \frac{g_\rho^2}{2m_\rho^2}\rho_\rho^2\right). \qquad \text{(A.55)}
\end{aligned}$$

We can now separate the interaction terms (in the square brackets) and we notice that these can be expressed in the same form as the free meson terms, so we collect these together and find that the signs of the vector terms are reversed

$$\begin{aligned}
\mathcal{E} &= \psi^\dagger\left[-i\vec\alpha\cdot\vec\nabla + \beta M^*\right]\psi + \bar\psi g_{N\omega}\gamma_0\langle\omega\rangle\psi + \bar\psi g_\rho\langle\rho\rangle\gamma_0\tau_3\psi + \frac{g_{N\sigma}^2}{2m_\sigma^2}\rho_\sigma^2 - \frac{g_{N\omega}^2}{2m_\omega^2}\rho_\omega^2 - \frac{g_\rho^2}{2m_\rho^2}\rho_\rho^2 \\
&= \psi^\dagger\left[-i\vec\alpha\cdot\vec\nabla + \beta M^*\right]\psi + \frac{g_{N\omega}^2}{m_\omega^2}\rho_\omega^2 + \frac{g_\rho^2}{m_\rho^2}\rho_\rho^2 + \frac{g_{N\sigma}^2}{2m_\sigma^2}\rho_\sigma^2 - \frac{g_{N\omega}^2}{2m_\omega^2}\rho_\omega^2 - \frac{g_\rho^2}{2m_\rho^2}\rho_\rho^2 \\
&= \psi^\dagger\left[-i\vec\alpha\cdot\vec\nabla + \beta M^*\right]\psi + \frac{g_{N\sigma}^2}{2m_\sigma^2}\rho_\sigma^2 + \frac{g_{N\omega}^2}{2m_\omega^2}\rho_\omega^2 + \frac{g_\rho^2}{2m_\rho^2}\rho_\rho^2 \\
&= \psi^\dagger\left[\vec\alpha\cdot\vec k + \beta M^*\right]\psi + \frac{g_{N\sigma}^2}{2m_\sigma^2}\rho_\sigma^2 + \frac{g_{N\omega}^2}{2m_\omega^2}\rho_\omega^2 + \frac{g_\rho^2}{2m_\rho^2}\rho_\rho^2, \qquad \text{(A.56)}
\end{aligned}$$

where we have used the relation $-i\vec{\nabla} = \vec{k}$. To further simplify the interaction term here we consider solutions to the Dirac Equation of the form

$$\psi = u(p)e^{-iE^*t}e^{i\vec{p}\cdot\vec{x}}, \tag{A.57}$$

where

$$u(p) = \frac{\not{k} + M^*}{\sqrt{2E^*}\sqrt{E^* + M^*}}\begin{pmatrix}\chi\\0\end{pmatrix}; \quad \chi = \begin{pmatrix}1\\0\end{pmatrix} \text{ or } \begin{pmatrix}0\\1\end{pmatrix}, \tag{A.58}$$

where we use a normalization factor of $\frac{1}{\sqrt{2E^*}}$. Written out in full, Eq. (A.58) becomes

$$\begin{aligned} u(p) &= \frac{1}{\sqrt{2E^*}\sqrt{E^* + M^*}}\left(\gamma_\mu k^\mu + M^*\right)\begin{pmatrix}\chi\\0\end{pmatrix} \\ &= \frac{1}{\sqrt{2E^*}\sqrt{E^* + M^*}}\begin{pmatrix}(M^* + E^*)I & -\vec{\sigma}\cdot\vec{k}\\ \vec{\sigma}\cdot\vec{k} & (M^* - E^*)I\end{pmatrix}\begin{pmatrix}\chi\\0\end{pmatrix} \\ &= \frac{1}{\sqrt{2E^*}\sqrt{E^* + M^*}}\begin{pmatrix}(M^* + E^*)\chi\\ \vec{\sigma}\cdot\vec{k}\,(\chi)\end{pmatrix} \\ &= \sqrt{\frac{E^* + M^*}{2E^*}}\begin{pmatrix}\chi\\ \frac{\vec{\sigma}\cdot\vec{k}}{E^* + M^*}(\chi)\end{pmatrix}. \end{aligned}$$

Given the relations

$$(\vec{\sigma}\cdot\vec{k}) = (\vec{\sigma}\cdot\vec{k})^\dagger, \quad (\vec{\sigma}\cdot\vec{k})^2 = \vec{k}^2, \quad \vec{\alpha} = \begin{pmatrix}0 & \vec{\sigma}\\ \vec{\sigma} & 0\end{pmatrix}, \tag{A.59}$$

we can calculate the interaction terms in Eq. (A.56) explicitly;

$$\begin{aligned} u^\dagger\left(\vec{\alpha}\cdot\vec{k}\right)u &= \frac{E^* + M^*}{2E^*}\begin{pmatrix}\chi^\dagger & \frac{\vec{\sigma}\cdot\vec{k}}{E^* + M^*}\chi^\dagger\end{pmatrix}\begin{pmatrix}0 & \vec{\sigma}\cdot\vec{k}\\ \vec{\sigma}\cdot\vec{k} & 0\end{pmatrix}\begin{pmatrix}\chi\\ \frac{\vec{\sigma}\cdot\vec{k}}{E^* + M^*}\end{pmatrix} \\ &= \frac{E^* + M^*}{2E^*}\begin{pmatrix}\frac{(\vec{\sigma}\cdot\vec{k})^2}{E^* + M^*}\chi^\dagger & (\vec{\sigma}\cdot\vec{k})\chi^\dagger\end{pmatrix}\begin{pmatrix}\chi\\ \frac{\vec{\sigma}\cdot\vec{k}}{M^* + E^*}(\chi)\end{pmatrix} \\ &= \frac{E^* + M^*}{2E^*}\left(\frac{(\vec{\sigma}\cdot\vec{k})^2}{E^* + M^*}\chi^\dagger\chi \;+\; \frac{(\vec{\sigma}\cdot\vec{k})^2}{E^* + M^*}\chi^\dagger\chi\right) \\ &= \frac{\vec{k}^2}{E^*}, \end{aligned} \tag{A.60}$$

$$
\begin{aligned}
u^\dagger(\beta M^*)u &= \frac{E^*+M^*}{2E^*}\begin{pmatrix}\chi^\dagger & \frac{\vec{\sigma}\cdot\vec{k}}{E^*+M^*}\chi^\dagger\end{pmatrix}\begin{pmatrix}M^* & 0\\ 0 & -M^*\end{pmatrix}\begin{pmatrix}\chi\\ \frac{\vec{\sigma}\cdot\vec{k}}{E^*+M^*}\end{pmatrix}\\
&= \frac{E^*+M^*}{2E^*}\begin{pmatrix}M^*\chi^\dagger & -\frac{(\vec{\sigma}\cdot\vec{k})}{E^*+M^*}\chi^\dagger\end{pmatrix}\begin{pmatrix}\chi\\ \frac{\vec{\sigma}\cdot\vec{k}}{M^*+E^*}(\chi)\end{pmatrix}\\
&= \frac{E^*+M^*}{2E^*}\left(M^* - \frac{(\vec{\sigma}\cdot\vec{k})^2}{(E^*+M^*)^2}\chi^\dagger\chi\right)\\
&= \frac{M^{*2}}{E^*}. \qquad \text{(A.61)}
\end{aligned}
$$

Combining these last two expressions, we can see that

$$u^\dagger(\vec{\alpha}\cdot\vec{k}+\beta M^*)u = \frac{(\vec{k})^2+(M^*)^2}{E^*} = E^* = \sqrt{\vec{k}^2+M^{*2}}. \qquad \text{(A.62)}$$

Furthermore, we see that

$$u^\dagger u = 1, \quad \bar{u}u = \frac{M^*}{E^*}. \qquad \text{(A.63)}$$

Inserting the results of Eq. (A.62) into Eq. (A.57), and summing over continuous momenta for each of the spin states of protons and neutrons, we find the expression for the energy density

$$\mathcal{E} = \frac{g_{N\omega}^2}{2m_\omega^2}\rho_\omega^2 + \frac{g_\rho^2}{2m_\rho^2}\rho_\rho^2 + \frac{g_{N\sigma}^2}{2m_\sigma^2}\rho_\sigma^2 + \sum_{p,n}\frac{(2J+1)}{(2\pi)^3}\int_0^{k_F}\left(\vec{k}^{\,2}+M^{*\,2}\right)^{1/2}d^3k, \qquad \text{(A.64)}$$

where J is the spin of the nucleons ($J_{p,n} = \frac{1}{2}$). Similarly, the equation for the pressure is derived to be

$$
\begin{aligned}
P = \frac{1}{3}\langle T_{ii}\rangle &= \frac{1}{3}\psi^\dagger\left[-i\vec{\alpha}\cdot\vec{\nabla}\right]\psi + \frac{g_{N\omega}^2}{2m_\omega^2}\rho_\omega^2 + \frac{g_\rho^2}{2m_\rho^2}\rho_\rho^2 + \frac{g_{N\sigma}^2}{2m_\sigma^2}\rho_\sigma^2,\\
&= \frac{g_{N\omega}^2}{2m_\omega^2}\rho_\omega^2 + \frac{g_\rho^2}{2m_\rho^2}\rho_\rho^2 - \frac{g_{N\sigma}^2}{2m_\sigma^2}\rho_\sigma^2 + \frac{1}{3}\sum_{p,n}\frac{(2J+1)}{(2\pi)^3}\int_0^{k_F}\frac{\vec{k}^{\,2}}{E^*}d^3k\ . \qquad \text{(A.65)}
\end{aligned}
$$

These two quantities—the energy density $\mathcal{E}$ and the pressure P—along with the baryon density ρ_{total} define the EOS for QHD.

A.4 Tolman–Oppenheimer–Volkoff Equations

The Tolman–Oppenhemier–Volkoff (TOV) Equation (refer to Section 2.11) is derived in General Relativity to produce a differential relation for the pressure of a perfect fluid as a function of radius for a sphere of material which is able to sustain itself against gravitational collapse.

To begin with, we define a general metric for a static, spherically symmetric (non-rotating) star as

$$ds^2 = -e^{2\Phi}dt^2 + e^{2\Lambda}dr^2 + r^2d\Omega^2, \qquad \text{(A.66)}$$

where Φ and Λ are functions of r such that in the Newtonian limit of $r \to \infty$, the functions vanish, i.e. $\Phi \to 0$ and $\Lambda \to 0$. Given this, we can find components of the Einstein Tensor $G_{\mu\nu}$, which is defined in terms of the Ricci Tensor $R_{\mu\nu}$, and Ricci Scalar R, as

$$G_{\mu\nu} = R_{\mu\nu} - \frac{1}{2} R \mathrm{g}_{\mu\nu}, \tag{A.67}$$

the temporal and radial components of which are

$$G_{tt} = \frac{1}{r^2} e^{2\Phi} \frac{d}{dr} \left(r - r e^{-2\Lambda} \right), \tag{A.68}$$

$$G_{rr} = -\frac{1}{r^2} e^{2\Lambda} \left(1 - e^{-2\Lambda} \right) + \frac{2}{r} \frac{d\Phi}{dr}. \tag{A.69}$$

We can also find the components of the energy-momentum tensor for a perfect fluid,

$$T_{\mu\nu} = (P + \mathcal{E})\, u_\mu u_\nu + P \mathrm{g}_{\mu\nu} \tag{A.70}$$

where P is the pressure of the system, and $\mathcal{E}$ is the energy density.

Since we are considering a time-like spacetime, we can use the following relations

$$u_\alpha u^\alpha = -1, \quad u_i = 0 \quad \Rightarrow \quad u_t u^t = -1, \quad \therefore \ \mathrm{g}^{tt} u_t^2 = -1, \quad \therefore \ u_t^2 = e^{2\Phi}, \tag{A.71}$$

since we consider a static star, we have no three-velocity components so $u_i = 0$. We can now evaluate the energy-momentum tensor components to be

$$T_{tt} = (P + \mathcal{E})\, u_t u_t + P \mathrm{g}_{tt} = \mathcal{E} e^{2\Phi}, \tag{A.72}$$

$$T_{rr} = (P + \mathcal{E})\, u_r u_r + P \mathrm{g}_{rr} = P e^{2\Lambda}. \tag{A.73}$$

The energy-momentum tensor is related to the Einstein tensor via

$$G_{\mu\nu} = 8\pi T_{\mu\nu}, \tag{A.74}$$

and thus the temporal and radial components are found by inserting Eqs. (A.68)–(A.69) and Eqs. (A.72)–(A.73) into Eq. (A.74);

$$G_{tt} = 8\pi \mathcal{E} e^{2\Phi} = \frac{1}{r^2} e^{2\Phi} \frac{d}{dr} \left(r - r e^{-2\Lambda} \right), \tag{A.75}$$

$$G_{rr} = 8\pi p e^{2\Lambda} = -\frac{1}{r^2} e^{2\Lambda} \left(1 - e^{-2\Lambda} \right) + \frac{2}{r} \frac{d\Phi}{dr}. \tag{A.76}$$

The mass within a given radius r is defined by integrating the energy density, thus

$$M(r) = \int_0^r 4\pi R^2 \mathcal{E}\, dR, \tag{A.77}$$

and Eq. (A.75) already has this form on the right hand side, so we can divide through by $2e^{2\Phi}/r^2$ and integrate to obtain a new relation for the mass within radius r, which is

$$M(r) = \frac{1}{2} \left(r - r e^{-2\Lambda} \right) \int r^2 dr = \frac{1}{2} \left(r - r e^{-2\Lambda} \right), \tag{A.78}$$

which we can rearrange to obtain an expression for the factor that accompanies the radial component of the metric in Eq. (A.66), thus

$$e^{2\Lambda} = \left(1 - \frac{2M(r)}{r}\right)^{-1}. \tag{A.79}$$

The conservation of local energy-momentum requires that the derivative of Eq. (A.70) vanishes, and thus

$$T^{\mu\nu}{}_{;\nu} = 0. \tag{A.80}$$

Inserting the expression for the energy-momentum tensor of Eq. (A.70) we have

$$T^{r\nu}{}_{;\nu} = [(\mathcal{E} + P)u^r u^\nu]_{;\nu} = (\mathcal{E} + P)u^r{}_{;\nu}u^\nu + P_{,\nu}\mathrm{g}^{r\nu} = 0, \tag{A.81}$$

where we have taken the $\mu = r$ components since pressure depends only on the radius, and where $u^r = 0$ for a static solution (no radial velocities). We have also used the fact that $\mathrm{g}^{r\nu}{}_{;\nu} = 0$. Also note that P and $\mathcal{E}$ are Lorentz scalar quantities, so the total derivative $P_{;\nu}$ reduces to a partial derivative $P_{,\nu}$.

Since the conservation property prescribes that Eq. (A.81) vanishes, we can multiply both sides by the metric to lower the r components

$$(\mathcal{E} + P)u_{r;\nu}u^\nu + P_{;r} = 0. \tag{A.82}$$

Expanding the covariant derivative in terms of Christoffel symbols $\Gamma^\alpha_{r\nu}$ gives

$$(\mathcal{E} + P)u_{r,\nu}u^\nu + P_{,r} = (\mathcal{E} + P)\Gamma^\alpha_{r\nu}u_\alpha u^\nu. \tag{A.83}$$

Once again we use the lack of radial velocity (and acceleration) to remove the $u_{r,\nu}$ term, thus the remaining terms are

$$P_{,r} = (\mathcal{E} + P)\Gamma^\alpha_{r\nu}u_\alpha u^\nu. \tag{A.84}$$

Einstein summation is assumed, and the sums over α and ν will only have contributions from the temporal components since this is a static solution, so we then have

$$P_{,r} = (\mathcal{E} + P)\Gamma^t_{rt}u_t u^t = -(\mathcal{E} + P)\Gamma^t_{rt}. \tag{A.85}$$

Slightly aside, the Christoffel symbol can be evaluated from its definition in terms of the metric

$$\Gamma^\alpha_{\mu\nu} = \frac{1}{2}\mathrm{g}^{\alpha\beta}\left(\mathrm{g}_{\beta\mu,\nu} + \mathrm{g}_{\beta\nu,\mu} - \mathrm{g}_{\mu\nu,\beta}\right), \tag{A.86}$$

which reduces to the following if we set $\nu = \alpha$

$$\begin{aligned}\Gamma^\alpha_{\mu\alpha} &= \frac{1}{2}\mathrm{g}^{\alpha\beta}\left(\mathrm{g}_{\beta\mu,\alpha} + \mathrm{g}_{\beta\alpha,\mu} - \mathrm{g}_{\mu\alpha,\beta}\right) \\ &= \frac{1}{2}\mathrm{g}^{\alpha\beta}\left(\mathrm{g}_{\beta\mu,\alpha} - \mathrm{g}_{\mu\alpha,\beta}\right) + \frac{1}{2}\mathrm{g}^{\alpha\beta}\mathrm{g}_{\alpha\beta,\mu},\end{aligned} \tag{A.87}$$

where, due to symmetry $\mathrm{g}_{\beta\alpha,\mu} = \mathrm{g}_{\alpha\beta,\mu}$. Furthermore, the terms in the brackets are anti-symmetric in α and β, so the bracketed term vanishes when contracted with the inverse (symmetric) metric $g^{\alpha\beta}$. We are then left with

$$\Gamma^\alpha_{\mu\alpha} = \frac{1}{2}\mathrm{g}^{\alpha\beta}\mathrm{g}_{\alpha\beta,\mu} \tag{A.88}$$

so if we use the indices we have just derived ($\alpha = t$, $\mu = r$), we obtain

$$\Gamma^t_{rt} = \frac{1}{2}\mathrm{g}^{t\beta}\mathrm{g}_{t\beta,r} = \frac{1}{2}\mathrm{g}^{tt}\mathrm{g}_{tt,r} = \frac{1}{2}\frac{-1}{e^{2\Phi}}(-e^{2\Phi})_{,r} = \frac{1}{2}\frac{-1}{e^{2\Phi}}2\Phi_{,r}(-e^{2\Phi}) = \Phi_{,r} \tag{A.89}$$

recalling that the metric is diagonal, thus $\mathrm{g}^{t\beta}\mathrm{g}_{t\beta} = \mathrm{g}^{tt}\mathrm{g}_{tt}$.

Inserting the result of Eq. (A.89) into Eq. (A.85) we now have

$$P_{,r} = -(\mathcal{E} + P)\Phi_{,r} \tag{A.90}$$

which without the comma notation is

$$\frac{dP}{dr} = -(\mathcal{E} + P)\frac{d\Phi}{dr}, \tag{A.91}$$

where if $P \ll \mathcal{E}$, Eq. (A.91) reduces to the Newtonian result of $\mathcal{E}\Phi_{,r} = -P_{,r}$ which describes the balance between gravitational force and the pressure gradient.

We can now substitute Eq. (A.79) into Eq. (A.76) and with some rearrangements we can obtain an expression for $\Phi_{,r}$

$$\frac{d\Phi}{dr} = \frac{M(r) + 4\pi r^3 P}{r\left(r - 2M(r)\right)}, \tag{A.92}$$

which we can then substitute into Eq. (A.91) to obtain the Tolman–Oppenheimer–Volkoff Equation

$$\frac{dP}{dr} = -\frac{(P + \mathcal{E})\left(M(r) + 4\pi r^3 P)\right)}{r(r - 2M(r))}. \tag{A.93}$$

Finally, if we remove the use of Planck units (for which $\hbar = c = G = 1$) by dimensional analysis we have

$$\frac{dP}{dr} = -\frac{G\left(P/c^2 + \mathcal{E}\right)\left(M(r) + 4r^3\pi P/c^2\right)}{r(r - 2GM(r)/c^2)}. \tag{A.94}$$

A.5 Calculated Quantities of Interest

Included here are the derivations for some quantities that are used throughout this work. This will hopefully provide a more detailed explanation of their origins and their correspondence to the numerical results.

A.5.1 Self-Consistent Scalar Field

The self-consistent mean-scalar-field $\langle\sigma\rangle$ (and hence effective mass M^* via Eq. (2.43)) is found such that the energy density of Eq. (A.64) is minimised with respect to the scalar density of Eq. (A.42) as

$$\rho_\sigma = \frac{m_\sigma^2}{g_{N\sigma}}\langle\sigma\rangle, \tag{A.95}$$

thus, for the case of the nucleons,

$$\frac{\partial\mathcal{E}}{\partial\rho_\sigma} = 0 = \frac{g_{N\sigma}^2}{m_\sigma^2}\rho_\sigma + \frac{\partial}{\partial\rho_\sigma}\sum_N \frac{(2J_N + 1)}{(2\pi)^3}\int_0^{k_{F_N}} \left(\vec{k}^2 + M_N^{*2}\right)^{1/2} d^3k\ . \tag{A.96}$$

At this point we recall the definition of the effective mass, and express this in terms of ρ_σ

$$M_N^* = M_N - g_{N\sigma}\langle\sigma\rangle = M_N - \frac{g_{N\sigma}}{m_\sigma^2}\rho_\sigma. \tag{A.97}$$

We can now evaluate the integrated terms of Eq. (A.96) as

$$\begin{aligned}\frac{\partial}{\partial\rho_\sigma}\sum_N \frac{(2J_N+1)}{(2\pi)^3}\int_0^{k_{F_N}}\sqrt{\vec{k}^2+M_N^{*2}}\,d^3k &= -\sum_N \frac{(2J_N+1)g_{N\sigma}}{(2\pi)^3} \\ &\times \int_0^{k_{F_N}} M_N^*\left(\sqrt{\vec{k}^2+M_N^{*2}}\right)^{-1}\left(\frac{\partial\langle\sigma\rangle}{\partial\rho_\sigma}\right)d^3k \\ &= -\sum_N \frac{(2J_N+1)g_{N\sigma}^2}{m_\sigma^2(2\pi)^3}\int_0^{k_{F_N}}\left(\frac{M_N^*}{E_N^*}\right)d^3k,\end{aligned} \tag{A.98}$$

so the total expression for the scalar density becomes

$$\frac{\partial\mathcal{E}}{\partial\rho_\sigma} = 0 = \frac{g_{N\sigma}^2}{m_\sigma^2}\rho_\sigma - \sum_N \frac{g_{N\sigma}^2}{m_\sigma^2}\frac{(2J_N+1)}{(2\pi)^3}\int_0^{k_{F_N}}\left(\frac{M_N^*}{E_N^*}\right)d^3k, \tag{A.99}$$

which reduces to

$$\rho_\sigma = \sum_N \frac{(2J_N+1)}{(2\pi)^3}\int_0^{k_{F_N}}\left(\frac{M_N^*}{E_N^*}\right)d^3k. \tag{A.100}$$

We also note that this expression can be concluded from the bilinears of Eq. (A.63) since the expressions

$$u^\dagger u = 1, \quad \bar{u}u = \frac{M^*}{E^*}, \tag{A.101}$$

can be inserted back into Eq. (A.57) to calculate the various densities in Eqs. (A.42)–(A.44).

A.5.2 Semi-Empirical Mass Formula

The (Bethe–Weizsäcker) Semi-Empirical Mass Formula (SEMF) for nuclei—which is a refined form of the liquid drop model—describes a binding energy in terms of the number of nucleons A, and atomic number (number of protons) Z as

$$B(A,Z) = a_v A - a_s A^{2/3} - a_c\frac{Z(Z-1)}{A^{1/3}} - a_{sym}\frac{(A-2Z)^2}{A} + \delta, \tag{A.102}$$

where a_v is the volume coefficient, a_s is the surface coefficient, and a_{sym} is the symmetry coefficient. We also define a_c as the Coulomb coefficient and δ as the pairing term, each defined by

$$a_c = \frac{3e^2}{5r_0}, \qquad \delta = \begin{cases} a_p A^{-1/2}\,, & \text{for even } N\text{–even } Z, \\ -a_p A^{-1/2}\,, & \text{for odd } N\text{–odd } Z, \\ 0\,, & \text{for odd } A, \end{cases} \tag{A.103}$$

where e is the electric charge, r_0 is the Coulomb radius constant which defines the spherical nuclear volume of radius $A^{1/3}r_0$, and a_p is the pairing coefficient. These parameters and terms have various empirical derivations; for example the $Z(Z-1)$ term in the Coulomb term

corresponds to Coulomb contributions of Z protons, subtracting the self-energy contribution of each of the Z protons, since a single proton should not have a Coulomb contribution.

If we consider the binding energy per baryon A

$$\frac{B(A,Z)}{A} = a_v - a_s A^{-1/3} - \frac{3e^2}{5r_0}\frac{Z(Z-1)}{A^{4/3}} - a_{sym}\frac{(A-2Z)^2}{A^2} + \frac{\delta}{A}, \tag{A.104}$$

then consider the case of nuclear matter, in which we have isospin symmetry, and thus $Z = N$ (where N is the number of neutrons), the symmetry term vanishes ($A = Z+N = 2Z$), leaving

$$\frac{B(A,Z)}{A} = a_v - a_s A^{-1/3} - \frac{3e^2}{5r_0}\frac{Z(Z-1)}{A^{4/3}} + \frac{\delta}{A}. \tag{A.105}$$

If we now consider the case in which Coulomb contributions are neglected, as we do in nuclear matter (via setting $e = 0$) then the Coulomb term vanishes, leaving

$$\frac{B(A,Z)}{A} = a_v - a_s A^{-1/3} + \frac{\delta}{A}. \tag{A.106}$$

Finally, if we consider the case of infinite nuclear matter neglecting Coulomb interactions ($A \to \infty$, $e = 0$), we find that the remaining two terms inversely proportional to A vanish and the binding energy per nucleon becomes simply the volume coefficient

$$\frac{B(A,Z)}{A} = a_v, \tag{A.107}$$

which has units MeV. This is the origin of the saturated binding energy in nuclear matter calculations. The numerical result is the value obtained when fitting finite nuclei data to the SEMF and obtaining values for each of the six parameters. At present, several of these parameter sets exist—hence the wide range of values—and the set used in this work is that of Ref. [83].

$$\frac{B(A,Z)}{A} = a_v = 15.86 \text{ MeV}. \tag{A.108}$$

The equation for energy per baryon used in this work however takes into account the rest mass energy of the baryons and defines the binding as negative, and hence we use

$$\frac{\mathcal{E}}{A} - M_N = -15.86 \text{ MeV}, \tag{A.109}$$

or, alternatively, for many baryon species with the possibility of non-degenerate masses

$$\frac{1}{\rho_{\text{total}}}(\mathcal{E} - \sum_B \rho_B M_B) = -15.86 \text{ MeV}. \tag{A.110}$$

A.5.3 Compression Modulus

The compression modulus is used as a test against experiment, and is related to the 'stiffness' of the EOS. This quantity is a definition, as the curvature of the energy per baryon at saturation;

$$K = \left[k_F^2 \frac{d^2}{dk_F^2}\left(\frac{\mathcal{E}}{\rho_{\text{total}}}\right)\right]_{k_{F_{\text{sat}}}} = 9\left[\rho_{\text{total}}^2 \frac{d^2}{d\rho_{\text{total}}^2}\left(\frac{\mathcal{E}}{\rho_{\text{total}}}\right)\right]_{\rho=\rho_0}. \tag{A.111}$$

The factor of 9 arises from using the density rather than the Fermi momentum, as per Section 2.4.

A.5.4 Symmetry Energy

When we include the ρ meson to the Lagrangian density, we introduce a term into the energy density that is proportional to $\langle\rho\rangle^2 \propto (\rho_p - \rho_n)^2$, which is thus quadratic in the deviation from isospin symmetry. We can define this deviation in terms of a new variable (using just the nucleons here) as

$$t = (\rho_p - \rho_n)/\rho_{\rm total}\,;\ \rho_{\rm total} = \rho_p + \rho_n. \tag{A.112}$$

We can write the energy density in terms of this new parameter, and then find the dependence of the energy per baryon on this to be

$$\begin{aligned} E/A = \mathcal{E}/\rho_{\rm total} &= \frac{1}{2}\left(\frac{g_\rho}{m_\rho}\right)^2 t^2\,\rho_{\rm total} + \frac{1}{\rho_{\rm total}}\sum_N \frac{(2J+1)}{(2\pi)^3}\int_0^{k_{F_N}} \sqrt{\vec{k}^2 + (M_N^*)^2}\,d^3k \\ &= \frac{1}{2}\left(\frac{g_\rho}{m_\rho}\right)^2 t^2\,\rho{\rm total} + \frac{1}{\pi^2\rho_{\rm total}}\sum_N \int_0^{k_{F_N}} \vec{k}^2\sqrt{\vec{k}^2 + (M_N^*)^2}\,dk, \end{aligned} \tag{A.113}$$

where the second line is due to the change to spherical coordinates (for more details, see Appendix A.7). If we wish to know the contribution to the energy due to the isospin symmetry (or asymmetry), we need to find the term defined as

$$a_{\rm sym} = \frac{1}{2}\left[\ \frac{\partial^2(\mathcal{E}/\rho_{\rm total})}{\partial t^2}\ \right]_{t=0}. \tag{A.114}$$

We must keep in mind that the integrals do indeed depend on the isospin symmetry since they depend on the Fermi momenta, which can be defined as

$$k_{F_n} = k_{F_{\rm sat}}(1+t)^{1/3} \quad ;\ k_{F_p} = k_{F_{\rm sat}}(1-t)^{1/3}, \tag{A.115}$$

in terms of the saturation Fermi momentum

$$k_{F_{\rm sat}} = \left(\ \frac{3\pi^2\rho_0}{2}\ \right)^{1/3}, \tag{A.116}$$

so when we take the first derivative we obtain

$$\begin{aligned} \frac{1}{2}\left[\ \frac{\partial(\mathcal{E}/\rho_{\rm total})}{\partial t}\ \right] &= \frac{1}{4}\left(\frac{g_\rho}{m_\rho}\right)^2 \rho_{\rm total} t + \frac{k_{F_{\rm sat}}^3}{6\pi^2\rho} \\ &\quad\times\left[\ \sqrt{(t+1)^{2/3}k_{F_{\rm sat}}^2 + M_n^{*2}} - \sqrt{(1-t)^{2/3}k_{F_{\rm sat}}^2 + M_p^{*2}}\ \right]. \end{aligned} \tag{A.117}$$

The second derivative produces

$$\begin{aligned} \frac{1}{2}\left[\ \frac{\partial^2(\mathcal{E}/\rho_{\rm total})}{\partial t^2}\ \right] &= \frac{1}{4}\left(\frac{g_\rho}{m_\rho}\right)^2 \rho_{\rm total} + \frac{k_{\rm sat}^5}{18\pi^2\rho_{\rm total}} \\ &\quad\times\left[\ \frac{1}{\sqrt[3]{(t+1)}\sqrt{(1+t)^{2/3}k_{F_{\rm sat}}^2 + M_n^{*2}}}\right. \\ &\quad\left. + \frac{1}{\sqrt[3]{(1-t)}\sqrt{(1-t)^{2/3}k_{F_{\rm sat}}^2 + M_p^{*2}}}\ \right]. \end{aligned} \tag{A.118}$$

If we take the limit of $t \to 0$ at saturation ($\rho = \rho_0$) we obtain

$$\begin{aligned} a_{\rm sym} &= \frac{1}{2}\left[\frac{\partial^2(\mathcal{E}/\rho_{\rm total})}{\partial t^2}\right]_{t=0} \\ &= \left(\frac{g_\rho}{m_\rho}\right)^2 \frac{k_{F_{\rm sat}}^3}{12\pi^2} + \left[\frac{k_{F_{\rm sat}}^2}{3\sqrt{k_{F_{\rm sat}}^2 + (M_n^{*2})_{\rm sat}}} + \frac{k_{F_{\rm sat}}^2}{12\sqrt{k_{F_{\rm sat}}^2 + (M_p^{*2})_{\rm sat}}}\right]. \end{aligned} \tag{A.119}$$

Alternatively, in the case of charge symmetry in which the proton and neutron masses are degenerate,

$$a_{\rm sym} = \left(\frac{g_\rho}{m_\rho}\right)^2 \frac{k_{F_{\rm sat}}^3}{3\pi^2} + \left[\frac{k_{F_{\rm sat}}^2}{6\sqrt{k_{F_{\rm sat}}^2 + (M_N^{*2})_{\rm sat}}}\right], \tag{A.120}$$

where now the subscript N refers to the degenerate nucleon mass.

It is this that we need to fit to the experimental result of $a_{\rm sym} = 32.5$ MeV using the ρ meson coupling g_ρ. We can therefore find the value that satisfies this by rearrangement

$$g_\rho = \left(\frac{3\pi^2 m_\rho^2}{k_{F_{\rm sat}}^3}\left[a_{\rm sym} - \frac{k_{F_{\rm sat}}^2}{12\sqrt{k_{F_{\rm sat}}^2 + (M_n^{*2})_{\rm sat}}} - \frac{k_{F_{\rm sat}}^2}{12\sqrt{k_{F_{\rm sat}}^2 + (M_p^{*2})_{\rm sat}}}\right]\right)^{1/2} \tag{A.121}$$

which only relies on knowing the saturation density (here, $\rho_0 = 0.16$ fm^{-3}) and the effective masses at saturation, and thus varies from model to model.

A.5.5 Chemical Potential

In this section we will consider Fermi–Dirac statistics—that of fermions with half-integer spin—in order to carefully define the chemical potential and associated quantities.

We consider the Grand Canonical Partition Function (GCPF), which describes a grand canonical ensemble in which the system can exchange both heat and particles with the environment at fixed temperature T, fixed volume V, and fixed chemical potential μ.

The general expression for a GCPF is

$$\mathcal{Z}_{\rm GC} = \prod_i \mathcal{Z}_i = \prod_i \sum_{\{n_i\}} e^{-\beta n_i(\epsilon_i - \mu)}, \tag{A.122}$$

where $\beta = 1/kT$, and $\{n_i\}$ is the set of occupation numbers which satisfy

$$\sum_i n_i = N, \tag{A.123}$$

for which the total number of particles is N, and for which i runs over the total number of states. Since we are considering fermions, the occupation numbers are restricted by the Pauli Exclusion Principle, and thus are only able to obtain the values 0 and 1, in which case the GCPF becomes

$$\mathcal{Z}_{\rm GC} = \prod_i \sum_{n_i=0}^{1} e^{-\beta n_i(\epsilon_i - \mu)} = \prod_i \left(1 + e^{-\beta(\epsilon_i - \mu)}\right). \tag{A.124}$$

The average number of particles in a state is defined in terms of the GCPF as

$$\langle N\rangle = \frac{1}{\beta}\frac{\partial}{\partial\mu}\ln\mathcal{Z}_{\mathrm{GC}}, \tag{A.125}$$

where the derivative for a natural logarithm dictates that

$$\langle N\rangle = \frac{1}{\beta\mathcal{Z}_{\mathrm{GC}}}\frac{\partial}{\partial\mu}\mathcal{Z}_{\mathrm{GC}}. \tag{A.126}$$

Inserting the expression for the GCPF of Eq. (A.124) into Eq. (A.126) we obtain

$$\langle N\rangle = \frac{1}{\beta\mathcal{Z}_{\mathrm{GC}}}\frac{\partial}{\partial\mu}\left[\prod_k\left(1+e^{-\beta(\epsilon_k-\mu)}\right)\right]. \tag{A.127}$$

Expanding the product notation gives

$$\langle N\rangle = \frac{1}{\beta\mathcal{Z}_{\mathrm{GC}}}\frac{\partial}{\partial\mu}\left[\left(1+e^{-\beta(\epsilon_1-\mu)}\right)\left(1+e^{-\beta(\epsilon_2-\mu)}\right)\ldots\right], \tag{A.128}$$

which makes clearer the action of the chain rule for the derivative, to give

$$\begin{aligned}\langle N\rangle \;=\; & \frac{1}{\beta\mathcal{Z}_{\mathrm{GC}}}\left[\left(\beta e^{-\beta(\epsilon_1-\mu)}\right)\prod_{i\neq1}\left(1+e^{-\beta(\epsilon_i-\mu)}\right)\right.\\ & \left.+\left(\beta e^{-\beta(\epsilon_2-\mu)}\right)\prod_{i\neq2}\left(1+e^{-\beta(\epsilon_i-\mu)}\right)+\ldots\right].\end{aligned} \tag{A.129}$$

Returning to the product notation, the result is

$$\langle N\rangle = \frac{1}{\beta\mathcal{Z}_{\mathrm{GC}}}\sum_k\left(\beta e^{-\beta(\epsilon_k-\mu)}\prod_{i\neq k}\left(1+e^{-\beta(\epsilon_i-\mu)}\right)\right). \tag{A.130}$$

Inserting again the expression for the CGPF, we obtain

$$\langle N\rangle = \frac{1}{\beta}\sum_k\frac{\beta e^{-\beta(\epsilon_k-\mu)}\prod_{i\neq k}\left(1+e^{-\beta(\epsilon_i-\mu)}\right)}{\prod_j\left(1+e^{-\beta(\epsilon_j-\mu)}\right)}, \tag{A.131}$$

which contracts neatly to

$$\langle N\rangle = \sum_k\frac{e^{-\beta(\epsilon_k-\mu)}}{1+e^{-\beta(\epsilon_k-\mu)}} = \sum_k\frac{1}{1+e^{\beta(\epsilon_k-\mu)}} = \sum_k\langle n_k\rangle = \sum_k n_F(\epsilon_k). \tag{A.132}$$

where $\langle n_i\rangle$ is the average occupation number also known as the Fermi–Dirac distribution.

Allowing for a continuous distribution rather than discrete sum, we can write this as

$$\langle N\rangle = \int_0^\infty \rho(\epsilon_k)\; n_F(\epsilon_k)\; d\epsilon_k, \tag{A.133}$$

where $\rho(\epsilon_k) = \sum_i \delta(\epsilon_k - \epsilon_i)$ is the density of states. In the zero temperature limit of $T \to 0$ ($\beta \to \infty$), the distribution $n_F(\epsilon_k)$ becomes a Heaviside step function

$$n_F(\epsilon_k) \to \theta(\mu - \epsilon_k) = \begin{cases} 0, & \text{if } \mu < \epsilon_k \\ 1, & \text{if } \mu \geq \epsilon_k \end{cases}, \tag{A.134}$$

and thus Eq. (A.133) becomes

$$\langle N \rangle = \int_0^\infty \rho(\epsilon_k)\ \theta(\mu - \epsilon_k)\ d\epsilon_k = \int_0^\mu \rho(\epsilon_k)\ d\epsilon_k, \tag{A.135}$$

since the largest value that ϵ_k can obtain is $\epsilon_k = \mu$, due to the Heaviside step function, Eq. (A.134). The lower limit is maintained since we still require that $\mu \geq 0$. The last level occupied therefore has energy $\epsilon_{k_{\max}} = \mu$, where μ is defined in Section 2.5, and thus the chemical potential is the energy of a particle at the top of the Fermi sea.

A.5.6 Relation to the First Law of Thermodynamics

The link between the equation of state for QHD/QMC written as

$$p = \rho_{\text{total}}^2 \frac{\partial}{\partial \rho_{\text{total}}} \left(\frac{\mathcal{E}}{\rho_{\text{total}}} \right), \tag{A.136}$$

and the first law of thermodynamics,

$$p\, dV = -dE, \tag{A.137}$$

can be seen when we consider that the number of particles A is constant, and so we can safely use this as a multiplicative factor,

$$p\, dV = -dE \quad \Rightarrow \quad p = -\frac{dE}{dV} = -\frac{d(E/A)}{d(V/A)}, \tag{A.138}$$

and recall that the particle number density (baryon density) is denoted by

$$\rho_{\text{total}} = A/V, \quad \therefore \frac{1}{\rho_{\text{total}}} = \frac{V}{A}. \tag{A.139}$$

We can differentiate Eq. (A.139) with respect to the baryon density to obtain

$$\frac{d}{d\rho_{\text{total}}} \left(\frac{V}{A} \right) = \frac{d}{d\rho_{\text{total}}} \left(\frac{1}{\rho_{\text{total}}} \right) = -\rho_{\text{total}}^{-2} \quad \Rightarrow \quad d\left(\frac{V}{A} \right) = -\rho_{\text{total}}^{-2}\, d\rho_{\text{total}}. \tag{A.140}$$

If we substitute this result back into Eq. (A.138) we find

$$p = \frac{-d(E/A)}{-\rho_{\text{total}}^{-2}\, d\rho_{\text{total}}}, \tag{A.141}$$

and if we note that the energy density is $\mathcal{E} = E/V = E\rho_{\text{total}}/A$, we can substitute the differential to find

$$dE = d\left(\frac{\mathcal{E} A}{\rho_{\text{total}}} \right) \quad \Rightarrow \quad d(E/A) = d\left(\frac{\mathcal{E}}{\rho_{\text{total}}} \right), \tag{A.142}$$

and our final result becomes

$$p = \rho_{\text{total}}^2 \frac{d}{d\rho_{\text{total}}} \left(\frac{\mathcal{E}}{\rho_{\text{total}}} \right) = -\frac{dE}{dV}. \tag{A.143}$$

and thus the EOS is related to the first law of thermodynamics.

A.6 Hartree QHD Energy Density

If we wish to extend the sophistication of the QHD model, we can include higher-order (in the baryon-meson coupling g) terms by using a perturbative method. The logical next term to include is the one-loop correction to the self-energy. In order to do this, we must first formulate Hartree QHD using propagators (see Appendix A.2) in order to understand how the next term is introduced. We begin with Dyson's Equation for baryons;

$$G(k) = G^0(k) + G^0(k)\Sigma G(k), \tag{A.144}$$

where $G(k)$ is the exact (dressed) baryon propagator, $G^0(k)$ is the bare baryon propagator, and Σ is the baryon self-energy. Eq. (A.144) can be represented as a Feynman diagram, as shown in Fig. A.5.

Up to second-order, this can be written as

$$iG^{(2)}(k) = iG^0(k) + iG^0(k)\Sigma G^0(k), \tag{A.145}$$

The second-order (in the coupling g) self-energy is written in terms of a scalar part and a Dirac-vector part (c.f. Eq. (2.67) in which we consider the case of Lorentz-covariance)

$$\begin{aligned} \Sigma(k) &= \Sigma^s(k) - \gamma_\mu \Sigma^\mu(k) \\ &= \Sigma^s(|\vec{k}|, k^0) - \gamma_0 \Sigma^0(|\vec{k}|, k^0) + \vec{\gamma}\cdot\vec{k}\,\Sigma^v(|\vec{k}|, k^0). \end{aligned} \tag{A.146}$$

where the scalar and vector contributions for a single baryon B (with interactions involving σ and ω mesons) are

$$\Sigma^{(2)}_{Bs} = -ig_{B\sigma}\sum_{B'} g_{B'\sigma}\Delta^0(0)\int \frac{d^4q}{(2\pi)^4}\,\mathrm{Tr}\left[G^0(q)\right]e^{iq^0\eta}, \tag{A.147}$$

$$\Sigma^{(2)\,\mu}_{Bv} = ig_{B\omega}\sum_{B'} g_{B'\omega}D^{0\,\mu\nu}(0)\int \frac{d^4q}{(2\pi)^4}\,\mathrm{Tr}\left[G^0(q)\gamma_\nu\right]e^{iq^0\eta}, \tag{A.148}$$

where the exponential factor ensures that the integrals are finite, and which can be represented as second-order baryon tadpole diagrams as per Fig. A.6.

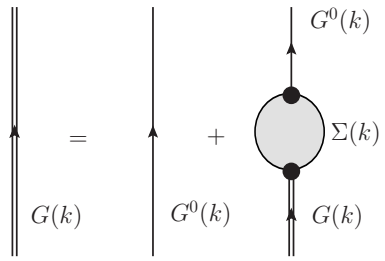

Fig. A.5: Feynman diagram for Dyson's Equation as per Eq. (A.144). Here, the double line represents $G(k)$; the full, self-consistent dressed baryon propagator, and the single line represents $G^0(k)$; the bare baryon propagator. $\Sigma(k)$ represents the self-energy.

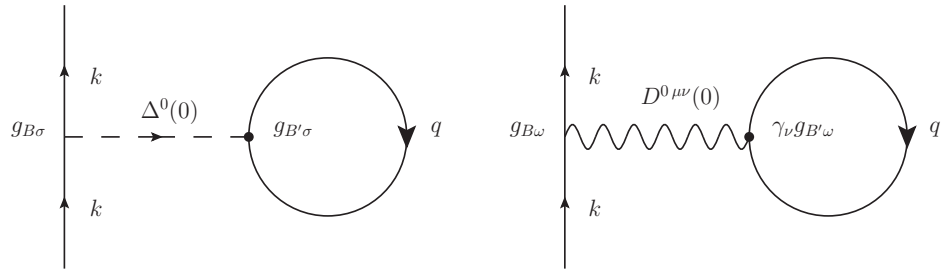

Fig. A.6: Feynman diagram for second-order self-energies (tadpoles) of Eqs. (A.147–A.148).

The second-order tadpole contributions to the meson propagators are given by

$$
\begin{aligned}
i\Delta^{(2)}(q) &= i\Delta^0(q)\left\{ i(2\pi)^4\delta^{(4)}(q)\left[\sum_{B'} g_{B'\sigma}\int \frac{d^4k}{(2\pi)^4}\,\mathrm{Tr}\left[G^0(k)\right]e^{ik^0\eta}\right]^2\right\}\Delta^0(q) \\
&= (2\pi)^4\delta^{(4)}(q)\left[\Sigma^{(2)}_{Bs}\right]^2/g^2_{B\sigma} \qquad \text{(A.149)} \\
iD^{(2)}_{\mu\nu}(q) &= (2\pi)^4\delta^{(4)}(q)\left[\sum_{B'}\Sigma^{(2)\,\mu}_{Bv}\Sigma^{(2)\,\nu}_{Bv}\right]/g^2_{B\omega} \qquad \text{(A.150)}
\end{aligned}
$$

which can be represented as Feynman diagrams as per Fig. A.7.

The lowest-order Dyson's equation is not strictly self-consistent, since the background particles in Σ are treated as non-interacting. However, since the *exact* Green's function can be expressed as a series containing the proper self-energy, self-consistency can be achieved, but only if we use the interacting propagators to determine the self-energy. This condition defines the Relativistic Hartree Approximation (RHA), thus Dyson's Equation is written in terms of the Hartree propagators as

$$G^H(k) = G^0(k) + G^0(k)\Sigma_{(H)}G^H(k), \qquad \text{(A.151)}$$

where $G^H(k)$ is the Hartree propagator, and $\Sigma_{(H)}$ is the Hartree self-energy given by

$$\Sigma_{(H)} = \Sigma_{(H)s} - \gamma_\mu\Sigma^\mu_{(H)v}. \qquad \text{(A.152)}$$

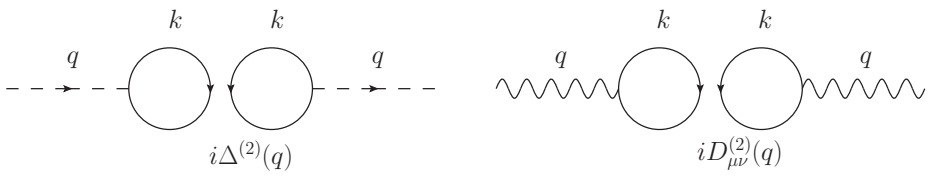

Fig. A.7: Feynman diagram for second-order meson tadpoles. Note that the momentum is conserved, as the loops flow in opposite directions.

Eq. (A.152) can be represented as a Feynman diagram as Fig. A.8, where the cross in the scalar tadpole indicates that it has been renormalized with counterterms, the result of which is that the free propagator is taken at $k = 0$. The expression for the Hartree self-energy is then

$$\Sigma_{(H)Bs} = ig_{B\sigma} \sum_{B'} \frac{g_{B'\sigma}}{m_\sigma^2} \int \frac{d^4q}{(2\pi)^4} \, \mathrm{Tr}\left[G^H(q)\right] e^{iq^0\eta} + \Sigma_{\mathrm{CTC}}, \tag{A.153}$$

$$\Sigma^\mu_{(H)Bv} = ig_{B\omega} \sum_{B'} \frac{g_{B'\omega}}{m_\omega^2} \int \frac{d^4q}{(2\pi)^4} \, \mathrm{Tr}\left[\gamma_\mu G^H(q)\right] e^{iq^0\eta}. \tag{A.154}$$

where we note that the bare meson propagator is replaced with the square of the meson mass. The expression for the scalar self-energy includes a counterterm Σ_{CTC} to render the integral finite via renormalization. This problem is however overcome easily, as we will show.

In this RHA case, the meson propagators are given by

$$\Delta^H(k) = \Delta^0(k) - i(2\pi)^4\delta^{(4)}(k)\left(\Sigma_{(H)Bs}\right)^2/g^2_{B\sigma} \tag{A.155}$$

$$D^H_{\mu\nu}(k) = D^0_{\mu\nu}(k) - i(2\pi)^4\delta^{(4)}(k)\left(\Sigma^\mu_{(H)Bv}\Sigma^\nu_{(H)Bv}\right)/g^2_{B\omega}. \tag{A.156}$$

and are represented as Feynman diagrams in Fig. A.9. The formal solution to Dyson's Equation gives

$$G^H(k) = \frac{G^0(k)}{1 - G^0(k)\Sigma_{(H)}}, \tag{A.157}$$

which we can rearrange in order to define the propagator, as

$$\left[G^H(k)\right]^{-1} = \left[G^0(k)\right]^{-1} - \Sigma_{(H)} = \gamma_\mu k^\mu - M - \Sigma_{(H)}, \tag{A.158}$$

where $\Sigma_{(H)}$ here represents the average interaction felt by propagating particles, and is independent of k. By considering the particles to be immersed in a Fermi sea, we can write the Hartree propagator as a sum of Fermi (corresponding to the antibaryon contributions) and Dirac (a direct result of the Fermi sea) components, as

$$\begin{aligned} G^H(k) &= G^H_F(k) + G^H_D(k) \\ &= (\gamma_\mu k^{*\mu} + M)\left[\left((k^*_\nu)^2 - M^{*\,2} + i\epsilon\right)^{-1} + \frac{i\pi}{E^*(k)}\delta(k^0 - E(k))\theta(k_F - |\vec{k}|)\right], \end{aligned} \tag{A.159}$$

Fig. A.8: Feynman diagram for the RHA self-energy, where the double line represents the exact (Hartree) propagator.

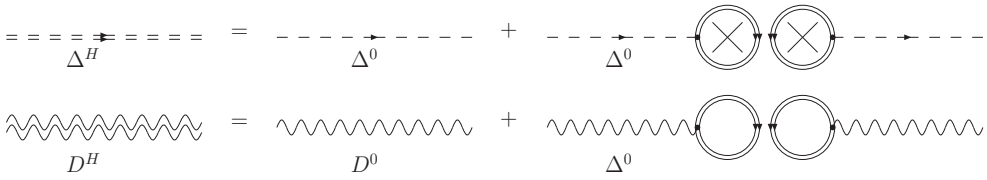

Fig. A.9: Feynman diagram for the meson propagators, where the double line represents the exact (Hartree) propagator.

where the following definitions have been applied

$$\begin{aligned} k^{*\mu} &= k^\mu + \Sigma^\mu_{(H)v}, & E^*(k) &= \left(\vec{k^*}^2 + M^{*\,2}\right)^{1/2}, \\ M^* &= M + \Sigma_{(H)s}, & E(k) &= E^*(k) - \Sigma^0_{(H)v}, \end{aligned} \tag{A.160}$$

where $E(k)$ is the self-consistent, single-particle energy, calculated on-shell.

Since the G_F^H term corresponds to the sum over all occupied states in the negative energy sea of quasibaryons, we can drop this term in the Hartree propagator, thus

$$G^H(k) = G_D^H(k) = (\gamma_\mu k^{*\mu} + M^*)\,\frac{i\pi}{E^*(k)}\delta(k^0 - E(k))\theta(k_F - |\vec{k}|). \tag{A.161}$$

The G_D^H term corresponds to the filled Fermi sea, and produces a finite MFT result. Thus the counterterms in Eq. (A.153) are of no concern. We may now drop the Hartree subscript, and all quantities are defined in the mean-field. If we now evaluate the scalar self-energy contributions we find

$$\begin{aligned} \Sigma_{Bs} &= ig_{B\sigma}\sum_{B'}\frac{g_{B'\sigma}}{m_\sigma^2}\int\frac{d^4q}{(2\pi)^4}\,\mathrm{Tr}\left[G_D^H(q)\right] \\ &= -g_{B\sigma}\sum_{B'}\frac{g_{B'\sigma}}{m_\sigma^2}\frac{(2J_{B'}+1)}{(2\pi)^3}\int_0^{k_{F_{B'}}}\frac{M_B^*}{E_B^*(q)}d^3q \\ &\equiv -g_{B\sigma}\langle\sigma\rangle. \end{aligned} \tag{A.162}$$

and for the vector self-energy contribution we find

$$\begin{aligned} \Sigma^\mu_{Bv} &= ig_{B\omega}\sum_{B'}\frac{g_{B'\omega}}{m_\omega^2}\int\frac{d^4q}{(2\pi)^4}\,\mathrm{Tr}\left[\gamma^\mu G_D^H(q)\right] \\ &= -g_{B\omega}\sum_{B'}\frac{g_{B'\omega}}{m_\omega^2}\frac{(2J_{B'}+1)}{(2\pi)^4}\int_0^{k_{F_{B'}}}d^3q\;\delta^{\mu 0} \\ &\equiv -g_{B\omega}\langle\omega_\mu\rangle\delta^{\mu 0}, \end{aligned} \tag{A.163}$$

where the factor of J accounts for the spin states; 2 for each species of baryon. This contribution is often accounted for by a factor of $\gamma = 2n_B$ for n_B baryons, since degenerate baryons result in the same contribution. Since we are summing baryons individually, and not assuming degenerate masses, we use the factor $(2J_B + 1)$ which also counts spin states,

where all the baryons have $J_B = \frac{1}{2}$, thus each baryon contributes a factor of 2. The Dirac trace over the baryon propagator exists in order to couple the scalar propagator to the Dirac propagator. The result of taking the trace for the scalar self-energy is

$$\begin{aligned}\mathrm{Tr}\left[\gamma_\mu k^\mu + M^*\right] &= \mathrm{Tr}\left[\gamma_0 k^0 - \gamma_i k^i + M^*\right] \\ &= \mathrm{Tr}\left[\begin{pmatrix} \mathbb{I} & 0 \\ 0 & -\mathbb{I} \end{pmatrix} k^0 - \begin{pmatrix} 0 & \sigma_i \\ -\sigma_i & 0 \end{pmatrix} k^i + \begin{pmatrix} \mathbb{I} & 0 \\ 0 & \mathbb{I} \end{pmatrix} M^*\right] \\ &= 4M^* \,, \end{aligned} \tag{A.164}$$

where $\mathbb{I}$ is the 2×2 identity matrix, $\vec{\sigma}$ are the Pauli matrices (here we are using the Dirac basis for the gamma matrices) and M^* is the (degenerate) effective baryon mass.

To this point, we have defined the (Hartree) self-energies and the meson propagators in terms of these self-energies. In order to calculate the energy density we require a definition; the energy density is defined by the temporal components of the energy-momentum tensor.

The energy-momentum tensor operator can be expressed in terms of the Lagrangian density, as per Eq. (3.14), and by evaluating this for the scalar part of the Lagrangian density we find the energy-momentum operator to be

$$\hat{T}_s^{\mu\nu} = -\frac{1}{2}\left[\partial_\alpha\sigma\partial^\alpha\sigma - m_\sigma^2\sigma^2\right]\mathrm{g}^{\mu\nu} + \partial^\mu\sigma\partial_\mu\sigma. \tag{A.165}$$

The 'physical' energy-momentum tensor for a particle is defined as the vacuum expectation value of the particle field subtracted from the ground-state expectation value of the energy-momentum tensor operator, thus for the scalar mesons, the energy-momentum tensor is

$$T_s^{\mu\nu} = \langle\Psi|\hat{T}_s^{\mu\nu}|\Psi\rangle - \mathrm{VEV} = \left\{-i\int\frac{d^4k}{(2\pi)^4}\left[\frac{1}{2}(k^2 - m_\sigma^2)\mathrm{g}^{\mu\nu} - k^\mu k^\nu\right]\Delta(k)\right\} - \Delta^0, \tag{A.166}$$

where the momenta arise from the derivatives above. The energy density is simply the temporal components of this expression, evaluated with the appropriate propagator;

$$\begin{aligned}\mathcal{E}_s &= \langle\Psi|\hat{T}_s^{00}|\Psi\rangle - \mathrm{VEV} \\ &= -i\int\frac{d^4k}{(2\pi)^4}\left[\frac{1}{2}(k^2 - m_\sigma^2)g^{00} - k^0k^0\right] \\ &\quad\times\left\{\Delta^0(k) - i(2\pi)^4\delta^{(4)}(k)\left(\Sigma_{H_s}\right)^2/g_{B\sigma}^2 - \Delta^0(k)\right\} \\ &= i^2\int\frac{d^4k}{(2\pi)^4}(2\pi)^4\delta^{(4)}(k)\left\{\frac{1}{2}(k^2 - m_\sigma^2) - (k^0)^2\right\}\langle\sigma\rangle^2 \\ &= \frac{1}{2}m_\sigma^2\langle\sigma\rangle^2, \end{aligned} \tag{A.167}$$

where we have used the fact that the VEV of a time-ordered product of operators produces the free propagator

$$\mathrm{VEV} \propto \langle 0|T[\phi(x)\phi(y)]|0\rangle = i\Delta^0(x-y). \tag{A.168}$$

The momentum k vanishes due to the integral over $\delta^{(4)}(k)$ and the contribution to the self-energy from the scalar meson is as found above. The vector contribution is similarly

$$\mathcal{E}_v = \langle\Psi|\hat{T}_v^{00}|\Psi\rangle - \mathrm{VEV} = -\frac{1}{2}m_\omega^2\langle\omega\rangle^2, \tag{A.169}$$

and the baryon contribution is

$$\begin{aligned}\mathcal{E}_B = \langle\Psi|\hat{T}_B^{00}|\Psi\rangle &= -i\sum_B \int \frac{d^4k}{(2\pi)^4}\,\mathrm{Tr}[\gamma_0 G_D^H(k)]k^0 \\ &= \sum_B \frac{(2J_B+1)}{(2\pi)^3}\int_0^{k_{F_B}} E_B^*(k)\,d^3k - \rho_{\mathrm{total}}\Sigma_v^0 \end{aligned} \tag{A.170}$$

where we do not require a VEV contribution for the baryon term because $G_D^H(k) \to 0$ as $k_F \to 0$, and

$$\rho_{\mathrm{total}}\Sigma_v^0 = -m_\omega^2\langle\omega\rangle^2, \tag{A.171}$$

which when added to the vector meson contribution changes the sign of that term. The total energy density for the system of scalar and vector mesons interacting with baryons for Hartree QHD is therefore the sum of these components,

$$\begin{aligned}\mathcal{E}_{\mathrm{QHD}} &= \mathcal{E}_B + \mathcal{E}_v + \mathcal{E}_s \\ &= \sum_B \frac{(2J_B+1)}{(2\pi)^3}\int_0^{k_{F_B}} E_B^*(k)\,d^3k + \frac{1}{2}m_\omega^2\langle\omega\rangle^2 + \frac{1}{2}m_\sigma^2\langle\sigma\rangle^2. \end{aligned} \tag{A.172}$$

We can now investigate the effects of additional terms in the self-energy and propagators to extend the sophistication of a model. By using this perturbative method we are able to identify the next leading order contributions, and we can include them into our calculations without changing the method.

A.7 Hartree–Fock QHD Energy Density

We can now calculate the effect of introducing the next order term in the baryon self-energy. To do this, we consider the next likely Feynman diagram based on the Lagrangian density. Analogous to the Hartree case, the self-energy contains a tadpole term, and now an additional exchange contribution

$$\Sigma_\sigma(k) = ig_{B\sigma}\int \frac{d^4q}{(2\pi)^4}\left[\sum_{B'} g_{B'\sigma}\frac{\mathrm{Tr}[G(q)]}{m_\sigma^2}e^{iq^0\eta} + \frac{g_{B\sigma}G(q)}{(k-q)_\mu^2 - m_\sigma^2 + i\epsilon}\right], \tag{A.173}$$

$$\Sigma_\omega(k) = ig_{B\omega}\int \frac{d^4q}{(2\pi)^4}\left[\sum_{B'} g_{B'\omega}\frac{\mathrm{Tr}[\gamma_\mu G(q)]}{m_\omega^2}e^{iq^0\eta} + \frac{g_{B\omega}\gamma_\mu \mathrm{g}^{\mu\nu}G(q)\gamma_\nu}{(k-q)_\lambda^2 - m_\omega^2 + i\epsilon}\right]. \tag{A.174}$$

These self-energy terms depend on the baryon propagator G, and in a fashion similar to that of the Hartree method, we can drop the $G_F(k)$ components (which correspond to antibaryons), leaving $G_D(k)$ (the component that arises as a result of the immersion in the Fermi sea) as the full propagator.

Using the expression for G_D of Eq. (A.161), the self-energies can be separated into terms proportional to the identity matrix $\mathbb{I}$, and terms proportional to gamma matrices as per Eq. (A.146) such that

$$\begin{aligned}\Sigma_B &= \Sigma_{Bs} - \gamma_\mu \Sigma_B^\mu \\ &= \Sigma_{Bs} - \gamma_0 \Sigma_{B0} + \vec{\gamma}\cdot\vec{k}\,\Sigma_{Bv}. \end{aligned} \tag{A.175}$$

These contributions can be represented as Feynman diagrams, as shown in Fig. A.10 where we have shown the effect of using Dyson's equation to illustrate the infinite sum of terms involved.

Some of the integrals can then be performed to produce the Hartree results plus the Fock additions due to the exchange terms in the self-energy. For the scalar meson σ, the component of the Eq. (A.173) proportional to $\mathbb{I}$ is

$$\begin{aligned}(\Sigma_\sigma)_{Bs} &= i g_{B\sigma} \int \frac{d^4q}{(2\pi)^4} \left[\sum_{B'} g_{B'\sigma} \frac{M^*_{B'} i\pi}{E^*_{B'} m_\sigma^2} \delta(q^0 - E(q)) \theta(q_F - |\vec{q}|) e^{iq^0\eta} \right. \\ &\quad \left. + g_{B\sigma} \frac{M^*_B i\pi}{E^*_B} D_\sigma \delta(q^0 - E(q)) \theta(q_F - |\vec{q}|) \right] \\ &= -g_{B\sigma} \sum_{B'} \pi \int_0^{q_F} \frac{d^3q}{(2\pi)^4} \frac{M^*}{E^*} \left(g_{B'\sigma} \frac{4}{m_\sigma^2} + g_{B\sigma} D_\sigma \right) \end{aligned} \tag{A.176}$$

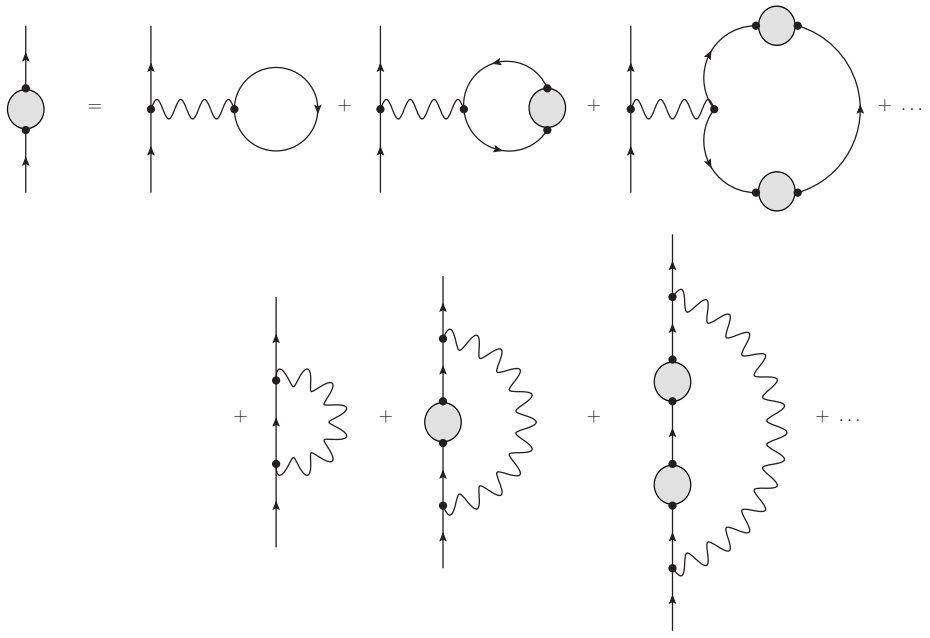

Fig. A.10: Summation of Feynman diagrams for all possible (vector) interaction terms contributing to the Hartree–Fock self-energy. Similar diagrams exist for the scalar meson interactions.

we can separate the two terms in Eq. (A.176) into Hartree and Fock components, as

$$(\Sigma_\sigma)_{Bs} = \underbrace{-g_{B\sigma}\sum_{B'}\frac{g_{B'\sigma}}{m_\sigma^2}\frac{(2J_{B'}+1)}{(2\pi)^3}\int_0^{q_F}\frac{M^*_{B'}}{E^*_{B'}}\,d^3q}_{\Sigma_{\rm Hartree}=-g_{B\sigma}\langle\sigma\rangle} \quad \underbrace{-\frac{g_{B\sigma}^2}{2(2\pi)^3}\int_0^{q_F}\frac{M^*_B}{E^*_B}D_\sigma\,d^3q}_{\Sigma_{\rm Fock}}. \tag{A.177}$$

We can expand the meson propagator in Fock term carefully, thus

$$\begin{aligned}
\Sigma_{\rm Fock} &= -\frac{g_{B\sigma}^2}{2(2\pi)^3}\int_0^{q_F}\frac{M^*}{E^*}\left[(k-q)_\mu^2 - m_\sigma^2 + i\epsilon\right]^{-1} d^3q \\
&= \frac{g_{B\sigma}^2}{2(2\pi)^3}\int_0^{q_F}\frac{M^*}{E^*}\left[\vec{k}^2+\vec{q}^{\,2} - (E(k)-E(q))^2 - 2|\vec{k}\,||\vec{q}|\cos\theta + m_\sigma^2 + i\epsilon\right]^{-1} d^3q \\
&= \frac{g_{B\sigma}^2}{2(2\pi)^3}\int_0^{q_F}\frac{M^*}{E^*}\left[A_\sigma(k,q) - 2|\vec{k}\,||\vec{q}|\cos\theta\right]^{-1} d^3q,
\end{aligned} \tag{A.178}$$

where we simplify this expression using

$$A_\sigma(k,q) = \vec{k}^2 + \vec{q}^{\,2} - (E(k)-E(q))^2 + m_\sigma^2 + i\epsilon. \tag{A.179}$$

Currently, this triple integral is over momentum $\vec{q} = (q_1, q_2, q_3)$ but we can change to spherical coordinates using the relation

$$\int d^3q = \int_0^\infty dq_1\int_0^\infty dq_2\int_0^\infty dq_3 \to \int_0^\infty q^2dq\int_0^\pi \sin(\theta)d\theta\int_0^{2\pi} d\phi. \tag{A.180}$$

We can also change the integration parameter $d\theta \to d(\cos(\theta))$ since $d(\cos(\theta)) = -\sin(\theta)d\theta$

$$\int d^3q \to \int_0^\infty q^2dq\int_0^\pi \sin(\theta)d\theta\int_0^{2\pi} d\phi \to \int_0^\infty q^2dq\int_{-1}^1 d(\cos(\theta))\int_0^{2\pi} d\phi. \tag{A.181}$$

Performing the integral over ϕ (since the integrand doesn't depend on this) we get

$$\int d^3q \to (2\pi)\int_0^\infty q^2dq\int_{-1}^1 d(\cos(\theta)). \tag{A.182}$$

The integral over $\cos(\theta)$ is possible using the identity

$$\int [A-Bx]^{-1}\,dx = -\frac{1}{B}\ln|A-Bx|, \tag{A.183}$$

and thus we have

$$\begin{aligned}
\Sigma_{\rm Fock} &= \frac{2\pi g_{B\sigma}^2}{2(2\pi)^3}\int_0^{q_F}\frac{M^*}{E^*}\frac{q^2}{2kq}\ln\left(\frac{A_\sigma(k,q)+2kq}{A_\sigma(k,q)-2kq}\right)dq \\
&= \frac{g_{B\sigma}^2}{16\pi^2k}\int_0^{q_F}\frac{M^*}{E^*}q\ln\left(\frac{A_\sigma(k,q)+2kq}{A_\sigma(k,q)-2kq}\right)dq \\
&= \frac{1}{4\pi^2k}\int_0^{q_F}\frac{M^*}{E^*}\frac{q}{4}g_{B\sigma}^2\Theta(k,q)\,dq,
\end{aligned} \tag{A.184}$$

where we use the definitions

$$\Theta_i(k,q) = \ln\left|\frac{A_i(k,q)+2kq}{A_i(k,q)-2kq}\right|, \tag{A.185}$$

$$\Phi_i(k,q) = \frac{1}{4kq}A_i(k,q)\Theta_i(k,q)-1, \tag{A.186}$$

$$A_i(k,q) = \vec{k}^{\,2}+\vec{q}^{\,2}+m_i^2-[E(q)-E(k)]^2, \tag{A.187}$$

and note that $q=|\vec{q}|$, $k=|\vec{k}\,|$. All of these self-energies are evaluated on shell at the self-consistent single-particle energies.

The total Hartree–Fock self-energy for the σ and ω mesons is given by

$$\begin{aligned}\Sigma_{Bs}(k,E(k)) &= g_{B\sigma}\sum_{B'}\frac{-(2J_{B'}+1)}{(2\pi)^3}\frac{g_{B'\sigma}}{m_\sigma^2}\int_0^{k_{F_{B'}}}\frac{M^*_{B'}(q)}{E^*_{B'}(q)}\,d^3q \\ &\quad+\frac{1}{4\pi^2k}\int_0^{k_{F_B}} q\,dq\frac{M^*_B(q)}{E^*_B(q)}\left[\frac{1}{4}g^2_{B\sigma}\Theta_\sigma(k,q)-g^2_{B\omega}\Theta_\omega(k,q)\right],\end{aligned} \tag{A.188}$$

$$\begin{aligned}\Sigma_{B0}(k,E(k)) &= g_{B\sigma}\sum_{B'}\frac{-(2J_{B'}+1)}{(2\pi)^3}\frac{g_{B'\omega}}{m_\omega^2}\int_0^{k_{F_{B'}}} d^3q \\ &\quad-\frac{1}{4\pi^2k}\int_0^{k_{F_B}} q\,dq\left[\frac{1}{4}g^2_{B\sigma}\Theta_\sigma(k,q)+\frac{1}{2}g^2_{B\omega}\Theta_\omega(k,q)\right],\end{aligned} \tag{A.189}$$

$$\Sigma_{Bv}(k,E(k)) = -\frac{1}{4\pi^2k}\int_0^{k_F} q\,dq\frac{q^*}{E^*(q)}\left[\frac{1}{2}g^2_{B\sigma}\Phi_\sigma(k,q)+g^2_{B\omega}\Phi_\omega(k,q)\right], \tag{A.190}$$

where the terms involving a sum over B' correspond to the Hartree results. The calculations that include only these Fock contributions are denoted by the term 'Fock1' in our presentation of results. These are calculated to provide an insight into the effect that these terms have on the EOS. The energy density can still be calculated as per the previous section, and although no new terms appear with the addition of the Fock contribution to the self-energy, the definitions of the terms appearing in the energy density now include this contribution.

We can however calculate an explicit additional contribution to the energy density; we recall from the previous section that the energy density is defined in terms of the physical energy momentum tensor, which involves propagators, as per Eq. (A.166). The second term that we can include is an additional component to the interacting meson propagators due to the effect of medium polarization, in analogy with electric polarization (see Section 3.5).

The Feynman diagram for the medium polarization contribution to the scalar propagator is given by the third term in Fig. A.11, where the first term corresponds to the bare propagator, and the second term corresponds to the Hartree contribution. The contribution due to medium polarization for the scalar propagator is given by

$$\Delta'(k) = \Delta^0\Pi_\sigma(k)\Delta^0(k) \tag{A.191}$$

$$\Pi_s(k) = -i\sum_B g^2_{B\sigma}\int\frac{d^4q}{(2\pi)^4}\,\mathrm{Tr}\left[G_D(q)G_D(k+q)\right], \tag{A.192}$$

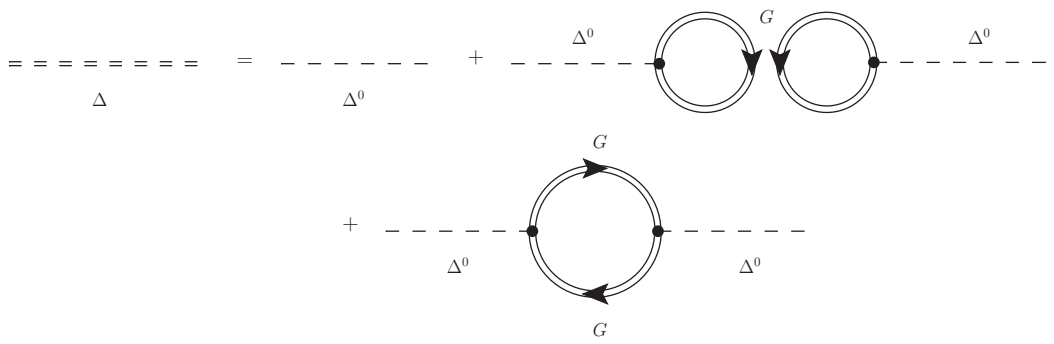

Fig. A.11: The three leading terms contributing to the meson propagator, in this case, the scalar meson. The first term corresponds to the bare propagator, the second term corresponds to the Hartree contribution, and the third term corresponds to the medium polarization term. Similar terms can be written for the vector meson.

and for the vector propagator,

$$D'_{\mu\nu}(k) = D^0_{\mu\lambda}\Pi^{\lambda\sigma}_{\omega}(k)D^0_{\sigma\nu}(k) \tag{A.193}$$

$$\Pi^{\lambda\sigma}_{\omega}(k) = -i\sum_B g^2_{B\omega}\int\frac{d^4q}{(2\pi)^4}\,\mathrm{Tr}\left[\gamma^\lambda G_D(k+q)\gamma^\sigma G_D(q)\right], \tag{A.194}$$

where Π_σ and $\Pi^{\lambda\sigma}_{\omega}$ are the medium polarizations. We can evaluate the physical energy-momentum tensor using the appropriate propagator which includes this medium polarization term. For example, the contribution due to baryon B for the scalar meson is given by

$$T^{\mu\nu}_s = \langle\Psi|\hat{T}^{\mu\nu}_s|\Psi\rangle - \mathrm{VEV} = \left\{-i\int\frac{d^4k}{(2\pi)^4}\left[\frac{1}{2}(k^2-m^2_\sigma)\mathrm{g}^{\mu\nu}-k^\mu k^\nu\right]\Delta(k)\right\} - \Delta^0, \tag{A.195}$$

where in this case, Δ is the three-part propagator in Fig. A.11, which we can separate into the three terms.

If we substitute Eq. (A.191) into the temporal components of the ground-state expectation value in Eq. (A.195) we have

$$\begin{aligned}\langle\Psi|\hat{T}^{00}_s|\Psi\rangle &= -i\int\frac{d^4k}{(2\pi)^4}\left[\frac{1}{2}(k^2-m^2_s)\mathrm{g}^{00}-(k^0)^2\right] \\ &\quad\times\Delta^0(k)\left\{-ig^2_{B\sigma}\int\frac{d^4q}{(2\pi)^4}\,Tr\left[G_D(q)G_D(k+q)\right]\right\}\Delta^0(k),\end{aligned} \tag{A.196}$$

where the Dirac part of the baryon propagator is defined as

$$G_D(k) = [\gamma^\mu k_\mu + M^*(k)]\,\frac{i\pi}{E^*(k)}\delta(k^0-E(k))\theta(k_F-|\vec{k}|), \tag{A.197}$$

in which we have neglected the vector component of the self-energy, since it is a k^{-2} term, and thus $k^* = k = (k^0, \vec{k}\,)$. Rather that working with the $G_D(k+q)$ term, since all of the above

integrals are over $(-\infty,\infty)$, we can shift the integration variables according to $k+q\to k'$, which can be rewritten as $k\to k'-q$. Eq. (A.196) then becomes

$$\begin{aligned}\langle\Psi|\hat{T}_s^{00}|\Psi\rangle &= -g_{B\sigma}^2\int\frac{d^4k'}{(2\pi)^4}\int\frac{d^4q}{(2\pi)^4}\left[\frac{1}{2}((k'-q)^2-m_s^2)\mathrm{g}^{00}-(k'^0-q^0)^2\right]\\ &\quad\times\Delta^0(k'-q)\left\{\mathrm{Tr}\left[G_D(q)G_D(k')\right]\right\}\Delta^0(k'-q),\end{aligned}\tag{A.198}$$

and so now we can work with the baryon Green's functions in single variables. The product of these is

$$\begin{aligned}G_D(q)G_D(k') &= -\frac{\pi^2}{E^*(q)E^*(k')}\left[\gamma^\mu q_\mu\gamma^\nu k'^\nu+\gamma^\mu q_\mu M^*(k')+\gamma^\nu k'_\nu M^*(q)+M^*(q)M^*(k')\right].\\ &\quad\times\delta(q^0-E(q))\theta(k_F-|\vec{q}|)\delta(k'^0-E(k'))\theta(k_F-|\vec{k'}|).\end{aligned}\tag{A.199}$$

Since γ_μ are traceless, and $\mathrm{Tr}[\gamma_a A^a\gamma_b B^b]=4A\cdot B$, the only terms to survive in the trace of Eq. (A.199) are

$$\begin{aligned}\mathrm{Tr}\left[G_D(q)G_D(k')\right] &= -\frac{4\pi^2}{E^*(q)E^*(k')}\left[q_\mu k'^\mu+M^*(q)M^*(k')\right]\\ &\quad\times\delta(q^0-E(q))\theta(k_F-|\vec{q}|)\delta(k'^0-E(k'))\theta(k_F-|\vec{k'}|).\end{aligned}\tag{A.200}$$

Substituting Eq. (A.200) back into Eq. (A.198), performing the temporal integrals, and applying the θ functions, we obtain

$$\begin{aligned}\langle\Psi|\hat{T}_s^{00}|\Psi\rangle &= \frac{4\pi^2 g_{B\sigma}^2}{(2\pi)^8}\int_0^{k_F}\frac{d^3q}{E^*(q)}\int_0^{k_F}\frac{d^3k'}{E^*(k')}\left[\frac{1}{2}((k'-q)^2-m_s^2)-(E(k')-E(q))^2\right]\\ &\quad\times\Delta^0(k'-q)\left[q_\mu k'^\mu+M^*(q)M^*(k')\right]\Delta^0(k'-q),\end{aligned}\tag{A.201}$$

noting that $\mathrm{g}^{00}=1$. With the definition of the free scalar propagator,

$$D_i^0(E(p),\vec{p})=(E(p)^2-\vec{p}^{\,2}-m_i^2)^{-1},\tag{A.202}$$

for which Δ^0 corresponds to D_σ^0. We can cancel the term that was proportional to g^{00}, leaving

$$\begin{aligned}\langle\Psi|\hat{T}_s^{00}|\Psi\rangle &= \frac{g_{B\sigma}^2}{(2\pi)^6}\int_0^{k_F}\frac{d^3q}{E^*(q)}\int_0^{k_F}\frac{d^3k'}{E^*(k')}\\ &\quad\times D_\sigma^0(k'-q)\left[\frac{1}{2}-D_\sigma^0(k'-q)(E(k')-E(q))^2\right]\\ &\quad\times\left[q_\mu k'^\mu+M^*(q)M^*(k')\right].\end{aligned}\tag{A.203}$$

The total energy contribution for all baryons is then the sum of these terms for all baryons. Further to this, we insert a factor of $(2J_B+1)$ for each baryon to account for spin counting, and an overall factor of $\frac{1}{2}$ due to the symmetry between q and k' which would otherwise result in overcounting.

A similar term exists for the vector meson contribution, in which the polarization term is

$$\Pi_\omega^{\delta\lambda}=-i\sum_B g_{B\omega}^2\int\frac{d^4q}{(2\pi)^4}\,\mathrm{Tr}\left[\gamma^\delta G_D(k+q)\gamma^\delta G_D(q)\right].\tag{A.204}$$

The combined energy contribution due to medium polarization of these mesons is therefore

$$\begin{aligned}\mathcal{E}_{\rm med-pol} = \; & \frac{1}{2}\sum_B \frac{2}{(2\pi)^6}\int_0^{k_{F_B}} \frac{d^3q}{E^*(q)}\int_0^{k_{F_B}} \frac{d^3k'}{E^*(k')} \\ & \left\{ g_{B\sigma}^2 D_\sigma^0(k'-q)\left[\frac{1}{2} - D_\sigma^0(k'-q)[E(k')-E(q)]^2\right]\right. \\ & \quad \times \left[q_\mu k'^\mu + M^*(q)M^*(k')\right] \\ & + g_{B\omega}^2 D_\omega^0(k'-q)\left[\frac{1}{2} - D_\omega^0(k'-q)[E(k')-E(q)]^2\right] \\ & \quad \left.\times \left[q_\mu k'^\mu - 2M^*(q)M^*(k')\right]\right\}. \end{aligned} \tag{A.205}$$

In order to perform numerical calculations for this quantity, we must expand this further. The propagator terms expand as

$$\begin{aligned} D_\sigma^0(k'-q) &= \left(\left[E(k')-E(q)\right]^2 - (\vec{k}-\vec{q})^2 - m_\sigma^2\right)^{-1} \\ &= \left(\left[E(k')-E(q)\right]^2 - \vec{k}^2 - \vec{q}^2 + 2|\vec{q}||\vec{k}'|\cos(\theta) - m_\sigma^2\right)^{-1}, \end{aligned} \tag{A.206}$$

and owing to the definition of the four-momentum,

$$k^\mu = \left[k^0 + \Sigma^0(k), \vec{k}\right] \overset{k^0\to E(k)}{=} \left[E^*(k), \vec{k}\right], \tag{A.207}$$

the product of the momentum four-vectors is

$$q_\mu k'^\mu = E^*(q)E^*(k') - |\vec{q}||\vec{k}'|cos(\theta), \tag{A.208}$$

so once again we need to shift the integration spherical coordinates according to Eq. (A.182), except that this time the $d(\cos(\theta))$ integral is non-trivial due to the $\cos(\theta)$ terms.

Expanding fully reveals the full expression,

$$\begin{aligned}\mathcal{E}_{\rm med-pol} = \; & \frac{1}{2}\sum_B \frac{(2J_B+1)}{(2\pi)^6}\int_0^{k_{F_B}} \frac{4\pi q^2 dq}{E^*(q)}\int_0^{k_{F_B}} \frac{2\pi k'^2 dk'}{E_B^*(k')}\int_{-1}^{1} d(\cos(\theta)) \\ & \left\{ g_{B\sigma}^2 D_\sigma^0(k'-q)\left[\frac{1}{2} - D_\sigma^0(k'-q)[E(k')-E(q)]^2\right]\right. \\ & \quad \times \left[E_B^*(q)E_B^*(k') - |\vec{q}||\vec{k}'|\cos(\theta) + M_B^*(q)M_B^*(k')\right] \\ & + g_{B\omega}^2 D_\omega^0(k'-q)\left[\frac{1}{2} - D_\omega^0(k'-q)[E(k')-E(q)]^2\right] \\ & \quad \left.\times \left[E_B^*(q)E_B^*(k') - |\vec{q}||\vec{k}'|\cos(\theta) - 2M_B^*(q)M_B^*(k')\right]\right\}. \end{aligned} \tag{A.209}$$

Combining the prefactors, we have

$$\begin{aligned}
\mathcal{E}_{\rm med-pol} &= \frac{1}{2}\sum_B \frac{1}{4\pi^4}\int_0^{k_{F_B}} \frac{q^2 dq}{E_B^*(q)} \int_0^{k_{F_B}} \frac{k'^2 dk'}{E_B^*(k')} \int_{-1}^{1} d(\cos(\theta)) \\
&\quad \left\{ g_{B\sigma}^2 D_\sigma^0(k'-q) \left[\frac{1}{2} - D_\sigma^0(k'-q)[E(k')-E(q)]^2\right]\right. \\
&\quad\quad \times \left[E_B^*(q)E_B^*(k') - |\vec{q}||\vec{k'}|\cos(\theta) + M_B^*(q)M_B^*(k')\right] \\
&\quad + g_{B\omega}^2 D_\omega^0(k'-q) \left[\frac{1}{2} - D_\omega^0(k'-q)[E(k')-E(q)]^2\right] \\
&\quad\quad \left. \times \left[E_B^*(q)E_B^*(k') - |\vec{q}||\vec{k'}|\cos(\theta) - 2M_B^*(q)M_B^*(k')\right]\right\}. \qquad \text{(A.210)}
\end{aligned}$$

Thus the total Hartree–Fock energy density is written as

$$\begin{aligned}
\mathcal{E}_{\rm HF} &= \sum_B \frac{(2J_B+1)}{(2\pi)^3}\int_0^{k_{F_B}} d^3k\ E(k) + \frac{1}{2}m_\sigma^2\langle\sigma\rangle^2 - \frac{1}{2}m_\omega^2\langle\omega\rangle^2 \\
&\quad + \frac{1}{2}\sum_B \frac{(2J_B+1)}{(2\pi)^6}\int_0^{k_{F_B}} \frac{d^3k}{E_B^*(k)} \int_0^{k_{F_B}} \frac{d^3q}{E_B^*(q)} \\
&\quad \times \left\{ g_{B\sigma}^2 D_\sigma^0(k-q)\left[\frac{1}{2} - [E(k)-E(q)]^2 D_\sigma^0(k-q)\right]\ \left[k^{*\mu}q_\mu^* + M^*(k)M^*(q)\right]\right. \\
&\quad \left. + 2g_{B\omega}^2 D_\omega^0(k-q)\ \left[\frac{1}{2} - [E(k)-E(q)]^2 D_\omega^0(k-q)\right][k^{*\mu}q_\mu^* - 2M^*(k)M^*(q)]\right\}, \\
& \qquad \text{(A.211)}
\end{aligned}$$

where the double integral is the contribution from the medium polarization.

Calculations performed that include the Fock contribution to the self-energy as well as this medium polarization energy are denoted by the term 'Fock2' in our presentation of results.

Particle Properties

Table B.1: Particle properties for selected leptons, baryons and mesons used in this work, as found in Ref. [17]. Shown here are the quark content (the valence quarks that define the particle), the isospin, spin, and parity quantum numbers, the mass, Lorentz character, and strangeness of each particle.

	quarks	$I(J^P)$	mass (MeV)	Lorentz	S
e^-	fundamental	$J = \frac{1}{2}$	0.51	scalar	—
μ^-	fundamental	$J = \frac{1}{2}$	105.66	scalar	—
τ^-	fundamental	$J = \frac{1}{2}$	1776.84	scalar	—
p	uud	$\frac{1}{2}(\frac{1}{2}^+)$	938.27	spinor	0
n	udd	$\frac{1}{2}(\frac{1}{2}^+)$	939.57	spinor	0
Λ	uds	$0(\frac{1}{2}^+)$	1115.68	spinor	-1
Σ^+	uus	$1(\frac{1}{2}^+)$	1189.37	spinor	-1
Σ^0	uds	$1(\frac{1}{2}^+)$	1192.64	spinor	-1
Σ^-	dds	$1(\frac{1}{2}^+)$	1197.45	spinor	-1
Ξ^0	uss	$\frac{1}{2}(\frac{1}{2}^+)$	1314.83	spinor	-2
Ξ^-	dss	$\frac{1}{2}(\frac{1}{2}^+)$	1321.31	spinor	-2
σ	$c_1(u\bar{u} + d\bar{d})$	$0(0^+)$	600	scalar i-scalar	0
f_0	$c_2(s\bar{s})$	$0(0^+)$	980	scalar i-scalar	0
a^0	$(u\bar{u} - d\bar{d})/\sqrt{2}$	$1(0^+)$	984.7	scalar i-vector	0
ω	$c_1(u\bar{u} + d\bar{d})$	$0(1^-)$	782.65	vector i-scalar	0
ϕ	$c_2(s\bar{s})$	$0(1^-)$	1019.46	vector i-scalar	0
$\rho^\pm$	$u\bar{d}/\bar{u}d$	$1(1^-)$	775.5	vector i-vector	0
ρ^0	$(u\bar{u} - d\bar{d})/\sqrt{2}$	$1(1^-)$	775.5	vector i-vector	0
η	$c_1(u\bar{u} + d\bar{d})$	$0(0^-)$	547.51	p-scalar i-scalar	0
η'	$c_2(s\bar{s})$	$0(0^-)$	957.78	p-scalar i-scalar	0
$\pi^\pm$	$u\bar{d}/\bar{u}d$	$1(0^-)$	134.98	p-scalar i-vector	0
π^0	$(u\bar{u} - d\bar{d})/\sqrt{2}$	$1(0^-)$	139.57	p-scalar i-vector	0

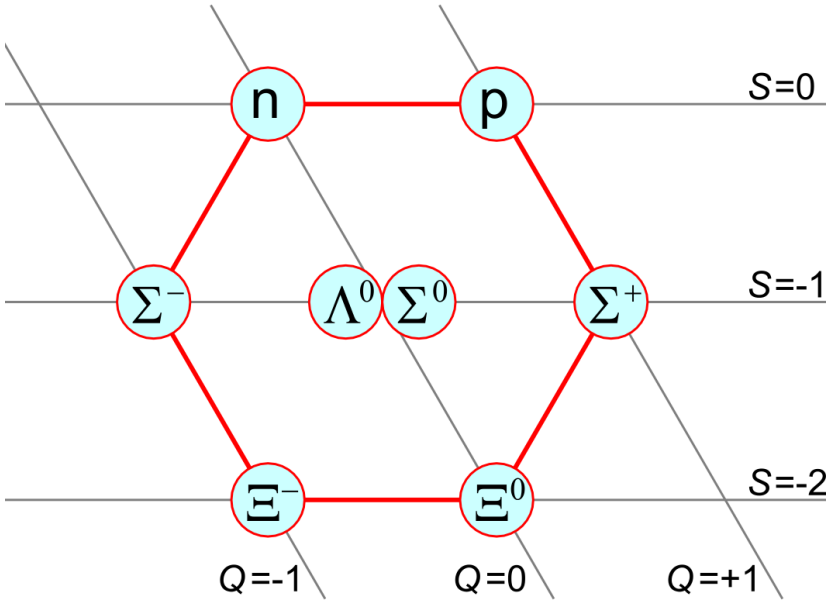

Fig. B.1: (Color Online) Diagram of the baryon octet showing strangeness and charge. Images for Figs. B.1–B.2 have been released into the public domain and published on wikipedia.org.

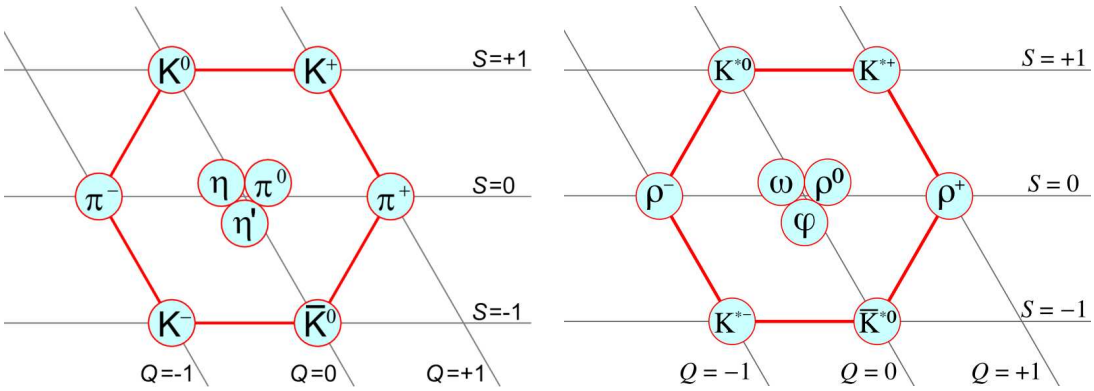

Fig. B.2: (Color Online) Diagrams of the spin-0 and spin-1 meson nonets showing strangeness and charge

Relevant Publication By The Author

The following pages contain a relevant article by the author, in which we describe the effects of the phase transition from the octet QMC model to various quark models, and which is published as Phys. Rev. C. 79, 045810 (Ref. [42]). The results presented in that article have not been performed and published by any other researchers, to the best of the author's knowledge, and as such constitute a novel contribution to the field.